GROWTH STUDY OF SIZE-SELECTED SILVER AND SILVER-COPPER CLUSTERS BY SCANNING TRANSMISSION ELECTRON MICROSCOPY

by

CHENG LI

A thesis submitted to the University of Birmingham for the degree of
DOCTOR OF PHILOSOPHY

Nanoscale Physics Research Laboratory
School of Physics and Astronomy
College of Engineering and Physical Sciences
University of Birmingham
April 2023

UNIVERSITY OF BIRMINGHAM

University of Birmingham Research Archive

e-theses repository

This unpublished thesis/dissertation is copyright of the author and/or third parties. The intellectual property rights of the author or third parties in respect of this work are as defined by The Copyright Designs and Patents Act 1988 or as modified by any successor legislation.

Any use made of information contained in this thesis/dissertation must be in accordance with that legislation and must be properly acknowledged. Further distribution or reproduction in any format is prohibited without the permission of the copyright holder.

Abstract

The unique physicochemical properties of nanoscale clusters highly depend on their sizes, morphologies, and atomic structures, which can be tuned during the cluster formation process. The physical synthesis procedures, especially the gas-phase synthesis approaches, exhibit great advantages on the atomic-precision size control with the usage of mass filters. However, understanding the relationship between the morphologies and atomic structures of clusters and their preparation parameters is still a big challenge for these physical methods. Transmission Electron Microscopy (TEM), a powerful tool in material science, provides the possibility to visualize the nanoscale clusters, investigate their morphologies and atomic structures, and further establish the relationship between these physical characteristics of clusters and their preparation parameters.

This thesis presents investigations on growth of size-selected Ag and AgCu clusters by magnetron sputtering. A magnetron sputtering inert gas condensation mass-selected cluster source was used to produce size-selected Ag and AgCu clusters, and aberration-corrected Scanning Transmission Electron Microscopy with high-angle annular dark field (HAADF-STEM) was used for morphology and atomic structure identification. By utilizing this information, the growth process of Ag and AgCu clusters in the magnetron chamber was revealed and understood.

The results demonstrate the tunability of morphologies for size-selected Ag clusters using different deposition parameters. When Ag clusters are deposited with sizes

smaller than the peak size observed in the mass spectrum, they exhibit a round shape. Conversely, larger Ag clusters exhibit an increased fraction of elongated morphologies as their size surpasses the peak size. With regard to the atomic structures of size-selected Ag clusters, despite the confirmation of Dh structure as the most stable form through e-beam irradiation and chip-heating experiments, the proportion of Ih structures predominates for size-selected Ag clusters within the size range of 1k to 14k. Additionally, the atomic structures of Ag8k clusters can be modified by varying the Ar and He gas flow rates. The increase in Ar gas flow rate promotes the cluster-cluster coalescence growth pathway, while the impact of increasing He gas flow rate on the growth pathway is negligible. Moreover, bimetallic core-shell Ag@Cu and Cu@Ag clusters were successfully prepared by adjusting the condensation lengths of two targets. In the case of prepared Ag@Cu clusters, the Cu atoms consistently arrange themselves according to the surface arrangement of the Ag core. However, it is common to observe a Cu-Ih or Cu-Dh core with an outer shell composed of Ag FCC domains in Cu@Ag core-shell clusters. This distinct atomic arrangement of the shell presents a novel approach for the controlled preparation of surface structures, offering potential insights into surface structure-controlled synthesis methods.

Acknowledgement

I would like to thank my supervisor Dr. Wolfgang Theis and Dr. Meng Gu for their continued encouragement and support. I appreciate Dr. Jun Yuan, Dr. Quanmin Guo, Dr. Andrey Kaplan, and Professor Leigh T. Canham for their helpful discussions on my project. Thanks should also go to Nanoscale Physics Research Laboratory (NPRL) in University of Birmingham and Southern University of Science and Technology (SUSTech) for providing me the opportunity to work on this project.

I'm also grateful for the support of my former supervisor, Dr. Ziyou Li. Without her endless encouragement and patience, I would have made no progress in such a new area for me. With great sadness, she passed away in December, 2020. I hope she can be healthy and happy in another world, and I will miss her forever.

I appreciate all my friends in NPRL and SUSTech, Yu Xia, Xutao Guo, Hanan Alhabeadi, Haoxuan Ding, Haoyu Zhao, Chunqiu Xia, Duojie Wu, and Cheng Zhen. We discussed a lot of things, not only about the academic research but also the interesting things in life.

Last but not the least, I would like to thank my parents and my love Rihan for their selfless love, understanding, support, and encouragement.

Contents

Abstract i
Acknowledgement iii
Contents iv
List of Figures vi
List of Tables xxii
List of Abbreviations xxiii
List of Publications xxiv
Chapter 1 Introduction 1
Chapter 2 Experimental Techniques 13
2.1 Magnetron sputtering inert gas condensation mass-selected cluster source 13
2.1.1 Components of the cluster source 13
2.1.2 Sputtering and cluster generation 14
2.1.3 Beam focusing and acceleration 20
2.1.4 Mass selection 21
2.1.5 Deposition of the clusters on the carbon film 22
2.1.6 Effects of preparation parameters on the size of clusters 24
2.2 Aberration-corrected Scanning Transmission Electron Microscopy (STEM) 29
2.2.1 Basic design of STEM and its components 29
2.2.2 Principle of imaging in STEM 31
2.2.3 Aberration corrected STEM 33
2.2.4 Data analysis with HAADF-STEM images 35
2.2.5 Structure identification of metal clusters using HAADF-STEM images 41
2.2.6 The effect of the deposition energy on the structures of Ag clusters 56
2.3 Protection of Ag clusters in high vacuum 58
2.3.1 Size evolution of Ag6525 exposed to air 59
2.3.2 Morphology evolution of Ag6525 exposed to the air 62
2.3.3 Composition evolution of Ag6525 exposed to the air 65
2.3.4 Ag6525 stored in a high vacuum for about one month 68
Chapter 3 Growth Study of Mass-selected Ag Clusters with HAADF-STEM 70
3.1 Introduction 70
3.2 Morphology distribution of size-selected Ag clusters 72
3.3 Structure distribution of size-selected Ag clusters with spherical shape 82
3.4 Structure distribution of size-selected Ag clusters with an elongated shape 86
3.5 Comparison between structures of spherical Ag clusters deposited with different parameters 94
3.6 Possible growth process of Ag clusters prepared in the magnetron sputtering chamber 97
3.7 Conclusions 108
Chapter 4 Exploration of the Equilibrium State of Ag Clusters in the Size Range of 1k to 14k by Electron Beam Irradiation and Chip-heating Experiments 110

4.1 Introduction 110
4.2 Structure transformation of Ag clusters under e-beam irradiation 110
4.3 Heating experiments of Ag8k clusters 123
4.3.1 Spherical Ag8k clusters heated to different temperatures 123
4.3.2 Aggregated Ag8k clusters heating at different temperatures 140
4.4 Heating experiment of Ag14k clusters 151
4.5 Conclusions 154
Chapter 5 Morphology- and Structure-controlled Deposition of Mass-selected Ag8k Clusters by Tuning the Gas Flow Rate of Ar and He 156
5.1 Introduction 156
5.2 Effects of Ar and He gas flow rate on growth ways of Ag clusters prepared by magnetron sputtering 157
5.3 Relationship between the shapes of mass spectra and cluster growth ways of Ag clusters 173
5.4 Conclusions 184
Chapter 6 Fabrication of Ag@Cu and Cu@Ag Core-shell Clusters by Magnetron Sputtering Cluster Source 186
6.1 Introduction 186
6.2 Fabrication of Ag@Cu core-shell clusters 187
6.2.1 The effect of the Cu target power on the preparation of Ag@Cu core-shell clusters 189
6.2.2 The effect of the selected size on the preparation of Ag@Cu core-shell clusters 196
6.2.3 The effect of the Cu target plasma on the preparation of Ag@Cu core-shell clusters 202
6.2.4 The atomic structures of Ag@Cu core-shell clusters 208
6.2.5 Summary 210
6.3 Fabrication of Cu@Ag core-shell clusters 211
6.4 Conclusions 216
Chapter 7 Conclusions and Outlook 218
7.1 Conclusions 218
7.2 Outlook 222
References 224
Appendix 232

List of Figures

Chapter 1

Figure 1.1: The schematic diagrams of Ih, Dh, Ino-Dh, and Marks-Dh structures. Replotted from the reference[42]. k is the atom number of the length of one edge in Ih. m and n are the atom numbers of the length and width of the {100} facets on the side surface in Ino-Dh and Marks-Dh. p is the atom number of the depth of re-entrant {111} facets in Marks-Dh. 5
Figure 1.2: The excess energies divided by the number of surface atoms of Ih, Dh, and FCC structures with increasing cluster size[8].....7

Chapter 2

Figure 2.1: (a) Photograph of the magnetron sputtering inert gas condensation mass-selected cluster source in NPRL; (b) schematic diagram of this cluster source. 14
Figure 2.2: Schematic diagrams of (a) magnetron sputtering and (b) cluster seed formation and growth process.....16
Figure 2.3: Photograph of the cluster generation chamber configured for dual-target sputtering.....17
Figure 2.4: (a) The relationship between the chamber pressure and the LN_2 cooling time for different gas flow rates. (b) The mass spectra of Ag clusters with different cooling times when only one 1-inch Ag target was applied. The parameters are a power of 10 W, an Ar gas flow rate of 120 sccm (standard cubic centimeter per minute), a He gas flow rate of 0 sccm, and a condensation length of 250 mm. (c) The mass spectrum of Ag when the cooling time is 30 min. 18
Figure 2.5: Schematic diagrams of (a) single-target magnetron gun and (b) dual-target magnetron guns.....20
Figure 2.6: A schematic drawing of the lateral time-of-flight mass filter used in the cluster source. x is the lateral displacement of the cluster beam, L is the segment of the cluster beam used in each pulse series, x_1 is the width of the entrance aperture and x_2 is the width of the exit aperture. 22
Figure 2.7: (a) The mass spectra of Ag clusters before and during deposition, respectively. The applied parameters are a power of 10 W, an Ar gas flow rate of 40 sccm, a He gas flow rate of 0 sccm, a condensation length of 250 mm, and a chamber pressure of 0.075 mbar. (b) Sample current at a fixed mass as a function of time to illustrate the noise level.....24
Figure 2.8: The effects of different parameters on maximum intensity cluster size of Cu clusters. The initial parameters are a power of 10 W, an Ar gas flow rate of 100 sccm, a He gas flow rate of 100 sccm, a condensation length of 250 mm, and a chamber pressure of 0.66 mbar. (a), (c), (e), and (g) are mass spectra of different adjusted parameters based on the initial parameters, i.e., (a) the power range of 10-30 W, (c) the Ar flow rate range of 60-140 sccm, (e) the He flow

rate range of 100-200 sccm, and (g) the chamber pressure range of 0.27-0.87 mbar. (b), (d), (f) and (h) are trends between obtained cluster peak sizes and different parameters. 26
Figure 2.9: (a) Photograph of Joel JEM 2100F in NPRL; (b) schematic diagram of aberration-corrected STEM. 30
Figure 2.10: Schematic diagram of (a) different types of scattered electrons and (b) different detectors in STEM. Normally, θ_3 is less than 10 mrads, θ_4 is between 10 mrads and 50 mrads, θ_5 is higher than 50 mrads. 32
Figure 2.11: Schematic diagram showing the formation of spherical aberration. 34
Figure 2.12: Schematic diagrams showing the analysis details of (a) integrated intensity, (b) project-area equivalent-circle diameter, and (c) aspect ratio. X Feret, max and X Feret, min is the maximum and minimum Feret diameter, respectively. 37
Figure 2.13: HAADF-STEM images of Ag6525 clusters in sample (a) Ar40 and (d) Ar160. (b) and (e) are their corresponding size distribution and (c) and (f) are corresponding integrated intensity distributions. Red, green, and yellow arrows show dual-cluster, triple-cluster, and quadra-cluster aggregation, respectively. Purple lines are Gauss fitting curves of every peak. 40
Figure 2.14: A schematic drawing of the different situations of dual-cluster aggregation. (a) The situation shows the minimum size of dual-cluster aggregation when two single Ag6525 clusters aggregated completely. (b) The situation shows a medium size of dual-cluster aggregation when two single Ag6525 clusters aggregated incompletely. (c) The situation shows the maximum size of dual-cluster aggregation when two single Ag6525 clusters are just touching each other.....41
Figure 2.15: HAADF-STEM images of Ag clusters with different sizes prepared by magnetron sputtering. 42
Figure 2.16: The workflow of the structure identification for Ag clusters in HAADF-STEM images. 42
Figure 2.17: The atomic models of COh, Ih, and square Ino-Dh structures for Ag6525 clusters. 44
Figure 2.18: (a) Simulation model of COh structure of Ag6525 cluster; (b) simulation image of Ag6525 COh (0, 0, 0) and the angles are defined as shown in (c); (d) simulation atlas of Ag6525 COh with different angular rotations. The angle α means the model is rotating around the X-axis, and the rotation around the Y-axis is described by the angle β. The enlarged atlas can be found in Appendix. 45
Figure 2.19: (a) Simulation model of Ih structure of Ag6525 cluster; (b) simulation image of Ag6525 Ih (0, 0, 0) and the angles are defined as shown in (c); (d) simulation atlas of Ag6525 Ih with different angular rotations. The angle α means the model is rotating around the X-axis, and the rotation around the Y-axis is described by the angle β. The enlarged atlas can be found in Appendix. 46
Figure 2.20: (a) Simulation model of Dh structure of Ag6525 cluster; (b) simulation

image of Ag6525 Dh (0, 0, 0) and the angles are defined as shown in (c); (d) simulation atlas of Ag6525 Dh with different angular rotations. The angle α means the model is rotating around the X-axis, and the rotation around the Y-axis is described by the angle β. The enlarged atlas can be found in Appendix. 47
Figure 2.21: Examples of comparison between simulation of typical Ih and Dh structure of Ag6525 and clusters found in samples. (a1) and (a4) are simulated HAADF-STEM image and its FFT image for Ag6525 Ih. (a2) and (a5) are experimental HAADF-STEM image and its FFT image of one Ag6525 cluster. (a3) is the comparison between normalized line profiles of (a1) and (a2). (b1) and (b4) are simulated HAADF-STEM image and its FFT simulation image of Ag6525 Dh. (b2) and (b5) are HAADF-STEM image and its FFT image of one Ag6525 cluster. (b3) is the comparison between normalized line profiles of (b1) and (b2). The yellow arrows show the position and direction of line profiles in every image. The blue arrows show the positions where the intensity of the real cluster is lower than that of simulated one. The green arrows show the additional atom columns. 49
Figure 2.22: (a1) and (b1) The simulated images of Ag6525 clusters. (a2) and (b2) The respective FFT images of (a1) and (b1). (a3) and (b3) The HAADF-STEM images of Ag6525 clusters. (a4) and (b4) The respective FFT images of (a3) and (b3). (a5) and (b5) The respective atomic models of (a1) and (b1). The scale bars in (a3) and (b3) are 2 nm. 50
Figure 2.23: (a1), (b1), and (c1) The simulated images of Ag6525 clusters. (a2), (b2), and (c2) The respective FFT images of (a1), (b1), and (c1). (a3), (b3), and (c3) The HAADF-STEM images of Ag6525 clusters. (a4), (b4), and (c4) The respective FFT images of (a3), (b3), and (c3). (a5), (b5), and (c5) The respective atomic models of (a1), (b1), and (c1). The scale bars in (a3), (b3), and (c3) are 2 nm. 51
Figure 2.24: Part of the simulation atlas of Ag6525 Dh with different angular rotations.....53
Figure 2.25: Part of the simulation atlas of Ag6525 Ih with different angular rotations.....53
Figure 2.26: Four HAADF-STEM images of Ag6525 clusters to show different cases that may be observed during imaging. The scale bars are 2 nm.....54
Figure 2.27: Simulated images and their relative FFT images of Ih structures with different sizes. 55
Figure 2.28: Simulated images and their FFT images of Dh structures with different sizes. 56
Figure 2.29: (a) The mass spectra when different substrate voltages were applied. The applied parameters are a power of 10 W, an Ar gas flow rate of 40 sccm, a He gas flow rate of 0 sccm, a condensation length of 250 mm, and a chamber pressure of 0.075 mbar. (b) The statistical results of the aspect ratios of four Ag1k samples deposited with different substrate voltages. The error bar comes from the standard deviation of the aspect ratios. The deposition parameters are

a power of 10 W, an Ar gas flow rate of 120 sccm, a He gas flow rate of 30 sccm, a condensation length of 250 mm, and a chamber pressure of 0.21 mbar. (c) The proportions of structures of the same four Ag1k samples in (b). More than 200 clusters were analyzed for every sample. (d) The mass spectra during deposition when the substrate voltage of 100 V and 200 V, respectively, were applied. 58
Figure 2.30: (a), (c), (e), (g), and (i) are HAADF-STEM images of Ag6525 clusters stored in air for 0, 1, 12, 21, and 31 days, respectively. (b), (d), (f), (h), and (j) are size distributions of Ag6525 clusters stored in air for 0, 1, 12, 21, and 31 days, respectively. The first peak of the size distribution shows sizes of single Ag6525 clusters and the second peak of the size distribution is formed by aggregation of two single Ag6525 clusters. The size distribution was fitted with Gaussian function. 61
Figure 2.31: The relationship between peak diameters of Ag6525 clusters and the time these Ag6525 clusters were exposed to the air. The first peak of the size distribution shows the sizes of single Ag6525 clusters, and the second peak of the size distribution is formed by the aggregation of two single Ag6525 clusters. The error bar represents the standard deviation of the statistical results. 62
Figure 2.32: (a) HAADF-STEM image of two Ag6525 clusters with icosahedron structure before being exposed to the air. (b) HAADF-STEM image of Ag6525 clusters exposed to the air for 31 days and (c) its partially enlarged image. . 63
Figure 2.33: HAADF-STEM image of Ag6525 clusters exposed to the air for 31 days. 63
Figure 2.34: HAADF-STEM image of Ag6525 clusters exposed to the air for (a) 1 day, (b) 12 days, (c) 21 days, and (d) 31 days. 64
Figure 2.35: HAADF-STEM image of one cluster with core-shell structure (a) before face scanning and (b) after face scanning for 5 minutes. 65
Figure 2.36: (a) HAADF-STEM image of clusters before line scanning. (b) and (c) HAADF-STEM images of the clusters after line scanning 1 and 2, respectively. (d) EDX spectrum of line scanning 1. (e) and (f) element distribution along the line scanning direction in line scanning 1 and 2, respectively. The Ag peak marked by the red arrow in (f) is related to the position marked by the red arrow in (c). 67
Figure 2.37: The relationship between peak diameters of Ag6525 clusters and time of these Ag6525 clusters stored in high vacuum. The first peak of size distribution shows sizes of single Ag6525 clusters and the second peak of size distribution is formed by aggregation of two single Ag6525 clusters. The error bar represents the standard deviation of the statistical results. 68
Figure 2.38: HAADF-STEM images of a typical clusters with Ih structures after stored in high vacuum for 26 days. No obvious core-shell structure can be observed. 69

Chapter 3

Figure 3.1: The mass spectrum of preparation parameters, i.e., a power of 10 W, an Ar gas flow rate of 120 sccm, a He gas flow rate of 30 sccm, a condensation length of 250 mm, and a sputtering chamber pressure of 0.21 mbar. 71
Figure 3.2: (a)-(h) Morphologies of Ag clusters in the size range of 1k to 14k revealed by HAADF-STEM images. Distinct elongated clusters are pointed out with red circles in Sample Ag8k and Ag10k. These aggregated Ag clusters are indicated by yellow arrows, which were formed by the same deposition locations of two or three single clusters or the multiple charge of these clusters. 73
Figure 3.3: (a) The relationship between the integrated intensity and aspect ratio of Ag clusters with different sizes based on the HAADF-STEM images in Figure 3.2. (b) The relationship between the integrated intensity and size of Ag clusters (about 150 clusters were analyzed per sample). For each point in (b), the error bar along the X-axis represents the mass resolution of the mass filter for different deposition sizes, while the error bar along the Y-axis represents the standard deviation of the statistical results. 74
Figure 3.4: (a) The plot of the relative frequency of aspect ratio distribution for Ag clusters with different sizes (approximately 150 clusters were analyzed per sample). (b) The average values and their standard deviations of aspect ratios for Ag clusters with different sizes, according to the same dataset of (a). 75
Figure 3.5: (a) Mass spectra with different peak sizes were obtained by using the same Ar gas flow rate of 120 sccm but different He gas flow rates. The curves have been fitted with the Gaussian function. (b) The red curve is the mean values of aspect ratios and their standard deviations for Ag clusters prepared with different parameters described in (a), and the result of the black curve is the replotted images of Figure 3.4 (b). 77
Figure 3.6: (a) Mass spectrum (red curve) obtained with the same deposition parameters as Figure 3.1 (black curve). (b) A plot of the relative frequency of aspect ratio distribution for Ag clusters deposited with mass spectra shown in (a). (c) The relationship between aspect ratios of Ag clusters and their sizes marked in (a). The error bar represents the standard deviation of the statistical results. 79
Figure 3.7: (a) Mass spectra of Ag clusters prepared with different Ar gas flow rates. Other parameters are the same, namely, a power of 10 W, a He gas flow rate of 0 sccm, and a condensation length of 250 mm. The mass spectra have been fitted with the Lognormal function. (b) Mass spectra of Ag clusters prepared with different He gas flow rates. Other parameters are the same, namely, a power of 10 W, an Ar gas flow rate of 120 sccm, and a condensation length of 250 mm. The mass spectra have been fitted with the Gaussian function. (c) and (d) The plots of the relative frequency of aspect ratio distribution for Ag8k clusters deposited with mass spectra shown in (a) and (b) (approximately 150 clusters were analyzed per sample). (e) and (f) The relative mean values and their standard deviations of aspect ratios for Ag8k clusters analyzed in (c) and (d). 81

Figure 3.8: (a) A HAADF-STEM image of Ag8k clusters. (b) The relationship between integrated intensity and aspect ratio of nine clusters in (a). (c), (d), (e), and (f) Enlarged HAADF-STEM images of Cluster 3, 5, 4, and 9, respectively. AR: aspect ratio.....83
Figure 3.9: (a), (b), and (c) Three HAADF-STEM images of prepared Ag12k clusters, their FFT images, and their respective simulated images. (d) The relationship between proportions of different structures and the size of Ag clusters. The curves have been fitted with linear relationships. About 250 clusters were analyzed per sample. The error bars in (d) are a result of the clusters displaying the characteristics of two structures simultaneously, such as in the case of clusters during the Ih-to-Dh transition process (which are considered to be half Ih and half Dh) or distorted Ih (which are considered to be half Ih and half UI).....85
Figure 3.10: (a) This figure shows the aspect ratio distributions of the Ag6k sample prepared with the same parameters as Figure 3.1. The respect ratio interval of analyzed spherical Ag6k clusters is [1.00, 1.22], from the lowest aspect ratio value (namely 1) to the value of $\mu+3\sigma$ for the Gaussian fitting (1.22 here). (b) The relationship between the percentage of aggregated Ag clusters and their sizes is presented. The black curve represents the results obtained by analyzing the aspect ratio datasets, while the red curve is from the HAADF-STEM images of every Ag cluster. About 200 and 250 clusters were analyzed for these two methods, respectively. The two curves can be well-fitted with a linear relationship in the size range of 1k to 6k, exponential functions for 6k to 12k, and a linear relationship from 12k to 16k. The error bars represent the standard deviation of the statistical results obtained from three repetitions. (c) This figure shows the fractions of elongated Ag clusters and different structures for spherical clusters in the size range of 1k to 14k. (d) The distribution of different structures for Ag clusters with different sizes is presented based on the mass spectrum shown in Figure 3.1.....87
Figure 3.11: (a) A HAADF-STEM image of an elongated cluster, which can be recognized as two domains of Ih structures with different sizes by comparison between FFT images and the relative simulated STEM images and FFT images. (b) A HAADF-STEM image of an elongated cluster with two domains of Ih and Dh structure with similar sizes. (c) A HAADF-STEM image of a standard Ag12k-Ih cluster and an elongated Ag12k cluster with a large identified Ih domain and a small unidentified domain. (d) A HAADF-STEM image of an elongated Ag12k cluster with a large identified Ih domain and a small unidentified domain, of which interface exhibits a five-fold structure. The yellow circles and arrows in (c) and (d) point out the main domains and the small domains, respectively. 90
Figure 3.12: The structures of domains with similar sizes (X+X) in elongated clusters. The curves have been fitted with a linear relationship. The black ticks on the X-axis are the size of elongated Ag clusters, while the blue ones on the X-axis are the size of domains in the elongated Ag clusters.....93

Figure 3.13: The relationship between proportions of different structures and the size of Ag clusters. The curves have been fitted with linear relationships. About 250 clusters were analyzed for every sample. The results of the black curves are from Figure 3.9 (d). 95
Figure 3.14: (a) The relationship between proportions of different structures and the size of Ag clusters deposited with the sizes shown in Figure 3.5 (a). About 250 clusters were analyzed for every sample. The error bars represent the uncertainties associated with the identification of the structure. (b) The relationship between proportions of different structures and the size of Ag clusters shown in Figure 3.9 (d). This figure is directly copied from Figure 3.9 (d) for comparison. 96
Figure 3.15: (a) The mass spectrum of Ag clusters deposited with the following parameters, i.e., a power of 10 W, an Ar gas flow rate of 40 sccm, a He gas flow rate of 0 sccm, a condensation length of 250 mm, and a sputtering chamber pressure of 0.075 mbar. (b) and (c) The HAADF-STEM images of Ag clusters prepared after the TOF mass filter and the nozzle, respectively. The deposited setting parameters after TOF mass filter are the mass range of 1 to 30k, deposition step of 100, one second deposition time per step, and a total deposition time of 100 s. (d) The size distributions of about 300 Ag clusters prepared after the TOF mass filter and the nozzle, respectively, and the mass spectrum replotted with the X-axis of cluster size in nm based on (a). 99
Figure 3.16: Two growth paths for clusters in the sputtering chamber, i.e., (a) atom addition and (b) cluster-cluster coalescence. 101
Figure 3.17: (a) A schematic diagram to describe the possible growth process in the sputtering chamber. (b) The relationship between cluster sizes and their numbers corresponds to different areas in the magnetron sputtering chamber. D: the size of clusters; N: the number of clusters. 103
Figure 3.18: Example of an elongated Ag18k cluster formed by three domains. The three domains in this cluster are indicated by the yellow dashed lines. 107

Chapter 4

Figure 4.1: Structure transformation process with time under electron irradiation with a dose of 8.55×10^4 e^-/angstrom^2/frame. The colored timeline shows the structure at every time point. Images (a1)-(f1) are HAADF-STEM images recorded at different time points. (a2)-(f2), (a3)-(f3), (a4)-(f4), and (a5)-(f5) are the corresponding simulated HAADF-STEM images, experimental FFT images, simulated FFT images and structure models of images in (a1)-(f1), respectively. Yellow dotted lines in (a1)-(f1) and (a2)-(f2) are used to show typical distinguishing features of different structures, which are two-fold geometry for the Ih structure and five-fold geometry for the Dh structure. Blue arrows in (d1) indicate the remnant characteristic of the Ih structure. Red triangles in (a5)-(f5) show the same facet when the cluster was rotating under e-beam irradiation. Blue balls in (b5) and (c5) show the same vertices before and after structure transformation. 112
Figure 4.2: Structure transformation process with time under electron irradiation

with a dose of 8.55 × 10^4 e^-/angstrom^2/frame. The colored timeline shows the structure at every time point. Images of (a1)-(f1) are HAADF-STEM images recorded at different time points. (a2)-(f2), (a3)-(f3), (a4)-(f4), and (a5)-(f5) are the corresponding simulated HAADF-STEM images, FFT images, simulated FFT images and structure models of images in (a1)-(f1), respectively. Yellow lines in (a1)-(f1) and (a2)-(f2) are used to show typical distinguishing features of different structures, which are two-fold geometry for the Ih structure and five-fold geometry for the Dh structure. Red triangles in (a5)-(f5) show the same facet when the cluster was rotating under electron irradiation. 114
Figure 4.3: The relationship between normalized integrated intensity and time under e-beam irradiation for the cluster investigated in Figure 4.2. The blue dotted line is guide to the eye. 115
Figure 4.4: HAADF-STEM images of a Ag1k cluster with initial Ih structure recorded at different time points under e-beam irradiation with a dose of 8.55 × 10^4 e^-/angstrom^2/frame. Some of the single atoms around the cluster are indicated by blue arrows. However, please note that the number of arrows does not necessarily correspond to the actual number of single atoms present. .. 116
Figure 4.5: HAADF-STEM images of a Ag1k cluster with initial Dh structure recorded at different time points under e-beam irradiation with a dose of 8.55 × 10^4 e^-/angstrom^2/frame. The inserted images are bright-field (BF) images to show clear atomic structures. Some of the single atoms around the cluster are indicated by blue arrows. However, please note that the number of arrows does not necessarily correspond to the actual number of single atoms present. .. 117
Figure 4.6: HAADF-STEM images of a Ag2k cluster with initial Ih structure recorded at different time points under e-beam irradiation with a dose of 8.55 × 10^4 e^-/angstrom^2/frame. Some of the single atoms around the cluster are indicated by blue arrows. However, please note that the number of arrows does not necessarily correspond to the actual number of single atoms present. .. 118
Figure 4.7: HAADF-STEM images of a Ag8k cluster with initial Ih structure recorded at different time points under e-beam irradiation with a dose of 8.55 × 10^4 e^-/angstrom^2/frame. Some of the single atoms around the cluster are indicated by blue arrows. However, please note that the number of arrows does not necessarily correspond to the actual number of single atoms present. .. 119
Figure 4.8: HAADF-STEM images of a Ag12k cluster with initial Ih-to-Dh structure recorded at different time points under e-beam irradiation with a dose of 8.55 × 10^4 e^-/angstrom^2/frame. Some of the single atoms around the cluster are indicated by blue arrows. However, please note that the number of arrows does not necessarily correspond to the actual number of single atoms present. 120
Figure 4.9: HAADF-STEM images of a Ag12k cluster with initial Ih structure recorded at different time points under e-beam irradiation with a dose of 3.8 × 10^4 e^-/angstrom^2/frame. Some of the single atoms around the cluster are indicated by blue arrows. However, please note that the number of arrows does

not necessarily correspond to the actual number of single atoms present. ..121
Figure 4.10: The effect of e-beam irradiation on the integrated intensity of Ag clusters with different sizes. 122
Figure 4.11: The schematic drawing of the heating program. Temperature range: from 20 °C to 800 °C; Cyclical increase of the temperature; 1 min for every temperature step; Heating rate: 1000 °C/min; Cooling rate: 2000 °C/min. . 124
Figure 4.12: The relationship between the normalized integrated intensity of Ag8k clusters and the e-beam irradiation time when the magnification of the image was 10M and 15M, respectively. The blue dashed line serves as a guide for the normalized intensity of 1. After 10-min e-beam irradiation, the integrated intensity of Ag8k obviously decreased after about 260 s with the magnification of 10M and 180 s with the magnification of 15M. 125
Figure 4.13: Overview HAADF-STEM images at different heating temperatures. 126
Figure 4.14: Comparison between HAADF-STEM images of 20 °C and 800 °C. The large pattern at the left corner is the defect of the heating chip. 126
Figure 4.15: Average integrated intensity of 96 Ag8k clusters after heating to different temperatures. The blue dashed line serves as a guide for the normalized intensity of 1. 127
Figure 4.16: The relationship between the proportions of structures for Ag8k clusters and the different heating temperatures. The error bars represent the uncertainties associated with the identification of the structure. 128
Figure 4.17: The number of Ih-to-Dh transition events after heating at different temperatures for Ag8k clusters. 130
Figure 4.18: One example of a Ag8k cluster with initial Ih structure but no change in the temperature range of 20-600 °C. It transformed to a Dh structure after heating at 700 °C with substantial mass loss. Red dotted lines are used to show typical distinguishing features of different structures, which are two-fold geometry for the Ih structure and five-fold geometry for the Dh structure. 131
Figure 4.19: One example of a Ag8k cluster with an initial Ih structure but gradually transformed to a Dh structure in the temperature range of 20-600 °C. It transformed to a standard Dh structure after heating at 700 °C with substantial mass loss. Three truncations are indicated by yellow arrows. Red dotted lines are used to show typical distinguishing features of different structures, which are two-fold geometry for the Ih structure and five-fold geometry for the Dh structure. 133
Figure 4.20: One example of a Ag8k cluster with initial Ih structure but suddenly transformed to Dh structure after heating at 600 °C. After heating at 700 °C, the cluster size decreased due to substantial mass loss. Red dotted lines are used to show typical distinguishing features of different structures, which are two-fold geometry for the Ih structure and five-fold geometry for the Dh structure. 134
Figure 4.21: One Ag8k cluster with initial Dh structure but no change in the temperature range of 20-600 °C. After heating at 700 °C, the cluster size

decreased due to substantial mass loss. Red dotted lines are used to show typical distinguishing features of the Dh structure. 135
Figure 4.22: One example of a Ag8k cluster with initial FCC structure but no change in the temperature range of 20-600 °C. After heating at 700 °C, the cluster size decreased due to substantial mass loss. 136
Figure 4.23: The aggregation process of two Ag8k domains with Ih structures in the temperature range of 20-600 °C. After heating at 700 °C, the cluster size decreased due to substantial mass loss. Red dotted lines are used to show typical distinguishing features of different structures, which are two-fold geometry for the Ih structure and five-fold geometry for the Dh structure. The yellow dotted lines are used to distinguish the domains in the elongated clusters. 137
Figure 4.24: The aggregation process of two Ag8k clusters with Ih and Dh structures in the temperature range of 20-600 °C. After heating at 700 °C, the cluster size decreased due to substantial mass loss. Red dotted lines are used to show typical distinguishing features of different structures, which are two-fold geometry for the Ih structure and five-fold geometry for the Dh structure. The yellow dotted lines are used to distinguish the domains in the elongated clusters. 138
Figure 4.25: The aggregation process of two Ag8k domains with Ih and Dh structures in the temperature range of 20-600 °C. After heating at 700 °C, the cluster size decreased due to substantial mass loss. Red dotted lines are used to show typical distinguishing features of different structures, which are two-fold geometry for the Ih structure and five-fold geometry for the Dh structure. The yellow dotted lines are used to distinguish the domains in the elongated clusters. 139
Figure 4.26: The aggregation process of an aggregated Ag8k cluster with Ih+Ih structure in the temperature range of 20-600 °C. The final structure is Dh. Red dotted lines are used to show typical distinguishing features of five-fold structures. The yellow dotted lines are used to distinguish the domains in the elongated clusters. 142
Figure 4.27: The aggregation process of an aggregated Ag8k cluster with Ih+UI structure in the temperature range of 20-600 °C. The final structure is Dh. The yellow dotted lines are used to distinguish the domains in the elongated clusters. 143
Figure 4.28: The aggregation process of an aggregated Ag8k cluster with Ih+Ih structure in the temperature range of 20-600 °C. The final structure is Ih. The yellow dotted lines are used to distinguish the domains in the elongated clusters. 144
Figure 4.29: The aggregation process of an aggregated Ag8k cluster with Ih+Dh structure in the temperature range of 20-600 °C. The final structure is Dh. Red dotted lines are used to show typical distinguishing features of five-fold structures. The yellow dotted lines are used to distinguish the domains in the elongated clusters. 145

Figure 4.30: The aggregation process of an aggregated Ag8k cluster with Ih+x structure in the temperature range of 20-600 °C. The final structure is Ih. The yellow dotted circles are used to point out the main domains in the elongated clusters. 147
Figure 4.31: The aggregation process of an aggregated Ag8k cluster with Ih+x structure in the temperature range of 20-600 °C. The final structure is Dh. The yellow dotted circles are used to point out the main domains in the elongated clusters. 148
Figure 4.32: The aggregation process of an aggregated Ag8k cluster with Ih+x structure in the temperature range of 20-600 °C. The final structure is UI. The yellow dotted circles are used to point out the main domains in the elongated clusters. 149
Figure 4.33: The aggregation process of an aggregated Ag8k cluster with Dh+x structure in the temperature range of 20-600 °C. The final structure is Dh. Red dotted lines are used to show typical distinguishing features of five-fold structures. The yellow dotted circles are used to point out the main domains in the elongated clusters. 150
Figure 4.34: One example of a Ag14k cluster with initial Ih structure but no change in the temperature range of 20-650 °C. After heating at 700 °C, only half of the cluster was left due to great mass loss. 153

Chapter 5

Figure 5.1: (a) Mass spectra of Ag clusters prepared with different Ar gas flow rates. Other parameters are the same, namely, a power of 10 W, a He gas flow rate of 0 sccm, and a condensation length of 250 mm. The mass spectra have been fitted with the Lognormal function. (b) Mass spectra of Ag clusters prepared with different He gas flow rates. Other parameters are the same, namely, a power of 10 W, an Ar gas flow rate of 120 sccm, and a condensation length of 250 mm. The mass spectra have been fitted with the Gaussian function. ... 157
Figure 5.2: Relationship between peak sizes of mass spectra with (a) Ar gas flow rates and (b) He gas flow rates. The values of the peak sizes are from the fitting curves shown in Figure 5.1. The red curves are the linear relationship fitting. The error bars are from the confidence interval of the fitting of the Figure 5.1. 158
Figure 5.3: (a) One of the HAADF-STEM overview images of Sample Ar40, which includes seven Ag clusters. (b) Relationship between integrated intensities and aspect ratios of these seven Ag clusters. (c)-(f) HAADF-STEM images with the atomic resolution for Cluster 1, 2, 3, and 5 in (a), respectively. AR: aspect ratio; UI: unidentified cluster; Ih: cluster with icosahedron structure. The yellow dashed lines are guidelines separating two individual Ih domains in the elongated clusters. The red dashed lines are guidelines for structure identification. 160
Figure 5.4: (a) and (b) are aspect ratios of all Ag8k clusters in samples prepared with different Ar and He gas flow rates as shown in Figure 5.1. The error bars represent the standard deviation of the statistical results. (c) and (d) are the

proportions of elongated clusters in about 160 Ag8k clusters for every sample prepared with different Ar and He gas flow rates. The red dashed lines are exponential fitting. The blue dashed lines show the Ar gas flow rate of 85 sccm and He gas flow rate of 23 sccm, which can obtain 8k atoms as peak size according to the linear fitting in Figure 5.2. 162
Figure 5.5: (a) Proportion of different structures of spherical Ag8k clusters in samples prepared with different Ar gas flow rates with no He gas. The dashed lines are linear fitting for the trend of every kind of structure. (b) The proportion of different structures of spherical Ag8k clusters in samples prepared with different He gas flow rates with the same Ar gas low rate of 120 sccm. The error bars represent the uncertainties associated with the identification of the structure. 163
Figure 5.6: (a) and (b) HAADF-STEM images of Cluster 2 and 3 in Figure 5.3 (a). (c) and (d) HAADF-STEM images of two elongated clusters. (a1)-(d1) Simulation images of left domains and (a2)-(d2) simulation images of right domains corresponding to (a)-(d), respectively. Yellow dashed lines are used to guide the domains in HAADF-STEM images and preserved areas in simulation images compared with HAADF-STEM images. The red dashed lines are guidelines for structure identification. 165
Figure 5.7: (a)-(e) HAADF-STEM images of five elongated Ag8k clusters composed of two domains with similar sizes. (a1) and (a2) Simulation images of left and right domains in (a). (b1) and (b2) Simulation images of left and right domains in (b). Yellow dashed lines are used to guide the preserved area in simulation images compared with HAADF-STEM images. The orange dashed area in (a) shows the additional atom layers compared with (a1). Red solid lines in (a) and (b) show the twisted axis caused by cluster-cluster aggregation, which should be 180° in normal Ih structures. Red dashed lines in (c), (d) and (e) are used to show the five-fold structures formed by cluster-cluster aggregation. 167
Figure 5.8: (a1)-(f1) HAADF-STEM images of six elongated Ag8k clusters composed by two domains with obviously different sizes. (a2)-(f2) Simulation images of the main-body clusters corresponding to (a1)-(f1), respectively. Yellow arrows show the positions of small domains in every elongated cluster. Red dashed lines are used to show the newly formed five-fold structures between two domains. The yellow dashed lines are guidelines for structure identification. 169
Figure 5.9: (a) A schematic diagram to show the compositions in the prepared Ag clusters. (b) The relationship between the percentage of cluster-cluster coalescence events for Ag8k clusters and gas flow rates. The error bars represent the uncertainties associated with the identification of the structure. 171
Figure 5.10: A schematic diagram to describe the possible growth process in the sputtering chamber. Copied from Figure 3.17 (a). 172
Figure 5.11: A detailed comparison between the Lognormal and Gaussian fitting

relationships for the mass spectra of Ag clusters prepared with different Ar gas flow rates. 174
Figure 5.12: The comparison of R-squares for the two fitting functions of Figure 5.11. 175
Figure 5.13: A schematic drawing of the simulation process for the size distribution. 177
Figure 5.14: The size distributions after every collision round. The red number in the right upper corner is the number of collision round. 178
Figure 5.15: The size distributions of the 12th collision round after three-time simulation. 179
Figure 5.16: The size distributions of different proportions of the initial particles after the 12th collision round. (a) used 50%, 30%, and 20% as the initial proportions of single atoms, dimers, and trimers, but 80%, 10%, and 10% were applied in (b). 179
Figure 5.17: A schematic drawing of simulation about the size distribution of clusters after collisions of 60% particles in every collision round. 180
Figure 5.18: The size distributions after collisions of 60% particles in every collision round. The red number in the right upper corner is the collision round. 181
Figure 5.19: The size distributions of different proportions of the initial particles after the 23rd collision round. The fraction of collided particles in every collision round is 60%. (a) used 50%, 30%, and 20% as the initial proportions of single atoms, dimers, and trimers, but 80%, 10%, and 10% were applied in (b). 182
Figure 5.20: The size distributions of different proportions of the initial particles after the 20th collision round. (a) used 50%, 30%, and 20% as the initial proportions of single atoms, dimers, and trimers, but 50%, 30%, and 20% were applied in (b). 183

Chapter 6

Figure 6.1: Mass spectra of single Ag or Cu target and AgCu dual-target when different parameters were applied to the dual-target system. The X-axis represents the number of atoms in the cluster when the units of Cu mass are used, calculated by dividing the mass of the cluster by the mass of Cu. (a)-(e) 10 W power of Ag target, 80 sccm Ar gas flow rate, no He gas, 250 mm condensation lengths of Ag target, 150 mm condensation lengths of Cu target, and different powers of Cu target. (a) 10 W; (b) 15 W; (c) 20 W; (d) 25 W; and (e) 30 W. 188
Figure 6.2: (a) Mass spectra of single Ag or Cu target and AgCu dual-target when the power of 10 W was applied on the two targets. (b) The relationship between integrated intensity and projected-area-equivalent circle diameter of 436 analyzed AgCu45k clusters. (c) The enlarged image of the blue box of (b). (d) HAADF-STEM images of prepared clusters. (e) and (f) Examples of prepared Ag-Ih and Ag-Dh clusters. 190
Figure 6.3: (a) Mass spectra of single Ag or Cu target and AgCu dual-target when

the power of 10 W and 15 W was applied on the Ag and Cu target, respectively. (b) The relationship between integrated intensity and projected-area-equivalent circle diameter of 353 analyzed AgCu45k clusters. (c) A HAADF-STEM image of prepared clusters. (d)-(f) Examples of prepared Ag@Cu clusters. (g)-(i) The corresponding false-color images of (d)-(f), in which different colors represent the intensities of pixels. The discontinuous Cu shells are marked with yellow arrows and the positions with no shell are pointed out with red arrows. 192
Figure 6.4: (a) Mass spectra of single Ag or Cu target and AgCu dual-target when the power of 10 W and 20 W was applied on the Ag and Cu target, respectively. (b) The relationship between integrated intensity and projected-area-equivalent circle diameter of 73 analyzed AgCu45k clusters. (c) The enlarged image of the blue box of (b). (d)-(i) HAADF-STEM images of prepared clusters. 193
Figure 6.5: (a) Mass spectra of single Ag or Cu target and AgCu dual-target when the power of 10 W and 25 W was applied on the Ag and Cu target, respectively. (b) The relationship between integrated intensity and projected-area-equivalent circle diameter of 142 analyzed AgCu45k clusters. (c) A HAADF-STEM image of prepared clusters. (d)-(f) Examples of prepared Ag@Cu clusters. (g)-(i) The corresponding false-color images of (d)-(f), in which different colors represent the intensities of pixels. The complete Cu shells are marked..... 194
Figure 6.6: HAADF-STEM images of clusters prepared with different powers of Cu target. (a) 10 W; (b) 15 W; (c) 20 W; and (d) 25 W. The discontinuous Cu shells are marked with yellow arrows and the positions with no shell are pointed out with red arrows in (b)..... 196
Figure 6.7: (a) Mass spectra of single Ag or Cu target and AgCu dual-target when the power of 10 W and 20 W was applied on the Ag and Cu target, respectively. (b) The relationship between integrated intensity and projected-area-equivalent circle diameter of 162 analyzed AgCu32k clusters. (c) The enlarged image of the blue box of (b). (d) and (j) Low-magnification HAADF-STEM images of prepared clusters. (e), (k), and (l) Examples of prepared Cu clusters. (f) and (h) Examples of prepared Ag@Cu clusters. (g) and (i) The corresponding false-color images of (f) and (h), in which different colors represent the intensities of pixels. 198
Figure 6.8: (a) Mass spectra of single Ag or Cu target and AgCu dual-target when the power of 10 W and 20 W was applied on the Ag and Cu target, respectively. (b) The relationship between integrated intensity and projected-area-equivalent circle diameter of 736 analyzed AgCu60k clusters. (c) The enlarged image of the blue box of (b). (d)-(g) HAADF-STEM images of prepared clusters. (h) The corresponding false-color image of (g), in which different colors represent the intensities of pixels. 200
Figure 6.9: (a) A HAADF-STEM image of prepared AgCu60k clusters. (b) The enlarged image of the green box of (a). (c) and (d) The elemental map of Cu

and Ag, respectively. The yellow arrows in different images indicate the existence of a Ag@Cu core-shell cluster, while the blue arrows provide the evidence to confirm a pure Cu cluster in (a). 201
Figure 6.10: (a) Mass spectra of single Ag or Cu target and AgCu dual-target when 10 W was applied on the two targets. (b) The relationship between integrated intensity and projected-area-equivalent circle diameter of 90 analyzed AgCu32k clusters. (c) The enlarged image of the blue box of (b). (d) An example of prepared Ag-Ih and Ag-Dh clusters. (e) and (h) HAADF-STEM images of prepared clusters. (f) The enlarged image of the green box in (e). (g) The corresponding false-color image of (f), in which different colors represent the intensities of pixels. (i) The high-magnification HAADF-STEM image of cluster 4 marked in (b) and (h). 204
Figure 6.11: (a) Mass spectra of single Ag or Cu target and AgCu dual-target when the power of 10 W and 30 W was applied on the Ag and Cu target, respectively. (b) The relationship between integrated intensity and projected-area-equivalent circle diameter of 298 analyzed AgCu32k clusters. (c), (d), and (f) HAADF-STEM images of prepared clusters. (e) The FFT pattern of the cluster shown in (d). The inserted image of (f) is the enlarged image of the yellow box to show the Cu [111] lattice. 205
Figure 6.12: (a) Mass spectra of single Ag or Cu target and AgCu dual-target when the power of 10 W and 30 W was applied on the Ag and Cu target, respectively. (b) The relationship between integrated intensity and projected-area-equivalent circle diameter of 593 analyzed AgCu45k clusters. (c) The enlarged image of the blue box of (b). (d)-(g) HAADF-STEM images of prepared clusters. 206
Figure 6.13: (a), (b), and (c) HAADF-STEM images of clusters prepared after the magnetron sputtering chamber. (d), (e), and (f) BF images of (a), (b), and (c), respectively. 207
Figure 6.14: HAADF-STEM images of clusters prepared after the mass filer in the size range of 10k to 50k. 208
Figure 6.15: (a)-(e) HAADF-STEM images of prepared Ag@Cu 45k clusters. (f) The intensity profile of the green box in (e). The green box is oriented perpendicular to the atomic plane and indicates the scanning direction of the intensity profile. A wider box width is chosen to maximize the signal strength, thereby obtaining a more precise measurement of the atomic plane distance. 209
Figure 6.16: (a) Mass spectra of single Ag or Cu target and AgCu dual-target when the power of 10 W was applied on the Ag and Cu target, respectively. The other parameters are 120 sccm Ar gas flow rate, no He gas, and the same condensation length of 250 mm for both the Ag and Cu target. (b) The relationship between integrated intensity and projected-area-equivalent circle diameter of 372 analyzed AgCu20k clusters. (c) The enlarged image of the blue box of (b). (d), (e), (g), and (i) HAADF-STEM images of prepared clusters. (f) The corresponding false-color image of (e), in which different

colors represent the intensities of pixels. (h) The intensity profile of the green box in (g). The green box is oriented perpendicular to the atomic plane and indicates the scanning direction of the intensity profile. A wider box width is chosen to maximize the signal strength, thereby obtaining a more precise measurement of the atomic plane distance. 212
Figure 6.17: (a), (c), and (e) HAADF-STEM images of prepared Cu@Ag 20k clusters. (b) The intensity profile of the green box in (a). The green box is oriented perpendicular to the atomic plane and indicates the scanning direction of the intensity profile. A wider box width is chosen to maximize the signal strength, thereby obtaining a more precise measurement of the atomic plane distance. (d) and (f) The FFT images of the green and blue box in (c) and (e), respectively. (g) and (h) Two possible structures for (e). The yellow trapezoids indicate three domains of Ag shell, and the possible inside Dh and Ih are shown with red and green structures in (g) and (h), respectively. (i) HAADF-STEM image of a Co-Ih core and a shell formed by 10 Au FCC domains. The inset is the schematic model of this Co@Au cluster[113]. 214
Figure 6.18: The phase separation process of prepared AgCu@Ag core-shell cluster under the e-beam irradiation for three minutes with a dose of 1.52×10^5 e^-/angstrom^2/frame. (a) and (c)-(g) HAADF-STEM images of the same cluster at different time. (b), (h), and (i) The FFT images of the yellow, orange, and blue boxes in (a) and (g), respectively. (f) The schematic image to show the core-shell structure in (e) can be considered as a Cu-Ih or Cu-Dh core and a shell formed by six Ag FCC domains. 216

Appendix

Figure 9.1: The enlarged simulation atlas of Ag6525 COh with α in 0-20° and β in 0-90°.....233
Figure 9.2: The enlarged simulation atlas of Ag6525 COh with α in 25-45° and β in 0-90°. 234
Figure 9.3: The enlarged simulation atlas of Ag6525 Dh with α in 0-40° and β in 0-90°.....235
Figure 9.4: The enlarged simulation atlas of Ag6525 Dh with α in 50-90° and β in 0-90°.....236
Figure 9.5: The enlarged simulation atlas of Ag6525 Ih with α in -30-10° and β in 0-90°.....237
Figure 9.6: The enlarged simulation atlas of Ag6525 Ih with α in 20-60° and β in 0-90°.....238

List of Tables

Chapter 2

Table 2.1: Parameters of the single-target magnetron gun and dual-target magnetron guns. OD: outside diameter. 19
Table 2.2: Magic numbers of Oh, COh, normal Ino-Dh, square Ino-Dh, and Ih. . 43

Chapter 3

Table 3.1: The proportions of structures of domains for aggregated clusters. 91
Table 3.2: The proportions of domains with similar sizes or with obvious size differences for aggregated clusters. 93

Chapter 4

Table 4.1: The number of Ag8k clusters with different structures after heating at 600 °C. 129
Table 4.2: The products of aggregated Ag8k clusters with domains of different structures. 140
Table 4.3: The number of Ag14k clusters with different structures after heating at 650 °C. 152
Table 4.4: The number of Ag14k clusters with different structures after heating at 700 °C. 152
Table 4.5: The number of Ag14k clusters with different structures after heating at 700 °C. 154

Chapter 6

Table 6.1: The main compositions of prepared clusters with different applied power on the Cu target. 211

List of Abbreviations

BCC Body-Centered Cubic

BF Bright Field

COh Cuboctahedron

DF Dark Field

Dh Decahedron

EDX/EDS Energy-Dispersive X-ray Spectroscopy

ETEM Environmental Transmission Electron Microscopy/Microscope

FCC Face-Centered Cubic

FFT Fast Fourier Transform

FWHM Full Width at Half Maximum

HAADF High-Angle Annular Dark Field

HCP Hexagonal Close-packed

HRTEM High Resolution Transmission Electron Microscopy/Microscope

Ih Icosahedron

LN_2 Liquid Nitrogen

Oh Octahedron

SAC Single-atom Catalyst

SCC Single-cluster Catalyst

SCCM Standard Cubic Centimeter per Minute

STEM Scanning Transmission Electron Microscopy/Microscope

TEM Transmission Electron Microscopy/Microscope

TOF Time-of-flight

List of Publications

1. **Cheng Li**#, Jun-Chi Chen#, Wolfgang Theis*, Jun Li*, and Meng Gu*. Going Beyond Atom Visualization-Characterization of Supported Two-Atom Single-Cluster Catalysts with Scanning Transmission Electron Microscopy. (Accepted by *Science China Materials*.)

2. Xingkun Wang#, Xinkun Zhou#, **Cheng Li**, Hanxu Yao, Canhui Zhang, Jian Zhou, Ren Xu, Lei Chu, Huanlei Wang, Meng Gu*, Heqing Jiang*, Minghua Huang*. Asymmetric Co-N_3P_1 Trifunctional Catalyst with Tailored Electronic Structures Enabling Boosted Activities and Corrosion Resistance in an Uninterrupted Seawater Splitting System. *Advanced Materials*, 2022: 2204021.

3. Hanxu Yao#, Xingkun Wang#, Kai Li#, **Cheng Li**#, Canhui Zhang, Jian Zhou, Zhengwen Cao, Huanlei Wang, Meng Gu, Minghua Huang*, Heqing Jiang*. Strong electronic coupling between ruthenium single atoms and ultrafine nanoclusters enables economical and effective hydrogen production. *Applied Catalysis B: Environmental*, 2022, 312: 121378.

4. Jinfa Chang#, Guanzhi Wang#, **Cheng Li**, Yaqi He, Yuanmin Zhu, Wei Zhang, Muhammad Sajid, Abdelkader Kara, Meng Gu, Yang Yang*. Rational design of septenary high-entropy alloy for direct ethanol fuel cells. *Joule* 2023, 7(3): 587-602.

5. Yanfang Wang, **Cheng Li**, Yingzhi Li, Zhiqiang Li, Ning Qin, Chun Zeng, Hongzhi Wang, Yulin Cao, Qingmeng Gan, Fangchang Zhang, Wen Luo, Joshua W. Makepeace, Fucai Zhang, Phoebe K. Allan*, and Zhouguang Lu*. A metastable O6 phase with stable cation and anion redox reactions. (Submitted to *Joule*. Major revision)

6. Xingkun Wang#, Liangliang Xu#, **Cheng Li**#, Canhui Zhang#, Hanxu Yao, Ren Xu, Peixin Cui, Xusheng Zheng, Meng Gu, Jinwoo Lee*, Heqing Jiang*, Minghua Huang*. Establishing libraries for transforming clusters to married dual-atom catalysts. (Submitted to *Nature Communications*. Major revision)

7. Wenjuan Wang#, **Cheng Li**#, Chuan Zhou#, Xin Xiao*, Fayan Li, Ningyu Huang, Lei Li*, Meng Gu*, Qiang Xu*. Ir clusters atomically enrooted into the lattice of WO_3 boosting acidic oxygen evolution. (Submitted to *Nature Catalysis*.)

8. Xinran Li#, **Cheng Li**#, Huimin Yan#, Yanggang Wang, Meng Gu, and Qiang Xu*. Superior catalytic performance and cycling stability of MnO_2-supported Ir-Ru dual sites for acidic oxygen evolution reaction: Effect of phase transition. (Submitted to *Nature Catalysis*.)

9. Wei Zhang, **Cheng Li**, Guangxia Feng, Guanzhi Wang, Yaping Shi, Jinfa Chang, Zhao Li, David Fox, Lei Zhai, Meng Gu, Xiaonan Shan, and Yang Yang*. Bio-inspired superhydrophobic SnO_x film for efficient electrocatalytic CO_2 reduction enabled by a spontaneous CO_2-capturing process. (Submitted to *Nature Energy*.)

10. Xingkun Wang#, Hanxu Yao#, Canhui Zhang, **Cheng Li**, Kecheng Tong, Meng Gu, Zhengwen Cao, Minghua Huang*, Heqing Jiang*. Synchronously accelerated Volmer/Tafel kinetics via integrating RuCo nanoalloy with dual-single-atoms for effective ampere-level-current-density hydrogen production. (Submitted to *Advanced Materials.*)

11. Guanzhi Wang#, Jinfa Chang#, Guangxia Feng, **Cheng Li**, Xiaonan Shan, Meng Gu, and Ynag Yang*. Electroncatalytic CO_2 Reduction with Tunable CO/H_2 Ratios on Cu-Sn Alloy via Controllable Field-Induced Reagent Concentration. (Submitted to *Nature Energy*.)

12. Canhui Zhang#, Xingkun Wang#, Zhentao Ma#, Hanxu Yao, Hengjun Liu, **Cheng Li**, Jian Zhou, Ren Xu, Xusheng Zheng, Huanlei Wang, Qang Li, MengCu*, Heging Jiang*, and Minghua Huang*. Spin state modulation on dual Fe center by adjacent Ni sites enabling the boosted activities and ultra-long stability in Zn-air batteries. (Submitted to *Advanced Functional Materials*. Major revision)

13. Ren Xu#, Xingkun Wang#, Mingzi Sun, Canhui Zhang, **Cheng Li**, Zhengwen Cao, Meng Gu*, Bolong Huang*, and Minghua Huang*. Promoting Oxygen Reduction Kinetics of Single Fe Sites for Robust Neutral Zn-air Batteries via Engineering Fe Nanocluster as Proton-feeding Center. (Submitted to *Advanced Materials*.)

14. Xingkun Wang#, Hanxu Yao#, Canhui Zhang, **Cheng Li**, Kecheng Tong, Meng Gu, Zhengwen Cao*, Minghua Huang*, and Heqing Jiang*. Double-tuned RuCo dual-single-atoms and nanoalloy with synchronously expedited Volmer/Tafel kinetics for effective and ultrastable ampere-level-current-density hydrogen production. (Submitted to *Advanced Functional Materials*.)

15. Growth study of mass-selected Ag clusters prepared by magnetron sputtering method. (In preparation)

16. Morphology- and structure-controlled deposition of mass-selected Ag8k clusters by magnetron sputtering method. (In preparation)

17. Fabrication of Ag@Cu and Cu@Ag core-shell clusters by magnetron sputtering cluster source. (In preparation)

18. In situ observation of dynamic phase separation in AuPd and PtPd clusters under $CO + O_2$ gas phase. (In preparation)

Chapter 1 Introduction

Clusters, with the number of atoms in the range of two to one million, have wide applications in catalysis[1,2], medicine[3], plasmonic[4,5], sensors[6], environmental materials[7], and so on due to their unique physicochemical properties compared with their respective bulk materials.

Two kinds of strategies are employed in the preparation of metal clusters, i.e., the top-down and bottom-up[8]. The top-down method is trying to break bulk materials down to the nanometer level. Typical examples are ball milling and etching, with difficulties in the precise control of the sizes, structures, and compositions of the products[9–12]. The bottom-up approach, with an atom-by-atom or cluster-by-cluster formation process, is more commonly applied. This approach can produce well-designed, complex structures with an excellent control on the size monodispersity, structural homogeneity, and chemical homotops. Both physical or chemical methods are employed in this method, including magnetron sputtering, vapor deposition, molecular beam epitaxy, co-precipitation, reduction, sol-gel, and so on[13–17]. It is worth noting that the magnetron sputtering method should be classified as a bottom-up approach. While it may appear that the clusters originate directly from the bulk target, they actually undergo a formation process wherein the bulk material is sputtered into individual atoms, which subsequently condense and aggregate to form clusters. Compared with various chemical preparation methods, physical synthesis procedures, especially the gas-phase synthesis approaches, provide two unique advantages, ligand-free surfaces of the

products and atomic-precision size selection by mass filters. Bao et al. have demonstrated that such catalysts with a clean surface will result in an obvious increase in the oxygen reduction reaction activity by 50%[18]. However, the chemical methods are more easily scaled for large-scale preparation, which is significant in real applications.

The fraction of surface atoms and the electronic structure of metal clusters greatly depend on their sizes, leading to the tunable properties of metal clusters. For example, metal clusters with the size of several nanometers have been selected as excellent catalysts in industry for many years. Since the pioneering work on Fe-based single-atomic site catalyst (Fe_1/FeO_x) was reported by Zhang et al. in 2011, single-atom catalysts (SACs) have attracted extensive research attention and become a frontier field in the field of catalysis[19]. The 100% atom utilization[20], high selectivity[21–24], unique electronic structure, and unsaturated coordination environment of the active center in SACs can greatly improve the catalytic activity[21,25,26]. However, the low metal loadings to avoid sintering and agglomeration during the reaction severely limit the development and application of SACs[27–30]. Moreover, while SACs feature well-defined, atomically precise active sites, they are limited by the simplistic single-atom active sites that are more or less incapable to catalyze the chemical transformation of complicated bulky molecules or multi-electron redox reactions. In recent years, researchers have gradually turned their attentions to the single-cluster catalysts (SCCs)[31–34]. Here, the SCCs specifically refers to those clusters with sub-nanometer sizes. Compared with SACs, SCCs have higher metal loadings, easily tunable electronic

structures by changing the atoms in small clusters[34,35], and unsaturated coordination sites that can simultaneously adsorb multiple reactants. Furthermore, the synergistic effect between metal atoms in SCCs can change the adsorption mode of key intermediates and optimize the reaction path, thus significantly improving the catalytic activity and selectivity[32,36–38]. All these results demonstrate the importance of well-controlled size distribution during the cluster synthesis.

The physicochemical properties of metal clusters are also related to their atomic structures. There are two groups of atomic structural motifs, i.e., crystalline motifs and non-crystalline motifs. Three common structures in bulk materials belong to the crystalline structures, including face-centered cubic (FCC), body-centered cubic (BCC), and hexagonal close-packed (HCP). All of these can be obtained by repeating the unit cell. When structures cannot be repeated to give a periodic pattern, these structures can be grouped into non-crystalline motifs, like icosahedron (Ih) and decahedron (Dh) structures.

A schematic diagram of the Ih structure is shown in Figure 1.1. An icosahedron can be considered as the product of 20 FCC tetrahedra. However, if 20 regular tetrahedra are packed with a common vertex in the central site, large interstices will remain among these tetrahedra. To fill these spaces, the tetrahedra must be distorted and generate a huge strain in the structure. It is the same case for a decahedron, which can be seen as composed of 5 regular FCC tetrahedra sharing a common axis in the center with a gap of 7.35° in the lattice[39,40]. So, the tetrahedra will also be distorted to form a

decahedron, and the strain in decahedra will be much smaller than that in the case of icosahedra. Apart from the normal Dh, there are another two variants shown in Figure 1.1. The Ino-decahedron (Ino-Dh) is formed by introducing five {100} facets on the side surface[39], and the Marks-decahedron (Marks-Dh) further introduces ten re-entrant {111} facets at the five twin boundaries[39,41]. The detailed geometry of the Ino-Dh depends on the size of the {100} facets (m × n atoms). When the m is equal to n in an Ino-Dh structure, then it will be named as square Ino-Dh due to the square side faces.

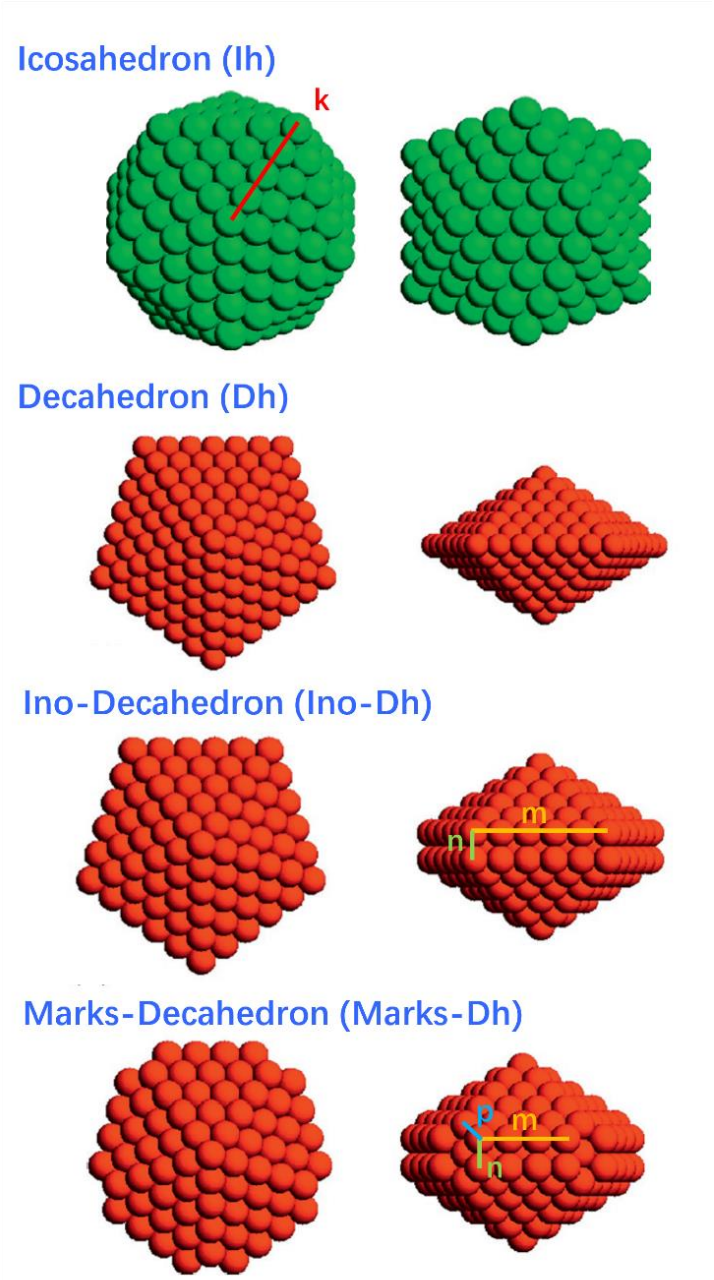


Figure 1.1: The schematic diagrams of Ih, Dh, Ino-Dh, and Marks-Dh structures. Replotted from the reference[42]. k is the atom number of the length of one edge in Ih. m and n are the atom numbers of the length and width of the {100} facets on the side surface in Ino-Dh and Marks-Dh. p is the atom number of the depth of re-entrant {111} facets in Marks-Dh.

The structures of bulk noble metals are always FCC structure. However, beyond FCC, Ih and Dh structures are common in noble metal clusters of small sizes. The excess energy of a specific structure compared with the energy of the same number of atoms

in a perfect bulk crystal is usually applied as one of the indicators of structural stability. The excess energies of FCC, Ih, and Dh structures are compared by simulation, and the results are shown in Figure 1.2[8]. When the cluster size is small, the Ih structure is the most stable one among these three structures, then followed by Dh structure with slightly increasing size. Due to the abrupt increasing internal strain of Ih and Dh structures with increasing cluster size, the most stable structure will finally become FCC structure for large clusters. However, metal clusters are not always in their stable structures during the formation process. Understanding the growth mechanism of clusters can help to generate clusters with well-controlled size, shape, and structures to obtain the desired physical and chemical properties[43]. For magnetron sputtering method, Simon R. Plant pointed out that lower power and longer condensation length are conducive to the formation of equilibrium isomers for size-selected Au_{923} clusters[44]. Siqi Lu also investigated the relationship between the atomic structures of Au_{923} clusters and the deposition power [45], which shows the same trend as the results of Simon's work. However, the effect of preparation parameters on the growth process of clusters is still unclear.

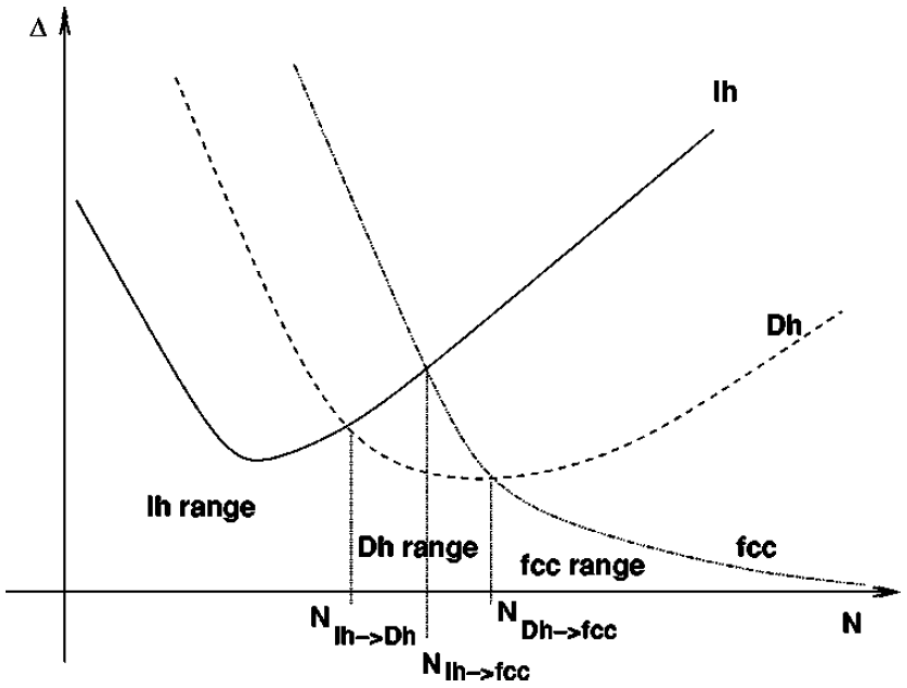


Figure 1.2: The excess energies divided by the number of surface atoms of Ih, Dh, and FCC structures with increasing cluster size[8].

Furthermore, nanoalloy clusters were widely investigated and applied in different fields due to their additional adjustable parameters than single metal clusters, including their compositions, atomic structures, and morphologies[46]. For example, there are four main possible mixing patterns for bimetallic nanoalloys, including core-shell, dumbbell, mixed, and multi-shell (also called onion). Combined with various atomic structures and different compositions, nanoalloys can evolve into a variety of possible microstructures, further leading to various and adjustable physicochemical properties. Many methods, including chemical and physical procedures, have been developed to achieve the precise preparation of nanoalloy clusters.

Among these procedures, the fast and non-equilibrium growth process of magnetron sputtering method can provide the possibility of different structural motifs which are

impossible or difficult for natural environment because of the unique physical characteristics of these materials. Some highly relevant work on bimetallic cluster preparation with magnetron sputtering had been published by other authors and is reviewed below.

Regarding the morphological structures of bimetallic clusters, Yin et al. prepared Cu@Au and Au@Cu core-shell clusters with an alloy target by controlling the Ar and He gas flow rates[47]. The results showed that the different core-shell structures are related to the nucleation of Cu clusters. With high He gas flow rates, Cu will exist mainly as atoms or small particles in the magnetron sputtering chamber and a Au@Cu core-shell structure can be formed. However, when the He gas flow rate is low, stable Cu clusters with larger size can form and the attachment of Au atoms generates Cu@Au core-shell clusters. Yin also investigated ageing of these mass-selected Cu@Au and Au@Cu core-shell clusters, which proved that the Au@Cu core-shell structure is unstable both in vacuum and in air[48].

Ayesh et al. tried to prepare CuSn bimetallic clusters by using a Sn target partially covered with Cu sheets[49]. They mainly discussed the relationship between gas flow rate and the size of bimetallic clusters, but the structure of CuSn bimetallic clusters was ignored.

Grammatikopoulos et al. observed Janus and Ag@Cu core-shell metastable structures with magnetron sputtering. They showed by molecular dynamics (MD) and Monte Carlo (MC) computer simulations that these are formed by aggregating at relatively low

temperature and stabilizing by subsequent quenching[50]. In their work, the ratio of Ag and Cu atoms in the clusters can be adjusted by the ratio of power applied on the Ag and Cu targets. Cai et al. also adjusted the atomic ratio of AuCu alloy clusters by controlling the sputtering powers[51].

Krishnan et al. successfully tuned the structural motifs of Mo-Cu bimetallic clusters by using a section target composed of half Mo and half Cu[52]. The structural motifs varied from a fully mixed alloy to a core-shell, then to an onion (multi-shell), and finally to a Janus/dumbbell structure. The different structural motifs can be seen as resulting from the different plasma energies and thermal environments during nucleation and growth process. In the fast growth regime, the bulk immiscible Mo and Cu atoms will form Janus or metastable core-shell structure. While with slow growth, there will be more time for Mo and Cu atoms to diffuse and form the observed alloy or stable core-shell structures.

Although the previous works have made great progress in the preparation parameters on the structural motifs of bimetallic clusters with alloy targets, single special-designed targets with two materials, or dual-target system. Several questions are still unresolved as follows. 1) For the same preparation parameters, how does the atomic ratio of components and the structural motif change with increasing size? 2) With an alloy target, once the different types of atoms (A and B) have been sputtered from the target surface, they will bond together based on the strength of the binding energies between A-A, A-B, and B-B. Thus, can the structural motifs be tuned with different powers and

condensation lengths and which factor is the most important one, surface energy or cohesive energy of these two different materials during growth? 3) In a dual-target system, the condensation lengths of different target can be adjusted individually. Thus, it might be possible to control the nucleation sequence of two materials such that core-shell structures can be formed. By doing heating experiments, the stability of A@B or B@A core-shell structures can be tested. Thus, can the structure transition process of unstable core-shell structure be recorded and revealed via in-situ observation? 4) Can the diameter of the core and/or the thickness of the shell be controlled for mass-selected bimetallic clusters by adjusting preparation parameters?

Additionally, apart from the morphological structures of bimetallic clusters discussed above, there have been few investigations regarding the atomic structures of bimetallic clusters. However, obvious Ih or Dh structure of bimetallic alloy or core-shell clusters can be observed in investigations[53–60]. The authors merely mentioned the topic in passing or disregarded it altogether, but no further discussion was presented. So, investigations about atomic structures of bimetallic clusters should be explored in order to answer the following questions. 1) Unstable Ih structure can be obtained for monometallic clusters with magnetron sputtering because of fast growth process. When it comes to the bimetallic clusters, can material B help to stabilize the unstable Ih structure of materials A? A further question is that what is the size range of Ih, Dh and bulk structures for bimetallic alloy or core-shell clusters. 2) For a core-shell cluster with Ih structure, how strain is distribute in this cluster and what is the atom arrangement of different kinds of atoms at the interface of core and shell? 3) Will bimetallic alloy

clusters with unstable Ih structure transform to other structures during heating, such as Dh, or will the alloy phase separate into core-shell structure?

To understand the growth process of mono- and bimetallic clusters, this thesis presents an investigation into the growth of size-selected Ag and AgCu clusters using magnetron sputtering. A mass-selected cluster source was employed for the preparation of the clusters, which were then characterized using aberration-corrected Scanning Transmission Electron Microscopy (STEM) to determine their morphology and atomic structure. This information allowed for a better understanding of the growth process of Ag clusters in the magnetron chamber. The results demonstrate that the morphologies and atomic structures of size-selected Ag clusters can be manipulated by adjusting the preparation parameters, which are highly related with the cluster growth pathways in the magnetron sputtering chamber.

Furthermore, the preparation of bimetallic core-shell Ag@Cu and Cu@Ag clusters was achieved by varying the condensation lengths of two targets. The magnetron sputtering method typically results in the formation of pure Ag clusters with an Ih structure, while Cu clusters tend to exhibit an FCC structure. However, in the case of Ag@Cu clusters, the Cu shell atoms conform to the surface arrangement of the Ag-Ih or Ag-Dh core. Conversely, Cu@Ag core-shell clusters often exhibit an outer shell comprising Ag FCC domains. This unique atomic arrangement of the shell gives rise to distinct surface structures when compared to their respective monometallic clusters. Such variations offer valuable insights into the synthesis of surface structure-controlled materials.

The first chapter of the thesis provides a brief introduction to the applications and atomic structures of metal clusters. The second chapter focuses on the sample preparation and characterization techniques used, including the magnetron sputtering method and aberration-corrected STEM. The third chapter presents the experimental results and discussions of the growth study of size-selected Ag clusters, followed by an exploration of the most stable structures for Ag clusters in the size range of 1k to 14k atoms in the fourth chapter. The fifth chapter discusses the effect of Ar and He gas flow rates on the growth process of Ag8k clusters in the magnetron sputtering chamber. The sixth chapter investigates the parameters for the preparation of Ag@Cu and Cu@Ag clusters and their atomic structures. Finally, the seventh chapter provides a summary of the conclusions and future outlook.

Chapter 2 Experimental Techniques

2.1 Magnetron sputtering inert gas condensation mass-selected cluster source

2.1.1 Components of the cluster source

A magnetron sputtering inert gas condensation mass-selected cluster source has been used for cluster preparation in the Nanoscale Physics Research Laboratory (NPRL). As shown in Figure 2.1, the cluster source is mainly composed of four parts, including sputtering and cluster generation, beam focusing and acceleration, mass selection, and deposition. Two-stage pump systems (rotary pumps and turbo pumps) are used to maintain a base pressure of about 10^{-7} mbar for the whole system. Details of different parts are presented in this section.

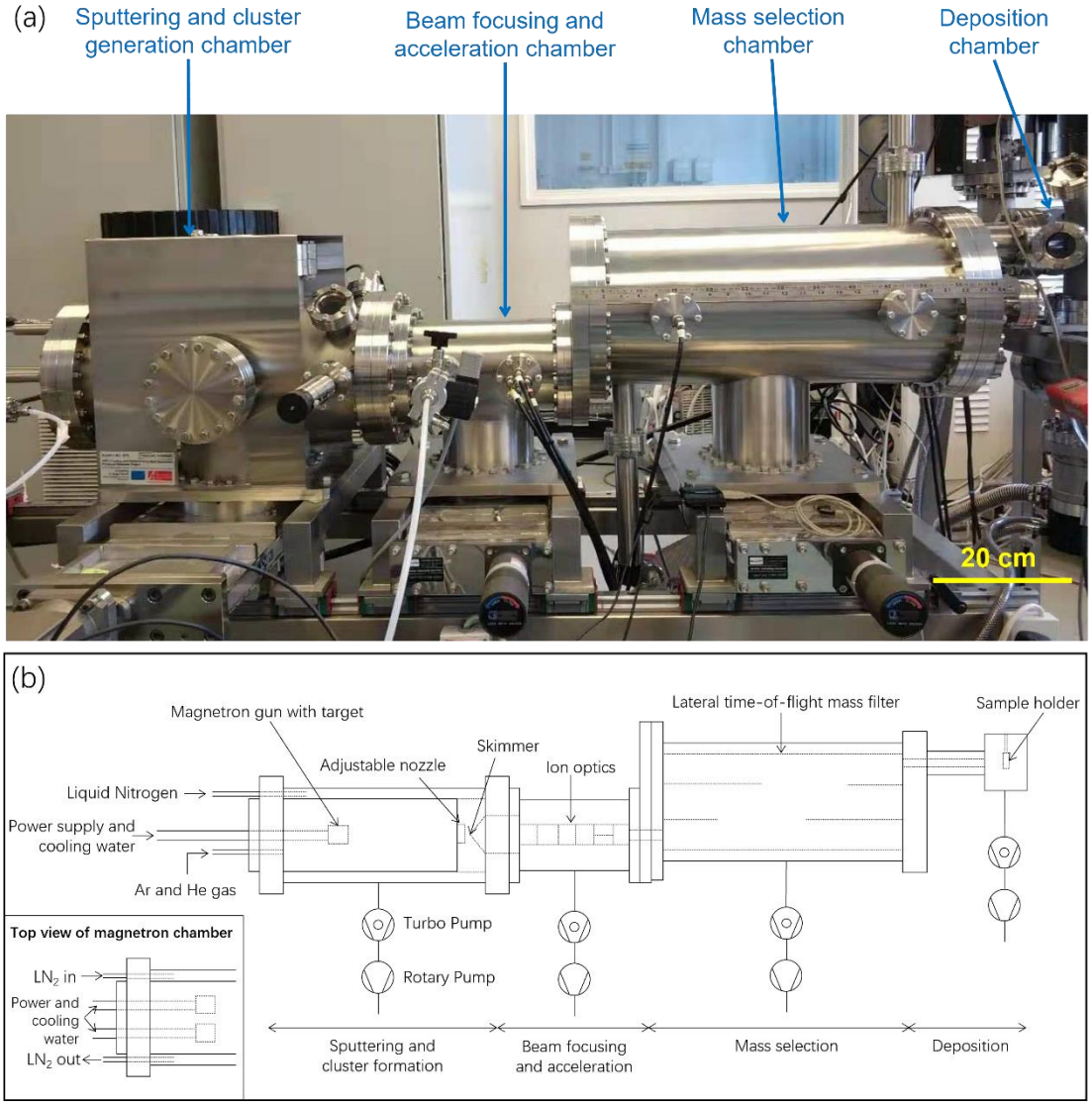


Figure 2.1: (a) Photograph of the magnetron sputtering inert gas condensation mass-selected cluster source in NPRL; (b) schematic diagram of this cluster source.

2.1.2 Sputtering and cluster generation

The magnetron sputtering method is applied for cluster preparation in this cluster source. As shown in Figure 2.2 (a), in order to initiate the plasma, a high voltage is applied to the sputtering target. Then, when the plasma is stable, electrons are accelerated away from the surface of the target and collide with sputtering gas molecules, i.e., Ar gas in this research, which results in the ionization of the Ar gas molecules and formation of

positive Ar ions. These Ar ions are accelerated towards the negatively charged cathode and impinge on the target surface. As a result, the target atoms are ejected into the environment with high kinetic energy. Electrons will be trapped in a magnetic field due to the application of two permanent magnets located behind the target, leading to a higher electron density and a higher sputtering rate, which is a unique advantage of magnetron sputtering compared with other sputtering methods[61]. The ejected atoms will generate cluster seeds by three-body collisions of two hot target atoms and one cold gas atom (Ar or He) as shown in Figure 2.2 (b). The high kinetic energy of target atoms can be released by three-body collision and a cluster seed can be stably preserved. Then, the cluster growth process can be achieved in two ways of two body collisions, the attachment of single target atoms, or collisions between two clusters. The role of Ar gas in the magnetron sputtering chamber is sputtering and cooling, while the He gas is applied only for cooling because there was no plasma without Ar gas under low power. Furthermore, the cooling ability of Ar atoms is more effective than that of He atoms due to the higher atom mass of Ar.

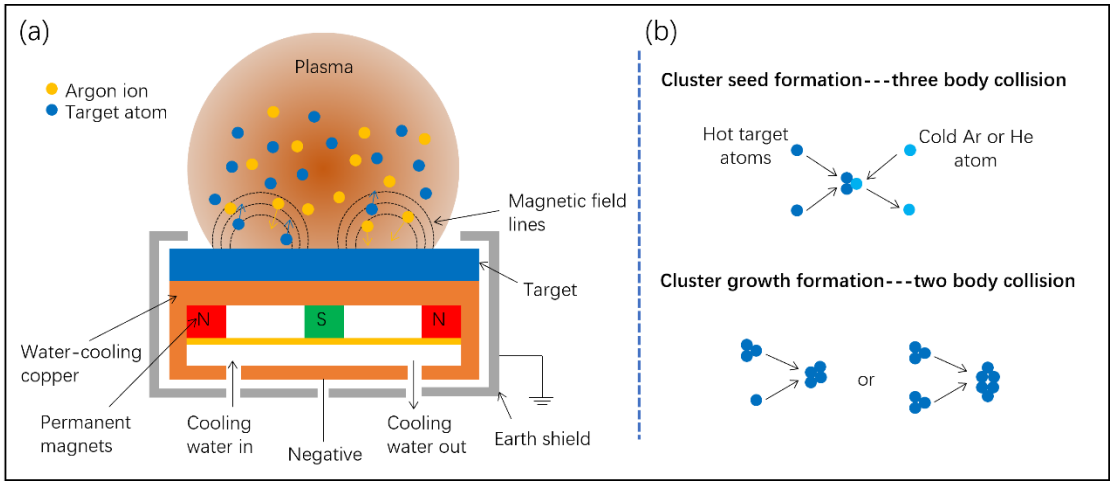


Figure 2.2: Schematic diagrams of (a) magnetron sputtering and (b) cluster seed formation and growth process.

Some other details of the sputtering and cluster generation chamber can be seen in Figure 2.3. The magnetron guns are cooled by cooling water to release the high heating energy caused by the plasma. The sputtering chamber can be cooled by liquid nitrogen (LN_2) or just work without any cooling, but the formation process of clusters can be more effective with LN_2 cooling because the heat exchange process between hot sputtered atoms and cooled gas atoms can be more powerful when LN_2 cooling is applied. With the LN_2 cooling, the temperature of the chamber wall and the pressure in the sputtering chamber will decrease gradually with the increasing LN_2 cooling time. The changes in the pressures when applying different gas flow rates was investigated, and the results are shown in Figure 2.4 (a). The decreasing chamber pressures with longer LN_2 cooling time indicate that the thermal environment of the magnetron sputtering chamber will achieve a stable state after the LN_2 cooling for about 5 hours. For the applied Ag target, the mass spectra at different LN_2 cooling times are shown in Figure 2.4 (b). Only for a cooling time longer than 3 hours, Ag clusters with large sizes

can be obtained. When the cooling time is shorter than 3 hours, only Ag single atoms, dimers, and trimers can be obtained after the mass filter, as shown in Figure 2.4 (c). After LN_2 cooling for more than 5 hours, large Ag clusters can be obtained due to the promotion of cooled gas atoms on the growth of Ag clusters and the mass spectrum can be reproducibly obtained, indicating that the preparation for Ag clusters should only be initiated after at least 5 hours of LN_2 cooling to ensure repeatable results between different experiment runs. Besides, the flow rate of LN_2 can be tuned for a shorter cooling time to achieve a stable chamber environment.

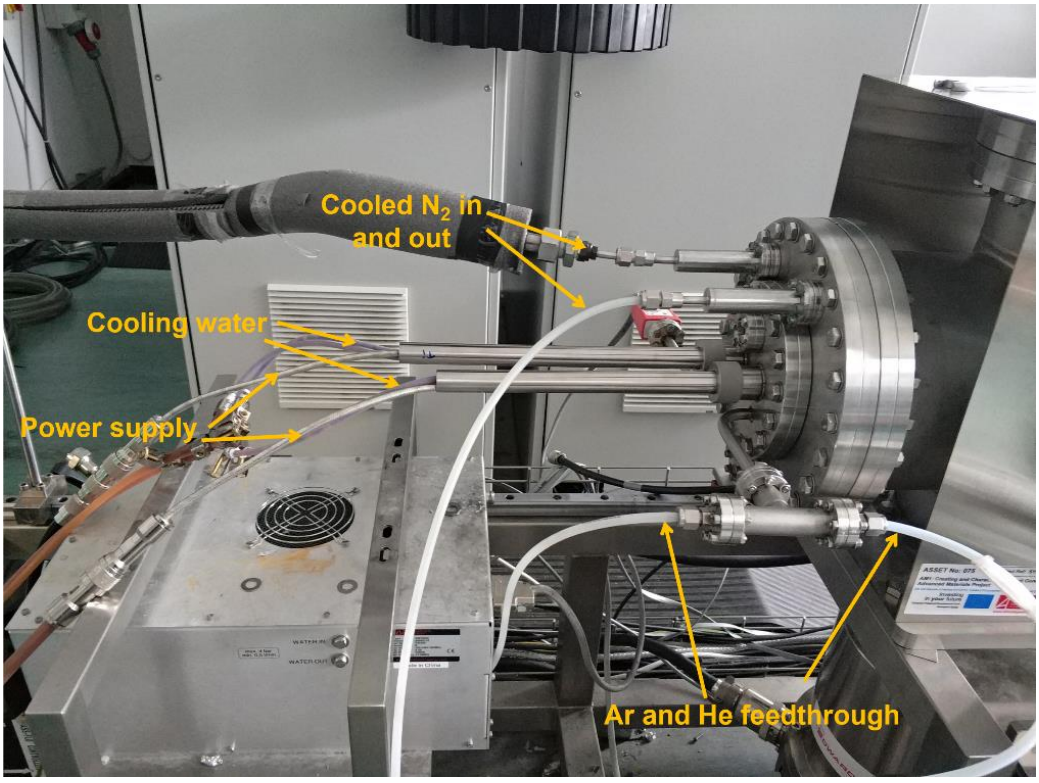


Figure 2.3: Photograph of the cluster generation chamber configured for dual-target sputtering.

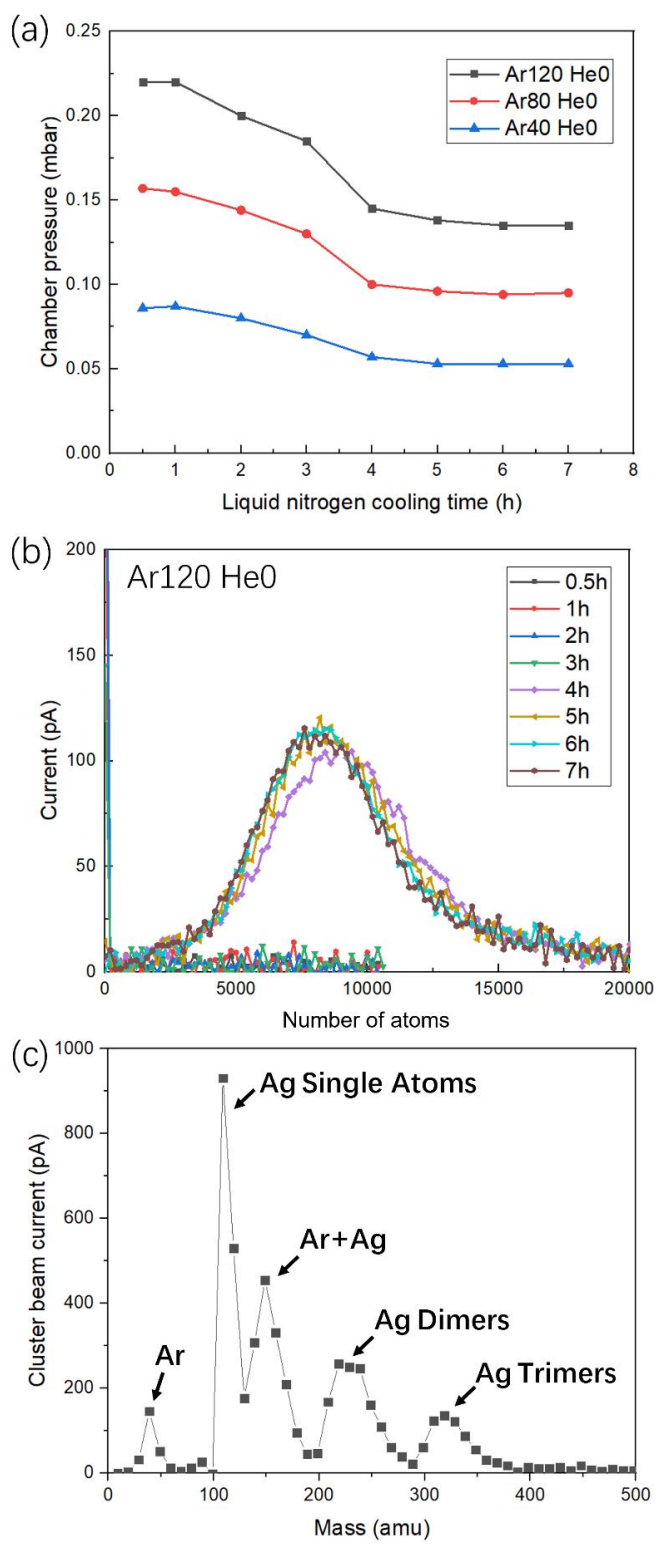


Figure 2.4: (a) The relationship between the chamber pressure and the LN_2 cooling time for different gas flow rates. (b) The mass spectra of Ag clusters with different cooling times when only one 1-inch Ag target was applied. The parameters are a power of 10 W, an Ar gas flow rate of 120 sccm (standard cubic centimeter per minute), a He gas flow rate of 0 sccm, and a condensation length of 250 mm. (c) The mass spectrum of Ag when the cooling time is 30 min.

Single- or dual-target magnetron guns both can be applied in this cluster source, providing a more flexible cluster generation process. Adjustable parameters of single- and dual-target magnetron guns are presented in Table 2.1 and their schematic diagrams are shown in Figure 2.5 (a) and (b), respectively. With dual-target magnetron guns, different structures like core-shell, Janus, and mixed morphologies of bimetallic clusters can be obtained by adjusting the preparation parameters of different targets, such as different power and condensation lengths.

Table 2.1: Parameters of the single-target magnetron gun and dual-target magnetron guns. OD: outside diameter.

Items	**Range**
Target material	A wide range of materials, including most metals and materials with excellent to poor electrical conduction
Target size	Single: 2 inches OD
	Double: 1 inch OD
Power	Single: 0-200 W
	Double: 0-75 W
Condensation length	150-250 mm
Exit nozzle size	1-10 mm
Ar and He flow rate	0-200 sccm for each
Working pressure of magnetron chamber	8×10^{-5}-10 mbar

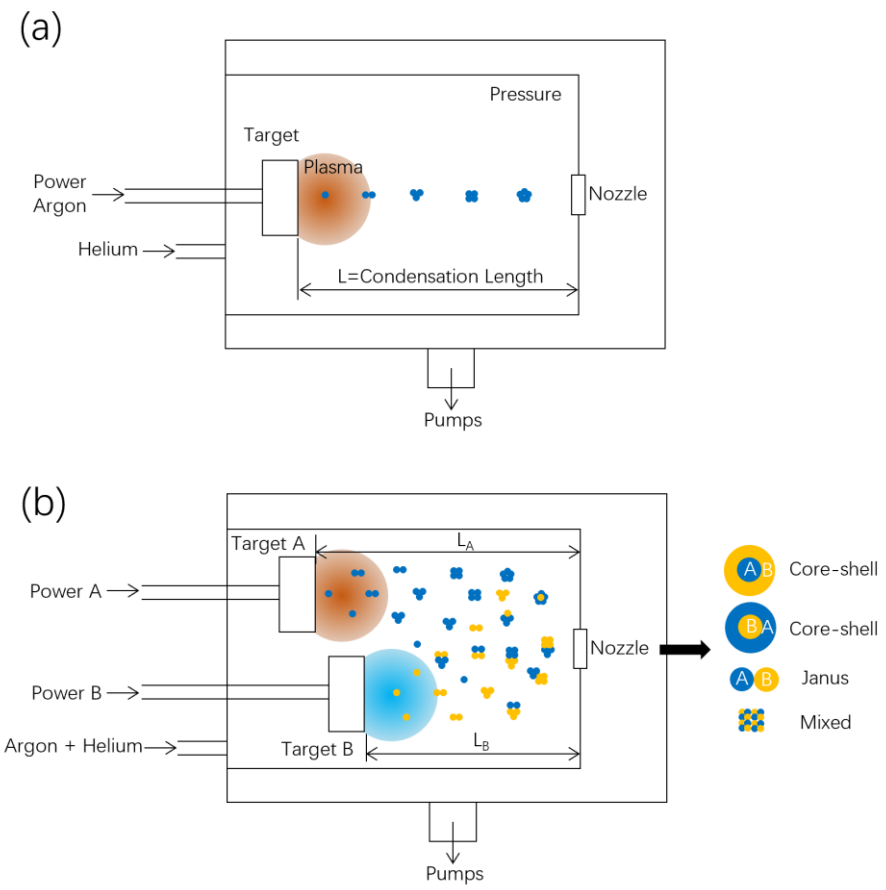


Figure 2.5: Schematic diagrams of (a) single-target magnetron gun and (b) dual-target magnetron guns.

2.1.3 Beam focusing and acceleration

When the cluster source is working, Ar and He gas will be continuously fed into the sputtering chamber, which will cause the increase of chamber pressure in the magnetron sputtering chamber. Then, due to the increasing pumping speeds from the sputtering chamber to the deposition chamber and flow-limiting apertures between them, a pressure gradient will form among different chambers. The introduced pressure difference will pull the gas and inside clusters out from the sputtering chamber and form a cluster beam. The cluster beam will be expanded after leaving the sputtering chamber from a nozzle. The divergence of the expanded beam is small, about 5°-10°, depending

on the pressure difference between these two chambers[62]. The gas pressure of the sputtering chamber can be well controlled because of the adjustable nozzle size. After passing the nozzle, the cluster growth process will stop. Then, the positively charged clusters will be selected because of a negatively biased skimmer and are further accelerated by a series of negatively biased ion optics[63].

2.1.4 Mass selection

A lateral time-of-flight mass filter is applied to achieve mass selection in the cluster source, as shown in Figure 2.6. High voltage pulses are applied to plates 1 and 4, thus generating an acceleration, free fly, and deceleration region between the different plates while the high voltages are switched on to generate electron fields. Only clusters with the desired mass can successfully pass through these three areas when using a certain set of pulses and the mass selection can be achieved in this way. If the cluster beam is well focused, then the theoretical mass resolution is given by[64]:

$$R = \frac{M}{\Delta M} = \frac{x}{x_2} \tag{2.1}$$

where M is the mass of the ion, and ΔM is the full-width half-maximum (FWHM) of masses that pass through the exit aperture. x is the lateral displacement of the cluster beam and x_2 is the width of the exit aperture.

However, if the beam is not well focused then the width of the entrance aperture, x_1 will affect the beam size and the resolution will be corrected as:

$$R = \frac{M}{\Delta M} = \frac{x}{\sqrt{x_1^2+x_2^2}} \tag{2.2}$$

Here, the length of x is 176 mm, and the widths of x_1 and x_2 are the same, which is 8 mm for the normal setting (the range for x_1 and x_2 can be 0-8 mm). So, we have a theoretical mass resolution of 22 and about 16 according to equations (2.1) and (2.2), respectively. In our work, the mass resolution can be in the range of 16-22, depending on whether the beam is well-focused or not.

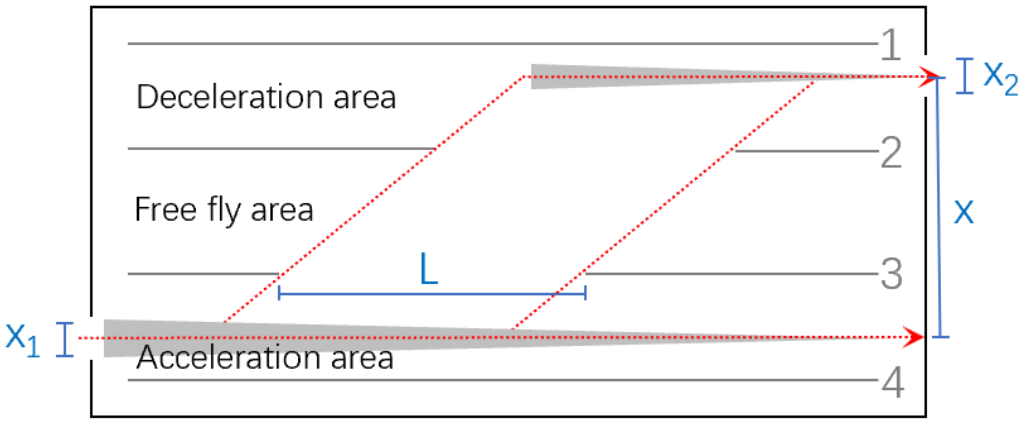


Figure 2.6: A schematic drawing of the lateral time-of-flight mass filter used in the cluster source. x is the lateral displacement of the cluster beam, L is the segment of the cluster beam used in each pulse series, x_1 is the width of the entrance aperture and x_2 is the width of the exit aperture.

2.1.5 Deposition of the clusters on the carbon film

The positively charged clusters can pass through the mass filter and be detected by the picoammeter, further forming a curve that describes the relationship between the beam current and the increasing size, i.e., the mass spectrum. The sample manipulator has two faces. One face is specifically designed for measuring the beam current and forming a mass spectrum, while the other face, which features a notch, is utilized for

securely fixing TEM grids and measuring the beam current during the deposition process. One mass spectrum obtained before the deposition is shown in Figure 2.7 (a), while the mass spectrum obtained during deposition is about half of that before deposition, which is because the shield with holes on the TEM grid blanked part of the deposited Ag clusters during deposition. To evaluate the effect of instrument noise on the mass spectra, a mass spectrum of only noises is presented in Figure 2.7 (b), indicating a mean noise signal of 2.81 pA with a standard deviation of 3.33 pA. After passing through the time-of-fight mass filter, the selected clusters will be deposited on the sample. Normally, copper TEM grids with carbon film are used as the deposition substrate. To achieve a suitable cluster density on the TEM grid, a total deposition mass will be set during deposition, leading to a longer deposition time at lower beam current. To save the target materials during deposition and considering the noise level in the mass spectrum, only cluster sizes with beam currents higher than 20 pA are considered as potential deposition sizes.

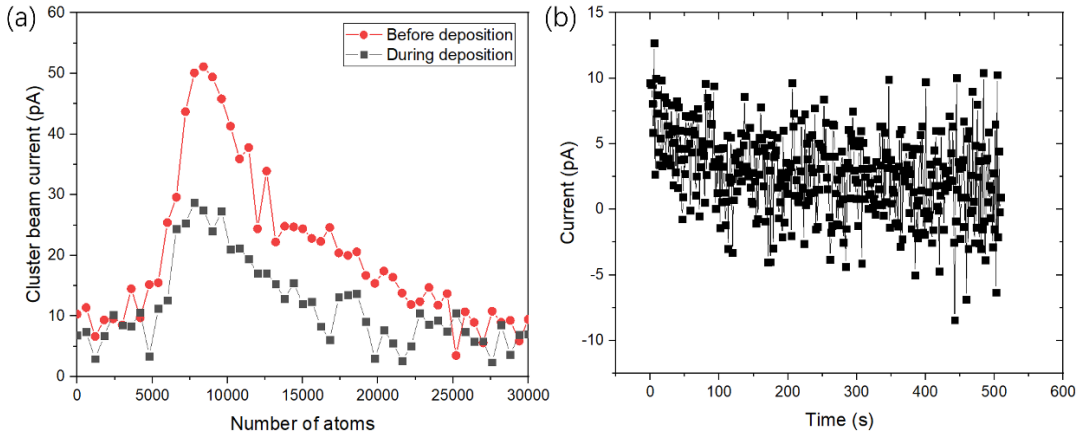


Figure 2.7: (a) The mass spectra of Ag clusters before and during deposition, respectively. The applied parameters are a power of 10 W, an Ar gas flow rate of 40 sccm, a He gas flow rate of 0 sccm, a condensation length of 250 mm, and a chamber pressure of 0.075 mbar. (b) Sample current at a fixed mass as a function of time to illustrate the noise level.

For deposition, clusters can be soft-landed, deformed, scattered, fragmented, implanted, or pinned on the surface of the substrate according to the impact energy[65]. The impact energy of the clusters is controlled by the bias voltage applied to the sample holder. An impact is considered to be "soft-landing" when the kinetic energy per atom in the cluster is less than the binding energy of atoms in the cluster (which is typically below the level of 1 eV/atom)[63,66,67]. In this case, the clusters can preserve their compositions, but the structure of the cluster may be distorted. So, "soft-landing" is usually applied when it is critical or beneficial to preserve the size and structure of clusters[68].

2.1.6 Effects of preparation parameters on the size of clusters

There are several parameters that can be adjusted when generating clusters, including sputtering power, chamber pressure (modified by adjusting the nozzle size but with a fixed gas flow rate), condensation length, and gas flow rate (tuned by changing the inserted Ar and He gas flow rate but with a fixed nozzle size). One important point to

note is that the alteration in gas flow rate will also result in a corresponding adjustment of chamber pressure. However, changing the gas flow rate and the nozzle size can be likened to adjusting the gas input and output of the magnetron chamber, respectively. While both cases may result in changes in chamber pressure, their effects on cluster formation are not identical, as will be discussed in the following content. In order to elucidate the effects of these parameters on the cluster size, experiments with Cu targets were performed. The results of Cu clusters are shown in Figure 2.8.

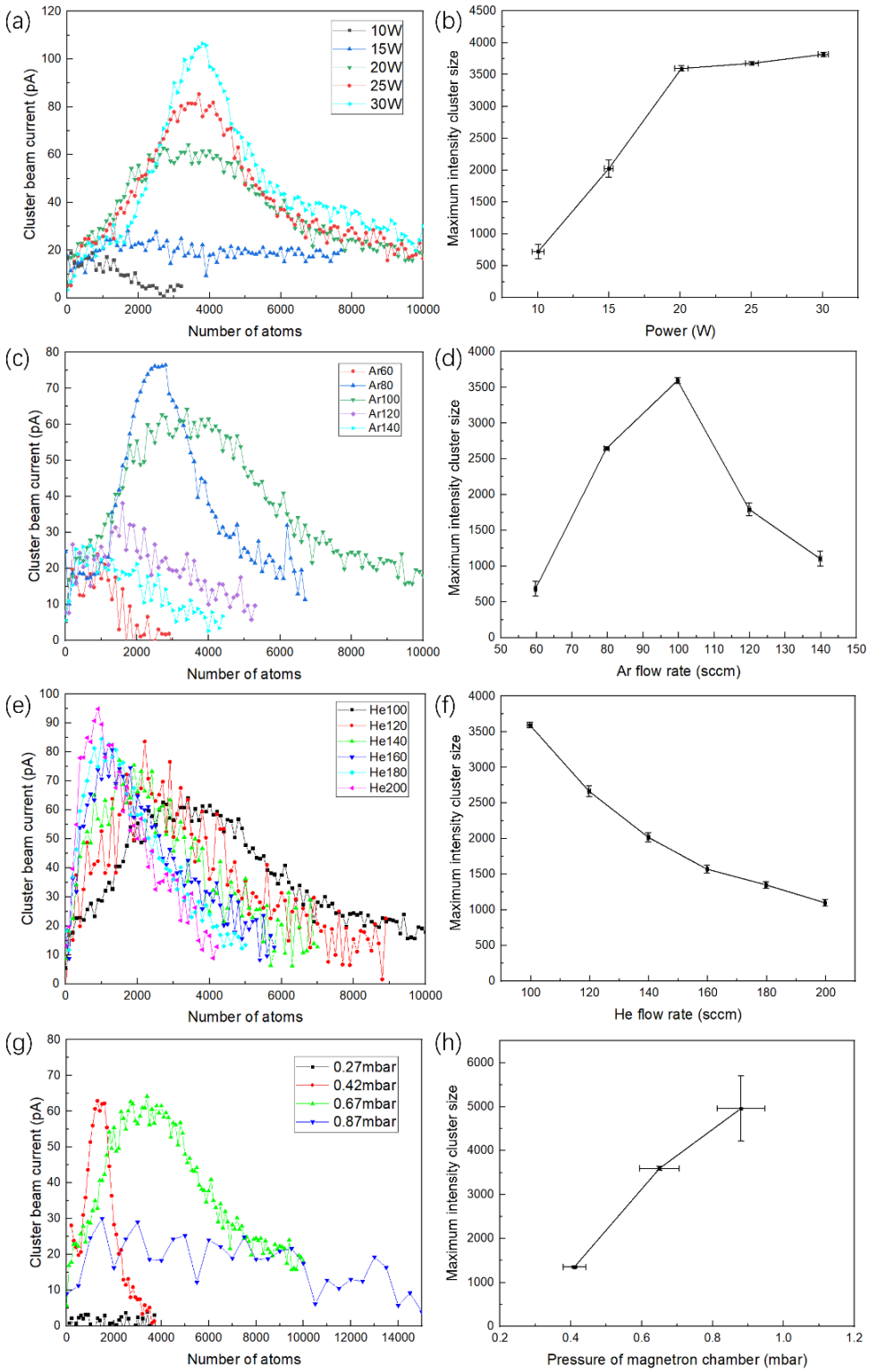


Figure 2.8: The effects of different parameters on maximum intensity cluster size of Cu clusters. The initial parameters are a power of 10 W, an Ar gas flow rate of 100 sccm, a He gas flow rate of 100 sccm, a condensation length of 250 mm, and a chamber pressure of 0.66 mbar. (a), (c), (e), and (g) are mass spectra of different adjusted parameters based on the initial parameters, i.e., (a) the power range of 10-30 W, (c) the Ar flow rate range of 60-140 sccm, (e) the He flow rate range of 100-200 sccm, and (g) the chamber pressure range of 0.27-0.87 mbar. (b), (d), (f) and (h) are trends between obtained cluster peak sizes and different parameters.

For the Cu target, the size of clusters increases with increasing power and with increasing chamber pressure. With an increasing Ar flow rate, the cluster size will first increase and then decrease. As for the He flow rate, the size of Cu clusters will decrease with an increasing He flow rate. And finally, for different chamber pressures, Cu clusters will only be generated in special pressure ranges. These results can be explained as follows.

Ar gas flow rate

Increasing Ar gas flow rate has the following effects: (1) increased Ar concentration and thus increased density of sputtered atoms because of a higher sputtering rate; (2) reduced residence time of clusters in the sputtering chamber due to the higher gas pressure differential between the interior and exterior of the chamber; (3) increased growth rate by a faster heat exchange process due to the higher Ar gas density; and (4) decreased density of sputtered atoms through reducing sputter yield at an extremely high flow rate because the scattering effect of Ar atoms on the sputtered metal atoms will be enhanced and a lot of sputtered atoms redeposit on the target surface[69–71]. In summary, the increasing Ar flow rate has both positive and negative effects on the size of clusters. When the increase of Ar gas flow rate is not so much, effect (1) and (3) play dominant roles and promote the cluster growth process. However, when the Ar gas flow rate reaches a relatively high level, effect (2) and (4) will hinder the growth of clusters, especially due to the decreasing growth time.

He gas flow rate

Increasing the He flow rate impacts the process in the magnetron chamber in two ways: (1) increased the number of small clusters by increasing three-body collisions and (2) reduced the residence time of clusters in the growth zone. Both two effects will result in a smaller mean cluster size. One important point to note is that the increase in chamber pressure resulting from a higher He gas flow rate only leads to an increase in the density of He atoms. However, it does not affect the sputtering rate.

Sputtering power

A higher power will increase the density of sputtered atoms in the magnetron chamber due to a higher ionization rate, thus increasing cluster size. However, when the power is too high, the plasma will be unstable, which is harmful to the formation of clusters, so the cluster size will decrease in this case. The decrease of the cluster size has not been observed in Figure 2.8 but was found in other works[69–71].

Chamber pressure

The chamber pressure can be changed by adjusting the nozzle size. Higher chamber pressure will lead to a larger cluster size, which is associated with the probability of collisions. Higher chamber pressure means a higher density of ions, atoms, and clusters, so that the probability of collisions can be increased and larger clusters can be generated.

Condensation length

Although experiments about the adjustable condensation length haven't been done in this research, it is pointed out by other researchers[72,73] that longer condensation length promotes the formation of larger clusters as it increases the residence time of clusters in the condensation chamber.

2.2 Aberration-corrected Scanning Transmission Electron Microscopy (STEM)

2.2.1 Basic design of STEM and its components

The aberration-corrected STEM (Joel JEM 2100F) installed at NPRL is shown in Figure 2.9 with a schematic to explain the basic design and main components in STEM. The STEM is mainly composed of four significant parts: the electron emission gun, electron optics, aberration corrector, and electron detectors.

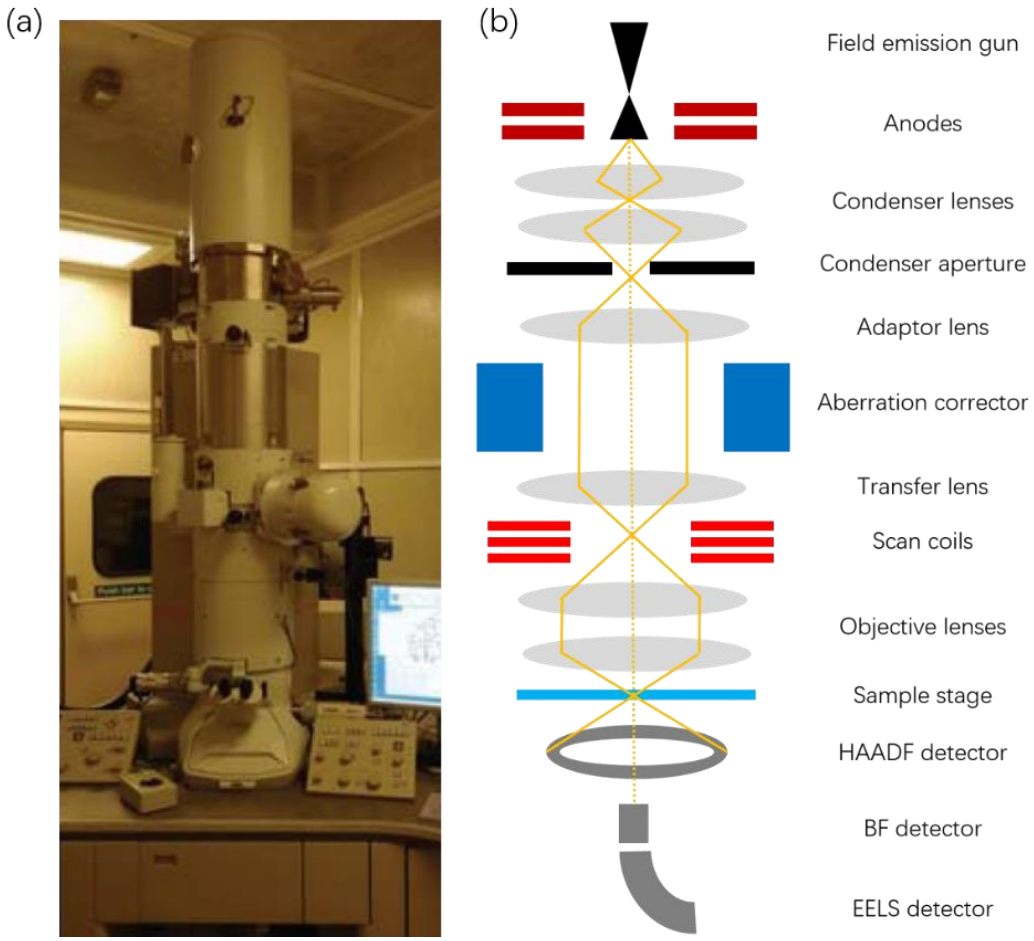


Figure 2.9: (a) Photograph of Joel JEM 2100F in NPRL; (b) schematic diagram of aberration-corrected STEM.

The electrons are generated in the electron gun and accelerated by two anodes up to the desired voltage, which in this system is 80 kV or 200 kV (more commonly used). The electrons are then focused by a series of electromagnetic lenses to form an electron beam. The strength of the magnetic field for these lenses can be precisely controlled by adjusting the current in the lens coils. However, since these lenses are not perfect, there will be aberrations. The aberration corrector is used to compensate for the spherical aberrations of the electron beam. After the aberration corrector, an electron probe is then formed by the objective lenses and scanned over the selected area of the specimen. The scatted electrons with different angles are collected by the high-angle annular dark

field (HAADF) detector and bright field (BF) detector, which will be recorded into HAADF-STEM and BF-STEM images, respectively.

2.2.2 Principle of imaging in STEM

When electrons pass through the specimen, they will interact with the nucleus and electron cloud. Figure 2.10 (a) shows the different trajectories of scattered electrons during this interaction process. The scattered angle decreases with the increasing distance from the nucleus. The weakly scattered and unscattered electrons are used to form BF images as shown in Figure 2.10 (b). The highly scattered electrons (greater than 50 mrads) are normally used for HAADF-STEM images, which are also known as Z-contrast images. The "Z-contrast" is from the Rutherford scattering model[74]. If the high-angle scattering only comes from the electron-nucleus interaction (also called Rutherford scattering), the differential cross section of this kind of scattering can be described by

$$\sigma_R(\theta) = \frac{e^4 Z^2}{16(4\pi\varepsilon_0 E_0)^2 \left(\sin\frac{\theta}{2}\right)^4} d\Omega \tag{2.3}$$

where θ is the scattering angle as shown in Figure 2.10 (a), Z is the atomic number, ε_0 is the dielectric constant, E_0 is the energy of the electron and Ω is the solid angle of scattering. From equation (2.3), it can be seen that $\sigma_R(\theta)$ is proportional to Z^2. However, the exponent is usually less than 2 because of other factors, such as the electron screening effect, detector geometry, and so on[75]. For two different elements A and B, the HAADF intensity relationship of these two elements can be written as

$$\frac{I_A}{I_B} = (\frac{Z_A}{Z_B})^n \tag{2.4}$$

Here, the power coefficient *n* should be calibrated with standard samples. Normally, if there is a large difference between the atomic numbers of these two elements, then these two kinds of atoms can be distinguished in HAADF-STEM images by their different intensities.

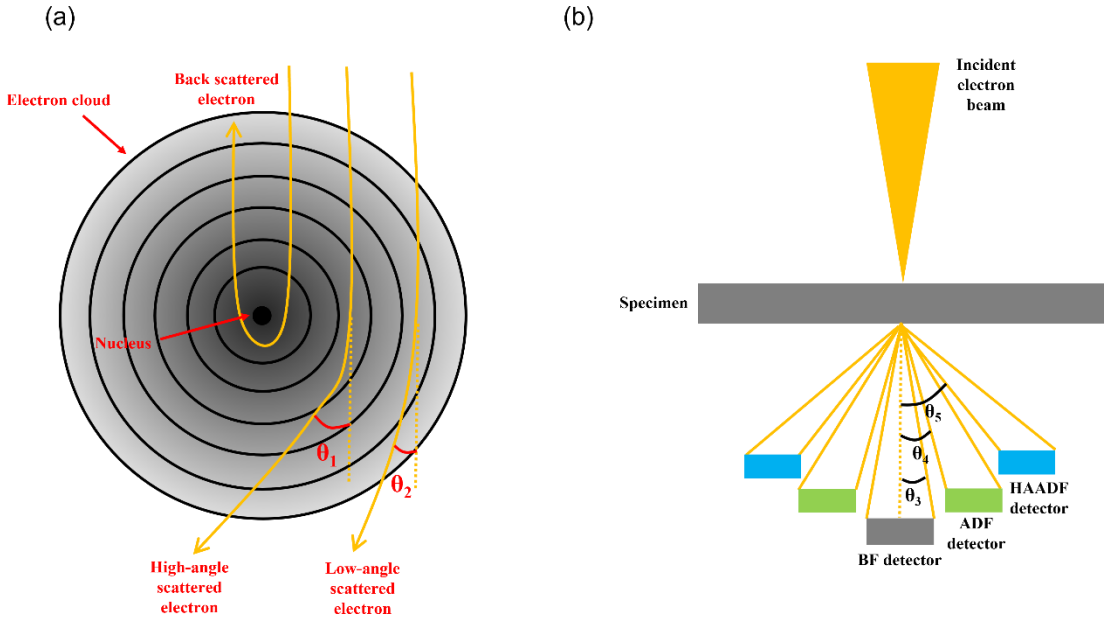


Figure 2.10: Schematic diagram of (a) different types of scattered electrons and (b) different detectors in STEM. Normally, θ_3 is less than 10 mrads, θ_4 is between 10 mrads and 50 mrads, θ_5 is higher than 50 mrads.

For HAADF-STEM images, the collection angles can be adjusted by changing the camera length, which is the effective distance from the specimen to the HAADF detector. There are two kinds of camera lengths, one without lenses called true camera length and the other one with lenses between the specimen and the detector called effective camera length[76]. For Joel 2100F in NPRL, the inner and outer diameters of the HAADF detector are 3 mm and 8 mm. Unless otherwise specified, an effective

camera length of 10 cm has been used, for which the inner and outer collection angles are 62 mrad and 164 mrad, respectively[75].

2.2.3 Aberration corrected STEM

The de Broglie wavelength of relativistic electrons can be obtained from the following equation[76]:

$$\lambda = \frac{h}{\sqrt{2meV(1+\frac{eV}{2mc^2})}} \tag{2.5}$$

where h is the Plank constant, m is the rest mass of an electron, e is the absolute value of electron charge, V is the accelerating voltage used in microscopy and c is the velocity of light. According to this equation, when the accelerating voltage is 200 kV, the wavelength of an electron beam is about 2.5 pm. Then, in STEM, the minimum distance (l) that can be distinguished for two spots, also known as resolution, can be obtained by the Rayleigh criterion[77]:

$$l = 1.22 \times \frac{\lambda}{\beta} \tag{2.6}$$

where β is the probe convergence angle in STEM mode. Equation (2.5) and (2.6) indicate that the sub-Angstrom resolution should be reached easily when the power of 200 kV is applied. However, the actual situation does not align with that assumption. The reason is that any lens used in microscopy is imperfect and the aberrations caused by these imperfect lenses will make the practical resolution much worse than the theoretical one.

There are two major types of aberration in STEM, which are chromatic and spherical aberration[76,78]. Chromatic aberration is caused by the energy difference of those electrons generated from the electron gun, so that they cannot be converged to the same focal point. On the other hand, spherical aberration is caused by the different convergent abilities of different parts of the magnetic field. The strength of the magnetic field is stronger when the distance is further from the axis, which will result in electrons on the edge of lens more strongly deflected. Therefore, the electron beams will finally be converged to a quite large spot rather than one point at the expected focal plane as shown in Figure 2.11. The spherical aberration can be compensated by multiple quadrupoles and octupole lenses in Nion method and hexapole and transfer lenses in CEOS system[78,79].

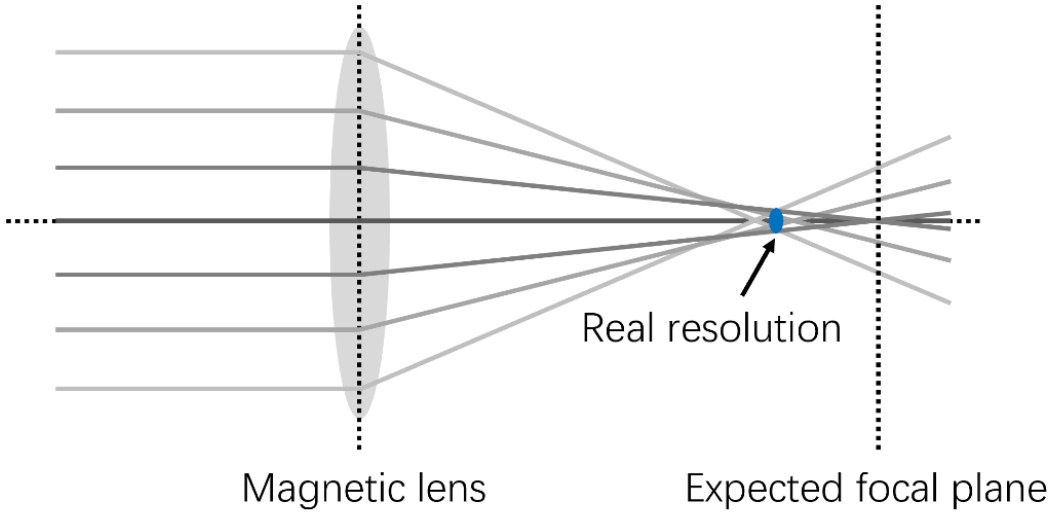


Figure 2.11: Schematic diagram showing the formation of spherical aberration.

2.2.4 Data analysis with HAADF-STEM images

After the HAADF-STEM images of metal clusters were recorded with the microscope, data analysis allows three main parameters to describe the characteristics of metal clusters to be obtained, i.e., integrated intensity, project-area equivalent-circle diameter, and aspect ratio. The details of the analysis process of these three parameters are shown in Figure 2.12.

The calculation details of the integrated intensity of a metal cluster in a HAADF-STEM image are described as follows. The edge of the metal cluster can be detected with Ostu's threshold[80], marked with the solid yellow curve in Figure 2.12 (a). Then, the edge curve can be enlarged to the surrounding substrate, as shown with the dashed yellow curve. To obtain the integrated intensity of the metal cluster, the intensity of the carbon substrate under the cluster should be excluded. Due to the locally homogeneous thickness of the carbon film, the intensity of the carbon substrate in the vicinity of the individual metal cluster is uniform. The average intensity of the substrate can be calculated with the following equation:

$$I_{Substrate} = (I_{Total} - I_{Cluster}) / (S_{Total} - S_{Cluster}) \quad (2.7)$$

where I_{Total} and S_{Total} are the integrated intensity and area of the area marked with the dashed yellow curve, and $I_{Cluster}$ and $S_{Cluster}$ are the integrated intensity and area of the area marked with the solid yellow curve. Then, the integrated intensity of the metal cluster can be obtained using the following equation:

$$I_{Int} = I_{Cluster} - I_{Substrate} * S_{Cluster} \quad (2.8)$$

As for the diameter of a metal cluster, the project-area equivalent-circle diameter was used in this thesis, the details of which are shown in Figure 2.12 (b). This is the diameter of a circle that has the same area as the projection area of the metal cluster. It is widely used for the evaluation of cluster sizes from the projection area of a non-spherical cluster.

The aspect ratio of a metal cluster can be obtained with its maximum and minimum Feret diameter. In general, the Feret diameter is defined as the distance between two parallel tangents of the particle at an arbitrary angle[81]. The Feret diameters for different angles are calculated, and their maximum and minimum are selected, as shown in Figure 2.12 (c). If a particle has an irregular shape, the Feret diameter varies more than with regularly shaped particles. The maximum Feret diameter is always larger than the diameter of the equivalent circle. The aspect ratio of the cluster is the ratio of the maximum to the minimum Feret diameter, whose value should be larger or equal to 1. It gives an indication for the elongation of the cluster. All these data analysis processes can be conducted with a macros-based program run in Image-J software, which was developed by a graduated student Isabel Ornelas in NPRL.

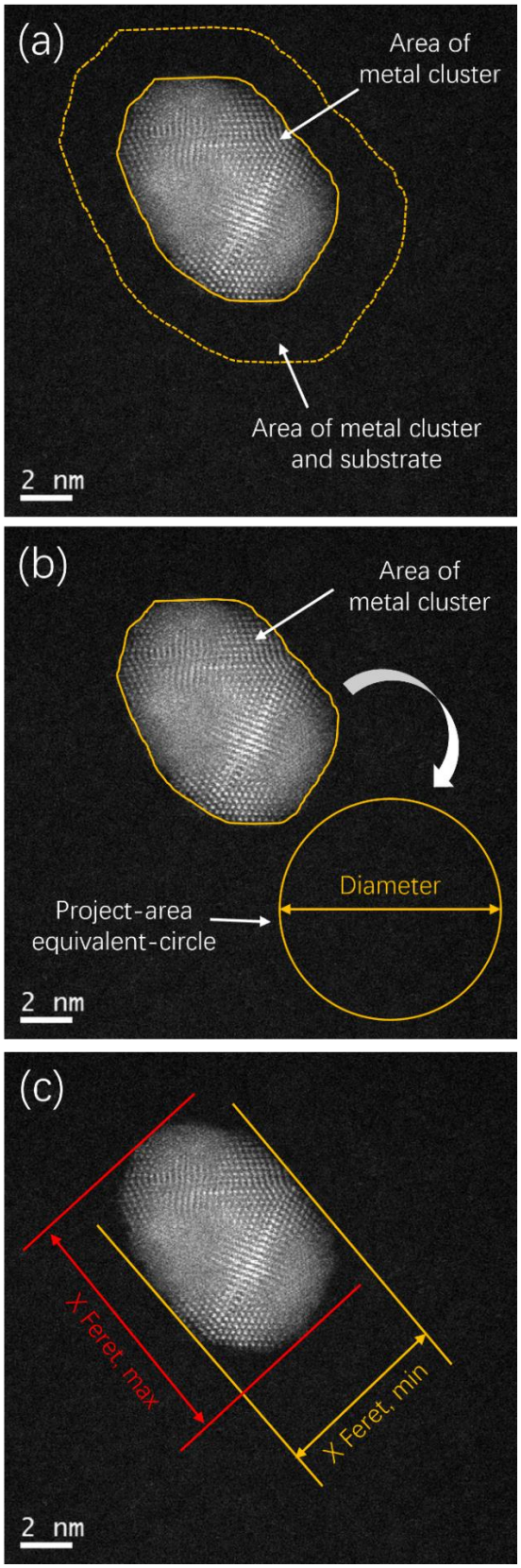


Figure 2.12: Schematic diagrams showing the analysis details of (a) integrated intensity, (b) project-area equivalent-circle diameter, and (c) aspect ratio. X Feret, max and X Feret, min is the maximum and minimum Feret diameter, respectively.

Figure 2.13 provides an example for the HAADF-STEM image analysis. The HAADF-STEM images, cluster size, and integrated intensity distribution of Ag6525 clusters deposited with different Ar gas flow rates, thus named Sample Ar40 and Ar160. The results are visualized as histograms showing that multiple-cluster aggregation exists in both samples. This is because the high density of clusters would lead to an overlap of multiple clusters when depositing the samples. The histograms also show that precise size control can be achieved with the used cluster source. On the one hand, according to the semiclassical model of a charged spherical metal cluster pointed out by Seidl[82], the diameter of a cluster with a certain size can be obtained using the following expression:

$$D = 2r_s N^{1/3} \tag{2.9}$$

where D is the cluster diameter (nm), r_s is the Wigner-Seitz radius (the radius of a sphere whose volume is equal to the mean volume per atom in a solid; for Ag, r_s = 0.166 nm) and N is the number of atoms in the cluster. Using the formula (2.9), the theoretical size of Ag6525 can be obtained as 6.20 nm. On the other hand, the size of Ag6525 clusters can be obtained from the data analysis. For example, the mean size of single Ag6525 clusters in Sample Ar40 is 6.20 nm with a standard deviation of 0.13 nm, as shown in Figure 2.13 (b), which is the same as the theoretical result. Furthermore, there is a very small difference, about 1%, in mean cluster size between Ag6525 clusters of Sample Ar40 and Ar160, which means that the mass filter has good control on size selection under different deposition parameters. Moreover, the

mass resolution of the cluster source is about 6.51 and 5.53 for Ag6525 clusters in Sample Ar40 and Ar160 according to Figure 2.13 (c) and Figure 2.13 (f), respectively, which is much smaller than the theoretical mass resolution mentioned before. The mass resolution can be obtained by dividing the mean cluster size by the full width at half maximum (FWHM). For Gauss fitting, the value of FWHM is the standard deviation times 2 × sqrt(ln(4)) (about 2.355). The difference between the practical and the theoretical mass resolution may be caused by the unfocused cluster beam and the distorted electron field in the mass filter during working due to the accumulation of metal clusters on the plates year-by-year.

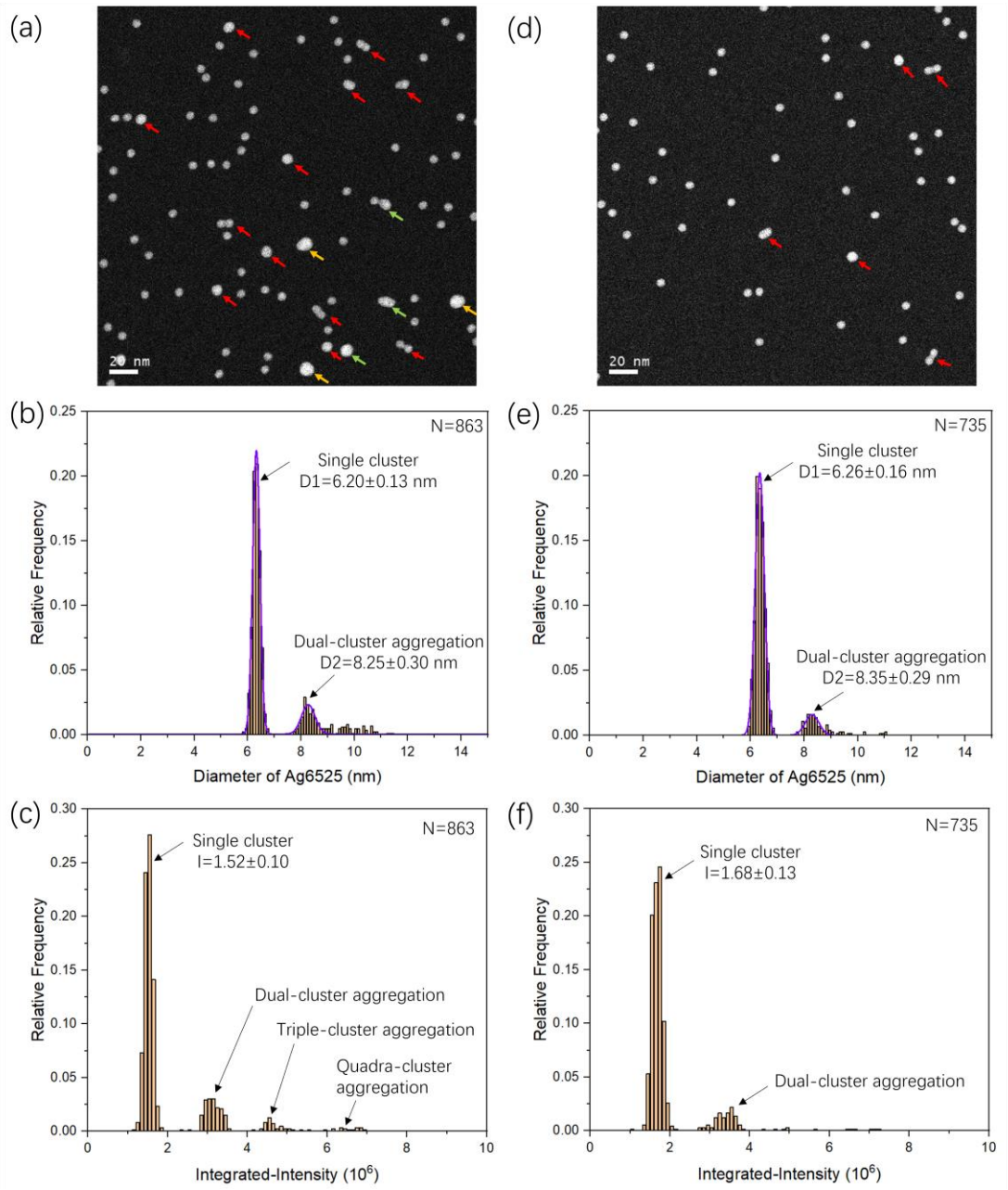


Figure 2.13: HAADF-STEM images of Ag6525 clusters in sample (a) Ar40 and (d) Ar160. (b) and (e) are their corresponding size distribution and (c) and (f) are corresponding integrated intensity distributions. Red, green, and yellow arrows show dual-cluster, triple-cluster, and quadra-cluster aggregation, respectively. Purple lines are Gauss fitting curves of every peak.

As for the project-area equivalent-circle diameter of dual-cluster aggregation, it can be in a certain size range. As shown in Figure 2.14, the minimum size of dual-cluster aggregation can be obtained when these two single clusters aggregated completely, which can be calculated as 7.82 nm using equation (2.9) with N = 6525 × 2 = 13050.

The maximum size can be obtained as 8.95 nm by calculating the diameter of a circle which has an area twice that of single Ag6525 cluster in HAADF-STEM images. So, the size of dual-cluster aggregation should be in the range of 7.82-8.95 nm, which is coincident with the experimental results shown in Figure 2.13 (b) and (e).

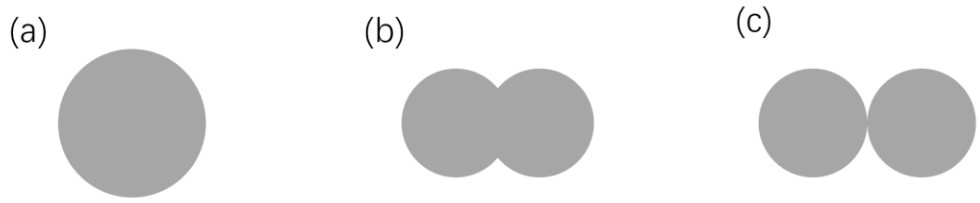


Figure 2.14: A schematic drawing of the different situations of dual-cluster aggregation. (a) The situation shows the minimum size of dual-cluster aggregation when two single Ag6525 clusters aggregated completely. (b) The situation shows a medium size of dual-cluster aggregation when two single Ag6525 clusters aggregated incompletely. (c) The situation shows the maximum size of dual-cluster aggregation when two single Ag6525 clusters are just touching each other.

2.2.5 Structure identification of metal clusters using HAADF-STEM images

For spherical Ag clusters, the high-magnification HAADF-STEM images show various atomic patterns, as shown in Figure 2.15. There are three groups of atomic structures for Ag clusters, Ih, Dh, and FCC. To confirm the atomic structure for each Ag cluster, a workflow for structure identification was set up following the steps shown in Figure 2.16. The key idea for structure identification is the comparison between the experimental images and the simulated structure atlas, including three aspects of morphology, intensity line profile, and FFT image.

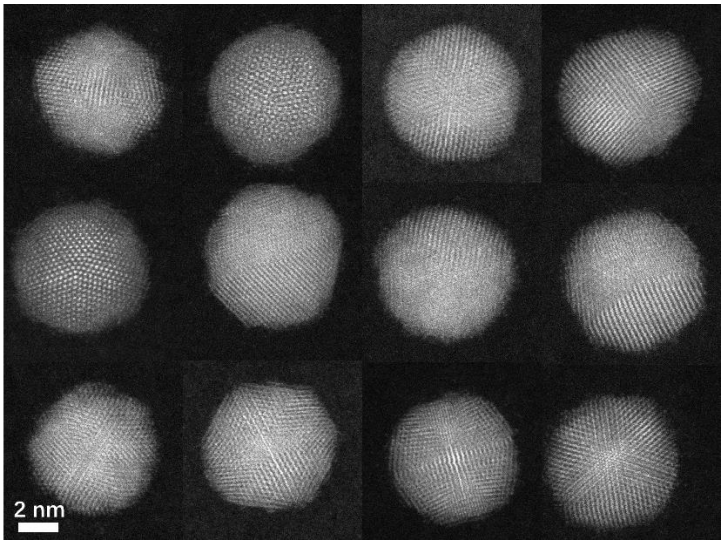


Figure 2.15: HAADF-STEM images of Ag clusters with different sizes prepared by magnetron sputtering.

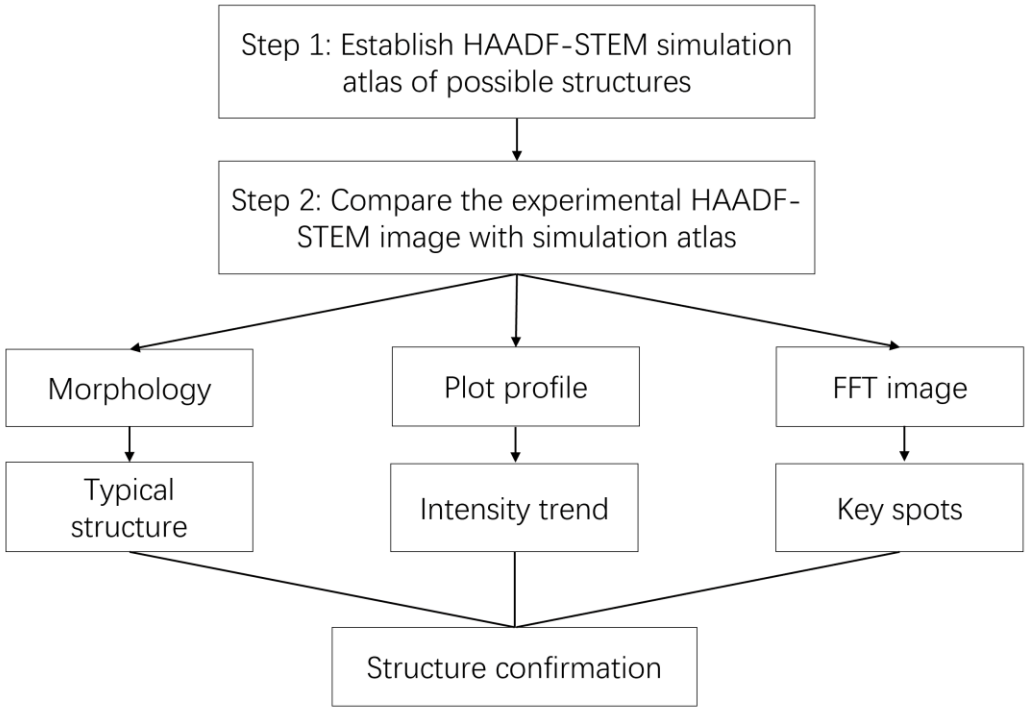


Figure 2.16: The workflow of the structure identification for Ag clusters in HAADF-STEM images.

For the atomic model of Ag clusters, Octahedron (Oh), Cuboctahedron (COh), normal Ino-Dh, square Ino-Dh, and Ih are considered as potential candidates. Certain sizes, corresponding to either closed geometric or closed electronic shells, are more energetically favorable; these sizes are called magic numbers[83]. The magic numbers of these five structures are shown in Table 2.2, which shows the same value for the same atom shell numbers for COh, square Ino-Dh, and Ih structures. Besides, the shapes of COh, square Ino-Dh, and Ih structures are closer to spherical, as shown in Figure 2.17, compared to that of Oh and normal Ino-Dh structures. Based on these considerations, COh, Ih, and square Ino-Dh are selected as the simulated structures.

Table 2.2: Magic numbers of Oh, COh, normal Ino-Dh, square Ino-Dh, and Ih.

Shell number	1	2	3	4	5	6	7	8	9	10	11	12	13	14
Oh	6	19	44	85	146	231	344	489	670	891	1156	1469	1834	2255
COh	13	55	147	309	561	923	1415	2057	2869	3871	5083	6525	8217	10179
normal Ino-Dh	7	23	54	105	181	287	428	609	835	1111	1442	1833	2289	2815
square Ino-Dh	13	55	147	309	561	923	1415	2057	2869	3871	5083	6525	8217	10179
Ih	13	55	147	309	561	923	1415	2057	2869	3871	5083	6525	8217	10179

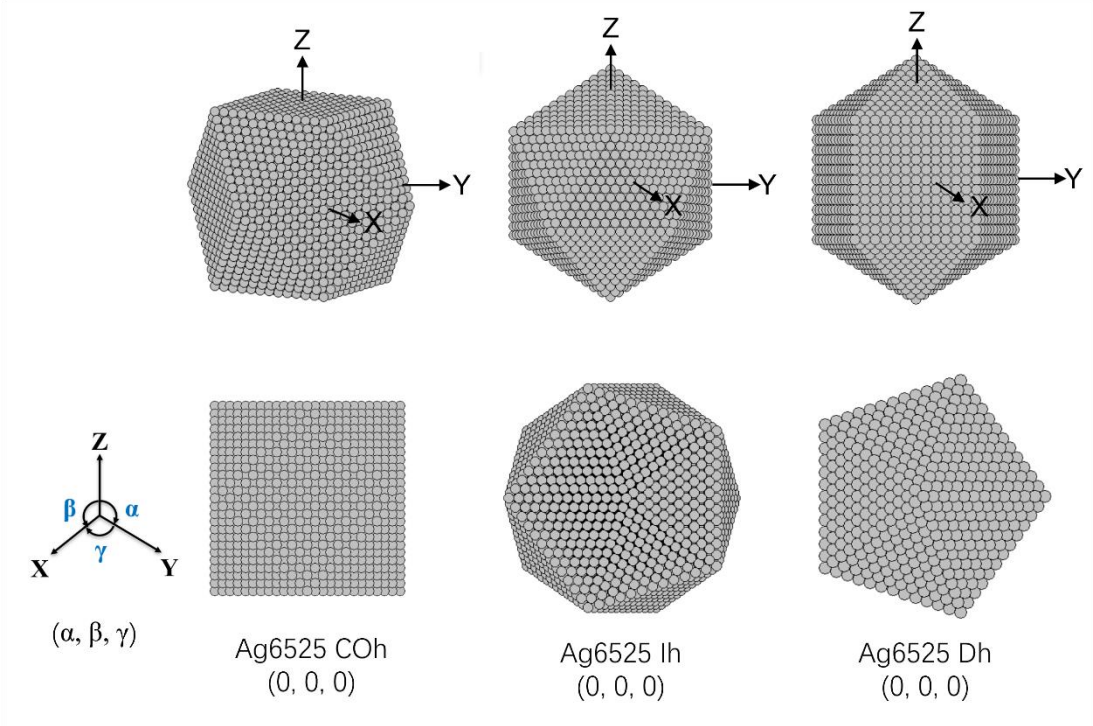


Figure 2.17: The atomic models of COh, Ih, and square Ino-Dh structures for Ag6525 clusters.

Figure 2.18-2.20 show simulation atlases of Ag6525 COh, Ih, and square Ino-Dh structures. For convenience, the square Ino-Dh structure will be shortened to Dh structure in the following contents. The models of the COh, Ih, and Dh structures are obtained based on a Python package called ASE (Atomic Simulation Environment). Then, the related simulated HAADF-STEM images from different angles are produced with the method proposed by He et al[84]. The introduction of a kinematic model in this method can accelerate the simulation of STEM, providing an almost 'real time' simulation.

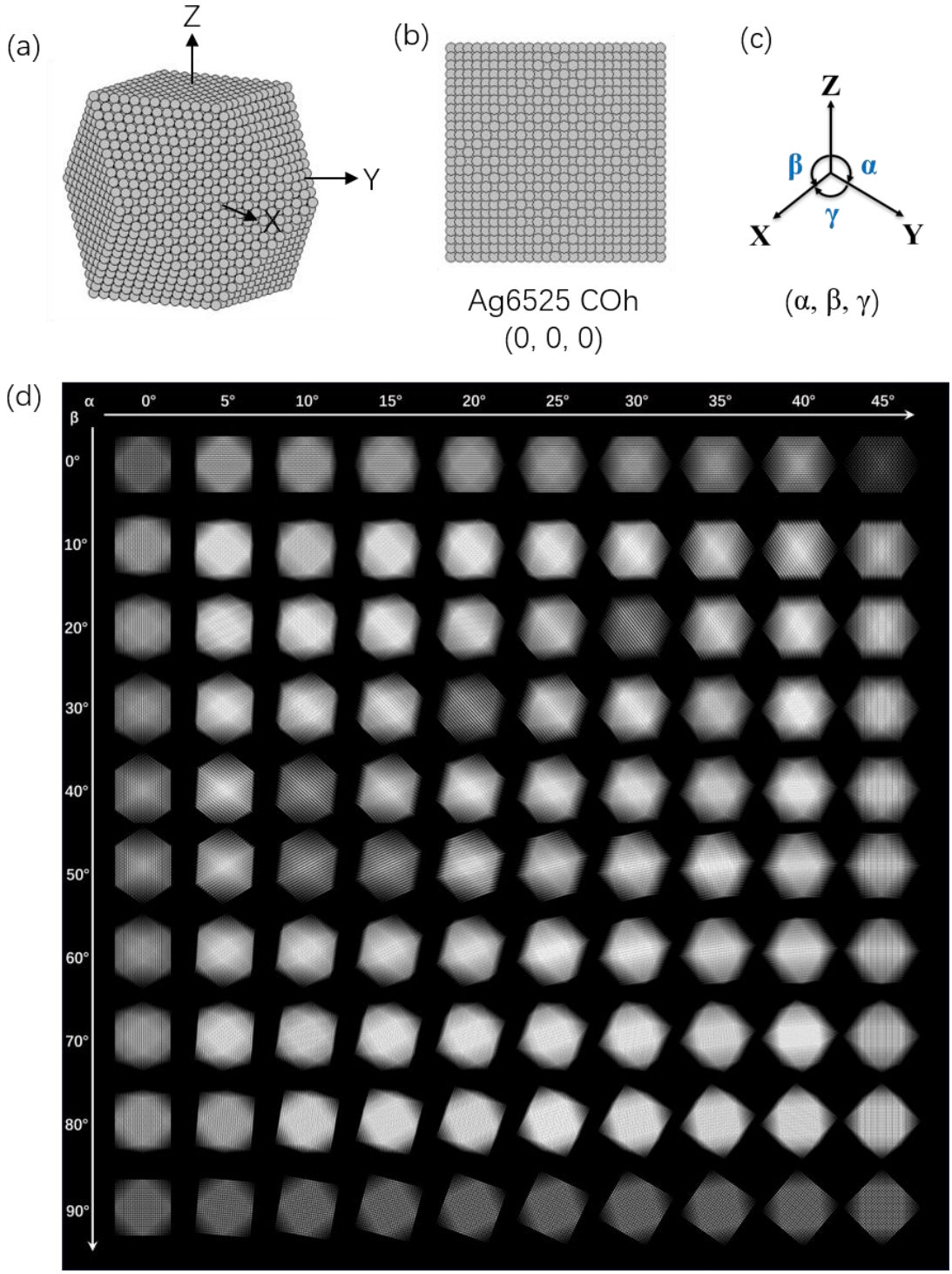


Figure 2.18: (a) Simulation model of COh structure of Ag6525 cluster; (b) simulation image of Ag6525 COh (0, 0, 0) and the angles are defined as shown in (c); (d) simulation atlas of Ag6525 COh with different angular rotations. The angle α means the model is rotating around the X-axis, and the rotation around the Y-axis is described by the angle β. The enlarged atlas can be found in Appendix.

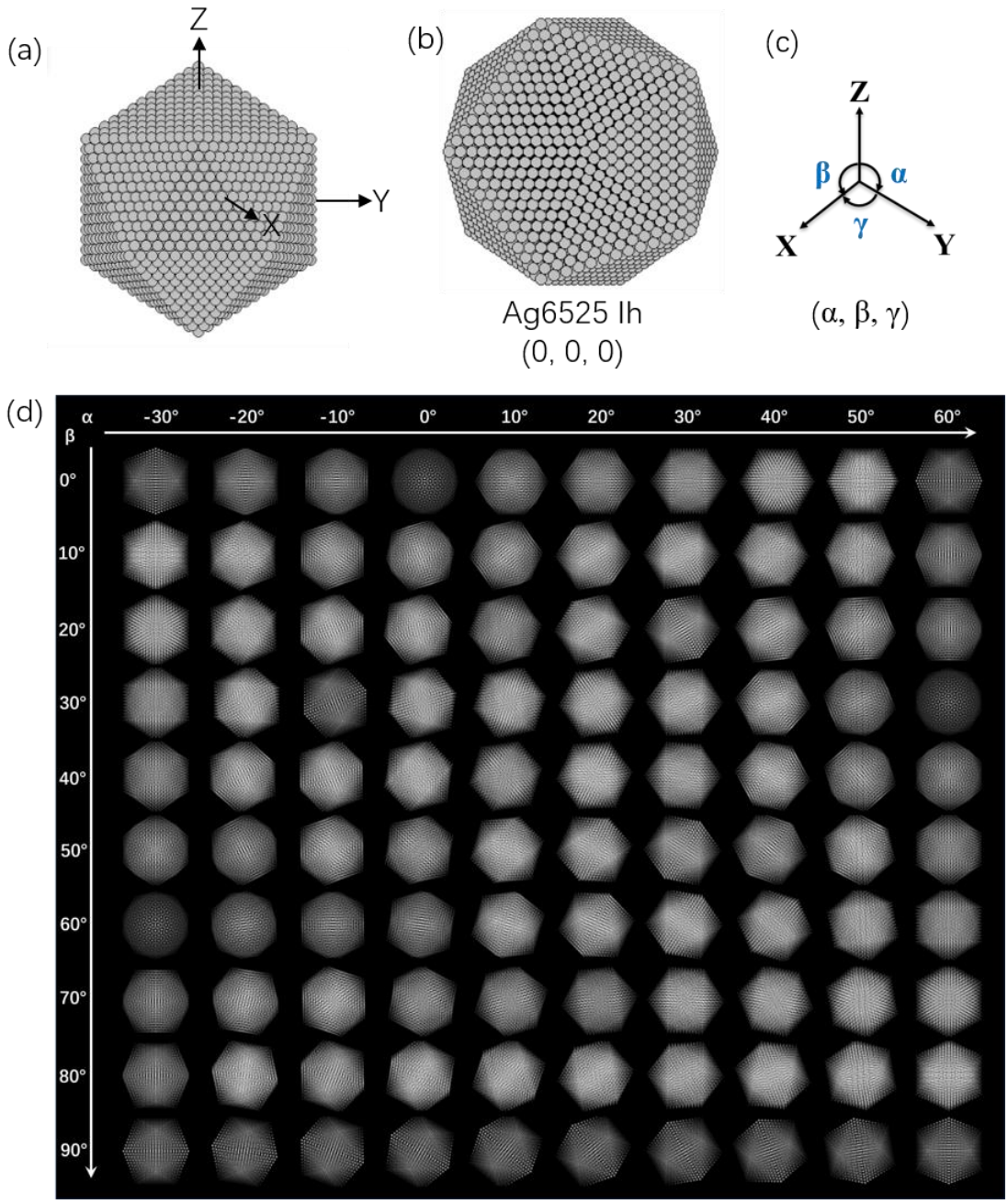


Figure 2.19: (a) Simulation model of Ih structure of Ag6525 cluster; (b) simulation image of Ag6525 Ih (0, 0, 0) and the angles are defined as shown in (c); (d) simulation atlas of Ag6525 Ih with different angular rotations. The angle α means the model is rotating around the X-axis, and the rotation around the Y-axis is described by the angle β. The enlarged atlas can be found in Appendix.

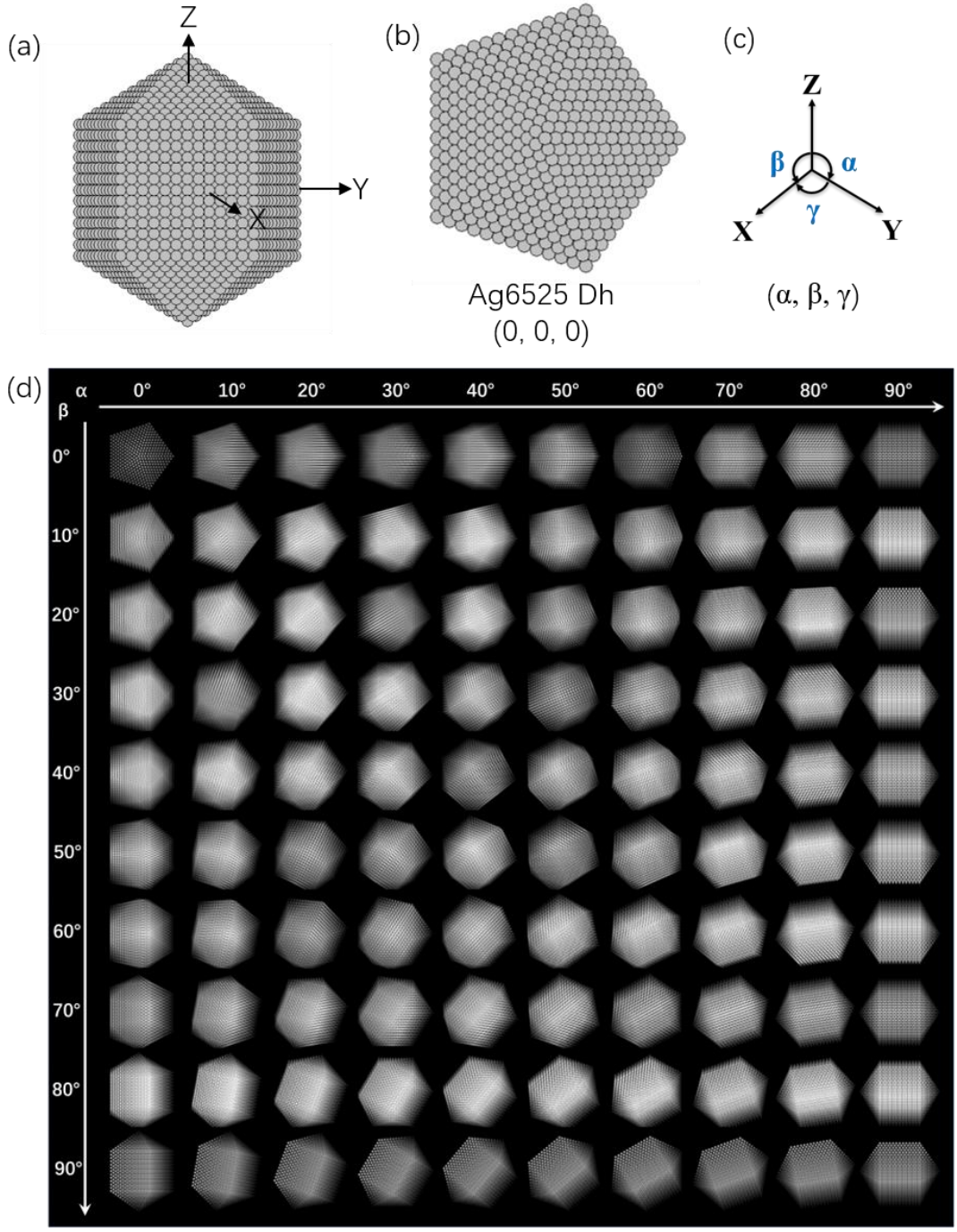


Figure 2.20: (a) Simulation model of Dh structure of Ag6525 cluster; (b) simulation image of Ag6525 Dh (0, 0, 0) and the angles are defined as shown in (c); (d) simulation atlas of Ag6525 Dh with different angular rotations. The angle α means the model is rotating around the X-axis, and the rotation around the Y-axis is described by the angle β. The enlarged atlas can be found in Appendix.

By comparing HAADF-STEM images of Ag6525 with these simulation atlases, the structure of Ag6525 clusters can be identified. The identification of the COh structure can be achieved fairly unambiguously, while distinguishing between Ih and Dh structures seems more difficult. Figure 2.21 shows examples of comparison between the simulation of typical Ih and Dh structures and clusters found in samples. Figure 2.21 (a2) shows a deposited Ag6525 cluster that is similar to the simulation image of Ag6525 Ih. Then, the normalized line profiles of the simulation and this cluster are compared. Although the layer numbers of atoms are different because of the imperfect atom distribution of the experimental cluster, both profiles show the same decreasing intensity trend from center to edges. Compared with the standard simulated Ih structure, the atoms on the vertices and edge positions cannot be found in the experimental images due to the high atom energy in these positions. To meet the total number of atoms, there will be more atom shells in experimental clusters than in the simulated ones, as indicated by green arrows in Figure 2.21 (a3) and (b3). Moreover, the cluster shown in Figure 2.21 (a2) can be finally identified as an Ih structure because of the coincidence between simulation FFT image of Ag6525 Ih and FFT image of this cluster. In the same manner, the cluster shown in Figure 2.21 (b2) can be identified as Ag6525 Dh.

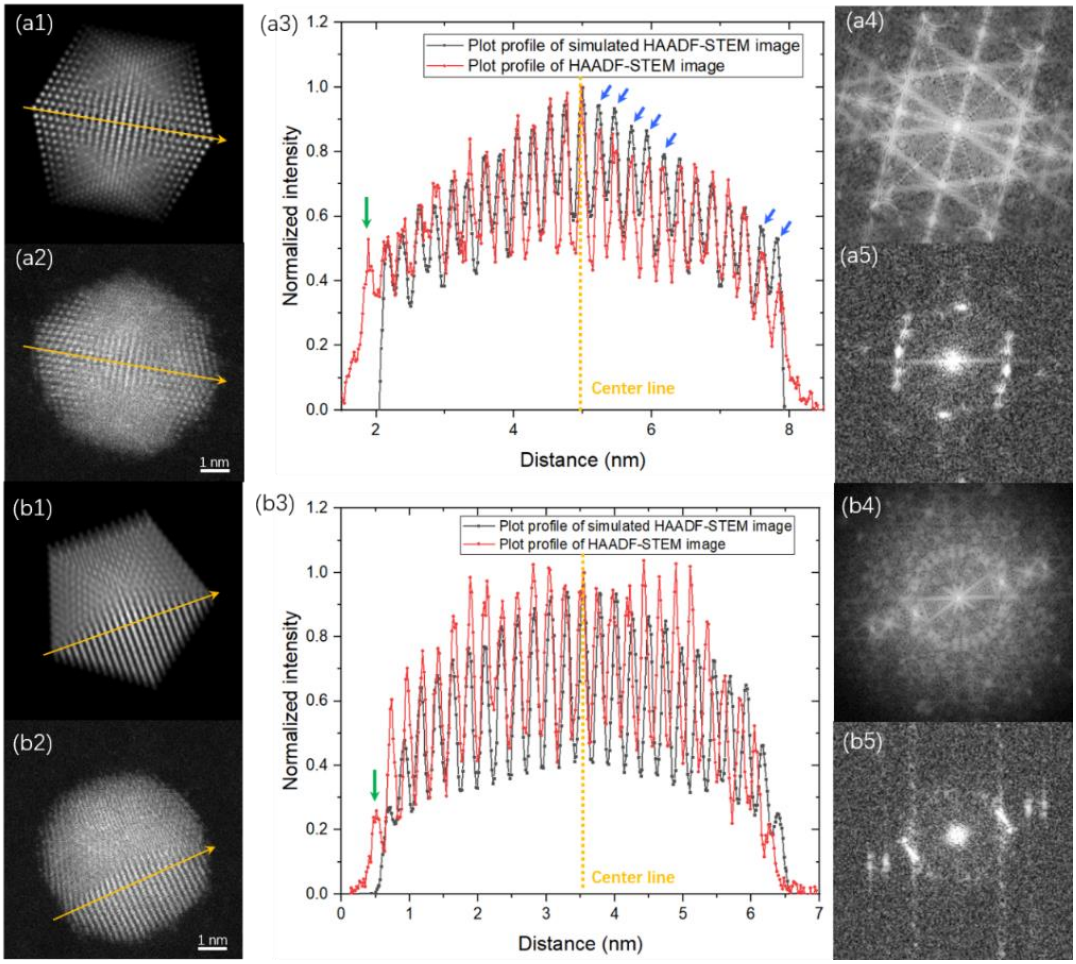


Figure 2.21: Examples of comparison between simulation of typical Ih and Dh structure of Ag6525 and clusters found in samples. (a1) and (a4) are simulated HAADF-STEM image and its FFT image for Ag6525 Ih. (a2) and (a5) are experimental HAADF-STEM image and its FFT image of one Ag6525 cluster. (a3) is the comparison between normalized line profiles of (a1) and (a2). (b1) and (b4) are simulated HAADF-STEM image and its FFT simulation image of Ag6525 Dh. (b2) and (b5) are HAADF-STEM image and its FFT image of one Ag6525 cluster. (b3) is the comparison between normalized line profiles of (b1) and (b2). The yellow arrows show the position and direction of line profiles in every image. The blue arrows show the positions where the intensity of the real cluster is lower than that of simulated one. The green arrows show the additional atom columns.

A further two examples of the identification of Ih structures are shown in Figure 2.22. For the Ag6525 cluster shown in Figure 2.22 (a3), it is observed from the top view orientation of the atomic model in Figure 2.19 (b). The cluster exhibits a distinctive pattern with bright spots in the middle of rings, which is a unique feature for Ih structure and always seen especially when the cluster size is small. The cluster in the Figure 2.22 (b3) shows a six-fold structure, which is caused by the symmetric atom arrangement of Ih structure.

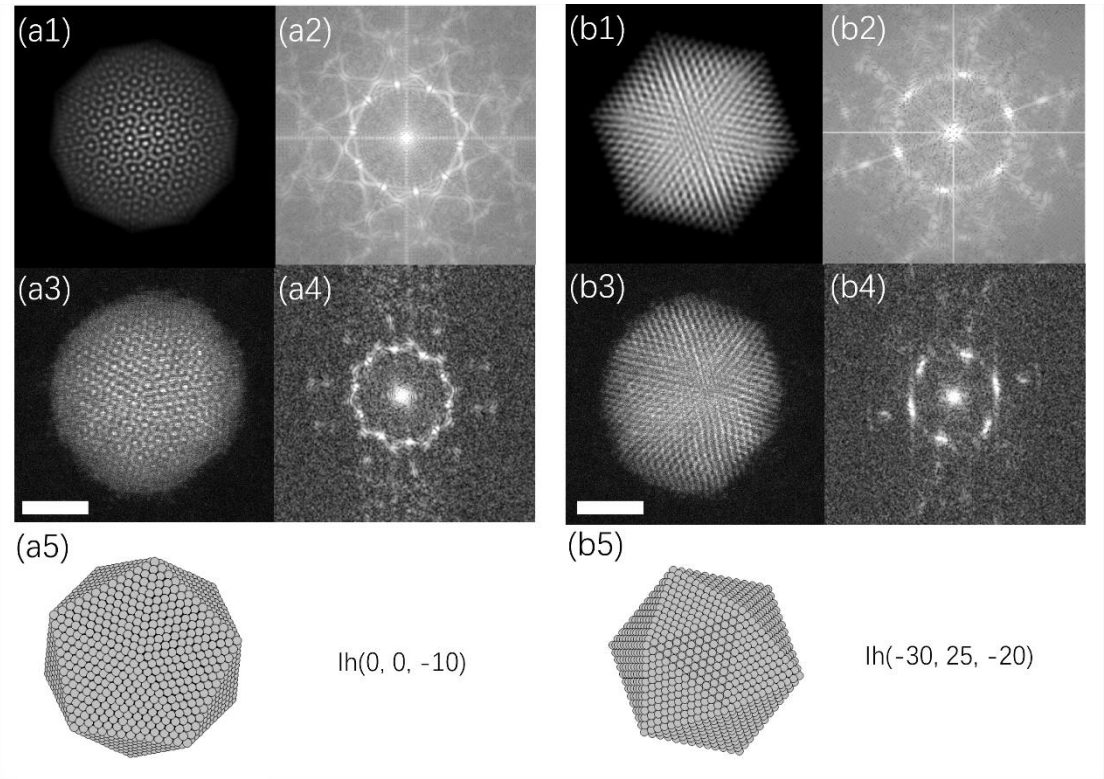


Figure 2.22: (a1) and (b1) The simulated images of Ag6525 clusters. (a2) and (b2) The respective FFT images of (a1) and (b1). (a3) and (b3) The HAADF-STEM images of Ag6525 clusters. (a4) and (b4) The respective FFT images of (a3) and (b3). (a5) and (b5) The respective atomic models of (a1) and (b1). The scale bars in (a3) and (b3) are 2 nm.

Three examples of the identification of Dh structures are shown in Figure 2.23, including the five-fold characteristic observed from the top view and other atomic patterns viewed from different angles.

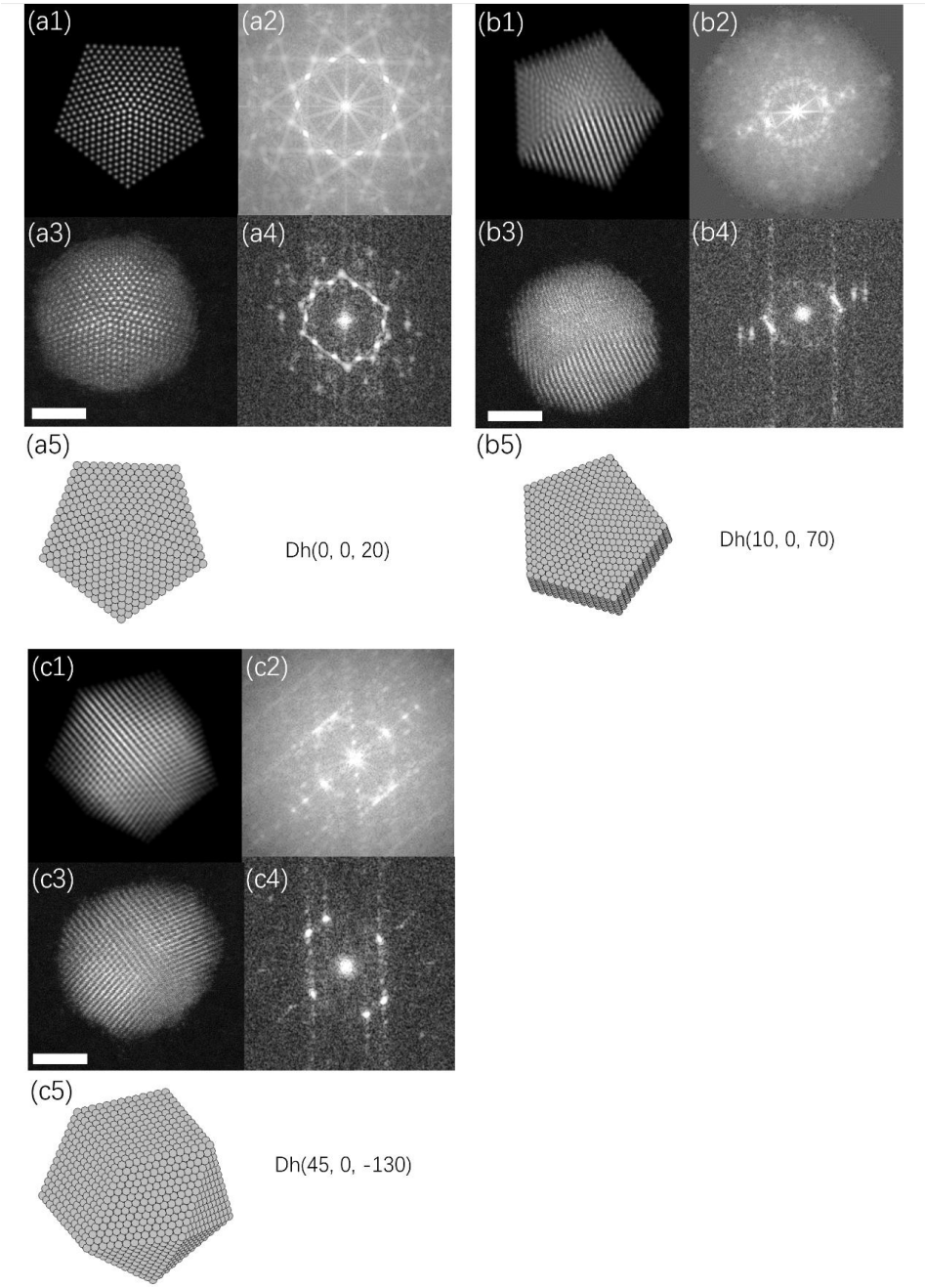


Figure 2.23: (a1), (b1), and (c1) The simulated images of Ag6525 clusters. (a2), (b2), and (c2) The respective FFT images of (a1), (b1), and (c1). (a3), (b3), and (c3) The HAADF-STEM images of Ag6525 clusters. (a4), (b4), and (c4) The respective FFT images of (a3), (b3), and (c3). (a5), (b5), and (c5) The respective atomic models of (a1), (b1), and (c1). The scale bars in (a3), (b3), and (c3) are 2 nm.

The structure identification of Ih and Dh can be easily and quickly recognized directly from the morphology of metal clusters in HAADF-STEM images, which has been summarized into several rules in the following.

- Clusters with obvious features can be identified easily. For example, five-fold structures can be grouped into Dh structures, like the cluster marked with a green box in Figure 2.24, because the five-fold structure is an obvious and unique feature in Dh structures. Furthermore, the patterns with periodic dots or lines are more likely to be grouped as FCC structures.

- Clusters with central symmetric structures (the pattern will not change after 180 degrees of rotation based on the center) but without obvious patterns of periodic dots or lines can be grouped into Ih structures. As shown in Figure 2.25, all the simulated clusters show central symmetric structures, proving this characteristic is a typical feature for the identification of Ih structures.

- Clusters with axisymmetric structures but not central symmetric structures can be grouped into Dh structures. The simulated clusters without any marks in Figure 2.24 indicate the axisymmetric characteristic is a general feature for the Dh structure observed from some angles.

- Clusters with asymmetric structure and lots of parallel lines in about half of the cluster can be grouped into Dh structures. For some special observation angles, the Dh structures presents the asymmetric structure rather than the axisymmetric

characteristic, but half of the cluster will be composed of many parallel lines, such as the simulated clusters marked with red boxes in Figure 2.24.

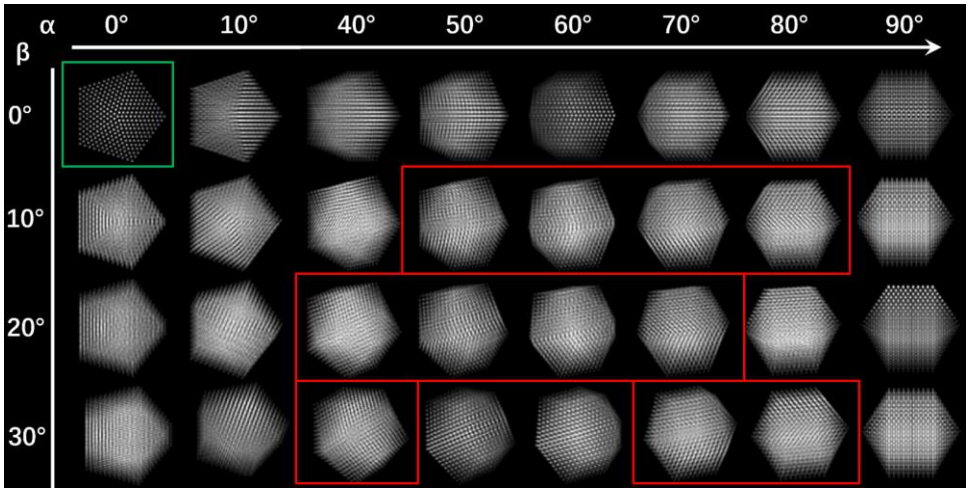


Figure 2.24: Part of the simulation atlas of Ag6525 Dh with different angular rotations.

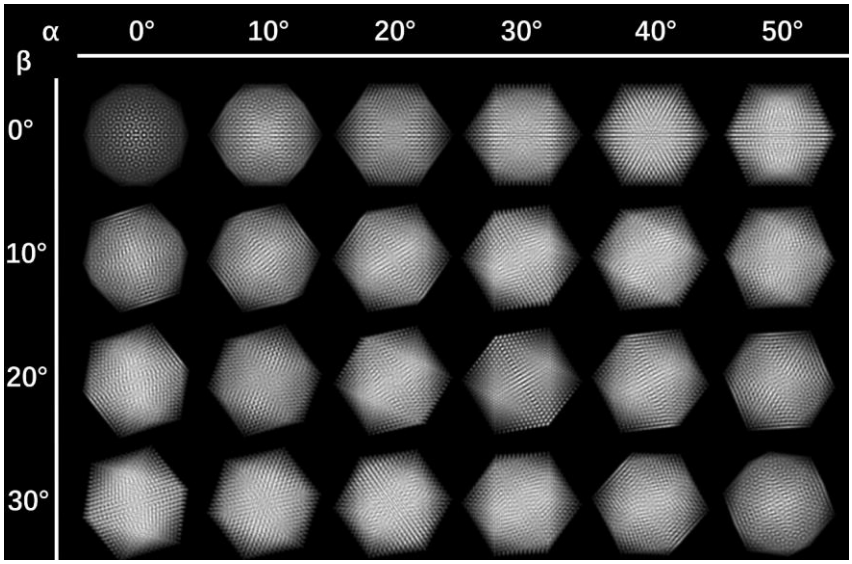


Figure 2.25: Part of the simulation atlas of Ag6525 Ih with different angular rotations.

Four HAADF-STEM images of Ag6525 clusters are selected to further clarify the fast structure identification from the atomic patterns. Clusters like Case 1 in Figure 2.26 (a), present a central symmetric feature and can be grouped into Ih structures. Cluster showing obvious five-fold structure will be grouped into Dh structures, such as Case 2 in Figure 2.26 (b). As for clusters that exhibit the axisymmetric characteristic, like Case 3 in Figure 2.26 (c), they are Dh structures. Finally, if clusters show unusual features as in Case 4 in Figure 2.26 (d), they may be Dh structures. If the structure cannot be confirmed easily from the atomic patterns, a comparison between the intensity line profile and the FFT image of the experimental images and simulated results will be further tried.

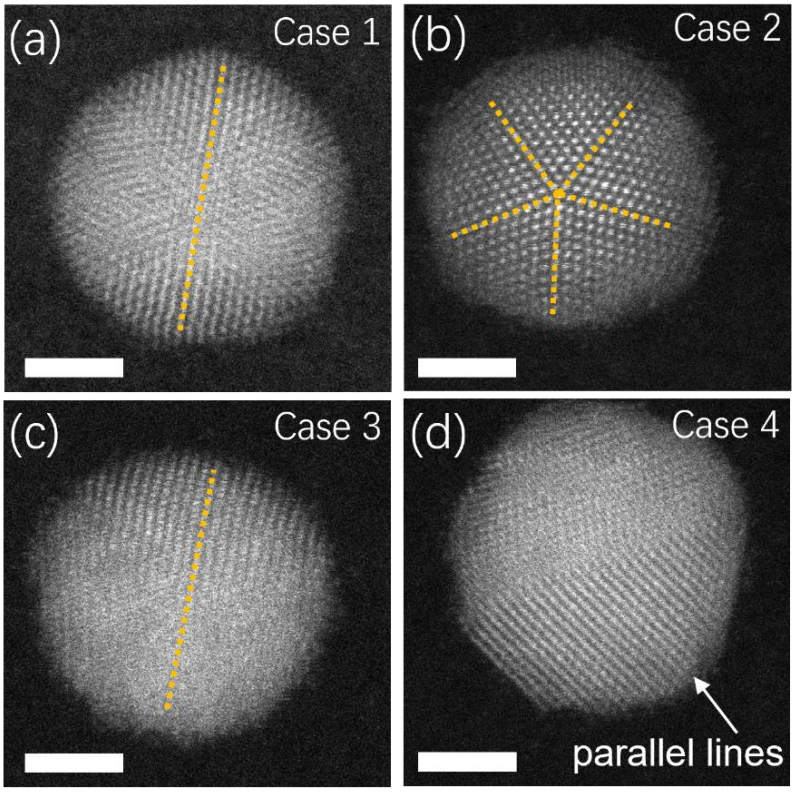


Figure 2.26: Four HAADF-STEM images of Ag6525 clusters to show different cases that may be observed during imaging. The scale bars are 2 nm.

The comparison among the simulated images and their FFT images of Ih structures with different sizes are shown in Figure 2.27. The results prove that the discussed atomic features of Ih structures are universal to different cluster sizes, indicating that the summarized rules for fast structure identification are suitable for Ag-Ih clusters of different sizes. This is also the case for Ag-Dh clusters, for which compared results are shown in Figure 2.28.

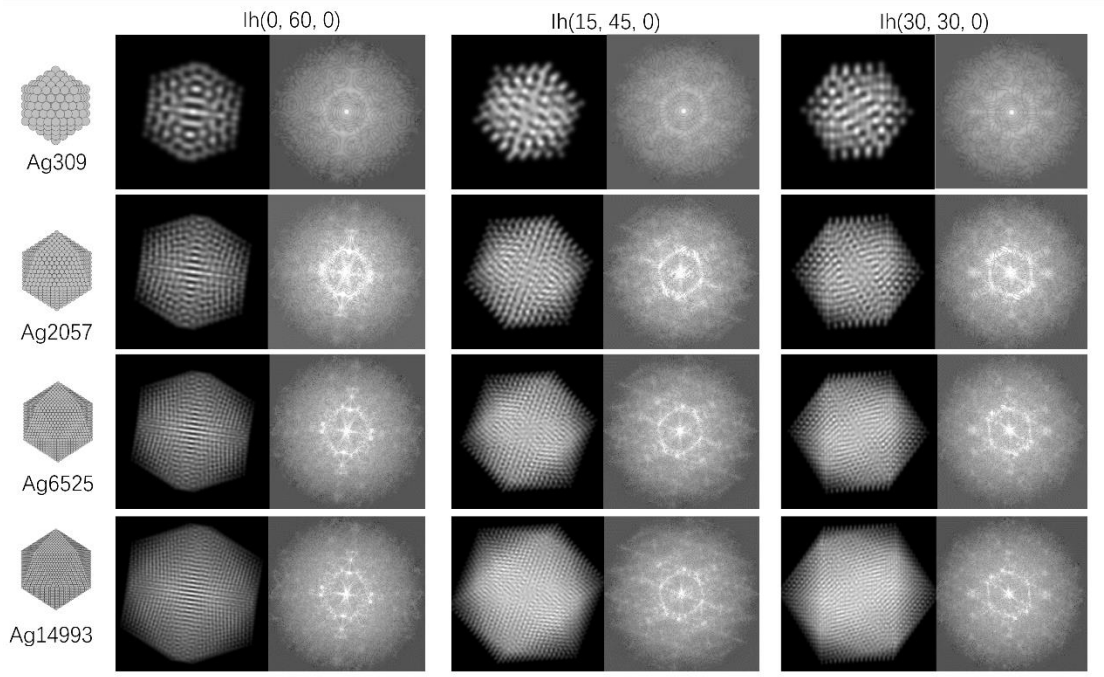


Figure 2.27: Simulated images and their relative FFT images of Ih structures with different sizes.

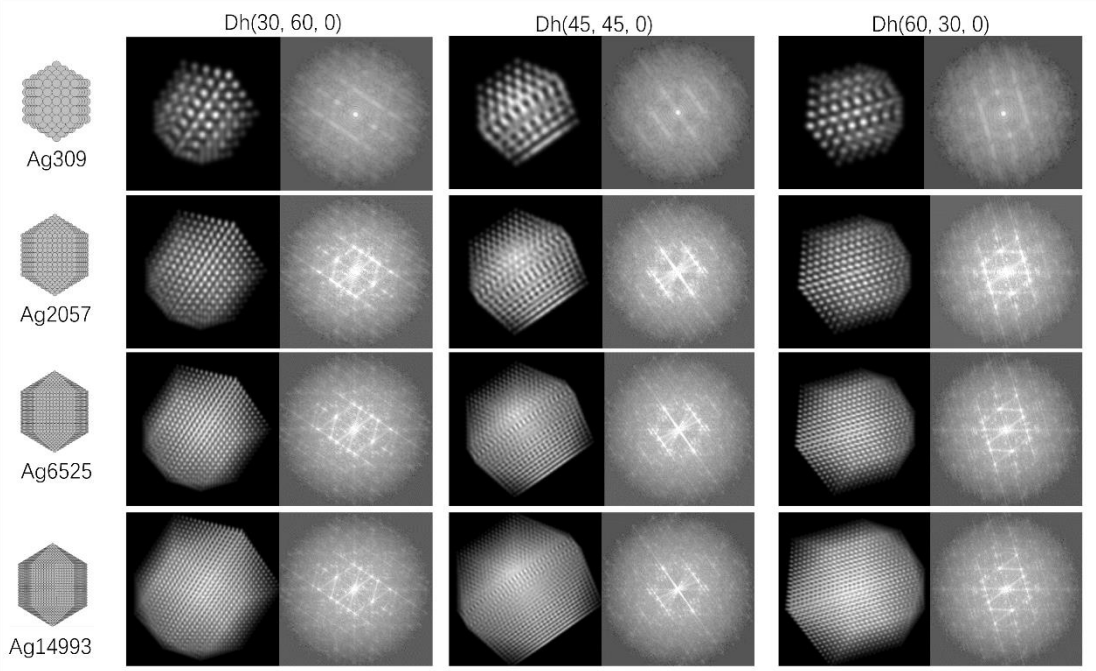


Figure 2.28: Simulated images and their FFT images of Dh structures with different sizes.

2.2.6 The effect of the deposition energy on the structures of Ag clusters

In most cases, the metal clusters are deposited in a soft-landing manner to maximally preserve the atomic structure and size. The deposition energy of clusters is controlled by the voltage applied to the substrate. The effect of substrate voltage on the mass spectrum is shown in Figure 2.29 (a). With substrate voltage ranging from 50 V to 1000 V, the cluster beam currents for different sizes will be slightly higher with higher substrate voltages. Without the substrate voltage, the current of Ag clusters with a size smaller than 3500 greatly decreases, while the number of Ag clusters with a size larger than 3500 does not change. This indicates that the existence of substate voltage is critical for the deposition of Ag clusters with small sizes because the small clusters are easier to be attracted to the substrate compared with large clusters when a voltage is

applied. With another set of preparation parameters, four Ag1k samples were deposited with different substrate voltages, for which aspect ratios were analyzed and shown in Figure 2.29 (b). The aspect ratios of Ag1k clusters are very similar, indicating that the shape of Ag1k clusters can be greatly preserved with substrate voltages in such a range. However, the proportions of different structures show a big difference among these four samples, as presented in Figure 2.29 (c). The higher proportion of Ih structure can be obtained with a smaller substrate voltage, suggesting that higher deposition energy caused by the higher substrate voltage can introduce a structure transition from Ih to Dh for Ag1k clusters though the cluster shapes didn't change too much. Figure 2.29 (d) shows the cluster beam during deposition when substrate voltages of 100 V and 200 V, respectively, were applied. As the same total deposition mass was set for these two samples during deposition, a higher cluster beam current of applied voltage of 200 V led to a shorter time for the deposition. Based on these results, to minimize the effect of deposition voltages, the substrate voltage of 100 V was applied to preserve the structures of Ag1k clusters in the further deposition, namely the deposition energy of 0.1 eV/atom. This rule was expanded to other cluster sizes, i.e., the substrate voltage of 200 V for Ag2k clusters and 400 V for Ag4k clusters. When the cluster sizes exceed 5k, the substrate voltage of 500 V was always applied during deposition.

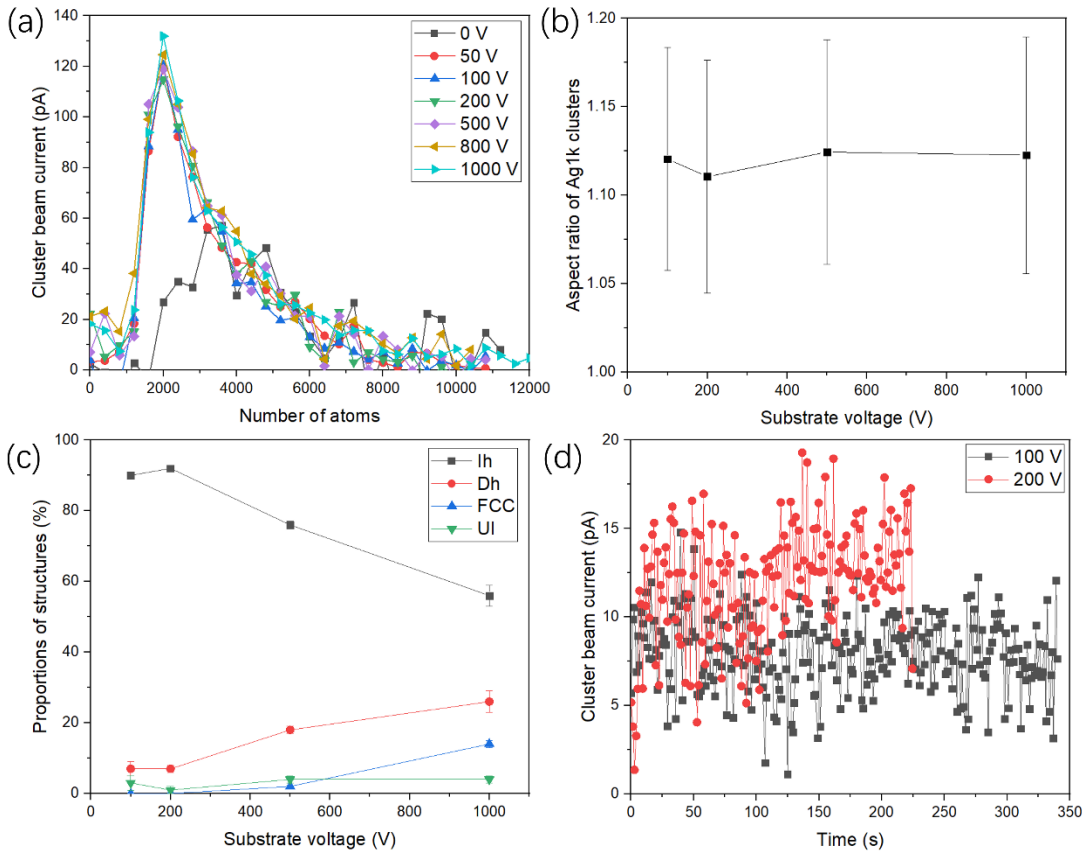


Figure 2.29: (a) The mass spectra when different substrate voltages were applied. The applied parameters are a power of 10 W, an Ar gas flow rate of 40 sccm, a He gas flow rate of 0 sccm, a condensation length of 250 mm, and a chamber pressure of 0.075 mbar. (b) The statistical results of the aspect ratios of four Ag1k samples deposited with different substrate voltages. The error bar comes from the standard deviation of the aspect ratios. The deposition parameters are a power of 10 W, an Ar gas flow rate of 120 sccm, a He gas flow rate of 30 sccm, a condensation length of 250 mm, and a chamber pressure of 0.21 mbar. (c) The proportions of structures of the same four Ag1k samples in (b). More than 200 clusters were analyzed for every sample. (d) The mass spectra during deposition when the substrate voltage of 100 V and 200 V, respectively, were applied.

2.3 Protection of Ag clusters in high vacuum

Ag clusters are prone to oxidation or sulfurization when exposed to air. To protect the deposited Ag clusters and obtain reliable HAADF-STEM data, Ag6525 clusters stored in both air and high vacuum conditions of $10E^{-7}$ mbar were compared. The differences between these two conditions are presented below.

Ag6525 clusters were prepared using the magnetron sputtering mass-selected inert gas condensation source with a power of 10 W, an Ar flow rate of 40 sccm, a chamber pressure of 0.05 mbar, and with LN_2 cooling. After preparation, these Ag6525 clusters were observed using the JEOL 2100F immediately and then stored in air. The sample shortly exposed to air during transfer process from the cluster source to TEM, but the time was about 20 seconds to minimum the effect of air on the initial size, structure, and composition of prepared Ag6525 clusters. In order to record the evolution of Ag6525 clusters exposed to air, the sample was characterized after being stored in air for 1, 12, 21, and 31 days, respectively.

2.3.1 Size evolution of Ag6525 exposed to air

The overview HAADF-STEM images and size distributions of Ag6525 clusters after being stored in air for different durations are shown in Figure 2.30. Compared with Ag6525 clusters before being exposed to air as shown in Figure 2.30 (a), these Ag6525 clusters exposed to air show larger diameters but no obvious cluster density decrease, meaning that the increased size isn't caused by the aggregation of clusters but by the reaction between clusters and air. Besides, there is a higher frequency of clusters with large sizes in the size distributions of Ag6525 clusters exposed to air than the size distribution shown in Figure 2.30 (b). This can be explained by the increasing size of clusters induced the aggregation of these clusters which were close to but separated from other clusters. Moreover, the gap between the mean size of single clusters and that of aggregations of two single clusters (the first peak and the second peak in size

distribution) in Figure 2.30 (b) is about 2 nm. However, after being exposed to the air, this size gap increases to about 2.1 or 2.2 nm. When exposed to air, these clusters with larger sizes had more reaction surface contact with air, so their size increase is greater than that of small clusters. The relationship between peak diameters of Ag6525 clusters and time of these Ag6525 clusters were exposed to air is shown in Figure 2.31, which illustrates that the size increase of Ag6525 clusters occurred within one day and the size of Ag6525 clusters kept constant in the next 30 days. This means that the size evolution is a quick process for Ag6525 clusters.

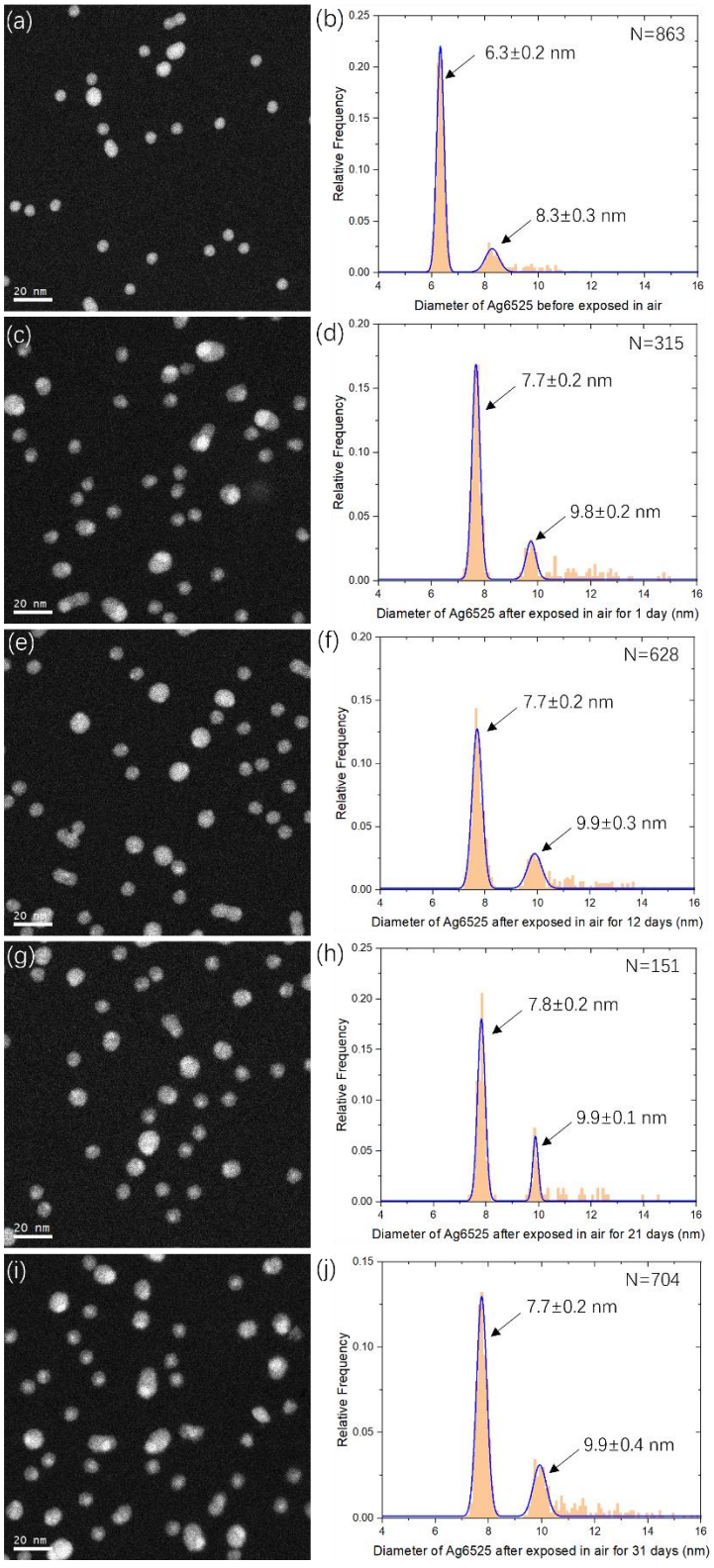


Figure 2.30: (a), (c), (e), (g), and (i) are HAADF-STEM images of Ag6525 clusters stored in air for 0, 1, 12, 21, and 31 days, respectively. (b), (d), (f), (h), and (j) are size distributions of Ag6525 clusters stored in air for 0, 1, 12, 21, and 31 days, respectively. The first peak of the size distribution shows sizes of single Ag6525 clusters and the second peak of the size distribution is formed by aggregation of two single Ag6525 clusters. The size distribution was fitted with Gaussian function.

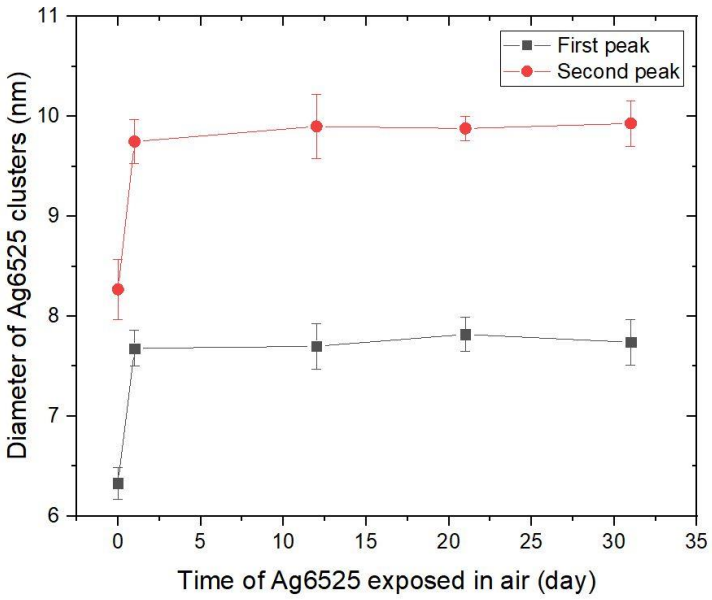


Figure 2.31: The relationship between peak diameters of Ag6525 clusters and the time these Ag6525 clusters were exposed to the air. The first peak of the size distribution shows the sizes of single Ag6525 clusters, and the second peak of the size distribution is formed by the aggregation of two single Ag6525 clusters. The error bar represents the standard deviation of the statistical results.

2.3.2 Morphology evolution of Ag6525 exposed to the air

The size increase of Ag6525 clusters exposed to the air is caused by the morphological structure evolution. As shown in Figure 2.32 (a), before being exposed to the air, most of these Ag6525 clusters can be recognized as Ih and Dh structures. However, after being exposed to the air, the structure of these clusters changed to obvious core-shell structures, as shown in Figure 2.32 (b) and (c). The bright core may be an Ag-rich area in this core-shell structure and the dark shell is the product of the reaction between the Ag cluster and air.

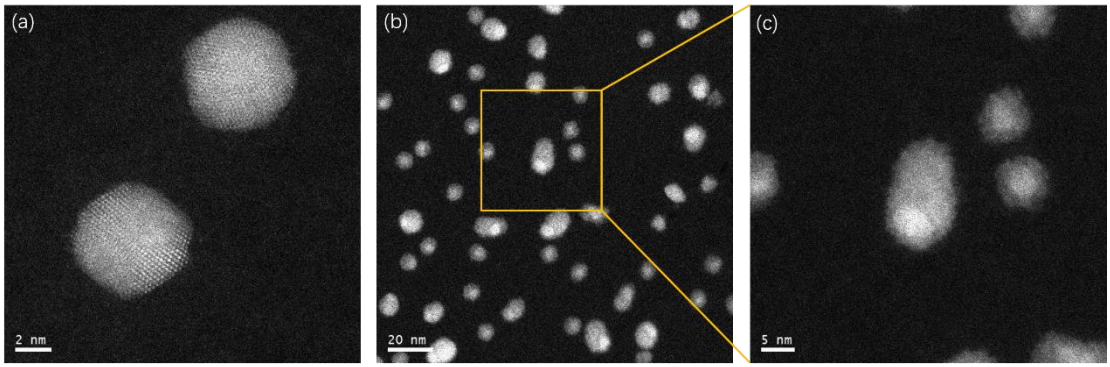


Figure 2.32: (a) HAADF-STEM image of two Ag6525 clusters with icosahedron structure before being exposed to the air. (b) HAADF-STEM image of Ag6525 clusters exposed to the air for 31 days and (c) its partially enlarged image.

For large ellipsoidal clusters and small spherical clusters, the positions of their bright cores are different. As shown in Figure 2.33, cores of large ellipsoidal Cluster 1, 2 and 3 are biased to one side. As for these small spherical clusters, some of them have central cores, like Cluster 4 and 5. However, cores of spherical Cluster 6 and 7 are biased to one side. This phenomenon may be related to the different reaction surface of clusters with air.

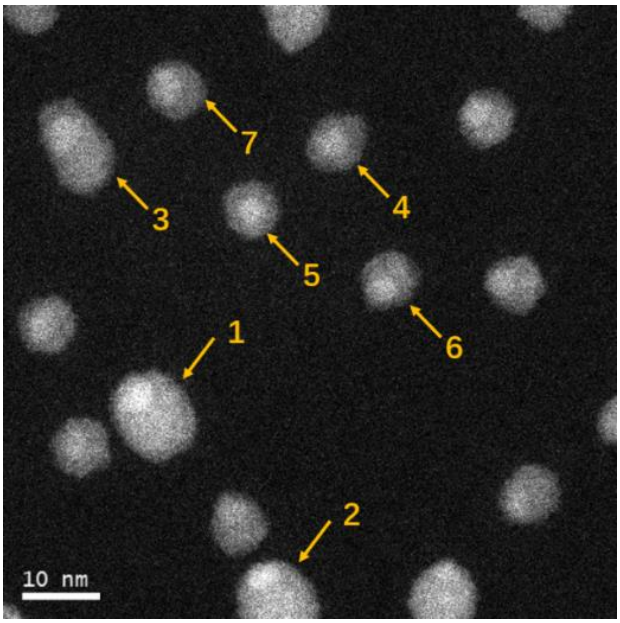


Figure 2.33: HAADF-STEM image of Ag6525 clusters exposed to the air for 31 days.

Figure 2.34 shows that some cores of Ag6525 clusters exposed to the air still have special structures, like the Dh structure in Figure 2.34 (b) and FCC structure in Figure 2.34 (d). Although structures of cores shown in Figure 2.34 (a) and (c) cannot be recognized, they obviously show crystalline structures rather than amorphous structure. However, whether these structures keep the same as their initial structure before exposing in air or induced by the reaction of Ag clusters and air is still unclear. As for the structures of shell, some of them show amorphous structure (like Figure 2.34 (b), (c), and (d)) but the others show crystalline structure (Figure 2.34 (a)).

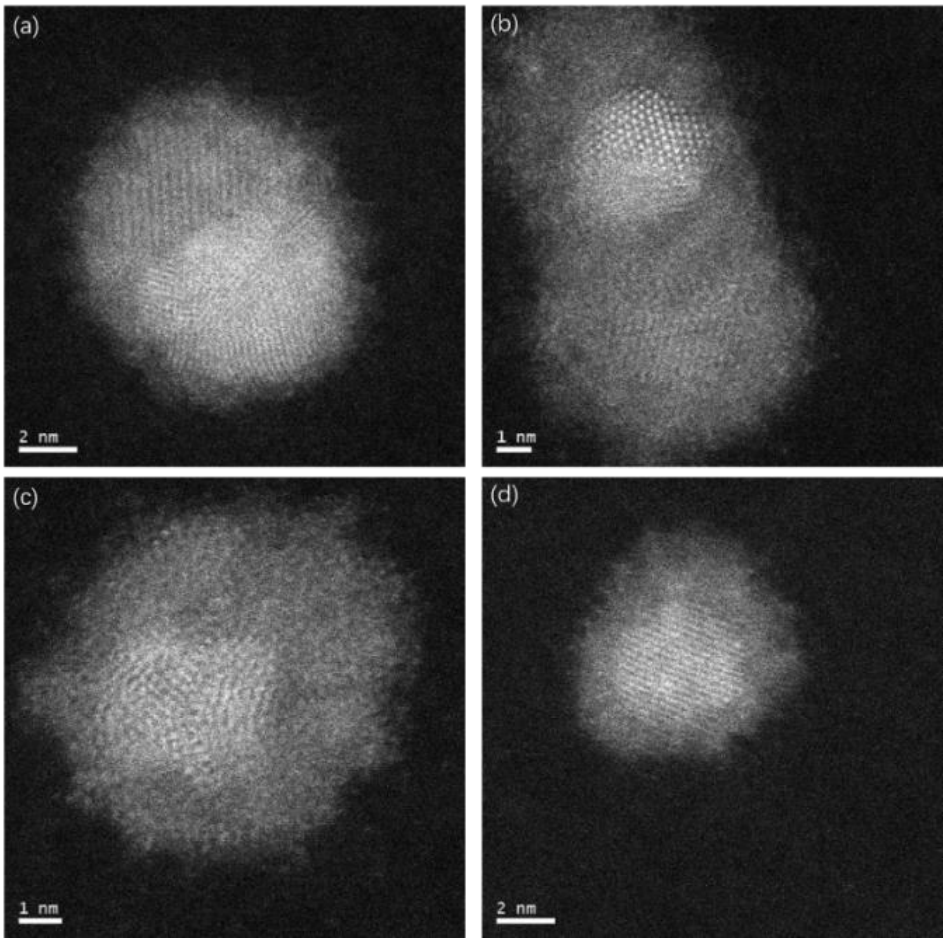


Figure 2.34: HAADF-STEM image of Ag6525 clusters exposed to the air for (a) 1 day, (b) 12 days, (c) 21 days, and (d) 31 days.

2.3.3 Composition evolution of Ag6525 exposed to the air

In order to confirm the composition of the core-shell structure, energy-dispersive X-ray (EDX) analysis was applied. However, experimental result as shown in Figure 2.35 proves that the core-shell structure is quite sensitive to electron beam and face scanning for about 5 minutes would cause serious damage to the core-shell structure and also induce contamination.

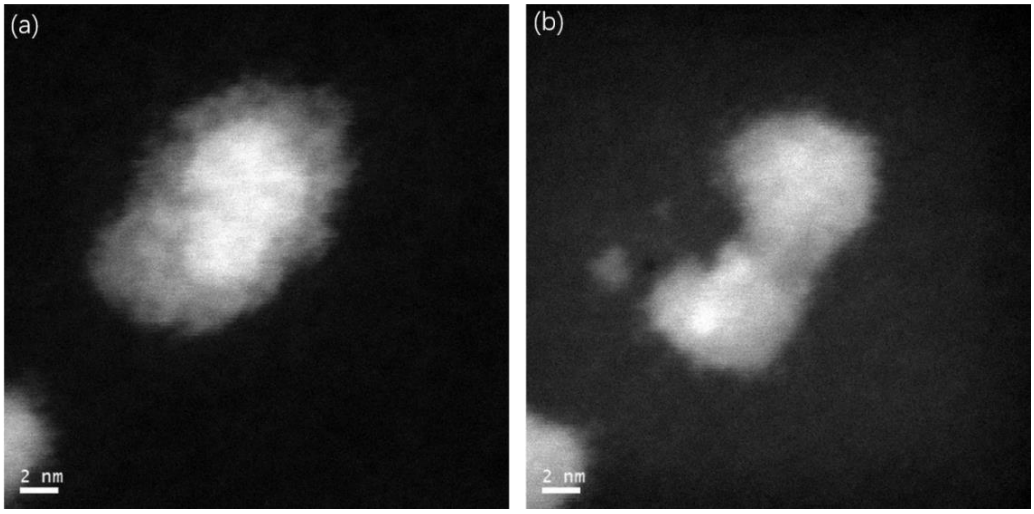


Figure 2.35: HAADF-STEM image of one cluster with core-shell structure (a) before face scanning and (b) after face scanning for 5 minutes.

Then, line scanning was applied to decrease the scanning time and reduce the effect of the electron beam on the core-shell structure. Typical line scanning results are shown in Figure 2.36. Normally, these clusters with core-shell structures are considered as oxidation products after the reaction between Ag clusters and oxygen in the air. However, the signal peak of O is relatively low in Figure 2.36 (d), proving that O is not a composition element in this core-shell structure. Figure 2.36 (e) and (f) show that the bright core is mainly Ag and the dark shell is composed of Ag and S. In addition,

comparing Figure 2.36 (b) and (c) with (a), it shows that the position of the bright core would change under beam irradiation, which means that electron beam will induce the diffusion of Ag atoms.

Early studies reveal that hydrogen sulfide (H_2S) is a reactive agent for silver sulfidation under atmospheric conditions[85]. The authors pointed out that the measured concentrations of H_2S and SO_2 are less than 0.2 parts per billion in normal laboratory air, which is extremely low compared to the concentration of O_2 in air. Then, Graedel et al.[86] reported that carbonyl sulfide (OCS) found in the atmosphere can also sulfidize silver. In addition, Filimon et al.[87] highlighted that Ag undergoes minimal oxidation during baking at temperatures below 300 °C, since the oxidation process has a very slow rate. For higher temperatures, oxidation may be significant. So, the reaction rate of sulfidation of Ag is much higher than that of oxidation at room temperature, even though the fraction of O_2 is much higher than those of sulfide in air. The high surface-to-volume ratios of nanoscale clusters and also the humid atmosphere in UK accelerate the sulfidation process.

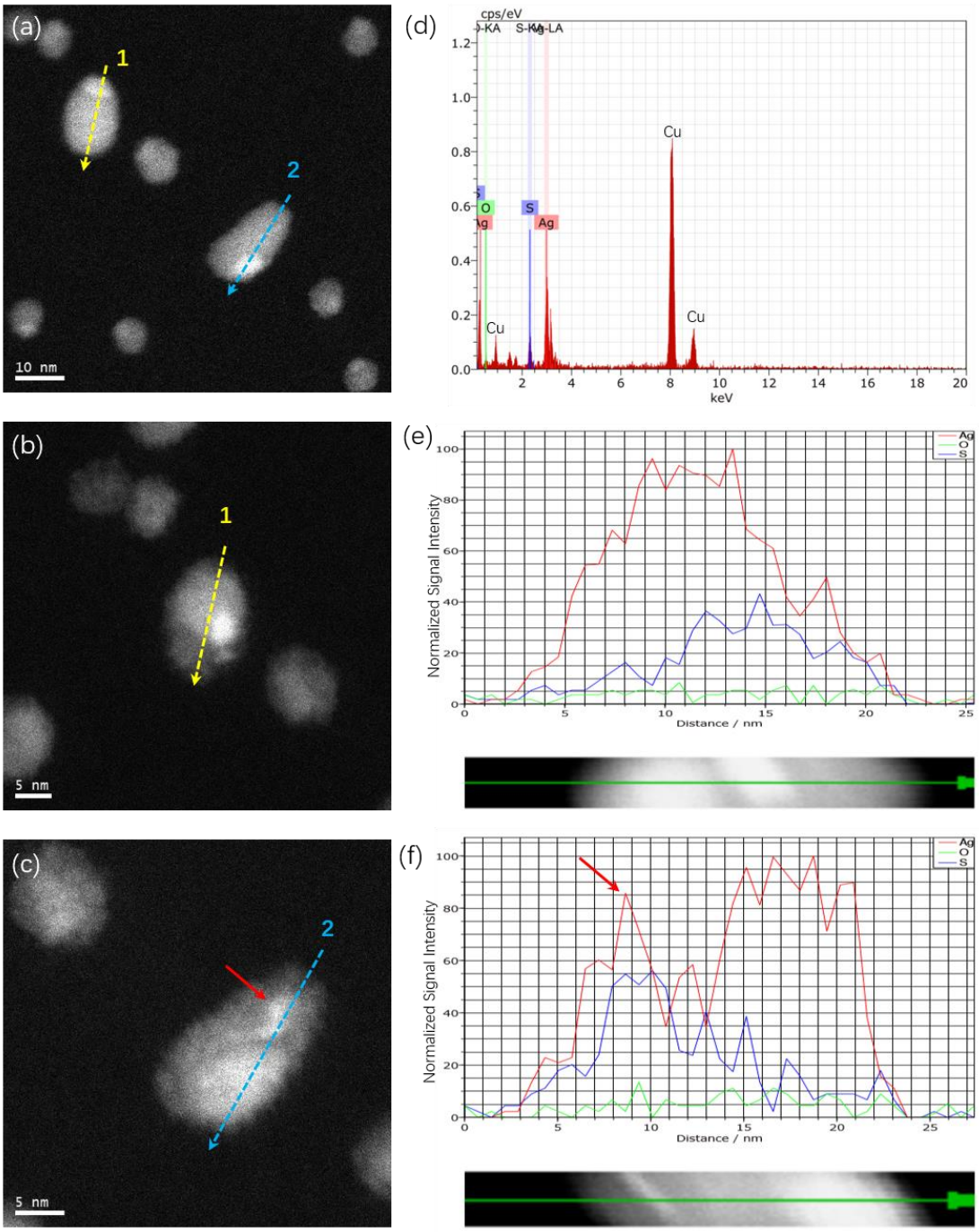


Figure 2.36: (a) HAADF-STEM image of clusters before line scanning. (b) and (c) HAADF-STEM images of the clusters after line scanning 1 and 2, respectively. (d) EDX spectrum of line scanning 1. (e) and (f) element distribution along the line scanning direction in line scanning 1 and 2, respectively. The Ag peak marked by the red arrow in (f) is related to the position marked by the red arrow in (c).

2.3.4 Ag6525 stored in a high vacuum for about one month

Apart from the experiments about exposure in air, Ag6525 clusters stored in high vacuum ($10E^{-7}$ mbar) were also observed after 7, 9, 14, and 26 days. As shown in Figure 2.37, the size of these clusters keeps constant in 26 days. Besides, clear structures of these clusters can also be observed after 26 days, one example of Ih structure is shown in Figure 2.38. All these results prove that Ag6525 clusters can be well-protected in such high vacuum, which proves a method for the store of Ag clusters in the following experiments.

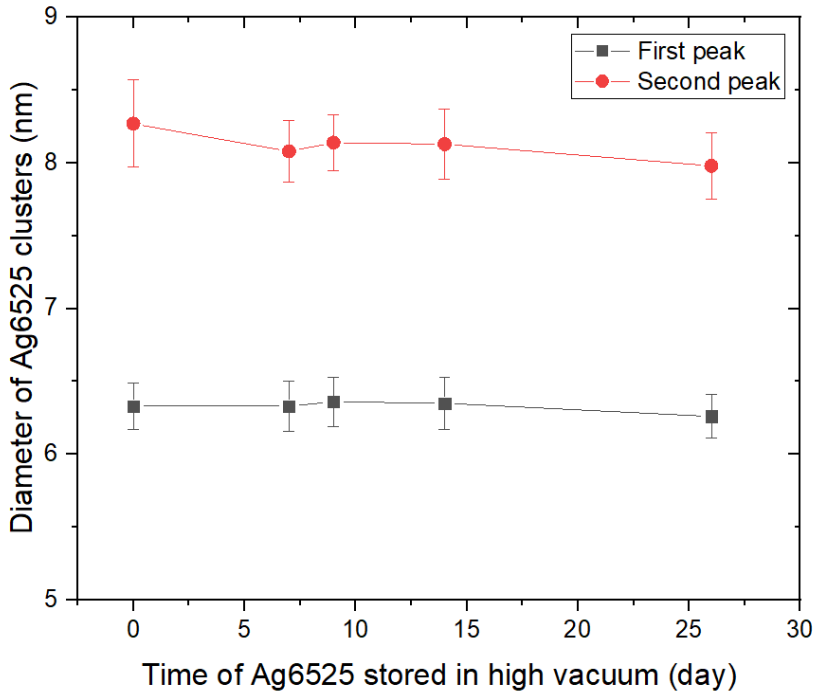


Figure 2.37: The relationship between peak diameters of Ag6525 clusters and time of these Ag6525 clusters stored in high vacuum. The first peak of size distribution shows sizes of single Ag6525 clusters and the second peak of size distribution is formed by aggregation of two single Ag6525 clusters. The error bar represents the standard deviation of the statistical results.

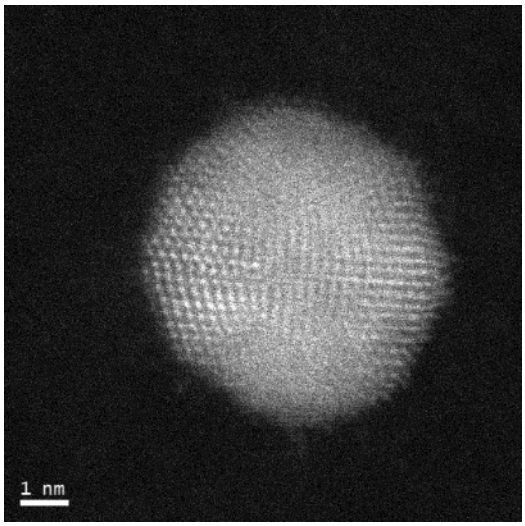


Figure 2.38: HAADF-STEM images of a typical clusters with Ih structures after stored in high vacuum for 26 days. No obvious core-shell structure can be observed.

Chapter 3 Growth Study of Mass-selected Ag Clusters with HAADF-STEM

3.1 Introduction

Nanoscale clusters with different sizes always show unique properties due to size effects. Since magnetron sputtering is applied as a physical approach to preparing nanoclusters, size-selected cluster preparation can be achieved with a range of different mass filters[88,89]. Experimental works on size evolutions[90] and catalysis performance[91,92] of size-selected clusters have been explored. However, a few experimental investigations about the morphologies with size dependence of size-selected clusters have been published. Only D. Pearmain pointed out that the mean aspect ratio of Pd clusters has a parabolic dependence on cluster size[93], but whether clusters of other metals follow the same rule is unknown. In addition, the equilibrium shapes of clusters with different sizes have been studied by simulations[94,95], however, clusters formed in experiments may reflect metastable structures. K. Koga investigated the different atomic structures of Au cluster as a function of cluster size by analyzing TEM images, and the results show that fewer (from 90% to 60%) Ih and more (from 10% to 30%) Dh structures can be found with increasing cluster diameter from 3 to 18 nm[96]. In this chapter, a systematic investigation has been done with Ag clusters in the size range of 1k to 14k atoms. The morphologies of Ag clusters were analyzed by using HAADF-STEM images, while their atomic structures were obtained by comparing the experimental images with related simulated images. Based on these experimental

results, a model to describe the possible growth process in the magnetron sputtering chamber was proposed.

In order to study the growth details of Ag clusters in the cluster source, a set of preparation parameters was selected to achieve a wide range of deposition sizes. These were a power of 10 W, an Ar gas flow rate of 120 sccm, a He gas flow rate of 30 sccm, a condensation length of 250 mm, and a sputtering chamber pressure of 0.21 mbar. The mass spectrum for these preparation parameters is shown in Figure 3.1 with a peak size of approximately 6k. Ag clusters of sizes 1k, 2k, 4k, 6k, 8k, 10k, 12k, and 14k were deposited using the same preparation parameters as described in Figure 3.1.

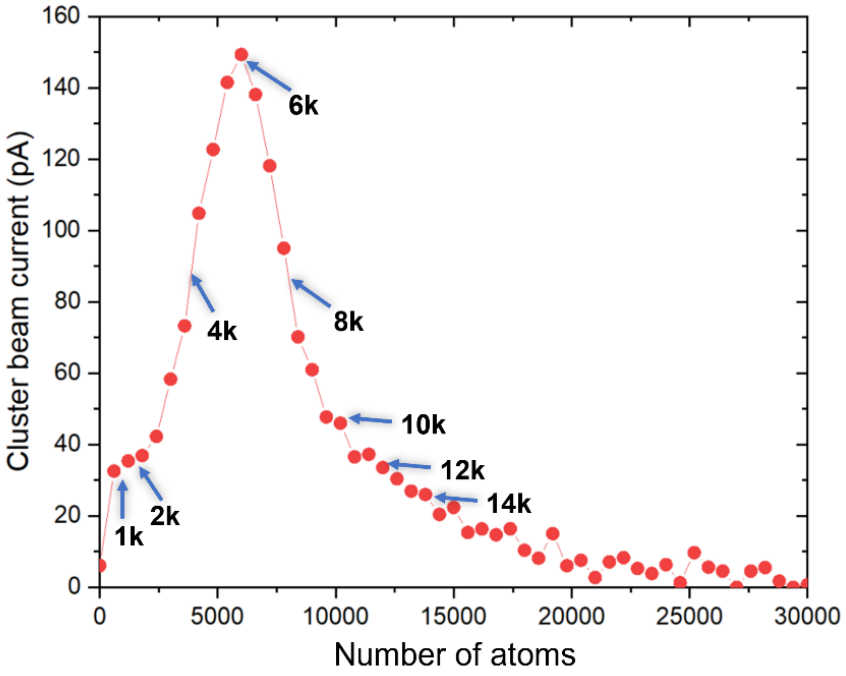


Figure 3.1: The mass spectrum of preparation parameters, i.e., a power of 10 W, an Ar gas flow rate of 120 sccm, a He gas flow rate of 30 sccm, a condensation length of 250 mm, and a sputtering chamber pressure of 0.21 mbar.

3.2 Morphology distribution of size-selected Ag clusters

Morphologies of Ag clusters with different sizes are presented in Figure 3.2. For the size range of 1k to 6k, almost all Ag clusters show round shapes in HAADF-STEM images. However, for the size range of 8k to 14k, more and more Ag clusters show elongated shapes, as indicated by red circles for Sample Ag8k and Ag10k in Figure 3.2. These Ag clusters with elongated shapes are formed due to incomplete cluster-cluster aggregation during the growth process in the sputtering chamber[93]. In addition, there are some Ag clusters with double or triple intensity compared to other clusters in the same images, which are pointed out by yellow arrows in Figure 3.2. These clusters are formed in two ways. One route is two or more individual clusters deposited close to each other on the carbon film and merging after deposition, like the cluster marked in Sample Ag8k. The second route is clusters having the same mass-to-charge ratio as the majority species, such as the clusters pointed out in Sample Ag2k, Ag6k, and Ag10k, so they can pass through the mass filter as smoothly as those singly charged clusters.

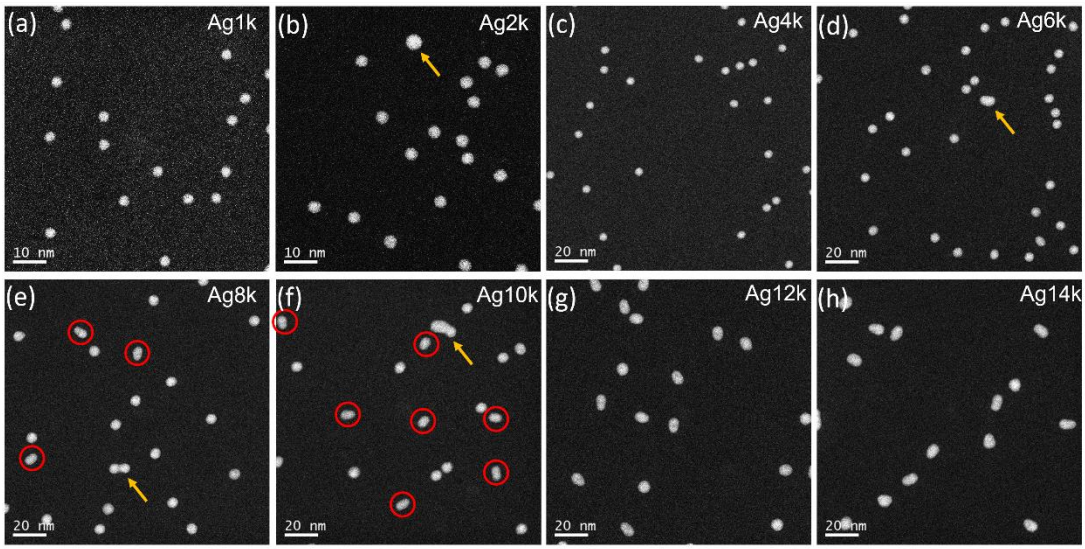


Figure 3.2: (a)-(h) Morphologies of Ag clusters in the size range of 1k to 14k revealed by HAADF-STEM images. Distinct elongated clusters are pointed out with red circles in Sample Ag8k and Ag10k. These aggregated Ag clusters are indicated by yellow arrows, which were formed by the same deposition locations of two or three single clusters or the multiple charge of these clusters.

The relationship between integrated intensity and aspect ratio for Ag clusters with different sizes is plotted in Figure 3.3 (a). For Ag clusters in the size range of 1k to 6k, no clusters with high aspect ratios were found. However, for Ag clusters in the 8k to 14k size range, more and more clusters exhibit elongated shapes with high aspect ratios. The relationship between integrated intensity and the size of Ag clusters is shown in Figure 3.3 (b), which can be fitted with a linear relationship. It has been pointed out in other papers[97,98] that the integrated intensity increases linearly with the cluster size.

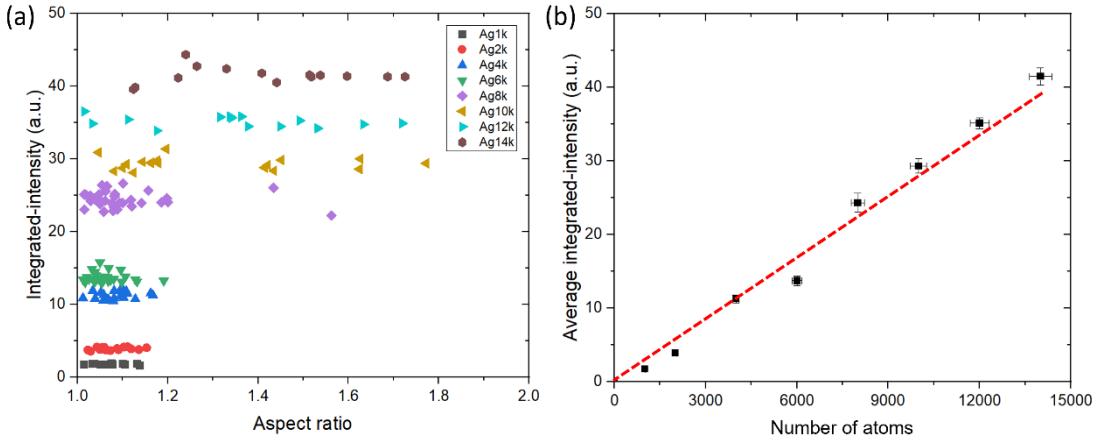


Figure 3.3: (a) The relationship between the integrated intensity and aspect ratio of Ag clusters with different sizes based on the HAADF-STEM images in Figure 3.2. (b) The relationship between the integrated intensity and size of Ag clusters (about 150 clusters were analyzed per sample). For each point in (b), the error bar along the X-axis represents the mass resolution of the mass filter for different deposition sizes, while the error bar along the Y-axis represents the standard deviation of the statistical results.

A plot of the relative frequency of aspect ratio distribution for Ag clusters with different sizes is shown in Figure 3.4 (a). For Ag clusters in the size range of 1k to 6k, the aspect ratio distributions contribute to the low-level region. When the cluster size reaches 8k, some Ag8k clusters with high aspect ratios appear. For the Ag10k and Ag12k clusters, the fraction of clusters with high aspect ratios greatly increases. However, only one peak with widely distributed aspect ratios can be seen for the Ag14k clusters. Based on the same dataset of Figure 3.4 (a), the mean and standard deviations of the aspect ratios for Ag clusters with different sizes are plotted in Figure 3.4 (b). In this plot, the average aspect ratios represent the morphologies of the analyzed clusters, and the error bars of the aspect ratios mean the shape difference between clusters of the same size. The higher the aspect ratio is, the more incomplete aggregated clusters can be observed. The larger the error bar of the aspect ratio is, the larger difference in the morphology of

clusters with the same size. When the size is smaller than 6k, the values of aspect ratios and error bars are similar. This means that clusters with a size smaller than the peak size are more likely to achieve complete aggregation during growth. When the size is larger than 6k, the average value of the aspect ratio becomes larger with increasing size, indicating that there will be more elongated clusters.

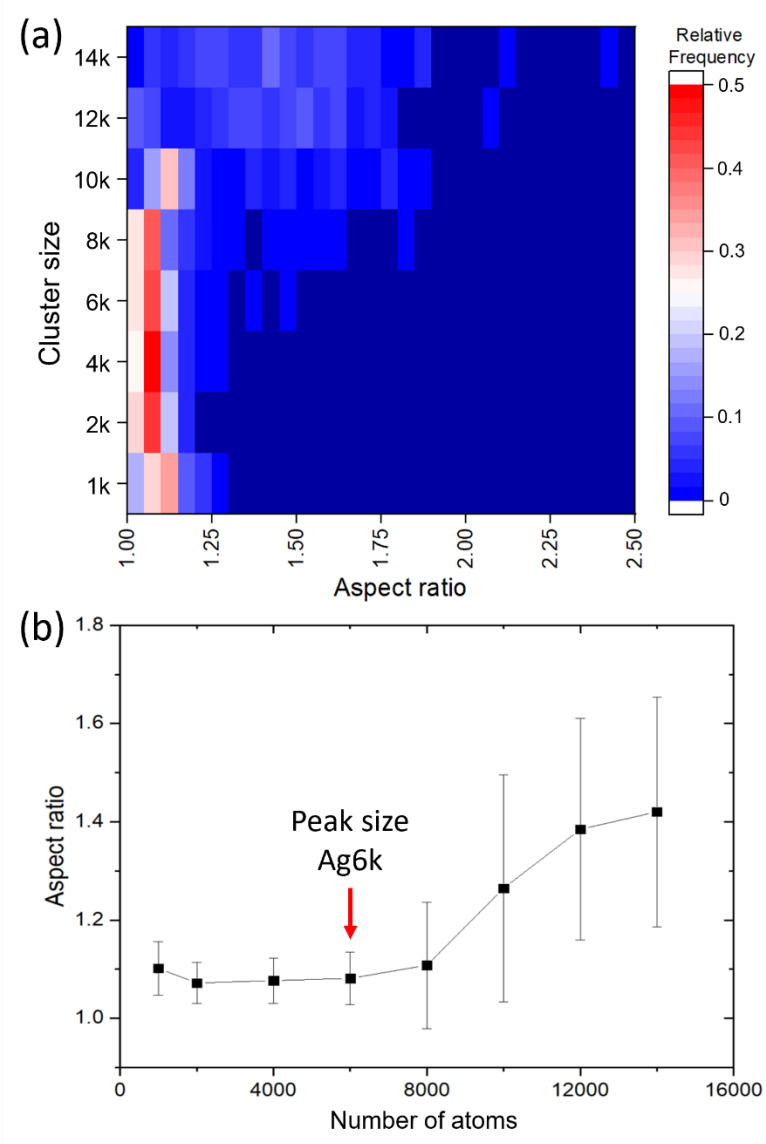


Figure 3.4: (a) The plot of the relative frequency of aspect ratio distribution for Ag clusters with different sizes (approximately 150 clusters were analyzed per sample). (b) The average values and their standard deviations of aspect ratios for Ag clusters with different sizes, according to the same dataset of (a).

Two questions arise from the results depicted in Figure 3.4 (b). The first question is whether the increase in aspect ratios is due to the increase in size. The second question is whether the peak size represents the turning point for the increase in aspect ratios. To investigate these two questions, additional experiments were conducted, as described in the following section.

Another series of mass spectra were obtained by using the same Ar gas flow rate of 120 sccm but different He gas flow rates, as shown in Figure 3.5 (a). Ag clusters with the peak sizes of these mass spectra were deposited to further confirm the positive correlation between the aspect ratios of Ag clusters and their sizes. The result is presented as the red curve in Figure 3.5 (b). Comparing the aspect ratios of clusters deposited with the same parameters, shown as the black curve in Figure 3.5 (b), the aspect ratios of these clusters deposited with different parameters do not show an increasing trend with increasing number of atoms, proving that the positive correlation between aspect ratio and number of atoms may only exist in Ag clusters deposited with the same parameters. Furthermore, the distinction between the two curves presented in Figure 3.5 (b) is only discernible beyond a size of 6k, which corresponds to the peak size observed in the mass spectrum displayed in Figure 3.1. This observation lends additional support to the hypothesis that the starting size featuring high aspect ratios may be the peak size of the mass spectrum.

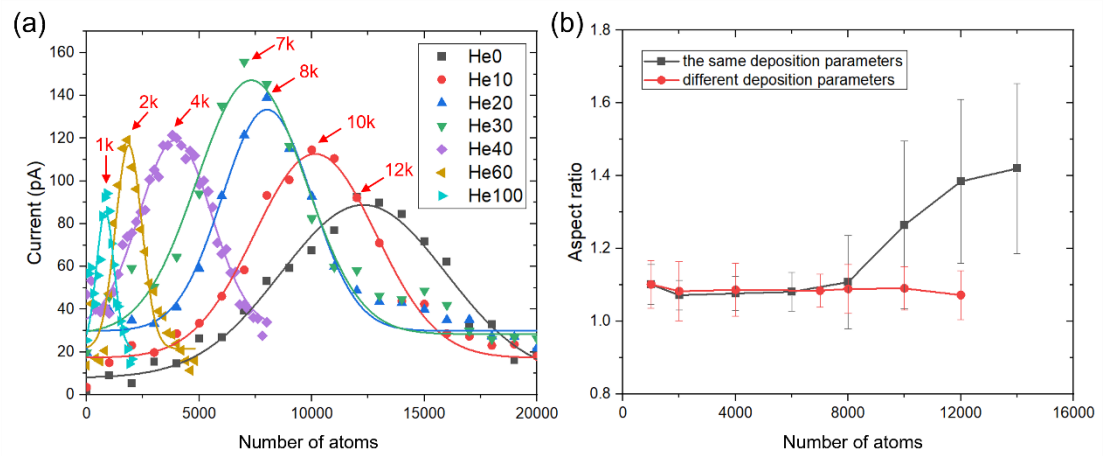


Figure 3.5: (a) Mass spectra with different peak sizes were obtained by using the same Ar gas flow rate of 120 sccm but different He gas flow rates. The curves have been fitted with the Gaussian function. (b) The red curve is the mean values of aspect ratios and their standard deviations for Ag clusters prepared with different parameters described in (a), and the result of the black curve is the replotted images of Figure 3.4 (b).

More experiments have been performed to confirm that peak size is the starting point for high aspect ratios. The same deposition parameters of the mass spectrum shown in Figure 3.1 were applied again, namely, a power of 10 W, an Ar gas flow rate of 120 sccm, a He gas flow rate of 30 sccm, a condensation length of 250 mm, and a pressure of 0.21 mbar in the sputtering chamber. A new mass spectrum shown in Figure 3.6 (a) was obtained, with a new peak size of 7k compared to that of the mass spectrum presented in Figure 3.1. In magnetron sputtering, the surface of the target undergoes continuous erosion in the area where electrons are confined. Consequently, a narrow and deep erosion groove is formed. With the Ag target being consumed during sputtering, the depth of the erosion groove will increase, resulting in the change of sputtering rate and causing a shift of the peak size in the mass spectrum, even when the same deposition parameters are applied[99]. The relationship between the aspect ratio and size of Ag clusters is plotted in Figure 3.6 (b) and (c). Ag clusters with sizes smaller

than the peak size of 7k have similar aspect ratios. But for Ag clusters with sizes larger than the peak size, aspect ratios increase with size, showing the same trend as described in Figure 3.4.

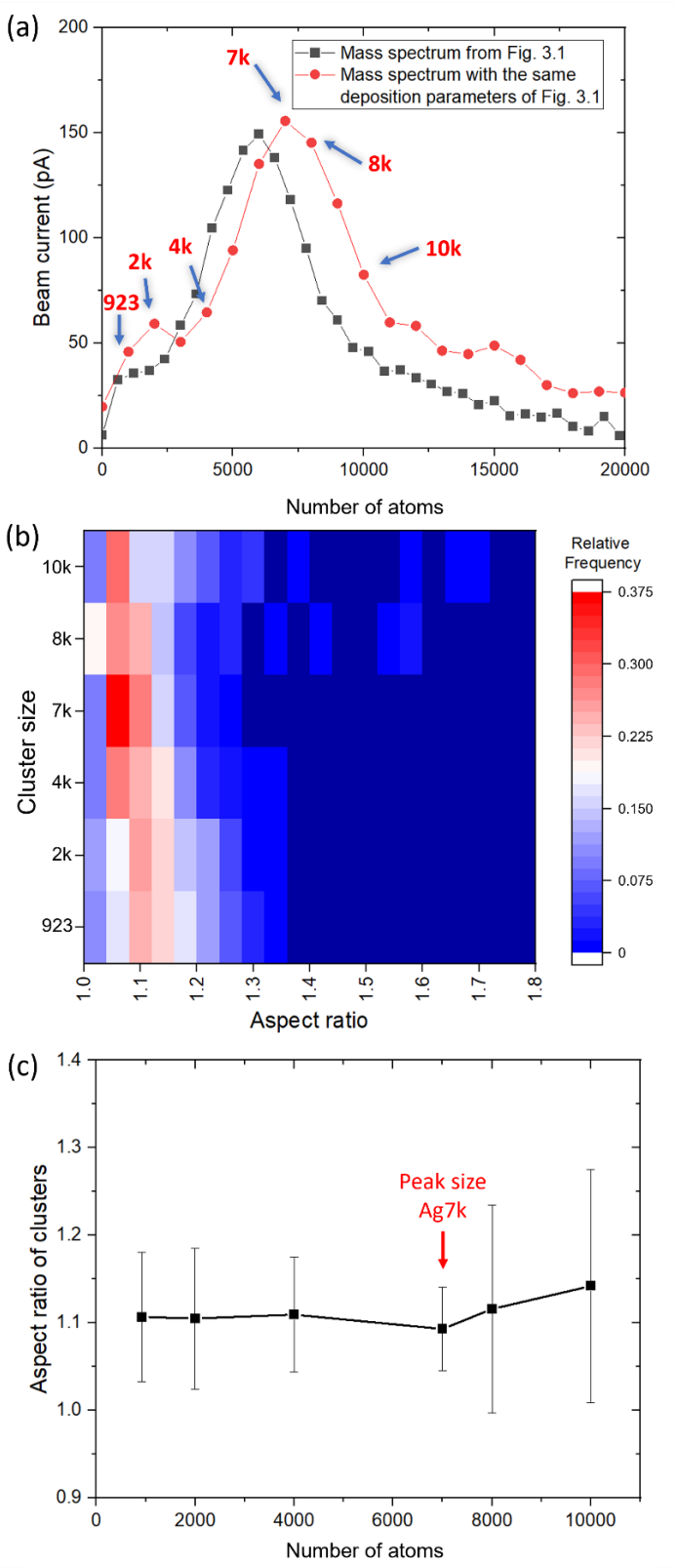


Figure 3.6: (a) Mass spectrum (red curve) obtained with the same deposition parameters as Figure 3.1 (black curve). (b) A plot of the relative frequency of aspect ratio distribution for Ag clusters deposited with mass spectra shown in (a). (c) The relationship between aspect ratios of Ag clusters and their sizes marked in (a). The error bar represents the standard deviation of the statistical results.

Furthermore, mass spectra with different peak sizes controlled by different deposition parameters were obtained, as shown in Figure 3.7 (a) and (c). Ag8k clusters associated with these mass spectra were deposited, and their aspect ratios are shown in Figure 3.7 (b) and (d), respectively. For the cluster size of 8k, its relative positions to peak sizes of different mass spectra are different. When 8k is smaller than the peak size, the related aspect ratio is small. However, larger aspect ratios and big error bars will be obtained when 8k is larger than the peak size. What's more, the further away from the peak size, the larger the aspect ratio is.

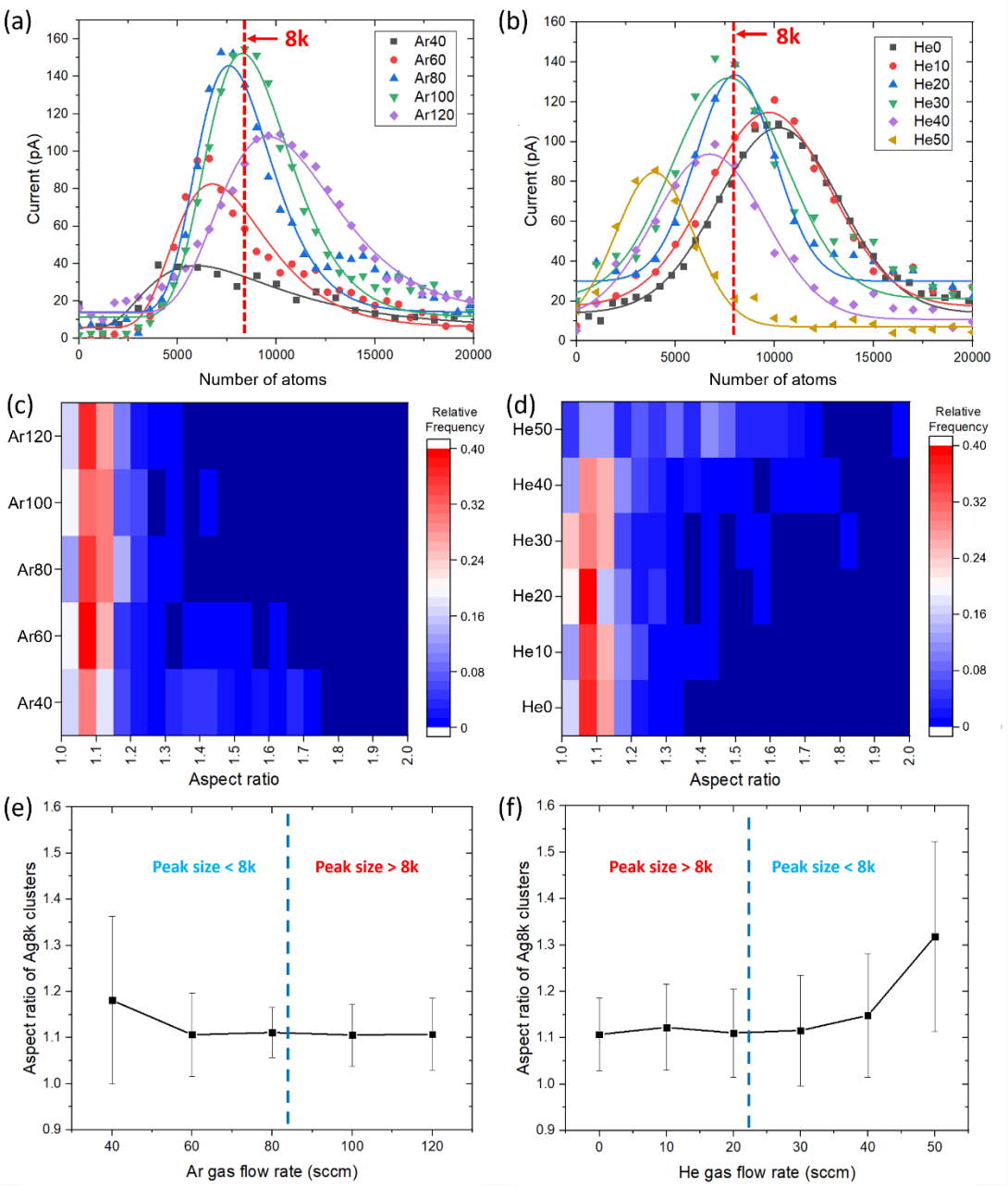


Figure 3.7: (a) Mass spectra of Ag clusters prepared with different Ar gas flow rates. Other parameters are the same, namely, a power of 10 W, a He gas flow rate of 0 sccm, and a condensation length of 250 mm. The mass spectra have been fitted with the Lognormal function. (b) Mass spectra of Ag clusters prepared with different He gas flow rates. Other parameters are the same, namely, a power of 10 W, an Ar gas flow rate of 120 sccm, and a condensation length of 250 mm. The mass spectra have been fitted with the Gaussian function. (c) and (d) The plots of the relative frequency of aspect ratio distribution for Ag8k clusters deposited with mass spectra shown in (a) and (b) (approximately 150 clusters were analyzed per sample). (e) and (f) The relative mean values and their standard deviations of aspect ratios for Ag8k clusters analyzed in (c) and (d).

According to the results of Figure 3.4-3.7, it can be concluded that the peak size is the starting point of increasing high aspect ratios, indicating that Ag clusters with sizes smaller than the peak size can achieve complete aggregation during the growth process, but it is difficult for those Ag clusters with larger sizes to fully aggregate into one spherical cluster. David Pearmain pointed out that the mean aspect ratios of Pd clusters will increase following a parabolic relationship with increasing number of atoms[93], which is not the same case with the results described here. However, the preparation parameters of clusters with different sizes in Pearmain's work are unknown, so it is difficult to confirm that the results are all from the same set of parameters. If only one set of parameters was applied for the deposition of Pd clusters with different sizes, a possible reason can explain the difference between Pearmain's results and the results presented here, which is that the bond dissociation energy of Ag atoms (163 kJ/mol) is lower than that of Pd atoms (339 kJ/mol) and the atom rearrangement process after aggregation can be easier for Ag clusters, finally leads to the similar aspect ratios of Ag clusters with small sizes rather than the parabolic relationship described in Pearmain's results.

3.3 Structure distribution of size-selected Ag clusters with spherical shape

According to the results in Figure 3.4, when the Ag cluster size exceeds the peak size, there will be some clusters with elongated shapes. An example of Ag8k clusters is presented in Figure 3.8 (a), with nine clusters in the field of view. The integrated

intensities of these clusters are similar, as shown in Figure 3.8 (b), indicating that all of them are single Ag8k clusters. However, the aspect ratio of Cluster 4 and 9 are much larger than that of other clusters. Their enlarged images are shown in Figure 3.8 (e) and (f), whose structures are quite difficult to be identified compared with the spherical clusters in Figure 3.8 (c) and (d) with easily recognizable structures.

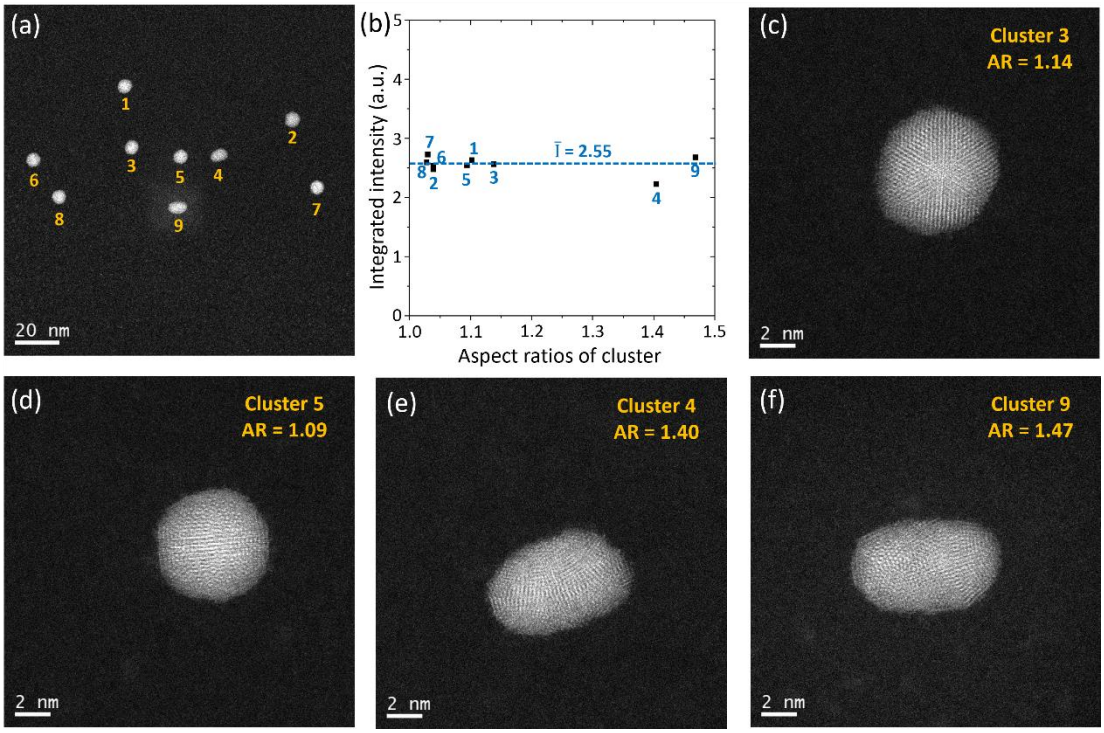


Figure 3.8: (a) A HAADF-STEM image of Ag8k clusters. (b) The relationship between integrated intensity and aspect ratio of nine clusters in (a). (c), (d), (e), and (f) Enlarged HAADF-STEM images of Cluster 3, 5, 4, and 9, respectively. AR: aspect ratio.

For these spherical clusters, structure identification can be easily performed following the method described in Chapter 2. Examples of structure identification are shown in Figure 3.9 (a), (b), and (c), which can be classified into Ih, Dh, and FCC structures by comparing the experimental images with the relative simulated images. The structures of spherical Ag clusters with the different sizes as marked in Figure 3.1 were analyzed

and the results are shown in Figure 3.9 (d). The percentage of Ag clusters with Ih structure decreases linearly with increasing size. However, the proportions of Ag clusters with Dh and FCC structures show linear increasing trends with increasing size. For Ag12k and Ag14k clusters, the percentage of UI structure abruptly increases to around 10%, as more clusters show non-classical structures due to insufficient aggregation, although their morphologies have been approximately spherical.

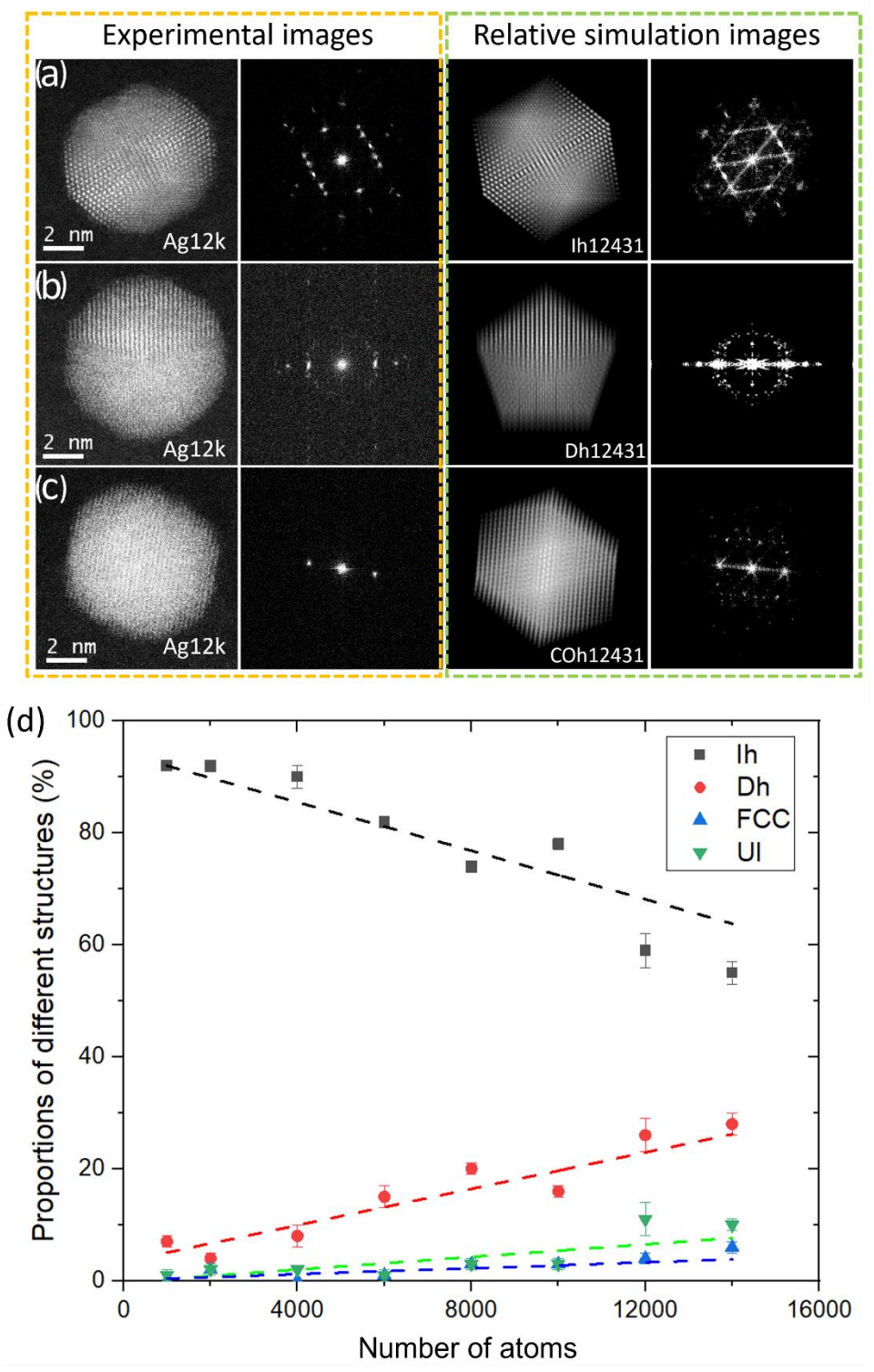


Figure 3.9: (a), (b), and (c) Three HAADF-STEM images of prepared Ag12k clusters, their FFT images, and their respective simulated images. (d) The relationship between proportions of different structures and the size of Ag clusters. The curves have been fitted with linear relationships. About 250 clusters were analyzed per sample. The error bars in (d) are a result of the clusters displaying the characteristics of two structures simultaneously, such as in the case of clusters during the Ih-to-Dh transition process (which are considered to be half Ih and half Dh) or distorted Ih (which are considered to be half Ih and half UI).

3.4 Structure distribution of size-selected Ag clusters with an elongated shape

Apart from the Ag clusters with spherical shapes shown in Figure 3.8 (c) and (d), there is a large number of Ag clusters with elongated morphology, such as the clusters in Figure 3.8 (e) and (f). These elongated clusters result when the domains in one cluster have not yet fully aggregated during the growth process in the sputtering chamber. These elongated clusters are impossible to be formed by collisions during flying after passing through the nozzle, because only two domains were observed in these elongated clusters rather than multiple domains formed by several random collisions. According to the results of Figure 3.4, when the cluster size exceeds the peak size of 6k, the aspect ratio and its standard deviation will increase, indicating that there will be more elongated clusters. To confirm the proportion of these so-called elongated or aggregated clusters, two methods were applied.

On the one hand, the proportions of aggregated clusters with different sizes were summarized from the aspect ratio dataset shown in Figure 3.4. A typical example of the aspect ratio distribution is shown in Figure 3.10 (a), and the distribution can be well fitted with a Gaussian function for clusters whose morphologies are close to perfect spheres. When using a Gaussian fit, a confidence level of 0.997 is applied, which yields a confidence interval of [μ-3σ, μ+3σ]. The value of μ+3σ is then used as the threshold value for separating spherical and aggregated clusters. After analyzing 14 samples that contained rare elongated clusters, the average value of μ+3σ was determined to be 1.23.

Therefore, a threshold aspect ratio of 1.23 was established to distinguish between completely aggregated spherical Ag clusters and elongated (incompletely aggregated) Ag clusters. The result of this method is shown as the black curve in Figure 3.10 (b).

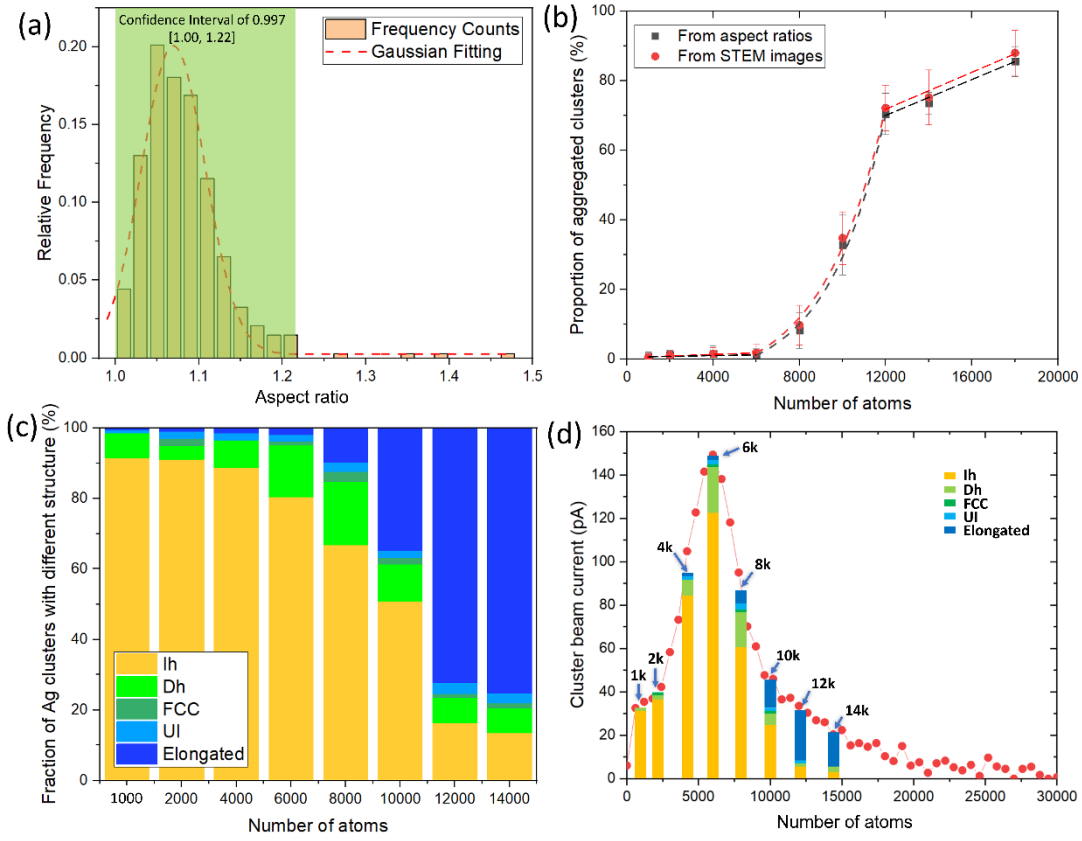


Figure 3.10: (a) This figure shows the aspect ratio distributions of the Ag6k sample prepared with the same parameters as Figure 3.1. The respect ratio interval of analyzed spherical Ag6k clusters is [1.00, 1.22], from the lowest aspect ratio value (namely 1) to the value of $\mu+3\sigma$ for the Gaussian fitting (1.22 here). (b) The relationship between the percentage of aggregated Ag clusters and their sizes is presented. The black curve represents the results obtained by analyzing the aspect ratio datasets, while the red curve is from the HAADF-STEM images of every Ag cluster. About 200 and 250 clusters were analyzed for these two methods, respectively. The two curves can be well-fitted with a linear relationship in the size range of 1k to 6k, exponential functions for 6k to 12k, and a linear relationship from 12k to 16k. The error bars represent the standard deviation of the statistical results obtained from three repetitions. (c) This figure shows the fractions of elongated Ag clusters and different structures for spherical clusters in the size range of 1k to 14k. (d) The distribution of different structures for Ag clusters with different sizes is presented based on the mass spectrum shown in Figure 3.1.

Alternatively, the proportions of aggregated clusters with different sizes can be obtained by analyzing the high-magnification HAADF-STEM images of every Ag cluster and determining whether it is aggregated or not. Approximately 250 clusters were analyzed for every sample each time, and the results of this method are presented as the red curve in Figure 3.10 (b). The results of both methods are very similar, showing an exponential relationship between the percentage of aggregated Ag clusters and their sizes when the sizes are in the range of 6k to 12k. For Ag clusters in the size range of 1k-6k and 12k-18k, the percentage of aggregated clusters remains almost constant and increases linearly, respectively. Investigating the proportion of aggregated Ag clusters further when the cluster size exceeds 18k is difficult due to the limitation of the deposition flux, as seen from the mass spectrum in Figure 3.1.

Figure 3.9 (d) and Figure 3.10 (b) provide the basis for summarizing the fractions of elongated Ag clusters and different structures for spherical clusters in the size range of 1k to 14k, as shown in Figure 3.10 (c). This figure reveals the distribution of various types of clusters for Ag at different sizes, highlighting two notable characteristics. The first is the continuous decrease in the fractions of Ih structure, and the increase in the fractions of elongated morphology. The second is the initial increase and subsequent decrease in the fraction of Dh structure. Combining the fractions of different kinds of Ag clusters and the mass spectrum, the distribution of different kinds of Ag clusters based on the mass spectrum can be obtained, as shown in Figure 3.10 (d).

For these elongated clusters, almost each of them is a combination of two regions with different structures. Figure 3.11 (a) and (b) provide two examples of domain structure recognition in Ag12k clusters. For Figure 3.11 (a), two domains with different sizes can be identified as Ih structures. The size of each domain is judged according to the number of atomic planes from the edge to the center of the domain. For example, the 11 atomic planes of Domain 1 in Figure 3.11 (a) are the same as the atomic planes of the simulated Ih structure with a magic number of 3871 and the similarity between the relative experimental and simulated FFT images can further confirm that the structure of this domain is Ih. In this way, the aggregated cluster shown in Figure 3.11 (b) can be identified as Ih structure in Domain 3 and the Dh structure in Domain 4, which show similar sizes. As for elongated Ag12k clusters shown in Figure 3.11 (c) and (d), they are products of large identified domains and small unidentified domains.

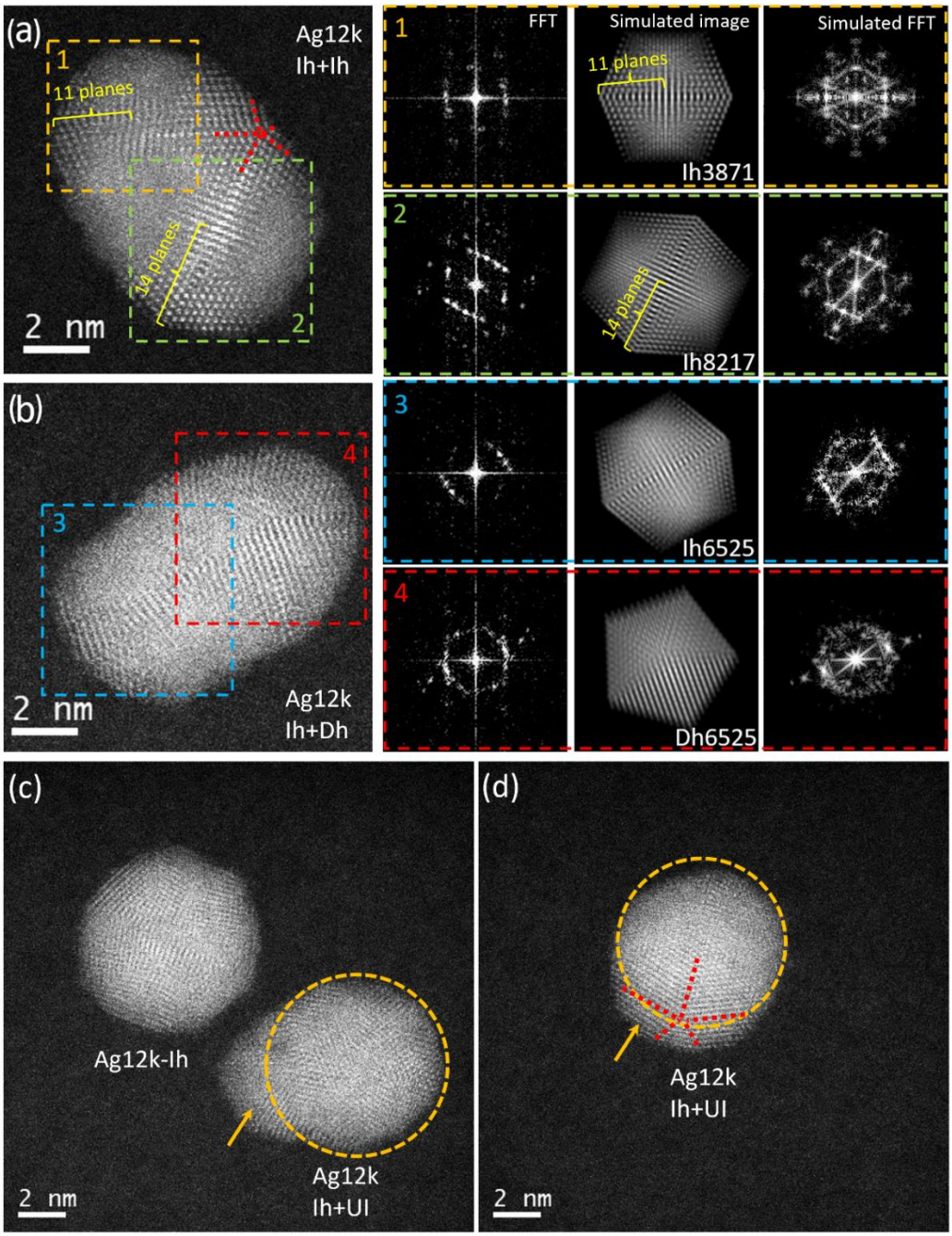


Figure 3.11: (a) A HAADF-STEM image of an elongated cluster, which can be recognized as two domains of Ih structures with different sizes by comparison between FFT images and the relative simulated STEM images and FFT images. (b) A HAADF-STEM image of an elongated cluster with two domains of Ih and Dh structure with similar sizes. (c) A HAADF-STEM image of a standard Ag12k-Ih cluster and an elongated Ag12k cluster with a large identified Ih domain and a small unidentified domain. (d) A HAADF-STEM image of an elongated Ag12k cluster with a large identified Ih domain and a small unidentified domain, of which interface exhibits a five-fold structure. The yellow circles and arrows in (c) and (d) point out the main domains and the small domains, respectively.

Based on the same dataset of the red curve of Figure 3.10, the elongated clusters can be grouped into eight kinds of groups according to the method described in Figure 3.11, i.e., Ih+Ih, Ih+Dh, Ih+FCC, Ih+UI, Dh+Dh, Dh+FCC, Dh+UI, and UI. The proportions of these groups for Ag clusters with different sizes are shown in Table 3.1. The Ih+Ih and Ih+UI structure groups account for more than 75% of the elongated clusters. With increasing sizes, the Dh structure of domains shows an increasing trend. The FCC structure is only found when the cluster size is 14k.

Table 3.1: The proportions of structures of domains for aggregated clusters.

	Ag1k	Ag2k	Ag4k	Ag6k	Ag8k	Ag10k	Ag12k	Ag14k
Ih+Ih	/	/	2 (67%)	2 (50%)	12 (50%)	53 (52%)	117 (60%)	105 (50%)
Ih+Dh	/	/	/	/	/	4 (4%)	12 (6%)	10 (5%)
Ih+FCC	/	/	/	/	/	/	/	1 (0.5%)
Ih+UI	1 (100%)	2 (100%)	1 (33%)	1 (25%)	11 (36%)	41 (40%)	48 (25%)	57 (27%)
Dh+Dh	/	/	/	/	/	/	1 (0.5%)	1 (0.5%)
Dh+FCC	/	/	/	/	/	/	/	1 (0.5%)
Dh+UI	/	/	/	/	/	2 (2%)	3 (1.5%)	18 (9%)
UI	/	/	/	1 (25%)	1 (4%)	2 (2%)	13 (6%)	18 (8.5%)
Total	1	2	3	4	24	102	194	212

The analysis of the structures of domains can help to understand the growth process of clusters in the sputtering chamber. The domains with similar sizes, as shown in Figure 3.11 (b), are seen as the products of the collision between two clusters with similar sizes. While the domains with obvious size differences, as shown in Figure 3.11 (a), (c), and (d), are formed by the attachment of a small cluster to a large cluster. Both kinds of collisions can cause the formation of five-fold structures, as shown in Figure 3.11 (a) and (d), which can be seen as the start state of the formation of Dh structures. The proportions of the domains with similar sizes and with obvious size differences were analyzed and the results are presented in Table 3.2. Ag clusters with sizes smaller than 8k are included in the table for reference, but not considered in the further discussion due to their low statistics. For Ag clusters in the size range of 8k to 14k, the domains with similar size account for the main number, which indicates that more than half of the elongated Ag clusters are formed with two clusters of similar size. Furthermore, the structures of domains with similar sizes were analyzed and the results are shown in Figure 3.12. The proportions of domains with Ih, Dh, and FCC structures show the same trends as the structures of spherical Ag clusters with different sizes shown in Figure 3.9 (d). However, the proportion of Ih structure of domains is higher than that of spherical clusters of the same size. For example, for the domains with the size of 7k, about 90% of these are Ih structures, while the Ih structure accounts for about 80% in Ag7k clusters in Figure 3.9 (d), indicating the different formation positions of the domains and clusters with the same sizes in the magnetron sputtering chamber.

Table 3.2: The proportions of domains with similar sizes or with obvious size differences for aggregated clusters.

	Ag1k	Ag2k	Ag4k	Ag6k	Ag8k	Ag10k	Ag12k	Ag14k
X+X	/	/	1 (33%)	2 (50%)	13 (54%)	64 (63%)	114 (59%)	106 (50%)
X+x	1 (100%)	2 (100%)	2 (67%)	1 (25%)	10 (42%)	36 (35%)	68 (35%)	88 (42%)
UI	/	/	/	1 (25%)	1 (4%)	2 (2%)	12 (6%)	18 (8%)
Total	1	2	3	4	24	102	194	212

(X+X means domains with similar sizes, as in Figure 3.11 (b); X+x means domains with an obvious size difference, as in Figure 3.11 (a), (c), and (d). The dataset is the same as that of Table 3.1.)

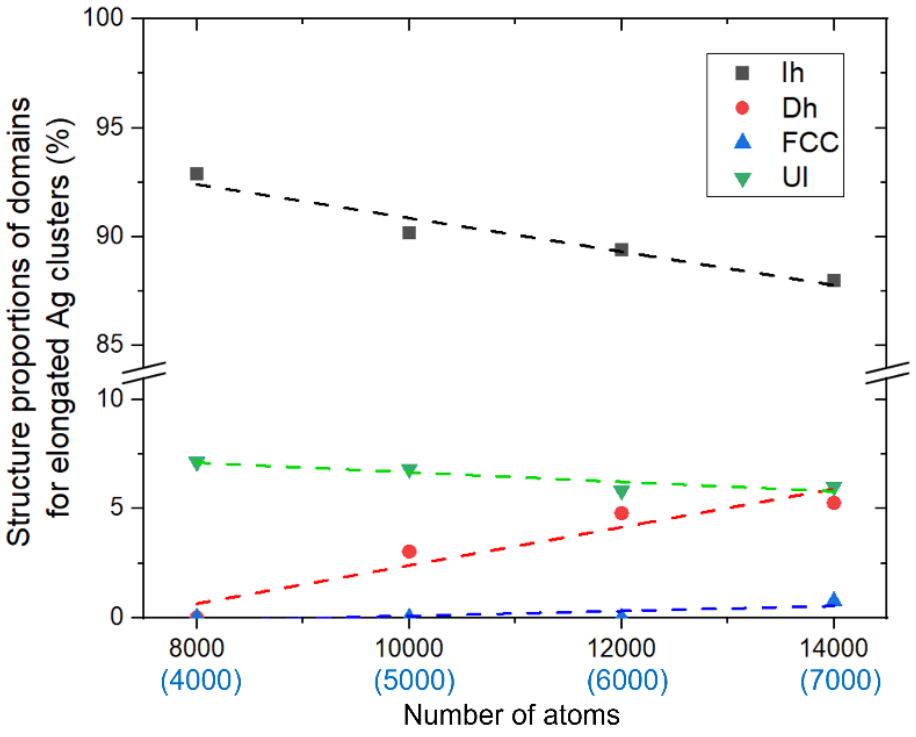


Figure 3.12: The structures of domains with similar sizes (X+X) in elongated clusters. The curves have been fitted with a linear relationship. The black ticks on the X-axis are the size of elongated Ag clusters, while the blue ones on the X-axis are the size of domains in the elongated Ag clusters.

3.5 Comparison between structures of spherical Ag clusters deposited with different parameters

Analyzing the structures of spherical Ag clusters deposited with different parameters can provide insights into the growth process of Ag clusters in the magnetron sputtering chamber. In this part, the structures of two series of Ag clusters with different sizes were analyzed: the Ag clusters prepared based on the red mass spectrum of Figure 3.6 (a) and the sizes marked in the mass spectra of Figure 3.5 (a).

Structures of spherical Ag clusters with the sizes marked in the red mass spectrum of Figure 3.6 (a) were analyzed and the results are presented as the red curves in Figure 3.13. Compared to the results of Figure 3.9 (d), shown as the black curves in Figure 3.13, the slope of the decreasing Ih structures is higher than that of the black curve. This result indicates that more Dh structures formed for Ag clusters with different sizes when the peak size of the mass spectrum moves from 6k to 7k.

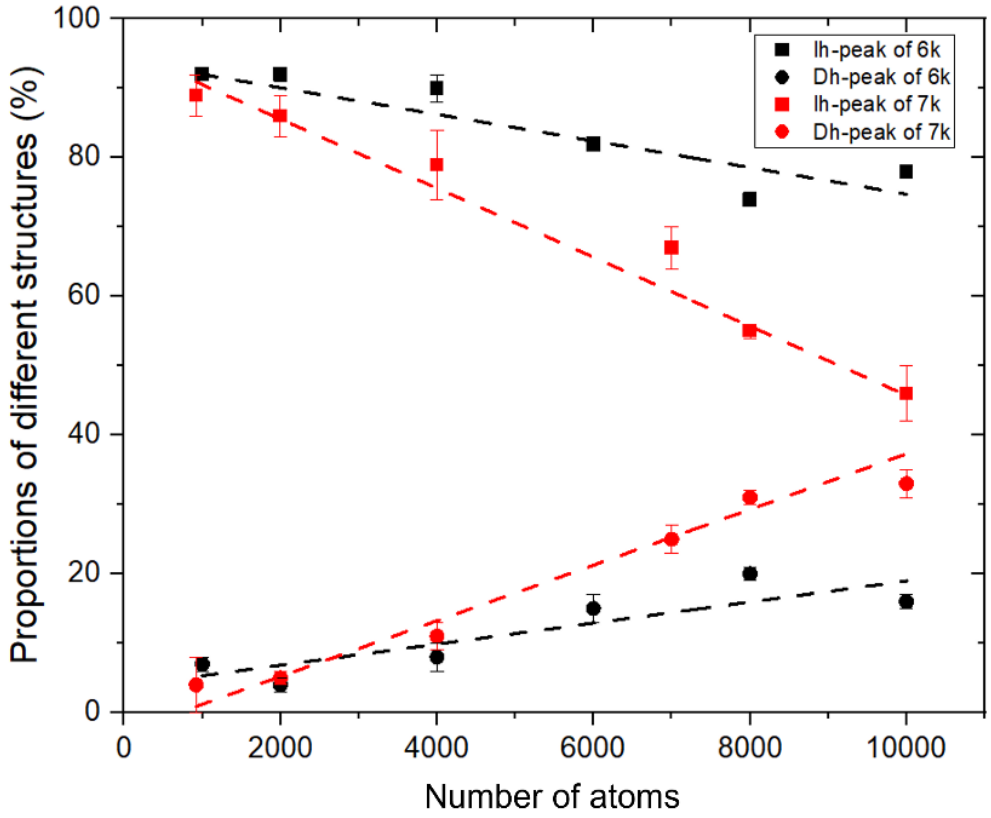


Figure 3.13: The relationship between proportions of different structures and the size of Ag clusters. The curves have been fitted with linear relationships. About 250 clusters were analyzed for every sample. The results of the black curves are from Figure 3.9 (d).

Furthermore, structures of Ag clusters with the sizes marked in the mass spectra of Figure 3.5 (a) were analyzed and the results are shown in Figure 3.14 (a). The proportions of different structures are similar to the results shown in Figure 3.14 (b) (copied from Figure 3.9 (d)) when the Ag cluster is in the size range of 1k to 4k. However, fewer Ih structures and more Dh structures were found for Ag clusters with the same sizes when the cluster size is larger than 4k, indicating that it is possible to control the atomic structures for selected size by tuning the preparation parameters.

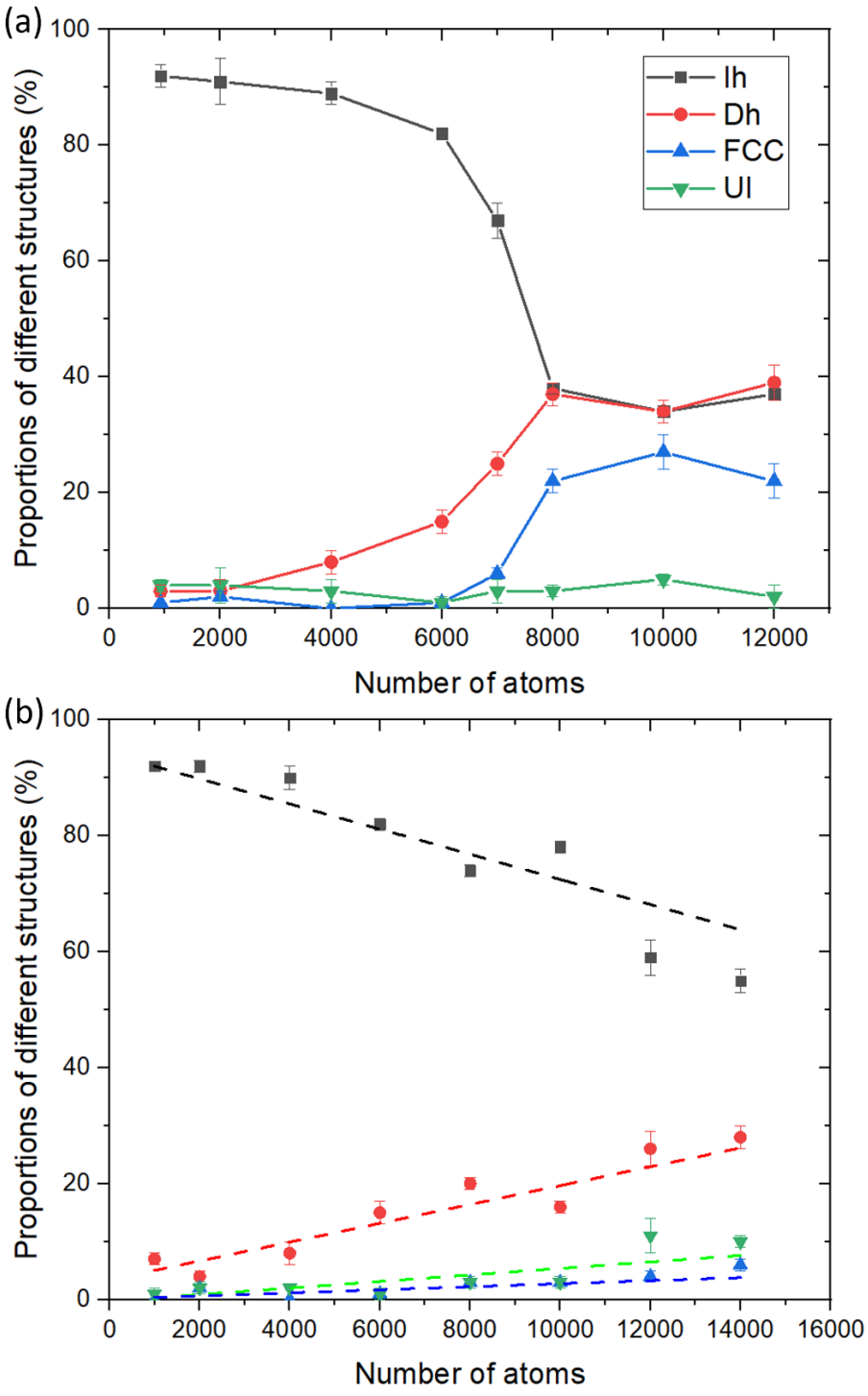


Figure 3.14: (a) The relationship between proportions of different structures and the size of Ag clusters deposited with the sizes shown in Figure 3.5 (a). About 250 clusters were analyzed for every sample. The error bars represent the uncertainties associated with the identification of the structure. (b) The relationship between proportions of different structures and the size of Ag clusters shown in Figure 3.9 (d). This figure is directly copied from Figure 3.9 (d) for comparison.

3.6 Possible growth process of Ag clusters prepared in the magnetron sputtering chamber

The formation of clusters in the magnetron chamber always goes through several processes, including the sputtering of atoms, the nucleation of small clusters, the growth of large clusters, the transport to the exit nozzle and diffusion to the chamber walls, the expansion through the nozzle, and the formation of the cluster beam accompanied with the termination of growth. As the clusters move through the magnetron chamber, the continuously changed local environment will introduce non-equilibrium dynamics to the cluster growth process, leading to the formation of clusters with metastable structures[100].

As described in Chapter 2, only the positive charged clusters can pass the time-of-flight (TOF) mass filter. These clusters are a subset of the clusters formed in the magnetron sputtering chamber. Before discussing the possible growth process of Ag clusters prepared in the magnetron sputtering chamber, the question of whether the positively charged Ag clusters prepared after the TOF mass filter are representative of all Ag clusters formed in the magnetron sputtering chamber needs to be discussed. All Ag clusters formed in the magnetron sputtering chamber can be deposited directly after the nozzle. The preparation parameters applied to explore the relationship between the Ag clusters deposited after the TOF mass filter and after the nozzle were a power of 10 W, an Ar gas flow rate of 40 sccm, a He gas flow rate of 0 sccm, a condensation length of 250 mm, and a sputtering chamber pressure of 0.075 mbar.

To eliminate the effect of the high cluster density when directly deposited after the nozzle, the deposition time was very short (less than one second) and the areas with low cluster density in the TEM grid were imaged. The mass spectrum obtained after the TOF mass filter is shown in Figure 3.15 (a), and the HAADF-STEM images of Ag clusters with a size range of 1-30k atoms prepared after the TOF mass filter and Ag clusters directly prepared after the nozzle are presented in Figure 3.15 (b) and (c), respectively. The deposited setting parameters of these clusters deposited after TOF mass filter are the mass range of 1 to 30k, deposition step of 100, one second deposition time per step, and a total deposition time of 100 s. After the statistical analysis of about 300 Ag clusters for each sample, the size distributions of the Ag clusters deposited after the TOF mass filter and the nozzle are obtained, as shown in Figure 3.15 (d). The size distributions of the two kinds of Ag clusters are quite similar, except that the peak size of Ag clusters deposited after the TOF mass filter is slightly smaller.

Furthermore, the X-axis of the mass spectrum in Figure 3.15 (a), i.e., the number of atoms was transformed to cluster size in nm by following the relationship between the cluster diameter and the number of atoms of Ag-Ih clusters. The newly plotted figure with the X-axis labeled as cluster size in nm is presented in Figure 3.15 (d), which is in good agreement with the size distribution of Ag clusters deposited after the nozzle. All these results indicate that the Ag clusters deposited after TOF mass filter can represent all Ag clusters formed in the magnetron sputtering chamber, and the investigation of Ag clusters deposited after the TOF mass filter can be helpful to reveal the growth process for all Ag clusters.

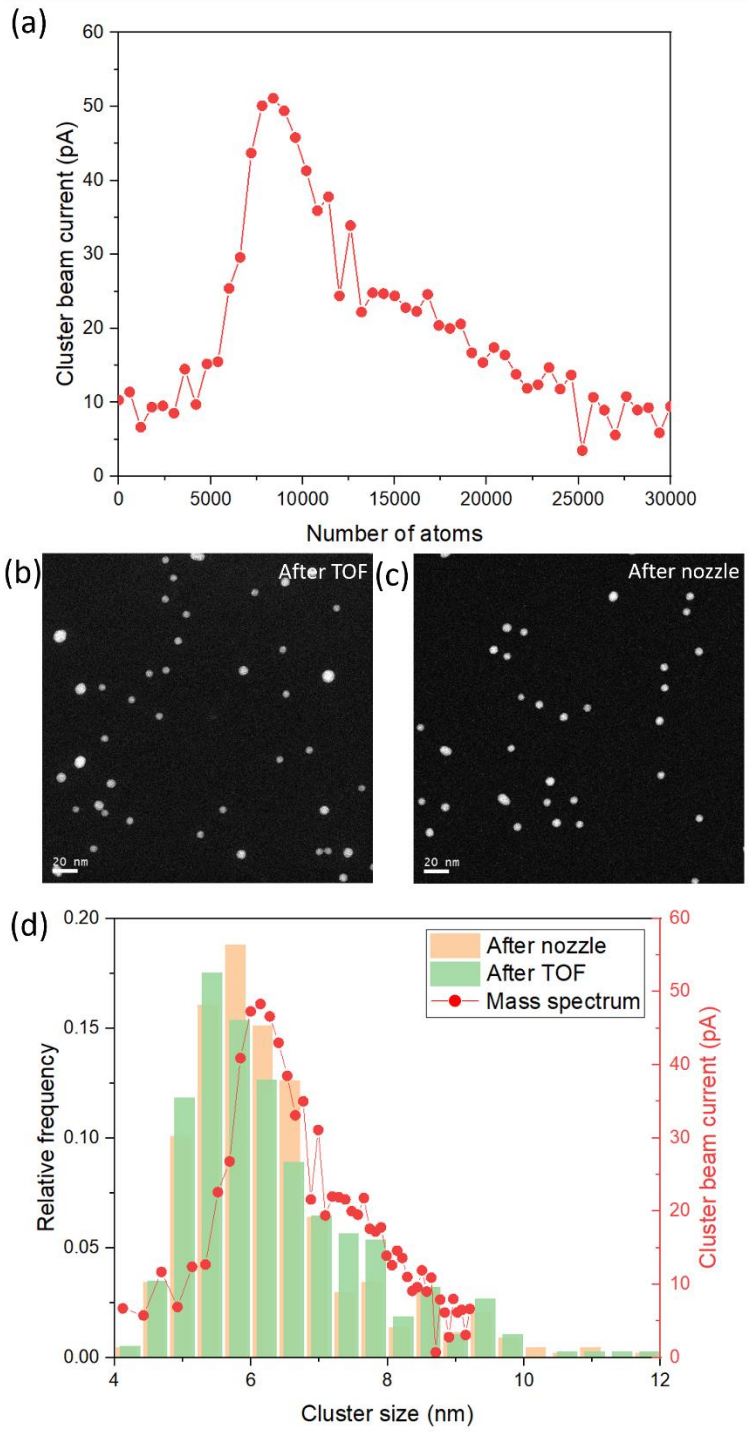


Figure 3.15: (a) The mass spectrum of Ag clusters deposited with the following parameters, i.e., a power of 10 W, an Ar gas flow rate of 40 sccm, a He gas flow rate of 0 sccm, a condensation length of 250 mm, and a sputtering chamber pressure of 0.075 mbar. (b) and (c) The HAADF-STEM images of Ag clusters prepared after the TOF mass filter and the nozzle, respectively. The deposited setting parameters after TOF mass filter are the mass range of 1 to 30k, deposition step of 100, one second deposition time per step, and a total deposition time of 100 s. (d) The size distributions of about 300 Ag clusters prepared after the TOF mass filter and the nozzle, respectively, and the mass spectrum replotted with the X-axis of cluster size in nm based on (a).

According to the simulated works[94,95], the equilibrium states of Ag clusters with increasing size are Ih, Dh, and then FCC. However, in this work, Ag clusters with these three different structures can be found in a wide size range, which is attributed to the unique fast and non-equilibrium growth process of the magnetron sputtering method.

There are two growth paths for clusters in the sputtering chamber, as shown in Figure 3.16. One is called the atom addition growth path, in which the cluster grows up by capturing surrounding single atoms or tiny clusters. This growth path is also called cluster-atom condensation or cluster-atom collisions. In this way, the single atoms or tiny clusters will load on the cluster surface following the initial atom arrangement of the cluster, thus the cluster preferentially keeps the initial structure during the growth process, which is always Ih structure due to its low energy for small clusters. Because of this characteristic, this growth path is also called template growth or frozen growth in other works[101]. The other growth path is cluster-cluster coalescence, and the structure of the product of coalescence may change because the abrupt increase in surface energy after coalescence can induce a structure transition. Many simulation studies have demonstrated that Ih is dominated in the atom-by-atom growth, while the coalescence preferentially produces Dh and FCC[102–105].

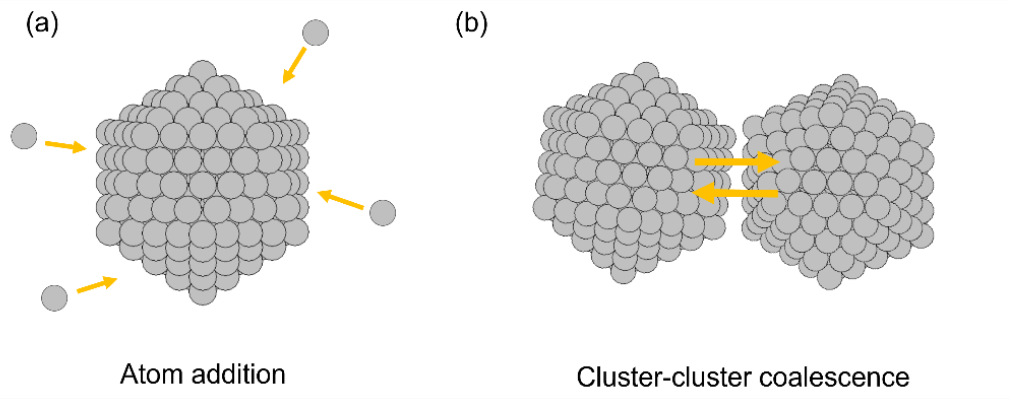


Figure 3.16: Two growth paths for clusters in the sputtering chamber, i.e., (a) atom addition and (b) cluster-cluster coalescence.

The abundance of Ih structures in large clusters is a common phenomenon in inert gas condensation sources[96,106]. There are two possible explanations for this. One is called kinetic trapping effect[107]. In the growth process of clusters, it's easy for Ih-to-Dh transition when the size of the cluster is small. However, the Ih structure is the most stable structure for Ag clusters with small size. Then, when the cluster size increases, the energy barrier for Ih-to-Dh transition also increases. It's difficult to overcome the energy barrier between Ih and Dh structures for large clusters and the clusters will keep growing based on Ih morphology by the atom addition growth mode. With the high velocity of Ag clusters in the magnetron sputtering chamber, like in a quenching process, the clusters will finally maintain their unstable Ih structure and leave the chamber. On the other hand, Baletto et al.[108] conducted molecular-dynamics simulations and found that the subsequent deposition of atoms can induce the transformation from small Dh structure to Ih at low temperature (450 K). The Dh-to-Ih transition takes place at the cluster surface with the nucleation of islands on icosahedral stacking and the creation of a new fivefold symmetry. The new fivefold symmetry will propagate fast to

the center of the cluster and finally result in the formation of Ih. Once a metastable icosahedron is formed, the growth can proceed again shell by shell.

Based on the results described in this chapter, the schematic diagram to describe a possible growth process model is shown in Figure 3.17 (a). The detailed explanation of this schematic diagram is as follows.

- Area A: metal vapor, including single atoms, dimers, trimers, and other tiny clusters sputtered from the surface of the target.
- Line I: at this temperature, the nucleation process starts.
- Area B: after nucleation, these nuclei start growing mainly by atom addition, because the density of single atoms and small particles is very high in this area.
- Line II: the density of single atoms and tiny particles greatly decreases after a large number of cluster-atom condensations.
- Area C: two growth ways, atom addition, and cluster-cluster coalescence, coexist in this area. The product of cluster-cluster coalescence depends on the size of collided clusters and the environment temperature, namely large size difference and high surrounding temperature promote the complete coalescence process.
- Line III: the density of single atoms and tiny clusters almost decreases to zero.
- Area D: the dominant growth path is cluster-cluster coalescence in this area.

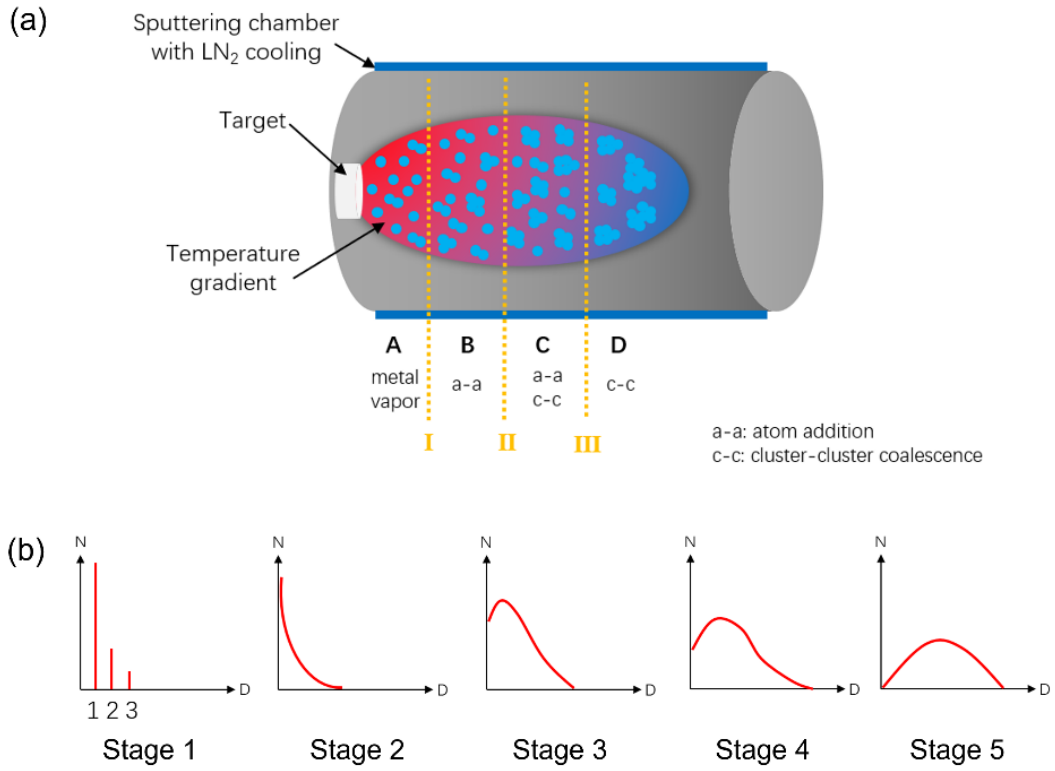


Figure 3.17: (a) A schematic diagram to describe the possible growth process in the sputtering chamber. (b) The relationship between cluster sizes and their numbers corresponds to different areas in the magnetron sputtering chamber. D: the size of clusters; N: the number of clusters.

Based on the growth process model depicted in Figure 3.17 (a), the corresponding evolution of cluster size can be predicted. The results of this prediction are presented in Figure 3.17 (b). In Stage 1, there are large numbers of single atoms, dimers, trimers, and tiny particles[109], which is related to Area A in Figure 3.17 (a). For Stage 2, Ag clusters with small sizes appear by consuming part of single atoms, dimers, trimers, and tiny particles. Then, in Stage 3, the number of single atoms decreases and a size peak is formed. The Stage 2 and 3 exist in Area B. For Stage 4 and 5, related to Area C and D, the peak size gradually moves to the larger size and the number of Ag clusters with peak size keeps decreasing.

Ag clusters with large sizes always show different morphologies, such as Ag8k clusters in Figure 3.8, indicating that the Ag8k clusters were formed in different positions of the magnetron sputtering chamber. These clusters with spherical shapes were formed closer to the target surface than those Ag clusters with elongated shapes due to two reasons. On the one hand, if the cluster was formed mainly by the atom addition growth way, the high density of tiny particles close to the target surface can help the cluster to keep its spherical shape during growth. On the other hand, if the cluster was formed by cluster-cluster coalescence growth way, the higher temperature close to the target surface can promote the aggregation process and achieve the formation of the spherical shape. This means that for clusters with spherical shapes, both growth paths are available. However, the proportions of the Ih structure linearly decrease with the increasing size of spherical clusters, as shown in Figure 3.9 (d), which indicates that more coalescence events happened for clusters with large sizes, so that more Dh and fewer Ih structures are obtained.

Furthermore, the comparison between the structure percentages of the domains shown in Figure 3.12 and those of the spherical clusters shown in Figure 3.9 (d) reveals that the proportions of the Dh structure are lower for the domains than those of the spherical clusters with the same sizes. This can be explained by some of the spherical Ag clusters being formed by cluster-cluster coalescence and then transformed into the Dh structures. In addition, the proportion of Dh structures in all the Ag clusters prepared shows an initial increase followed by a decrease trend in Figure 3.10 (c). This is different from the continuous increase trend observed for the fraction of Dh structures in the spherical

Ag clusters. As the size of the Ag clusters increases, the ideal proportion of Dh structure in all Ag clusters should increase because Dh structure is more stable than Ih, particularly for clusters with larger sizes. However, incomplete aggregation and unsuccessful formation of Dh structure during cluster-cluster coalescence events for large clusters lead to fewer Dh structures but more elongated clusters, resulting in the observed decreasing trend of the proportion of Dh structures in all the Ag clusters.

Regarding the findings presented in Figure 3.13, only the Ih structure will be discussed in this paragraph, as the proportion of Dh structure consistently shows an opposite trend to that of the Ih structure. When the mass spectrum has a higher peak size due to target aging, there will be fewer Ih structures obtained for Ag clusters within the size range under investigation. A higher peak size indicates a greater density of particles in the sputtering chamber, increasing the likelihood of collisions and ultimately resulting in a lower proportion of elongated clusters and more spherical clusters with Dh structure for large Ag clusters.

The results of Figure 3.5 and Figure 3.14 (a) indicate that all Ag clusters exhibit a spherical shape, suggesting complete aggregation during the growth process. However, larger Ag clusters such as Ag8k, Ag10k, and Ag12k experience more collisions to reach their sizes during growth, resulting in a higher proportion of Dh structures after the growth process. Moreover, when comparing the structure fractions of Ag1k and Ag2k clusters shown in Figure 3.13 and Figure 3.14, the Ih fraction is consistently dominant, regardless of changes in the deposition parameters. This is because these small clusters

are formed in Area A and B of Figure 3.17 (a) with the atom-attachment growth path, indicating that modifying the structures of small Ag clusters is not easy by simply adjusting the gas flow rate.

In summary, spherical clusters are more likely to form in Area B, while elongated clusters are more likely to form in Areas C and D. Thus, atom addition growth path is dominant for small spherical clusters, but cluster-cluster coalescence is dominant for elongated clusters. Clusters formed in Area B always exhibit Ih structure. One reason for this is the dominant atom addition growth path in this area. The other reason is that the Ih structure is the most stable structure at high temperatures even for Ag clusters with a size of several thousand atoms[94]. With the high velocity of clusters in magnetron sputtering chamber, the Ih structure can be maintained due to the limited residence time in the area with high temperature.

The growth paths of elongated clusters and their domains are different because these domains were mainly formed in Area B and their growth way mainly was atom addition. When clusters travel through Areas C and D, they collide with each other and form larger aggregated clusters. These aggregated clusters that have not yet fully aggregated into spherical clusters due to the low local temperature and insufficient aggregation time in Areas C and D, finally form elongated (incompletely aggregated) clusters. However, some aggregated clusters with huge size differences on the domains will quickly merge into one spherical cluster. The possibility of structure transition in the aggregated clusters depends on the size of smaller domains. There will be a critical size

of the collided cluster to induce the structure transition for the main clusters with any size. Only clusters with the domains that are difficult to achieve complete aggregation are left after the growth process. This is the reason that many domains with similar sizes dominate in Table 3.2. In addition, only two domains were observed for elongated clusters in the size range of 1k to 14k, indicating that the cluster-cluster coalescence event only happened for once before the formation of these elongated clusters. However, for Ag clusters with larger sizes, like Ag18k clusters, 9 of 74 (about 12%) elongated clusters are formed by three domains, an example of which is as shown in Figure 3.18.

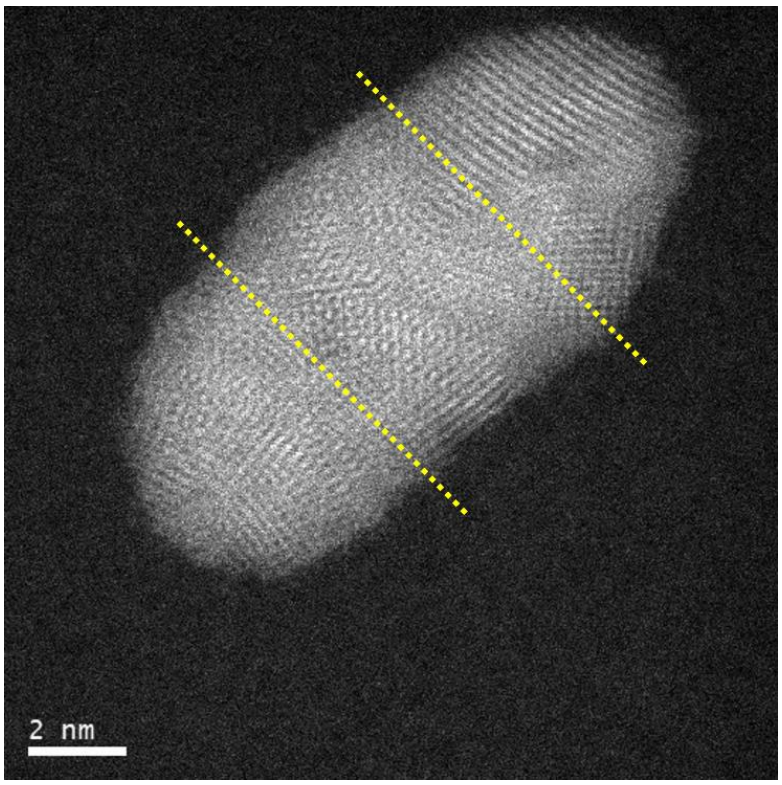


Figure 3.18: Example of an elongated Ag18k cluster formed by three domains. The three domains in this cluster are indicated by the yellow dashed lines.

3.7 Conclusions

In order to investigate the growth process of Ag clusters deposited via magnetron sputtering, size-selected Ag clusters ranging from 1k to 18k were prepared and their atomic structures and morphologies were analyzed using HAADF-STEM images. Several series of Ag cluster with different sizes were analyzed, and the results show that when the size of the Ag clusters is smaller than the peak size of the mass spectrum, nearly all of them exhibit spherical shapes. Conversely, when the size is larger than the peak size, more elongated clusters are observed as the size increases. Therefore, the peak size is considered to be the largest size for which the Ag clusters can maintain a spherical shape.

The atomic structures of Ag clusters depend on their morphologies and sizes. For spherical Ag clusters, there is a linear relationship between their structures and sizes, where the proportion of the Ih structure decreases, while that of the Dh and FCC structure increases as the size increases. Furthermore, the fraction of the Ih structure decreases more rapidly for the spherical Ag clusters deposited with a mass spectrum having a higher peak size. In contrast, for Ag clusters with elongated shapes, the Ih structure dominates the structures of domains in aggregated clusters of various sizes. However, the proportion of the Ih structure in the domains is higher than that of spherical Ag clusters of the same size.

A possible model of the growth process is proposed for Ag clusters in the magnetron sputtering chamber. Most spherical clusters are formed in the region close to the target,

so there will be a high fraction of Ih structures for spherical clusters because the Ih structure is the most stable structure for clusters with small sizes and the atom-addition growth path can help these clusters keep their initial Ih structure during growth. In contrast, most elongated clusters are formed in areas away from the target by cluster-cluster coalescence. Some of these aggregated clusters undergo complete aggregation and transition to spherical shapes, while others remain elongated even after leaving the magnetron chamber.

Chapter 4 Exploration of the Equilibrium State of Ag Clusters in the Size Range of 1k to 14k by Electron Beam Irradiation and Chip-heating Experiments

4.1 Introduction

As described in the last chapter, the Ih structure is the most common one for Ag clusters in the size range of 1k to 14k, which seems to be the most stable structure for Ag clusters. However, in the simulation research of Wang et al., Ag clusters with truncated Dh structure have the lowest energy for $3000 < N < 30000$[110]. On the other hand, from the results of Baletto et al. [95], Dh are the best structures for Ag clusters in the interval $300 < N < 20000$. The conflict between the experimental and simulation results[94,111,112] leads to the experimental exploration of the equilibrium state of Ag clusters. In this chapter, electron-beam (e-beam) irradiation and chip-heating were applied to explore the most stable structure for Ag clusters in the size range of 1k to 14k.

4.2 Structure transformation of Ag clusters under e-beam irradiation

To confirm the most stable structure of Ag clusters by experiments, Ag clusters with sizes of 1k, 2k, 6525, 8k, and 12k were selected to be exposed under electron beam irradiation for an extended time to see the structure transition. Ag6525 is selected as a detailed example to show the typical transformation processes, as shown in Figure 4.1.

HAADF-STEM images were captured continuously every ten seconds with a dose of 8.55×10^4 e^-/angstrom^2/frame during observation, and the structure transition process is presented along the timeline. Structures of Ag6525 clusters were confirmed by comparing the morphology and FFT images with the relevant simulated data. The observed Ag6525 cluster depicted in Figure 4.1 shows an Ih structure initially and then enters an Ih-to-Dh transition regime after 418 s. The obvious characteristic of Ag clusters in the Ih-to-Dh transition state is the coexistence of a five-fold structure and some characteristics of the Ih structure, such as the cluster shown in Figure 4.1 (d1). The lattice fringe marked with blue arrows is the remnant of the Ih structure, indicating that the structural transformation to Dh has not yet been completed. When the transformation is complete, a perfect five-fold Dh structure will be obtained, as shown in Figure 4.1 (e1) after e-beam irradiation for 906 s. The Dh structures remained to the end of observation.

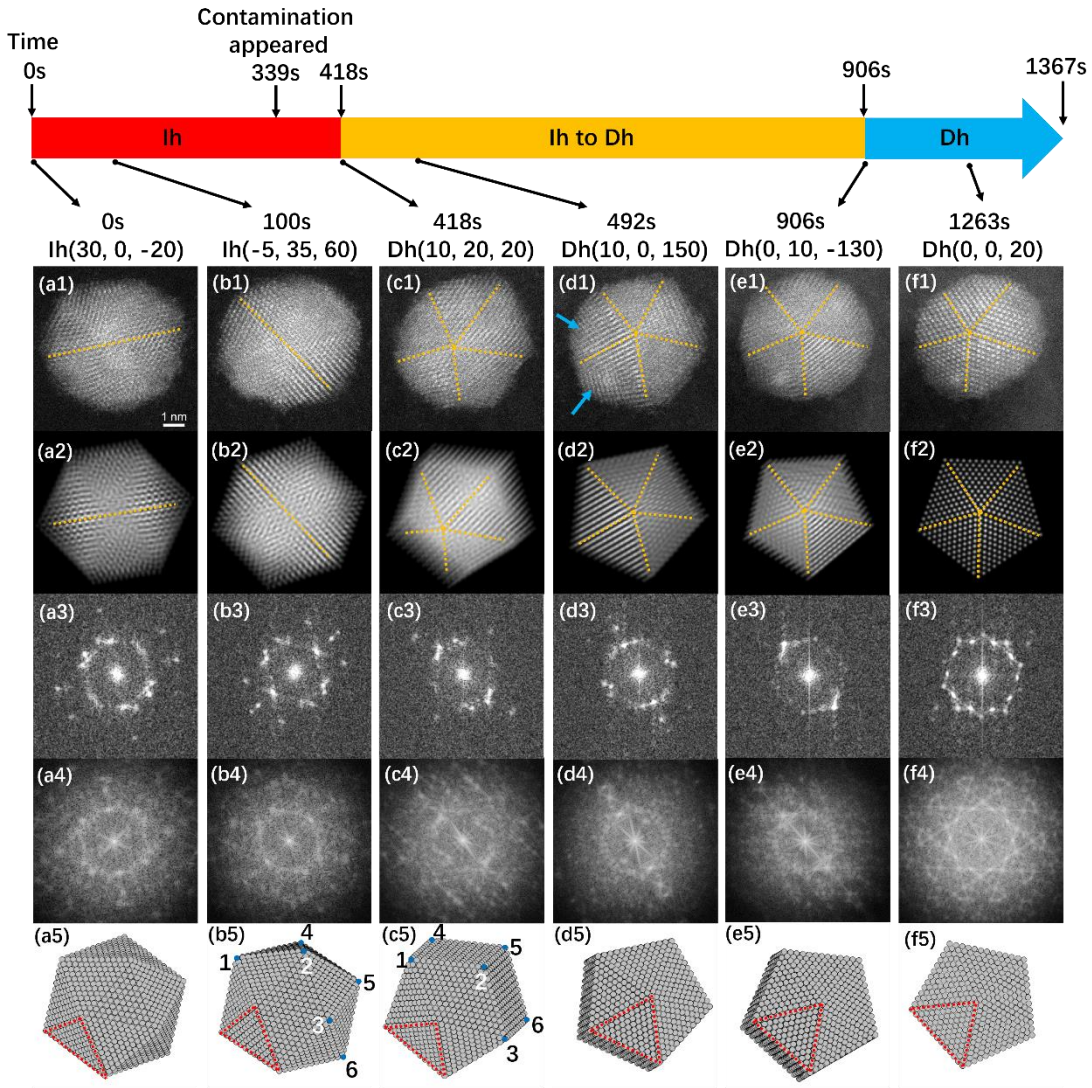


Figure 4.1: Structure transformation process with time under electron irradiation with a dose of 8.55 × 10^4 e^-/angstrom^2/frame. The colored timeline shows the structure at every time point. Images (a1)-(f1) are HAADF-STEM images recorded at different time points. (a2)-(f2), (a3)-(f3), (a4)-(f4), and (a5)-(f5) are the corresponding simulated HAADF-STEM images, experimental FFT images, simulated FFT images and structure models of images in (a1)-(f1), respectively. Yellow dotted lines in (a1)-(f1) and (a2)-(f2) are used to show typical distinguishing features of different structures, which are two-fold geometry for the Ih structure and five-fold geometry for the Dh structure. Blue arrows in (d1) indicate the remnant characteristic of the Ih structure. Red triangles in (a5)-(f5) show the same facet when the cluster was rotating under e-beam irradiation. Blue balls in (b5) and (c5) show the same vertices before and after structure transformation.

Baletto et al. claimed that the Ih-to-Dh transition would go through a melting process of the cluster and a formation of the Dh structure from the melted cluster[108], which is obviously not the case here. A cooperative slip-dislocation mechanism proposed for the Ih-to-Dh transition of the Au cluster was also indicated by Koga et al., which is considered to have a much lower energy barrier when compared with diffusion and rearrangement of all atoms[106]. The same mechanism is also pointed out in the research of Tal et al in the morphology transitions during the growth of Cu nanoclusters[113]. In this work, a similar Ih-to-Dh transition process was observed. As shown in Figure 4.1 (b5) and (c5), blue balls show the same vertices before and after the Ih-to-Dh transition. It is apparent that these two triangular (111) facets Δ124 and Δ245 merge into one square (100) facet □1254 after the Ih-to-Dh transition. It is the same case for Δ235 and Δ356 in Figure 4.1 (b5). In this way, the Ih structure can transform into the Dh structure by twisting only about 36° between two pentagonal bipyramids with a common fivefold axis.

Contamination, a phenomenon caused by the electron beam cracking residual hydrocarbons in the vacuum and forming a layer on the surface of the sample, appeared in the cluster shown in Figure 4.1 under electron irradiation after 339 s. To avoid the influence of contamination on the intensity analysis of the cluster, another cluster was applied to obtain the relationship between integrated intensity and time under e-beam irradiation. The structure timeline in Figure 4.2 indicates that this cluster struggled in the transition of Ih to Dh for about 913 s and then finally transformed to Dh. The result in Figure 4.3 shows that integrated intensity will decrease after about 4-minute e-beam

irradiation because beam-induced atomic displacement will result in enhanced surface diffusion and even cause intensity decrease due to the sputtering of atoms from the surface. This provides a suggestion that it is better to finish imaging Ag6525 clusters within 4 minutes to avoid the damage from the electron beam.

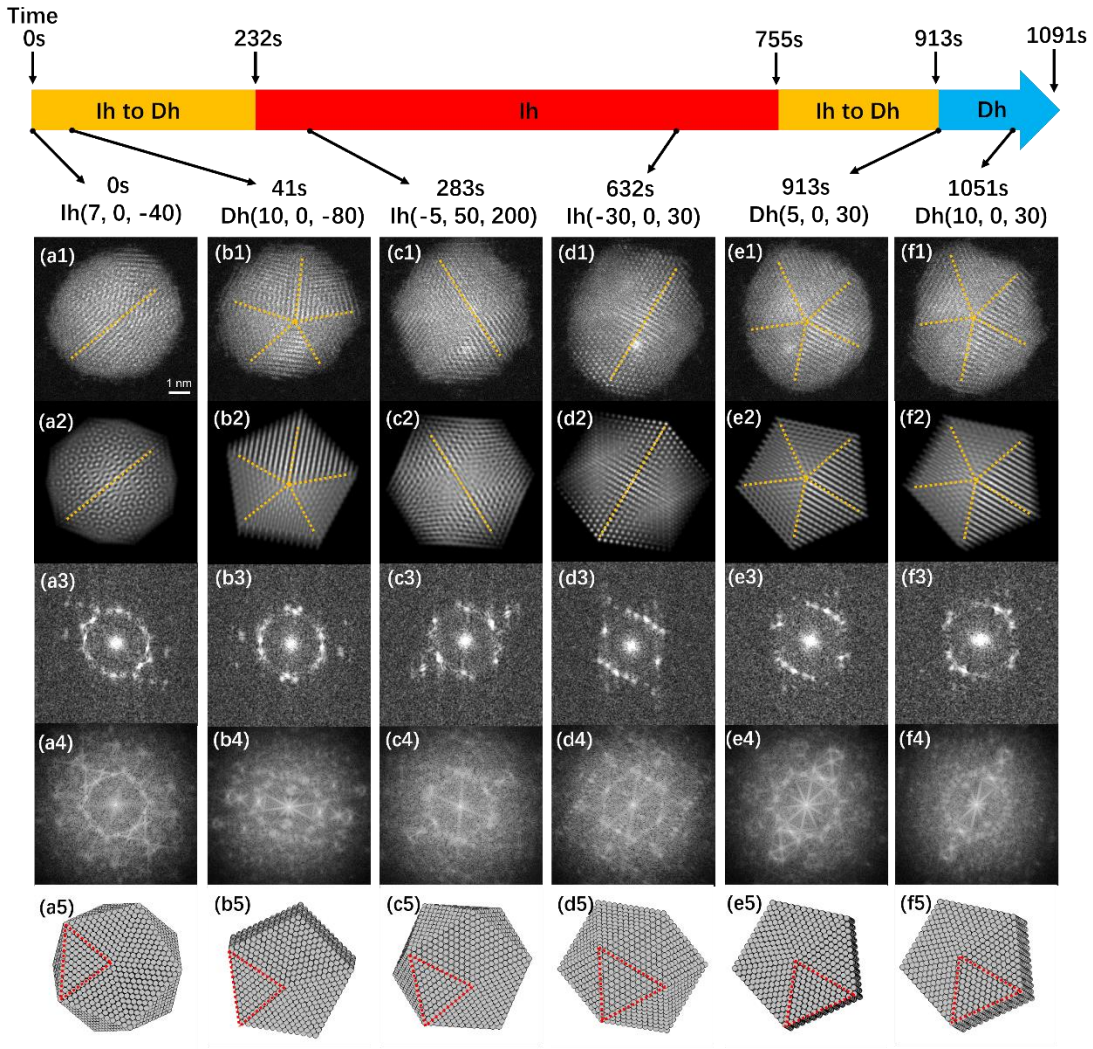


Figure 4.2: Structure transformation process with time under electron irradiation with a dose of 8.55 × 10^4 e^-/angstrom^2/frame. The colored timeline shows the structure at every time point. Images of (a1)-(f1) are HAADF-STEM images recorded at different time points. (a2)-(f2), (a3)-(f3), (a4)-(f4), and (a5)-(f5) are the corresponding simulated HAADF-STEM images, FFT images, simulated FFT images and structure models of images in (a1)-(f1), respectively. Yellow lines in (a1)-(f1) and (a2)-(f2) are used to show typical distinguishing features of different structures, which are two-fold geometry for the Ih structure and five-fold geometry for the Dh structure. Red triangles in (a5)-(f5) show the same facet when the cluster was rotating under electron irradiation.

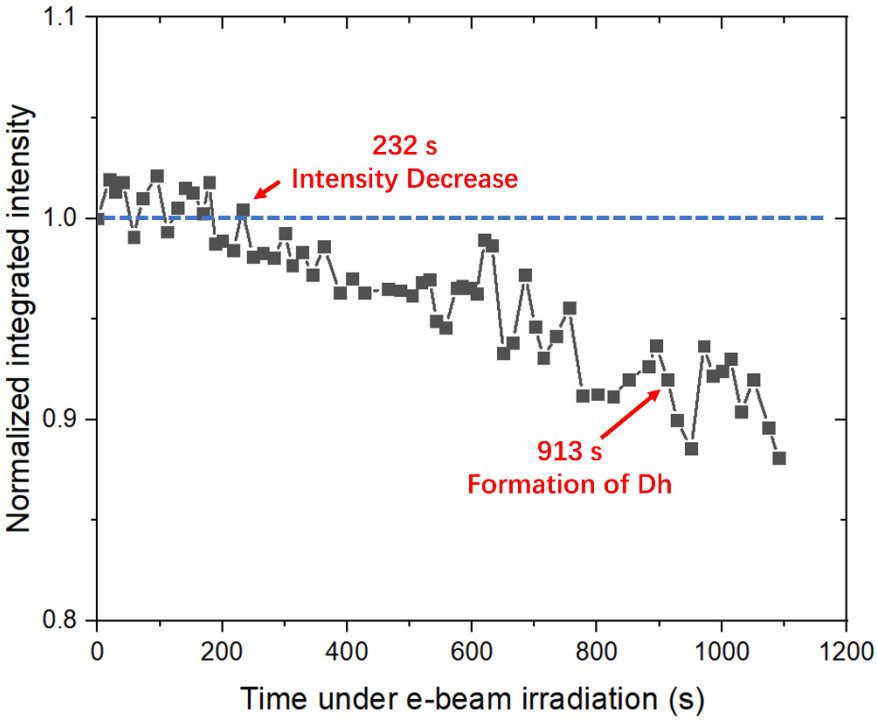


Figure 4.3: The relationship between normalized integrated intensity and time under e-beam irradiation for the cluster investigated in Figure 4.2. The blue dotted line is guide to the eye.

The e-beam irradiation will provide energy to the clusters and help to overcome the energy barrier between structures. If the Ih structure is not the most stable structure for Ag6525, then the Ih structure will transform into other structures under e-beam. The results show that a Ih-to-Dh transition occurs and the Dh structure could exist stably when clusters were exposed to electron irradiation, which indicates that Dh is the most stable structure for Ag6525.

Similar experiments have also been done for Ag clusters with other sizes. Figure 4.4 presents the structure transition process of an Ag1k-Ih cluster under e-beam irradiation with a dose of 8.55×10^4 e^-/angstrom^2/frame. After about 160 s, the cluster transformed to Dh. Furthermore, an Ag1k-Dh cluster was selected to conduct the e-beam irradiation experiment. The Dh structure was always observed during the whole period, as shown in Figure 4.5. Combining the results of Ag1k-Ih and Ag1k-Dh clusters, the Dh structure is considered the most stable structure for the Ag cluster with the size of 1k. There are always many single atoms observed around the cluster both in Figure 4.4 and Figure 4.5, indicating that the Ag1k clusters are very easy to be damaged under the applied e-beam dose.

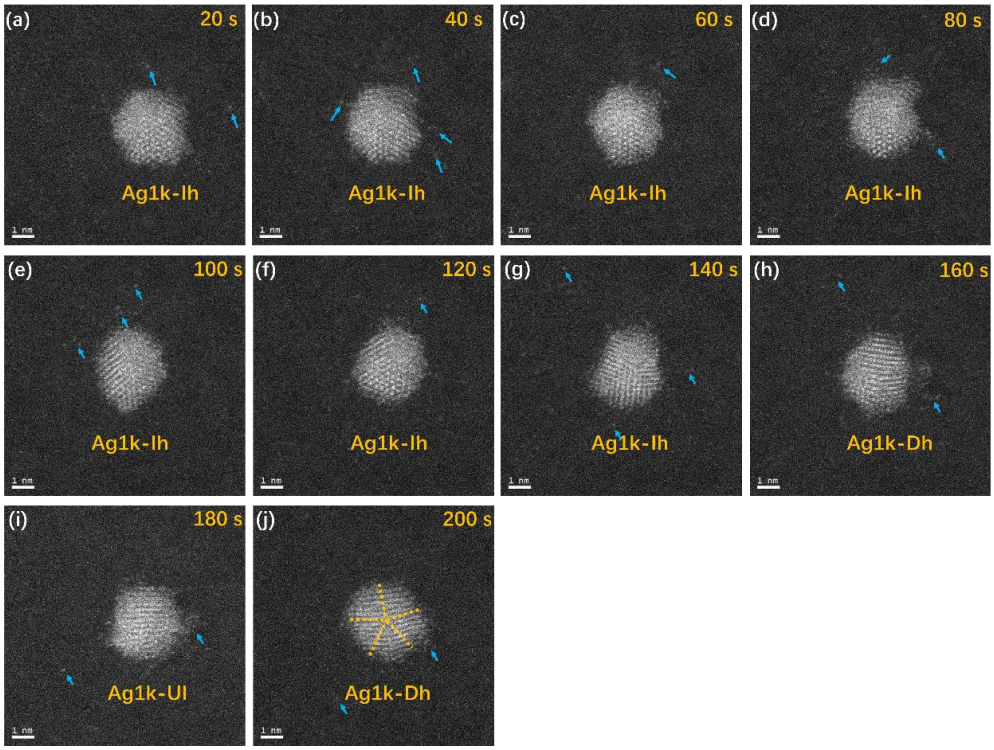


Figure 4.4: HAADF-STEM images of a Ag1k cluster with initial Ih structure recorded at different time points under e-beam irradiation with a dose of 8.55×10^4 e^-/angstrom^2/frame. Some of the single atoms around the cluster are indicated by blue arrows. However, please note that the number of arrows does not necessarily correspond to the actual number of single atoms present.

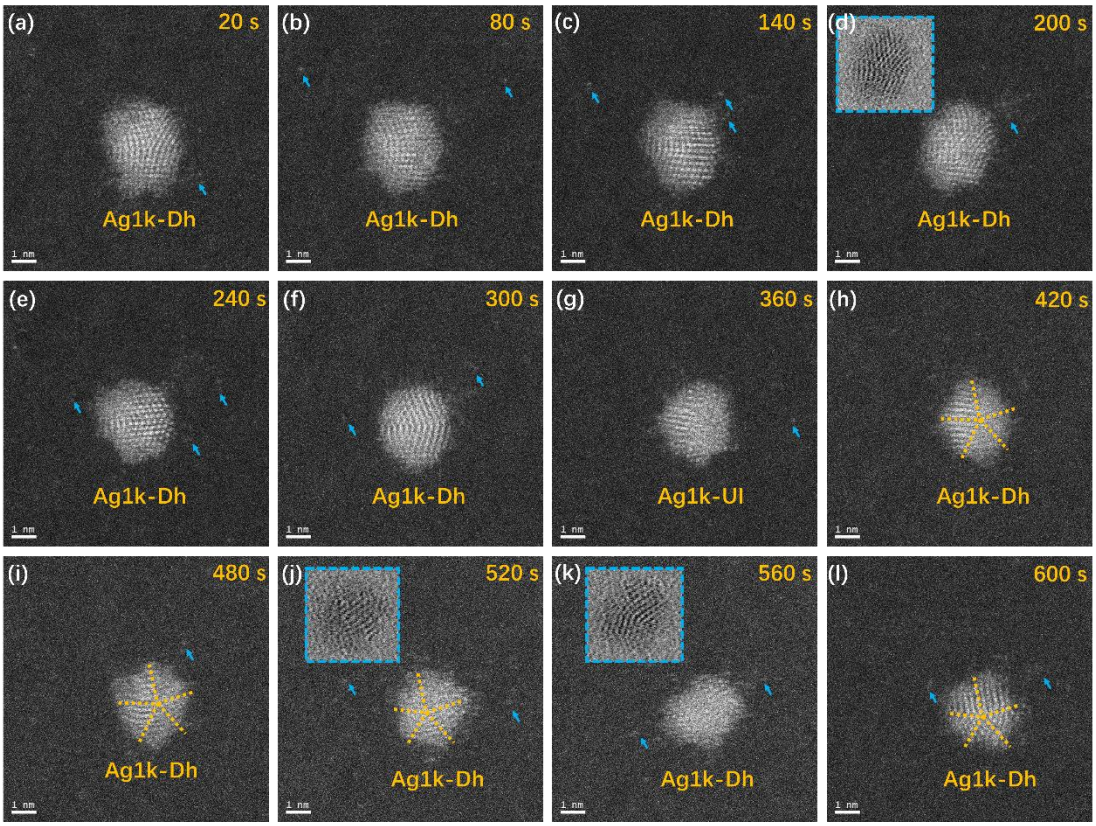


Figure 4.5: HAADF-STEM images of a Ag1k cluster with initial Dh structure recorded at different time points under e-beam irradiation with a dose of 8.55×10^4 e^-/angstrom^2/frame. The inserted images are bright-field (BF) images to show clear atomic structures. Some of the single atoms around the cluster are indicated by blue arrows. However, please note that the number of arrows does not necessarily correspond to the actual number of single atoms present.

For Ag2k clusters, the Ih-to-Dh transformation process was also observed as shown in Figure 4.6. The cluster with Ih structure started transforming after the e-beam irradiation for 360 s, and finally became a cluster with the Dh structure, confirming that the Dh structure is also the equilibrium state for Ag2k clusters.

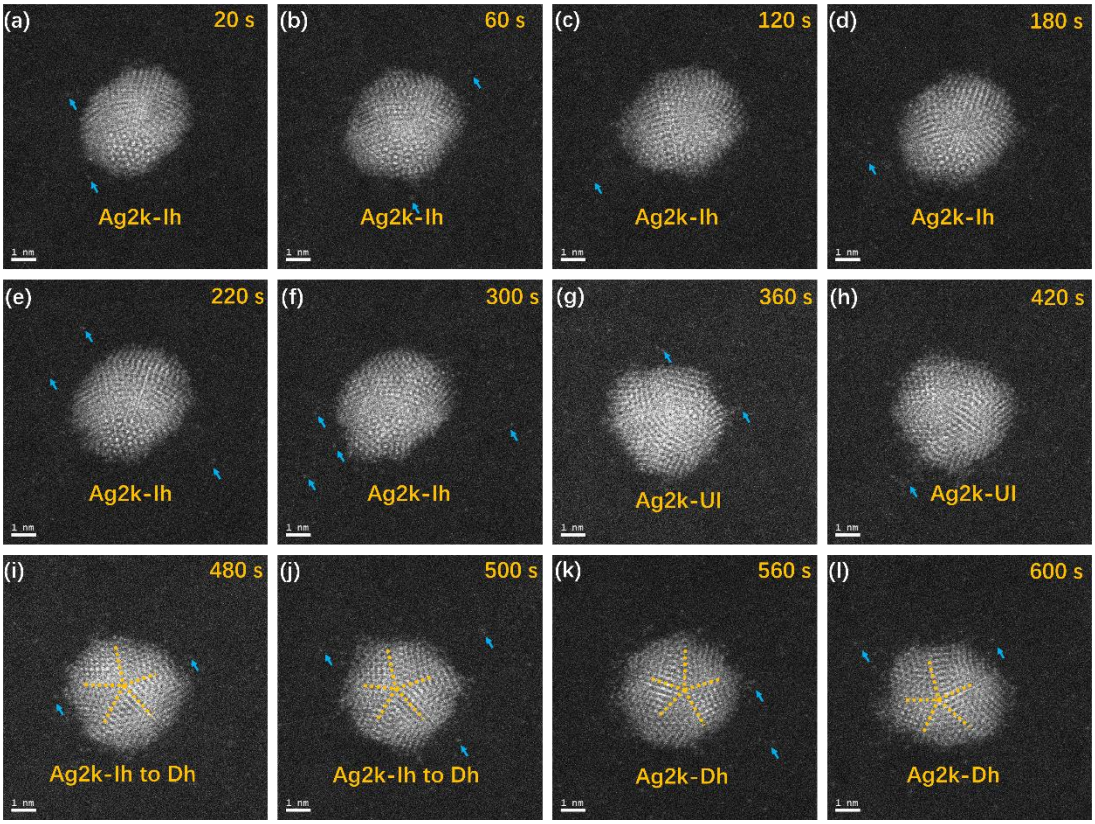


Figure 4.6: HAADF-STEM images of a Ag2k cluster with initial Ih structure recorded at different time points under e-beam irradiation with a dose of 8.55×10^4 e^-/angstrom^2/frame. Some of the single atoms around the cluster are indicated by blue arrows. However, please note that the number of arrows does not necessarily correspond to the actual number of single atoms present.

However, a Ag8k-Ih cluster kept its Ih structure to the end of the 10-minute e-beam irradiation, shown in Figure 4.7. Although the most stable structure of Ag8k clusters cannot be confirmed with the e-beam irradiation experiment, the Ih-to-Dh transition state appeared during observation, as shown in Figure 4.7 (d). Another Ag8k-Dh cluster was exposed to the e-beam irradiation with the same dose, it kept its Dh structure after 10 minutes.

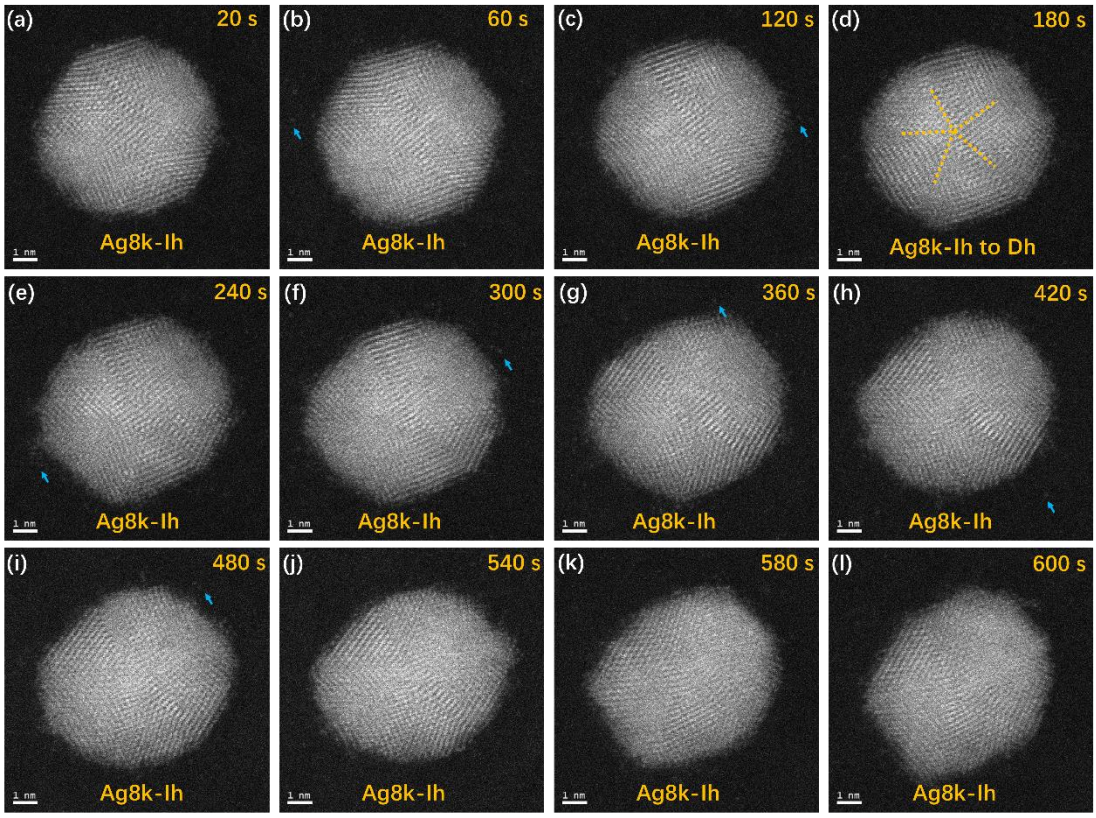


Figure 4.7: HAADF-STEM images of a Ag8k cluster with initial Ih structure recorded at different time points under e-beam irradiation with a dose of 8.55×10^4 e^-/angstrom^2/frame. Some of the single atoms around the cluster are indicated by blue arrows. However, please note that the number of arrows does not necessarily correspond to the actual number of single atoms present.

For the cluster size of 12k, two Ag12k clusters were studied under the e-beam irradiation. The first cluster is shown in Figure 4.8, starting with the Ih-to-Dh transition state, and finishing with a perfect five-fold Dh structure. The second was a Ag12k-Ih cluster observed at a lower magnification, presented in Figure 4.9. It transformed to the Ih-to-Dh transition state after 10-minute e-beam irradiation. Although the Ih-to-Dh transition state was found in these two experiments, the complete Ih-to-Dh transformation process hasn't been observed. The larger clusters and thus lower dose per atom in the cluster might indicate that a longer irradiation period might have been required for a full transition.

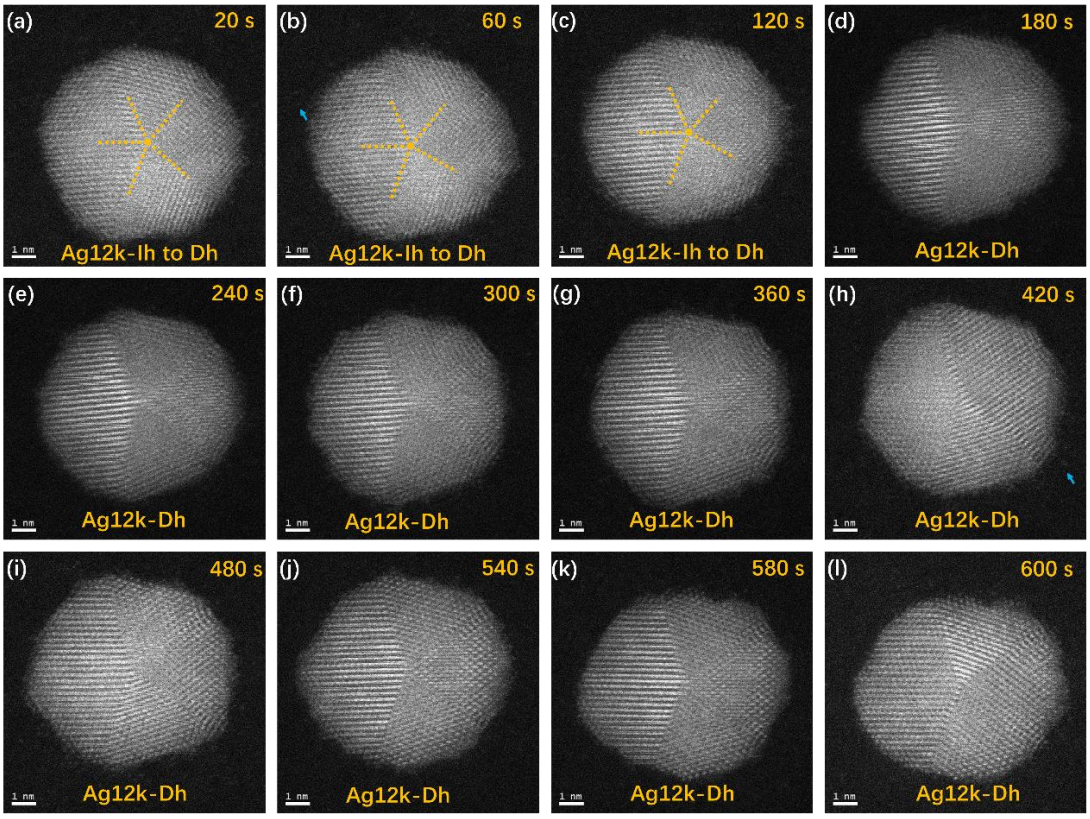


Figure 4.8: HAADF-STEM images of a Ag12k cluster with initial Ih-to-Dh structure recorded at different time points under e-beam irradiation with a dose of 8.55×10^4 e^-/angstrom^2/frame. Some of the single atoms around the cluster are indicated by blue arrows. However, please note that the number of arrows does not necessarily correspond to the actual number of single atoms present.

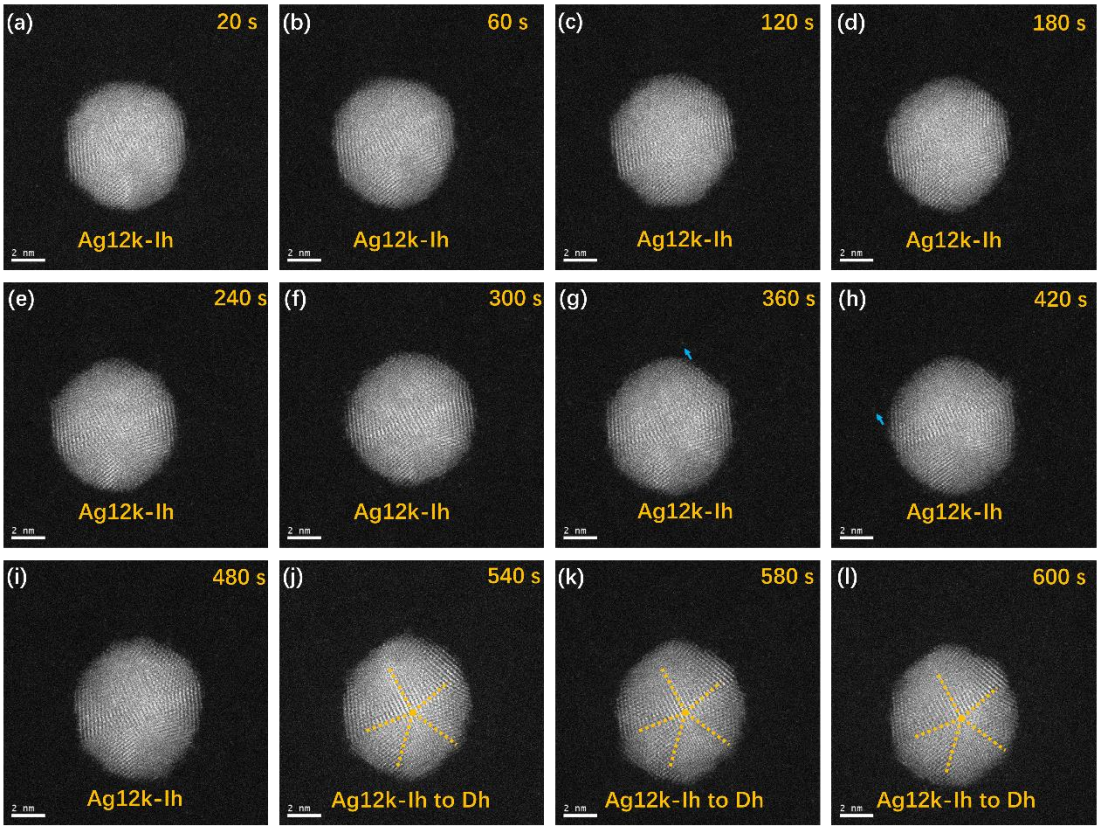


Figure 4.9: HAADF-STEM images of a Ag12k cluster with initial Ih structure recorded at different time points under e-beam irradiation with a dose of 3.8×10^4 e^-/angstrom^2/frame. Some of the single atoms around the cluster are indicated by blue arrows. However, please note that the number of arrows does not necessarily correspond to the actual number of single atoms present.

The damage of e-beam irradiation on Ag1k, 2k, 8k, and 12k can be compared according to the change of integrated intensity during observation, because the same dose was applied in the observation of Figure 4.5, 4.6, 4.7, and 4.8. The normalized integrated intensity was used to reveal the mass change of Ag clusters, and the results are shown in Figure 4.10. For Ag1k clusters, the normalized integrated intensity greatly decreases during e-beam irradiation. However, for Ag2k, Ag8k, and Ag12k clusters, the normalized integrated intensities only slightly decrease to around 0.9 after 10-minute e-beam irradiation. Under e-beam irradiation, the atom arrangement of the Ag clusters will fluctuate due to the influence of electron beam. For the same dose, the larger size

the cluster is, the lower electron beam on every atom in the cluster will be. So, the atoms in Ag1k clusters are much easier to be sputtered and many single atoms could be observed around the clusters during e-beam irradiation. On the other hand, the energy barrier for Ih-to-Dh structure transition is also lower for small clusters, leading to the observation of Ih-to-Dh transition for Ag1k and Ag2k clusters in this work. The similar trends of Ag2k, Ag8k, and Ag12k clusters on the normalized integrated intensity in Figure 4.10 are caused by the balance between the decreasing dose per atom and the increasing surface area exposed to the surrounding environment. Also, the higher energy barrier for Ih-to-Dh structure transition for large clusters makes it difficult to observe the complete transition process for Ag8k and Ag12k clusters.

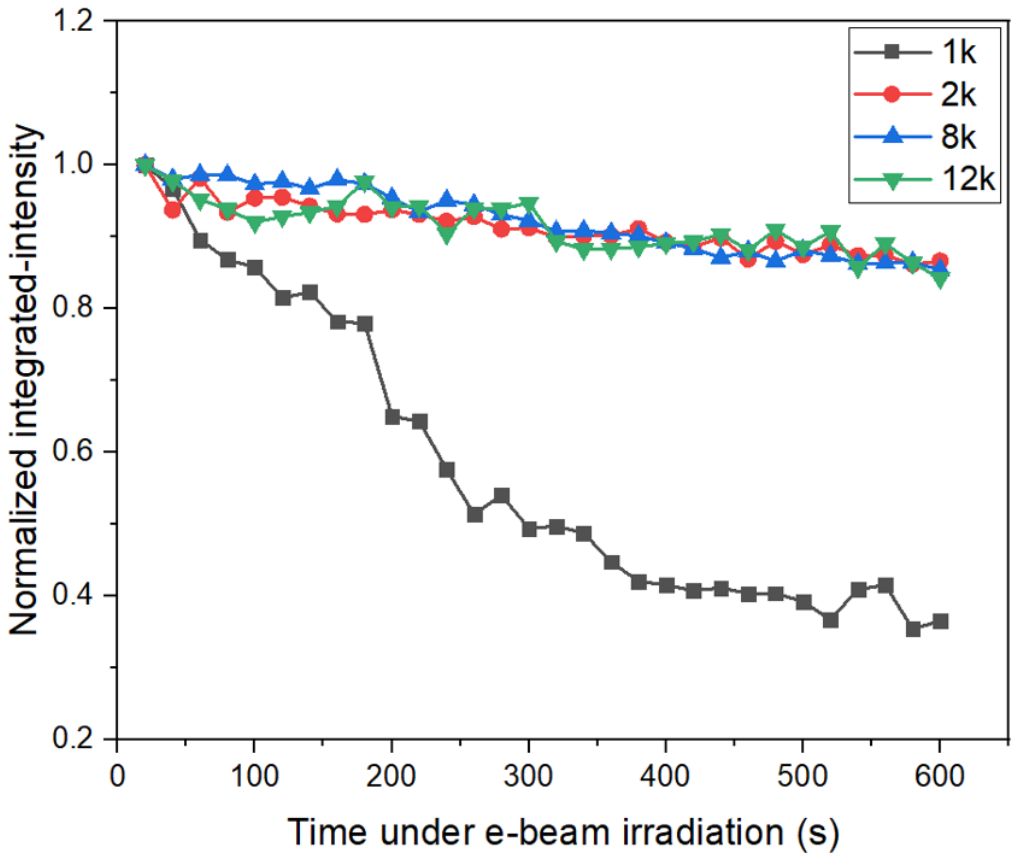


Figure 4.10: The effect of e-beam irradiation on the integrated intensity of Ag clusters with different sizes.

In summary, the equilibrium state for Ag1k, Ag2k, and Ag6525 clusters can be confirmed by e-beam irradiation experiments as the Dh structure. For Ag8k and Ag12k clusters, the results are more ambiguous. The reason for this may be the energy from the e-beam is not enough to help the Ag clusters with large sizes overcome the Ih-to-Dh transformation energy barrier. So, chip-heating experiments were conducted to explore the most stable structure for these large Ag clusters, whose details can be found in the next part.

4.3 Heating experiments of Ag8k clusters

4.3.1 Spherical Ag8k clusters heated to different temperatures

The simulated melting point of Ag8k is about 1000 K, namely 727 °C, according to the simulations by Doye and Calvo[94]. Thus, for the heating experiments, a temperature range from 20 to 800 °C was chosen. Cyclical temperature increase was applied because it is more flexible, especially when 113 clusters need to be imaged for every temperature step. Heating for a long time may induce mass loss, especially at high temperatures, so a dwell time of 1 min was applied for every temperature step. The e-beam was blanked during heating. The heating program is shown in Figure 4.11.

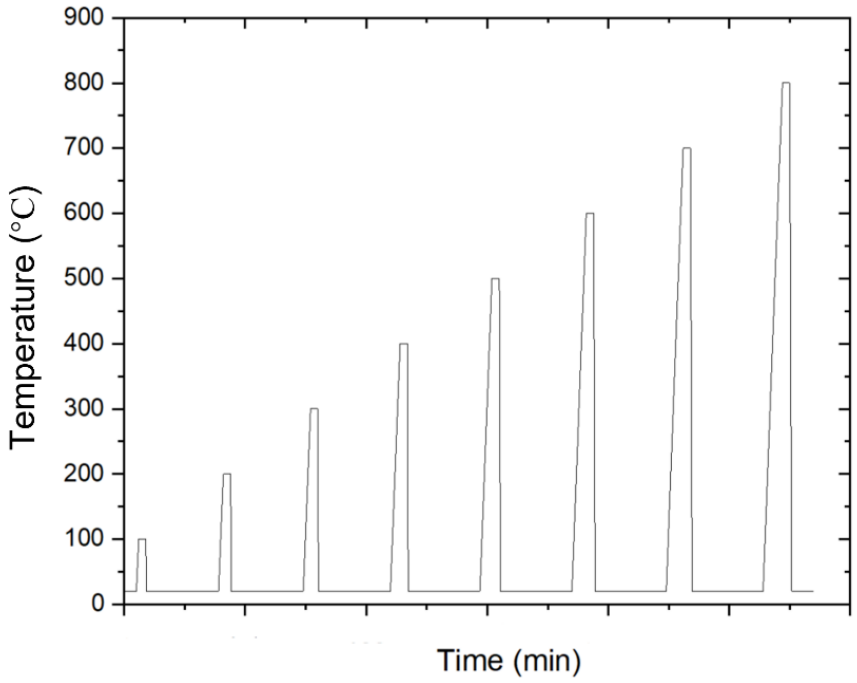


Figure 4.11: The schematic drawing of the heating program. Temperature range: from 20 °C to 800 °C; Cyclical increase of the temperature; 1 min for every temperature step; Heating rate: 1000 °C/min; Cooling rate: 2000 °C/min.

To confirm the effect of the e-beam on the Ag8k clusters, an e-beam irradiation experiment was conducted, and the results are shown in Figure 4.12. After 10-min e-beam irradiation, the integrated intensity of Ag8k decreased after about 260 s with the magnification of 10M and 180 s with the magnification of 15M. So, if the total imaging time is less than 260 s with the imaging magnification of 10M, the mass loss of Ag8k clusters caused by the e-beam can be minimized.

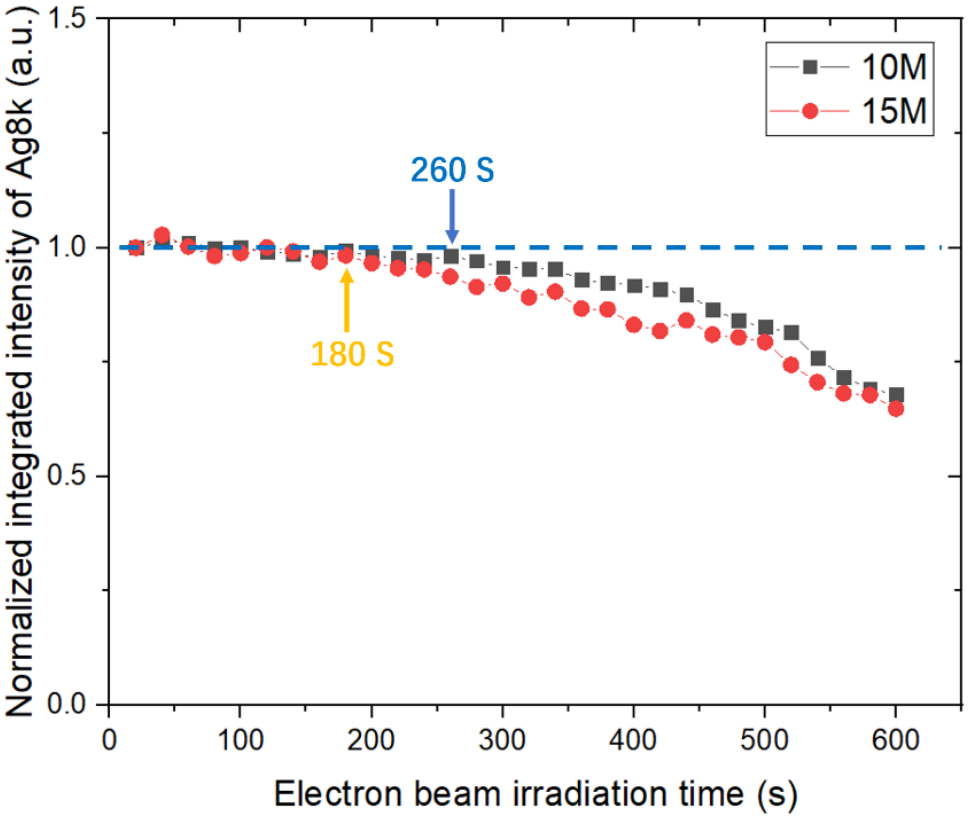


Figure 4.12: The relationship between the normalized integrated intensity of Ag8k clusters and the e-beam irradiation time when the magnification of the image was 10M and 15M, respectively. The blue dashed line serves as a guide for the normalized intensity of 1. After 10-min e-beam irradiation, the integrated intensity of Ag8k obviously decreased after about 260 s with the magnification of 10M and 180 s with the magnification of 15M.

The overview HAADF-STEM images of observed Ag8k clusters at different temperatures are shown in Figure 4.13. No obvious difference can be found when the heating temperature was lower than 700 °C. There was a great mass loss for Ag8k clusters after heating at 700 °C, which is close to the theoretical melting point of Ag8k clusters. When the heating temperature increased to 800 °C, no Ag8k clusters were left compared to the initial image, as shown in Figure 4.14.

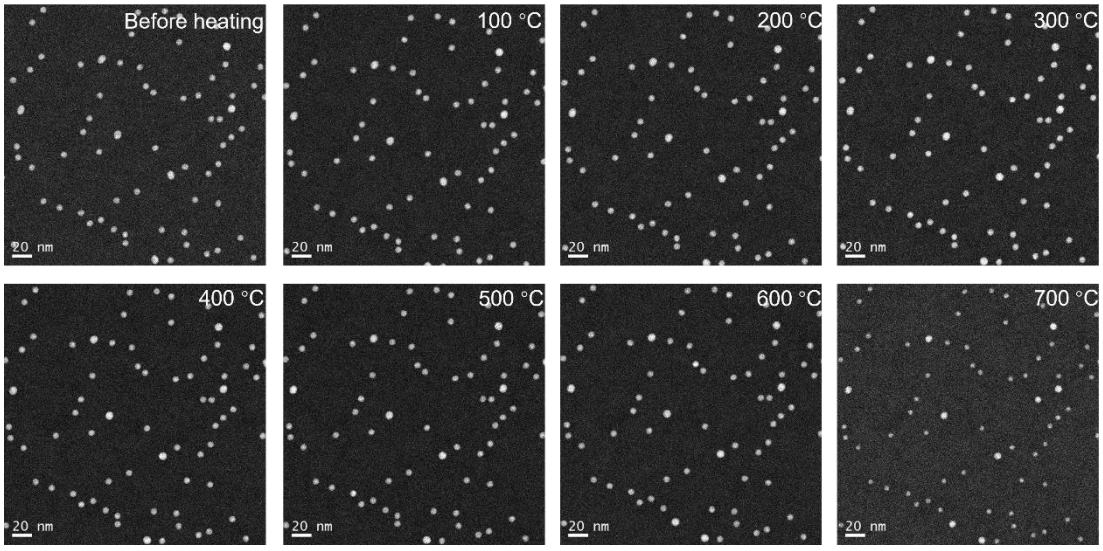


Figure 4.13: Overview HAADF-STEM images at different heating temperatures.

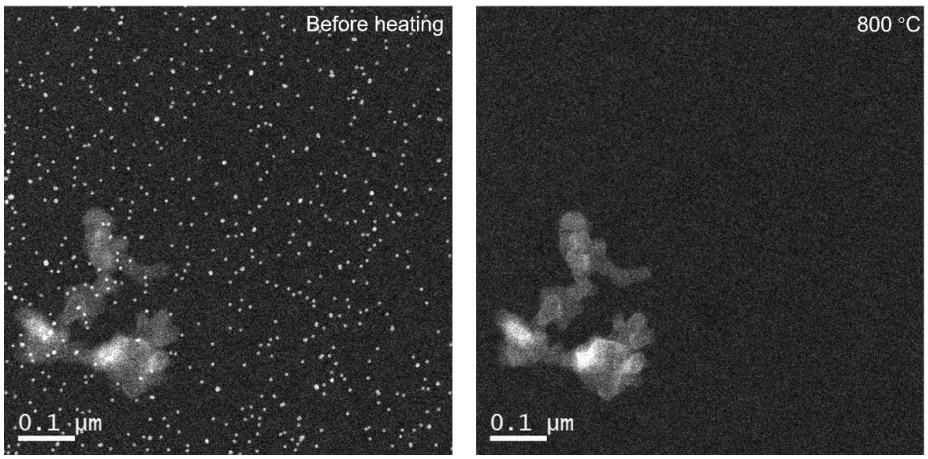


Figure 4.14: Comparison between HAADF-STEM images of 20 °C and 800 °C. The large pattern at the left corner is the defect of the heating chip.

The average integrated intensity of Ag8k clusters after different heating temperatures, shown in Figure 4.15, clearly reveals the size evolution of Ag8k clusters. In the temperature range of 20-500 °C, the average intensity of Ag8k clusters did not change too much, indicating that there was no mass loss under these heating temperatures. The intensity decreased slightly when the heating temperature is 600 °C, and sharply decreased when heating at 700 °C. As for heating at 800 °C, no Ag8k clusters were left. This means that the mass loss of Ag8k clusters started when the heating temperature was higher than 500 °C. The mass loss of Ag clusters is caused by sublimation, i.e., the Ag atoms directly go to the surrounding environment without the melting process, which can be further confirmed from the following HAADF-STEM images with high magnification.

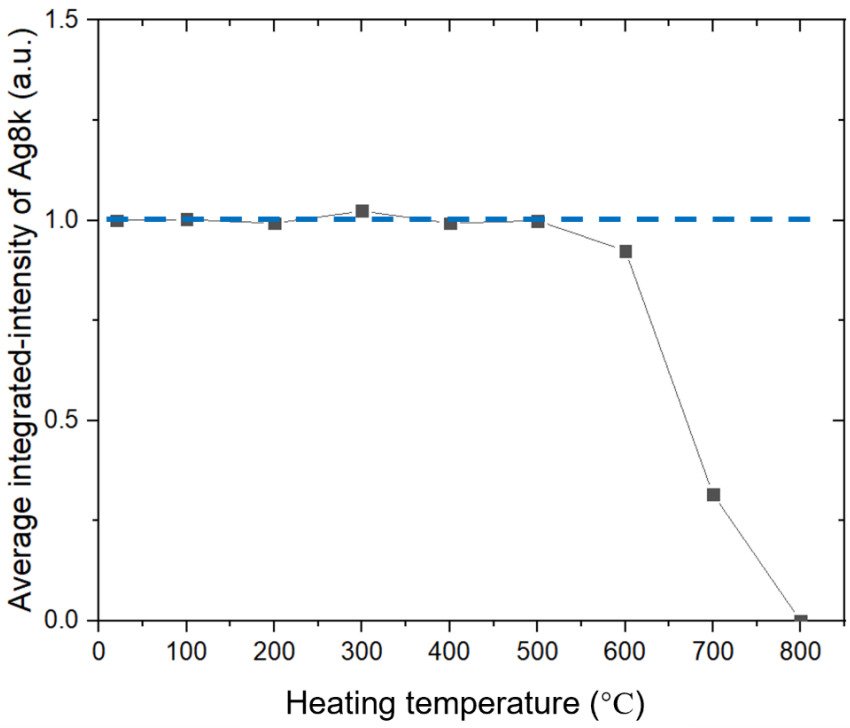


Figure 4.15: Average integrated intensity of 96 Ag8k clusters after heating to different temperatures. The blue dashed line serves as a guide for the normalized intensity of 1.

All observed Ag8k clusters after heating to the different temperatures were analyzed and their structure proportions are shown in Figure 4.16. For Ag8k clusters heating at 100 to 600 °C, the structure percentage of Ih decreases but that of Dh increases, the proportion of FCC structure does not change too much, and Ag8k clusters with UI structure increase because the rearrangement of atoms makes some structures cannot be identified after heating. After heating to 700 °C, the Dh structure is dominant.

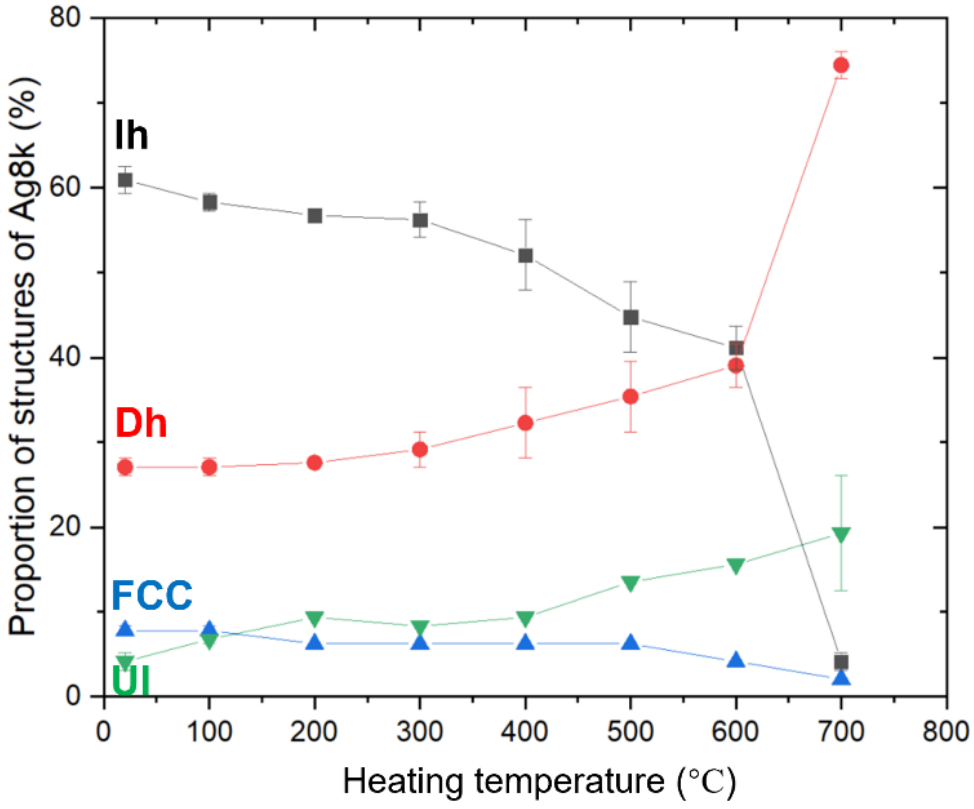


Figure 4.16: The relationship between the proportions of structures for Ag8k clusters and the different heating temperatures. The error bars represent the uncertainties associated with the identification of the structure.

The details of the structural transition during heating are shown in Table 4.1 and Figure 4.17. No structure transition event of Dh and FCC structures was observed after heating in the range of 100 to 600 °C. The Ih-to-Dh transitions of 16 clusters with initial Ih structure were observed after heating at 600 °C. The specific numbers of Ih-to-Dh transition events after heating at different temperatures are shown in Figure 4.17. These Ih-to-Dh transition events mainly happened at 300-600 °C, causing the large error bar for the fraction of Ih and Dh structures in Figure 4.16. All results of Figure 4.16, Table 4.1, and Figure 4.17 indicate that the Dh structure is the most stable structure for Ag8k clusters.

Table 4.1: The number of Ag8k clusters with different structures after heating at 600 °C.

Cluster number before heating	Structures after heating at 600 °C			
	Ih	Dh	FCC	UI
Ih: 57	38	16	/	3
Dh: 26	/	23	/	3
FCC: 6	/	/	3	3
UI: 3	/	/	/	3

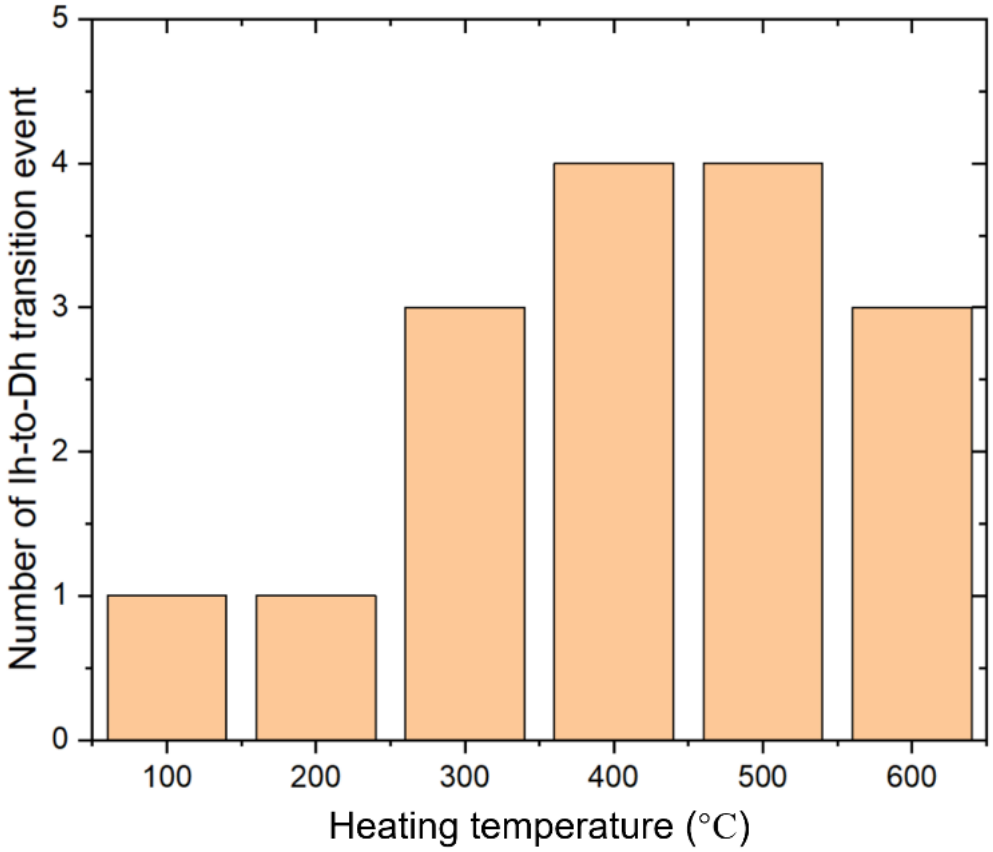


Figure 4.17: The number of Ih-to-Dh transition events after heating at different temperatures for Ag8k clusters.

Examples of Ag8k clusters with different structures during heating are shown in the following part. 38 of 57 Ag8k clusters kept their initial Ih structure after heating in the range of 100-600 °C. One typical example of such Ag8k clusters is presented in Figure 4.18.

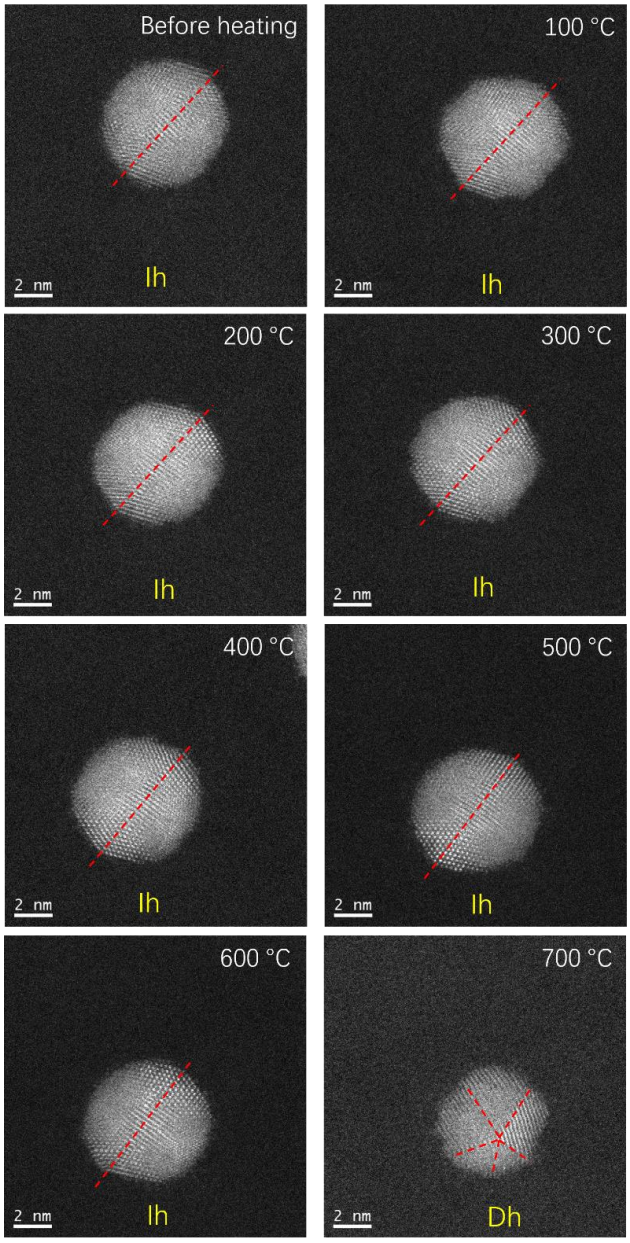


Figure 4.18: One example of a Ag8k cluster with initial Ih structure but no change in the temperature range of 20-600 °C. It transformed to a Dh structure after heating at 700 °C with substantial mass loss. Red dotted lines are used to show typical distinguishing features of different structures, which are two-fold geometry for the Ih structure and five-fold geometry for the Dh structure.

One example of a gradual Ih-to-Dh transition is shown in Figure 4.19. After heating at 200 °C, the central axis of Ih was distorted. Then, a new five-fold structure was formed after heating at 300 °C. After heating in the range of 400-600 °C, in order to balance the inside strain and reduce the overall energy of the cluster, the angles between axes (especially for α and β) were trying to go to 72°, which is the standard angle for a Dh structure. In addition, three truncations indicated with yellow arrows were formed to further reduce the total energy of the Dh structure. This transition process was also observed by Barnard[114].

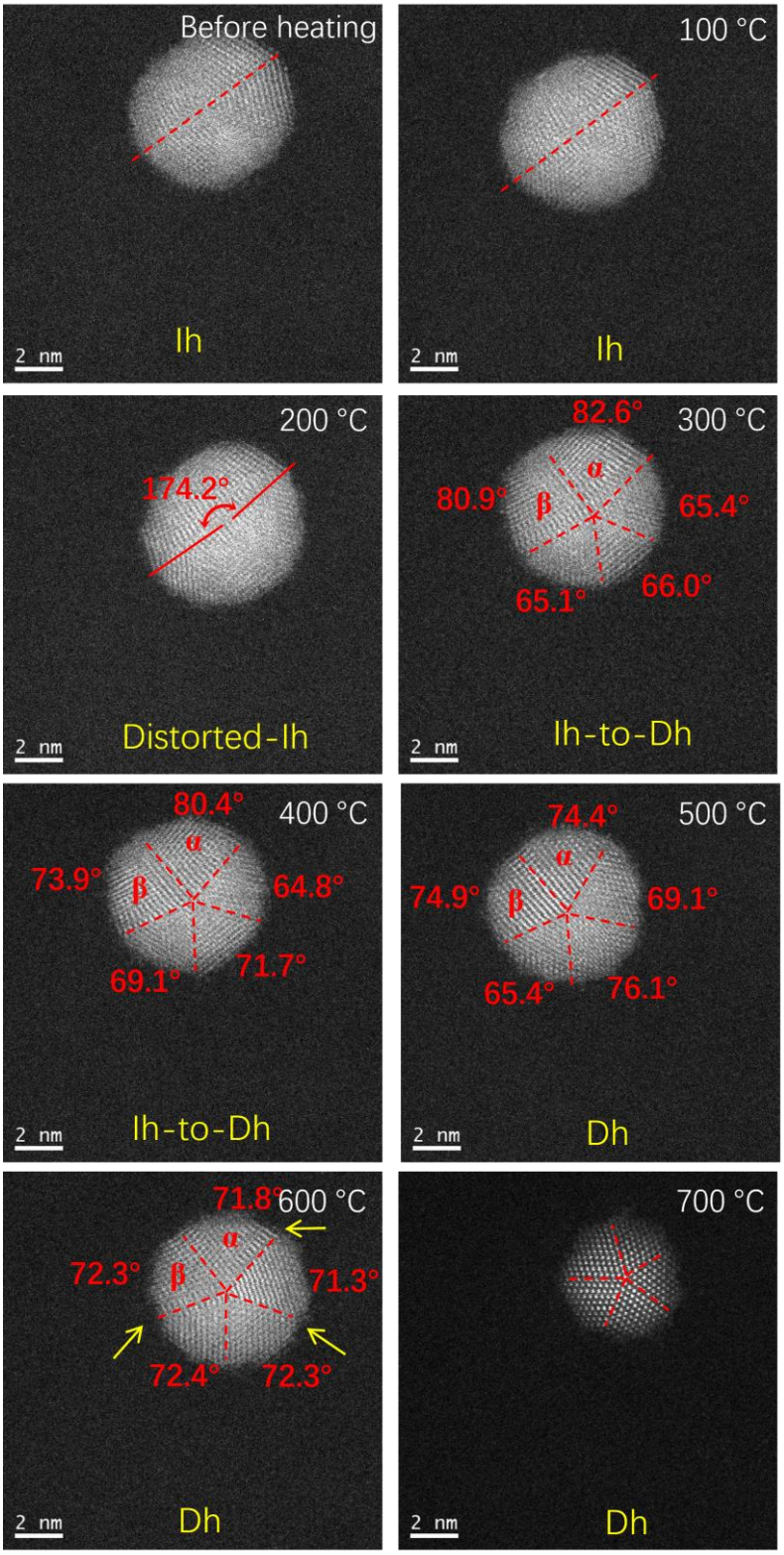


Figure 4.19: One example of a Ag8k cluster with an initial Ih structure but gradually transformed to a Dh structure in the temperature range of 20-600 °C. It transformed to a standard Dh structure after heating at 700 °C with substantial mass loss. Three truncations are indicated by yellow arrows. Red dotted lines are used to show typical distinguishing features of different structures, which are two-fold geometry for the Ih structure and five-fold geometry for the Dh structure.

Another example of a sudden Ih-to-Dh transition is shown in Figure 4.20. No obvious structure change was observed after heating in the range of 100-500 °C. However, the Dh structure suddenly formed after heating at 600 °C.

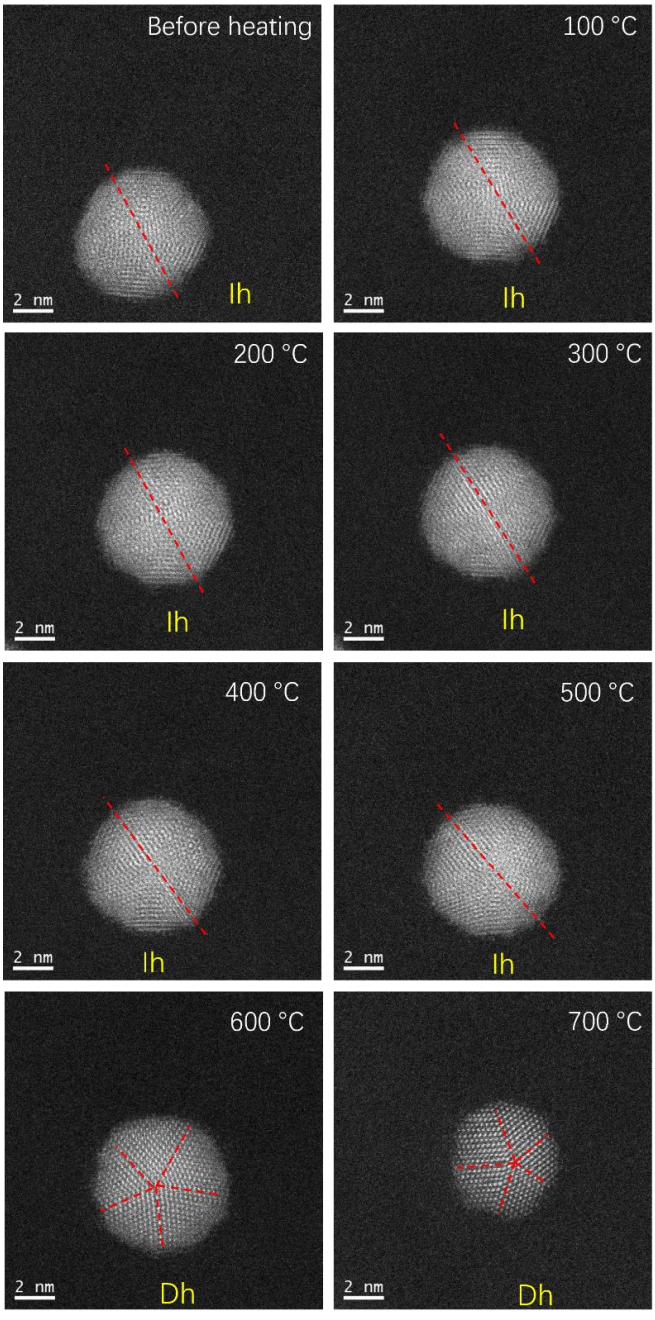


Figure 4.20: One example of a Ag8k cluster with initial Ih structure but suddenly transformed to Dh structure after heating at 600 °C. After heating at 700 °C, the cluster size decreased due to substantial mass loss. Red dotted lines are used to show typical distinguishing features of different structures, which are two-fold geometry for the Ih structure and five-fold geometry for the Dh structure.

22 of 25 Ag8k clusters kept the initial Dh structure after heating in the range of 100-600 °C. The remaining 3 clusters were grouped as UI after heating at 600 °C because the orientation of the clusters did not allow their structures to be identified. One representative example of a Ag8k cluster with an initial and final Dh structure is presented in Figure 4.21.

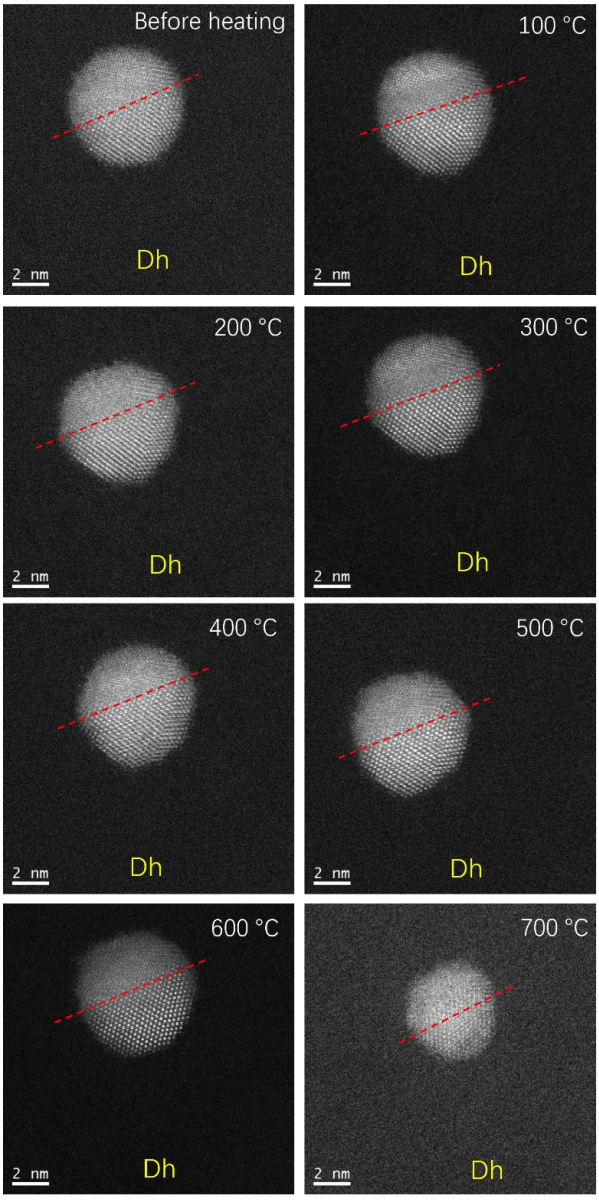


Figure 4.21: One Ag8k cluster with initial Dh structure but no change in the temperature range of 20-600 °C. After heating at 700 °C, the cluster size decreased due to substantial mass loss. Red dotted lines are used to show typical distinguishing features of the Dh structure.

4 of 7 Ag8k clusters kept the initial FCC structure after heating in the range of 100-600 °C. The other 3 clusters were grouped as UI after heating at 600 °C. One typical example of Ag8k clusters with an initial and final FCC structure is presented in Figure 4.22.

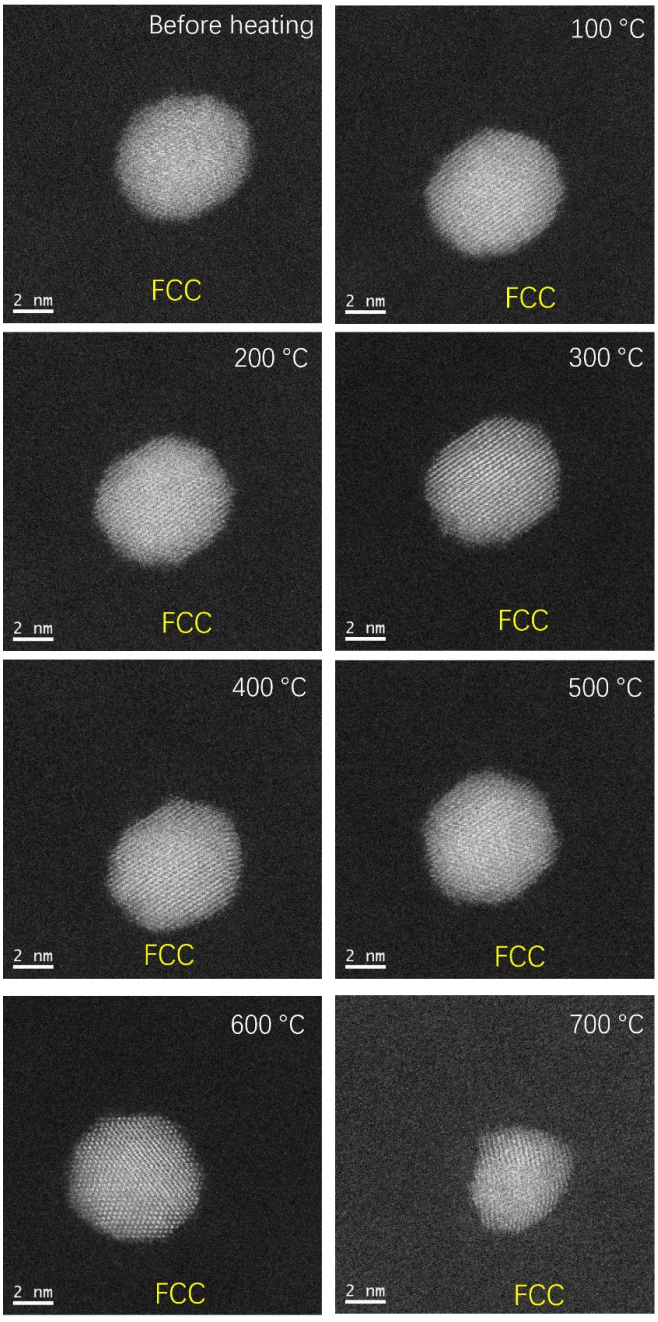


Figure 4.22: One example of a Ag8k cluster with initial FCC structure but no change in the temperature range of 20-600 °C. After heating at 700 °C, the cluster size decreased due to substantial mass loss.

Apart from the single Ag8k clusters, some Ag16k clusters with two aggregated Ag8k clusters were also observed during heating. In Figure 4.23, two Ag8k domains with Ih structures aggregated incompletely before heating and finally formed a distorted Dh structure after heating at 600 °C. The five-fold structure of the final Dh structure is still off the center axis.

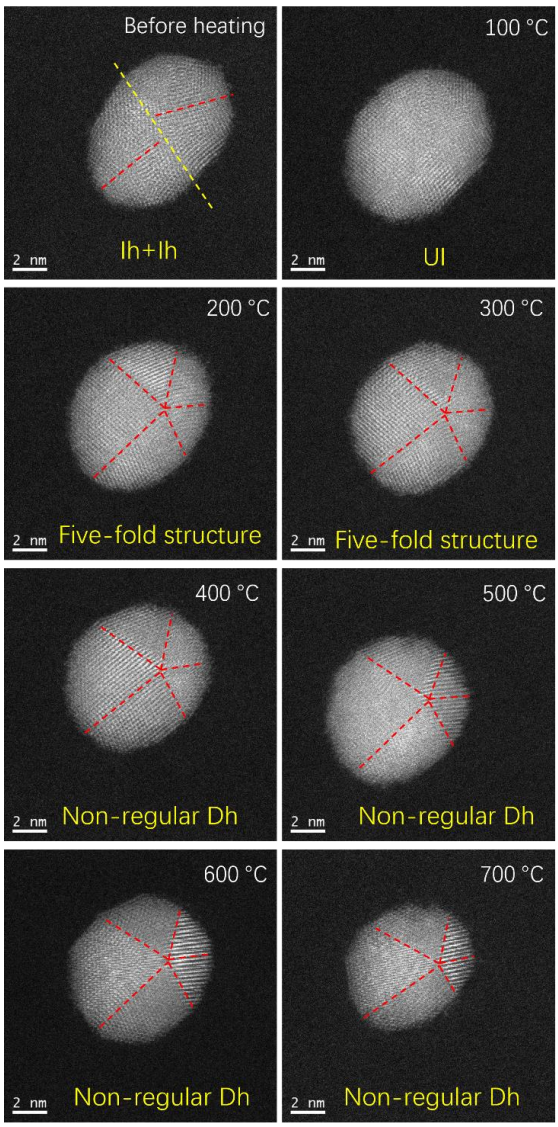


Figure 4.23: The aggregation process of two Ag8k domains with Ih structures in the temperature range of 20-600 °C. After heating at 700 °C, the cluster size decreased due to substantial mass loss. Red dotted lines are used to show typical distinguishing features of different structures, which are two-fold geometry for the Ih structure and five-fold geometry for the Dh structure. The yellow dotted lines are used to distinguish the domains in the elongated clusters.

In Figure 4.24, two Ag8k domains with Ih and Dh structures aggregated incompletely before heating and finally formed a Dh structure after heating at 600 °C. The aggregation process can be divided into two parts when taking the central axis of Dh as the boundary. The final Dh structure was formed by the atom rearrangement within these two parts.

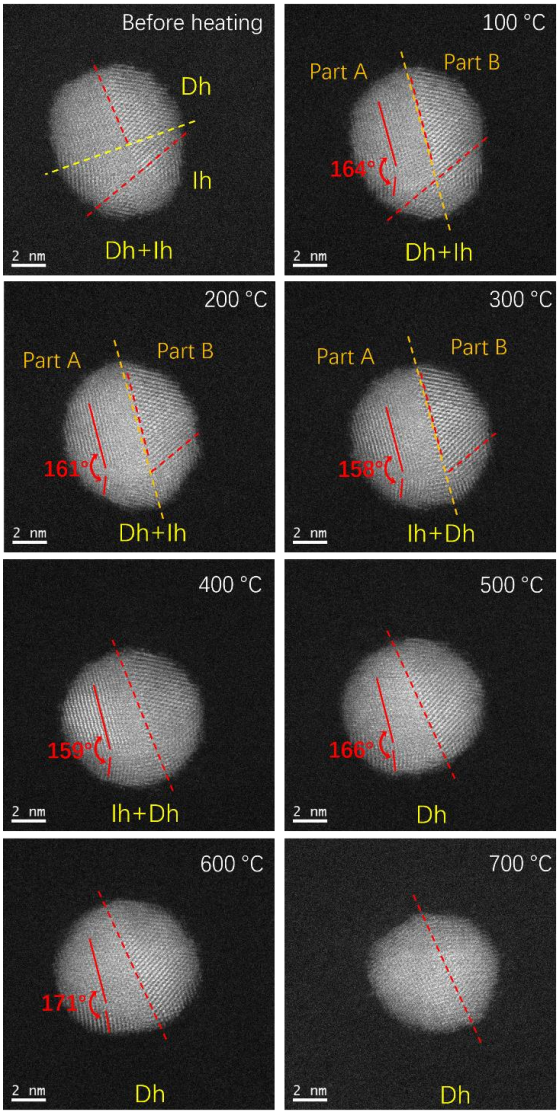


Figure 4.24: The aggregation process of two Ag8k clusters with Ih and Dh structures in the temperature range of 20-600 °C. After heating at 700 °C, the cluster size decreased due to substantial mass loss. Red dotted lines are used to show typical distinguishing features of different structures, which are two-fold geometry for the Ih structure and five-fold geometry for the Dh structure. The yellow dotted lines are used to distinguish the domains in the elongated clusters.

Another aggregation pathway is shown in Figure 4.25. Two Ag8k clusters with Ih and Dh structures aggregated incompletely before heating and finally formed a Dh structure after heating at 600 °C. During the aggregation process, a five-fold structure was first formed after heating at 200 °C based on the initial five-fold structure of the Dh domain and a Dh structure was finally formed by following atom rearrangement.

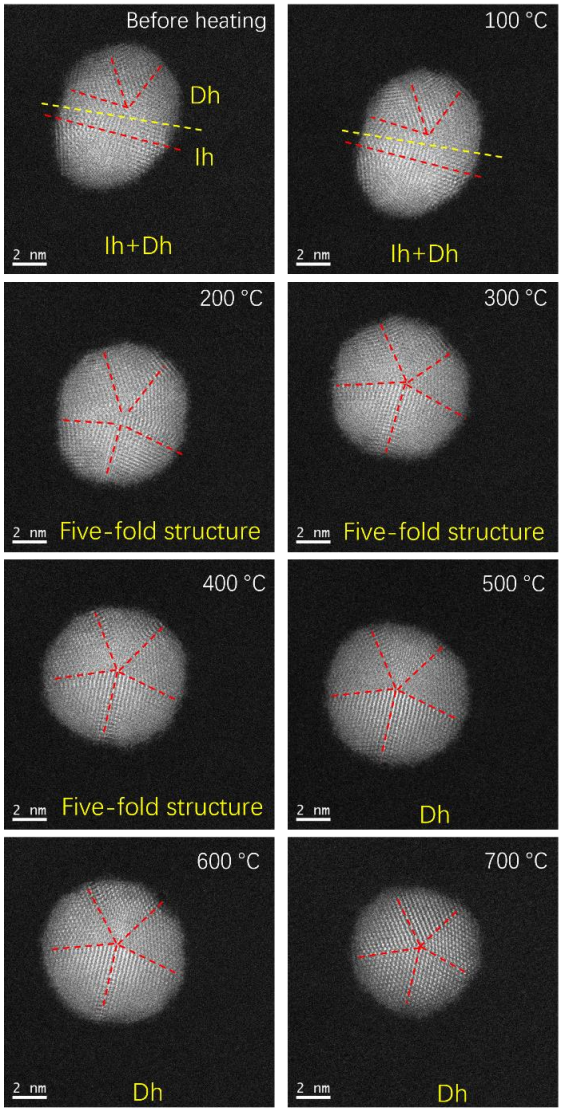


Figure 4.25: The aggregation process of two Ag8k domains with Ih and Dh structures in the temperature range of 20-600 °C. After heating at 700 °C, the cluster size decreased due to substantial mass loss. Red dotted lines are used to show typical distinguishing features of different structures, which are two-fold geometry for the Ih structure and five-fold geometry for the Dh structure. The yellow dotted lines are used to distinguish the domains in the elongated clusters.

4.3.2 Aggregated Ag8k clusters heating at different temperatures

All results of the aggregated Ag16k clusters shown in Figure 4.23 to 4.25 indicate that the aggregation of two Ag8k clusters with the same or different structures all lead to the formation of Dh structures. To further investigate the products of Ag cluster-cluster coalescence events, aggregated Ag8k clusters were deposited on the heating chip. The heating program is very close to the one shown in Figure 4.11, only the highest heating temperature was set to 600 °C to maintain the cluster size. After heating at 600 °C, the products of aggregated Ag8k clusters are shown in Table 4.2.

Table 4.2: The products of aggregated Ag8k clusters with domains of different structures.

Cluster number before heating	Structures after heating at 600 °C			
	Ih	Dh	FCC	UI
Ih+Ih or Ih+UI: 27	3	17	/	7
Ih+Dh: 2	/	2	/	/
Ih+x: 34	8	10	/	16
Dh+x: 4	/	4	/	/

In Table 4.2, aggregated Ag8k clusters denoted by Ih+Ih, Ih+Dh, or Ih+UI structures are aggregated clusters formed by two domains with similar sizes. The structures labelled as Ih+x and Dh+x are aggregates of small domains on large Ih or Dh domains, respectively. The details of these five kinds of aggregated structures are provided in the following part.

For aggregated Ag8k clusters with Ih+Ih or Ih+UI structures, Figure 4.26, 4.27, and 4.28 provide three typical examples to show the structure transition process in these clusters aggregated under high temperatures. 17 of 27 aggregated Ag8k clusters finally formed Dh structure by the atom rearrangement of Ih+Ih and Ih+UI structures. Figure 4.26 and 4.27 shows the detailed formation process of the Dh structure in this case. However, a small part of the aggregation of Ih+Ih and Ih+UI structures led to the formation of the Ih structure, as shown in Figure 4.28.

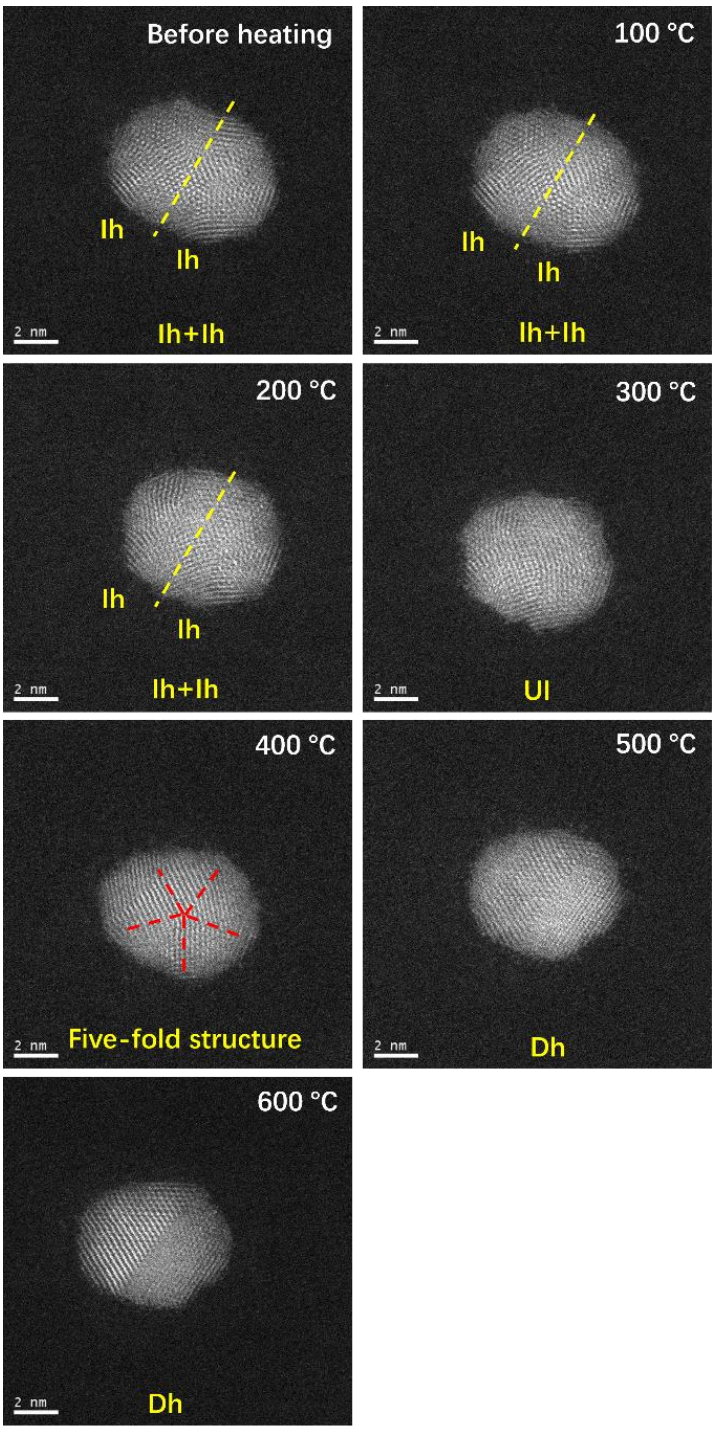


Figure 4.26: The aggregation process of an aggregated Ag8k cluster with Ih+Ih structure in the temperature range of 20-600 °C. The final structure is Dh. Red dotted lines are used to show typical distinguishing features of five-fold structures. The yellow dotted lines are used to distinguish the domains in the elongated clusters.

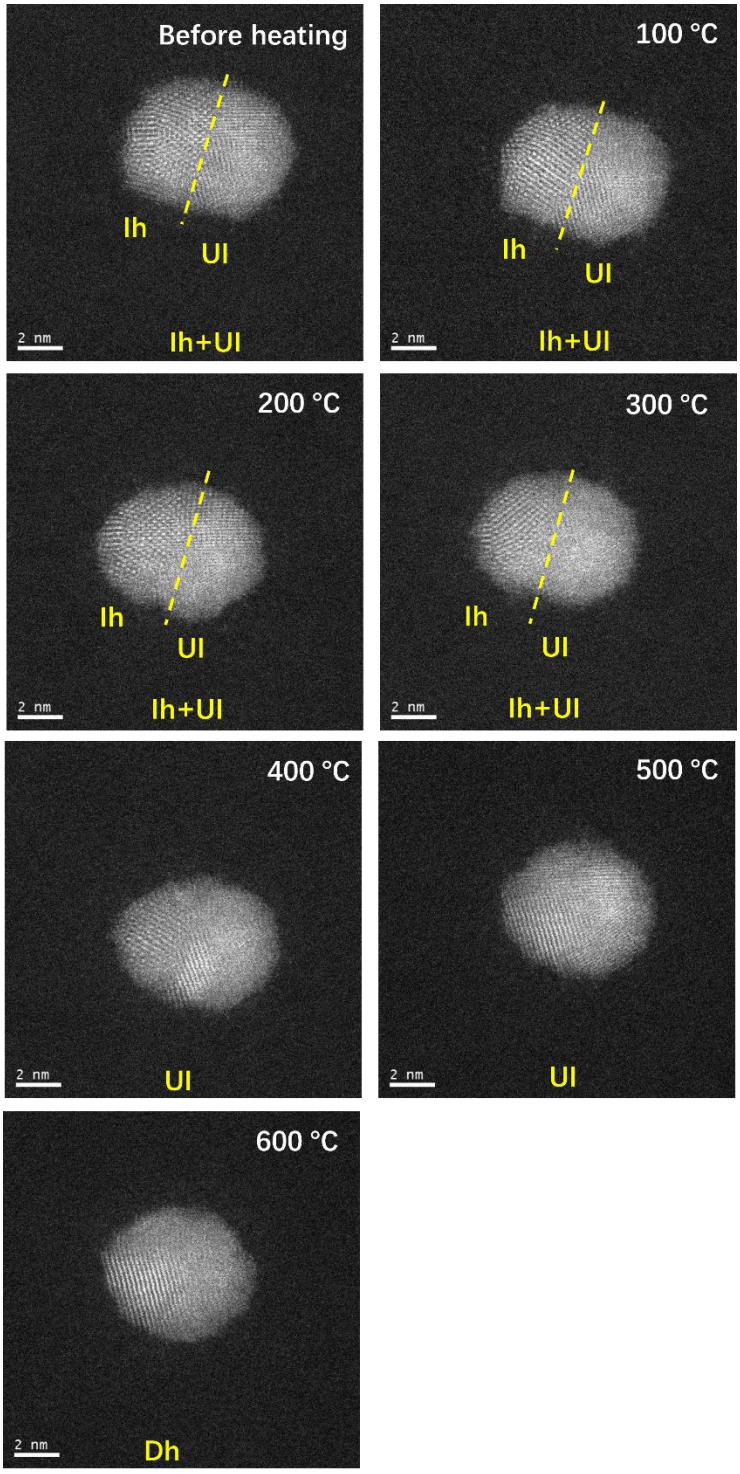


Figure 4.27: The aggregation process of an aggregated Ag8k cluster with Ih+UI structure in the temperature range of 20-600 °C. The final structure is Dh. The yellow dotted lines are used to distinguish the domains in the elongated clusters.

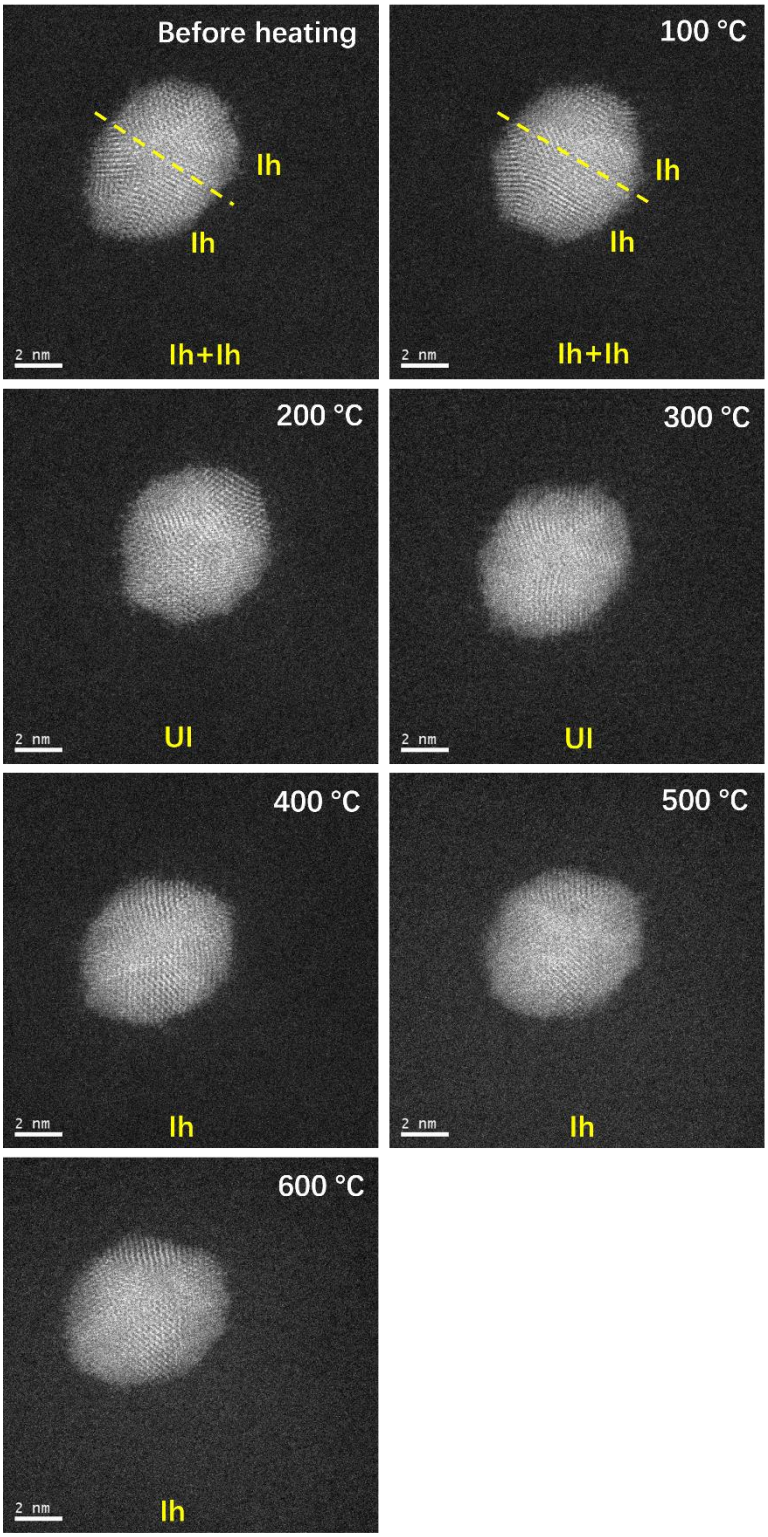


Figure 4.28: The aggregation process of an aggregated Ag8k cluster with Ih+Ih structure in the temperature range of 20-600 °C. The final structure is Ih. The yellow dotted lines are used to distinguish the domains in the elongated clusters.

As for the product of the aggregation of Ih+Dh structures, only two Ag8k clusters were observed in this case, and the final structures are both Dh structures. Figure 4.29 presents the detailed aggregation process during heating.

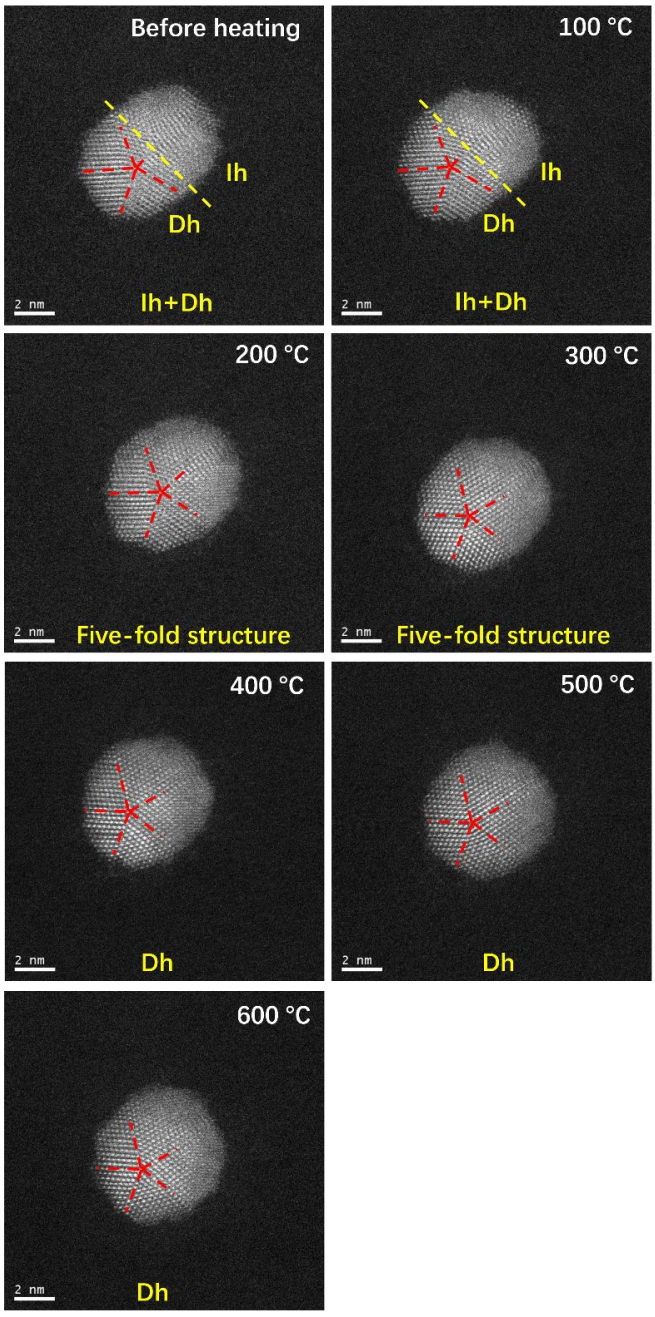


Figure 4.29: The aggregation process of an aggregated Ag8k cluster with Ih+Dh structure in the temperature range of 20-600 °C. The final structure is Dh. Red dotted lines are used to show typical distinguishing features of five-fold structures. The yellow dotted lines are used to distinguish the domains in the elongated clusters.

For Ag8k clusters formed by two domains with the obvious size difference, the products of these aggregated clusters are various. 8 of 34 aggregated Ag8k clusters with Ih+x structures kept the structure of the main domain, i.e., Ih structure after the heating at 600 °C. One typical example of this situation is shown in Figure 4.30. In contrast, 10 of 34 aggregated Ag8k clusters with Ih+x structures transformed to Dh structure after heating, as shown in Figure 4.31. The post-annealed structure of the remaining aggregated Ih+x Ag8k clusters could not be identified as fully formed Ih, Dh, or FCC structures. An example is shown in Figure 4.32.

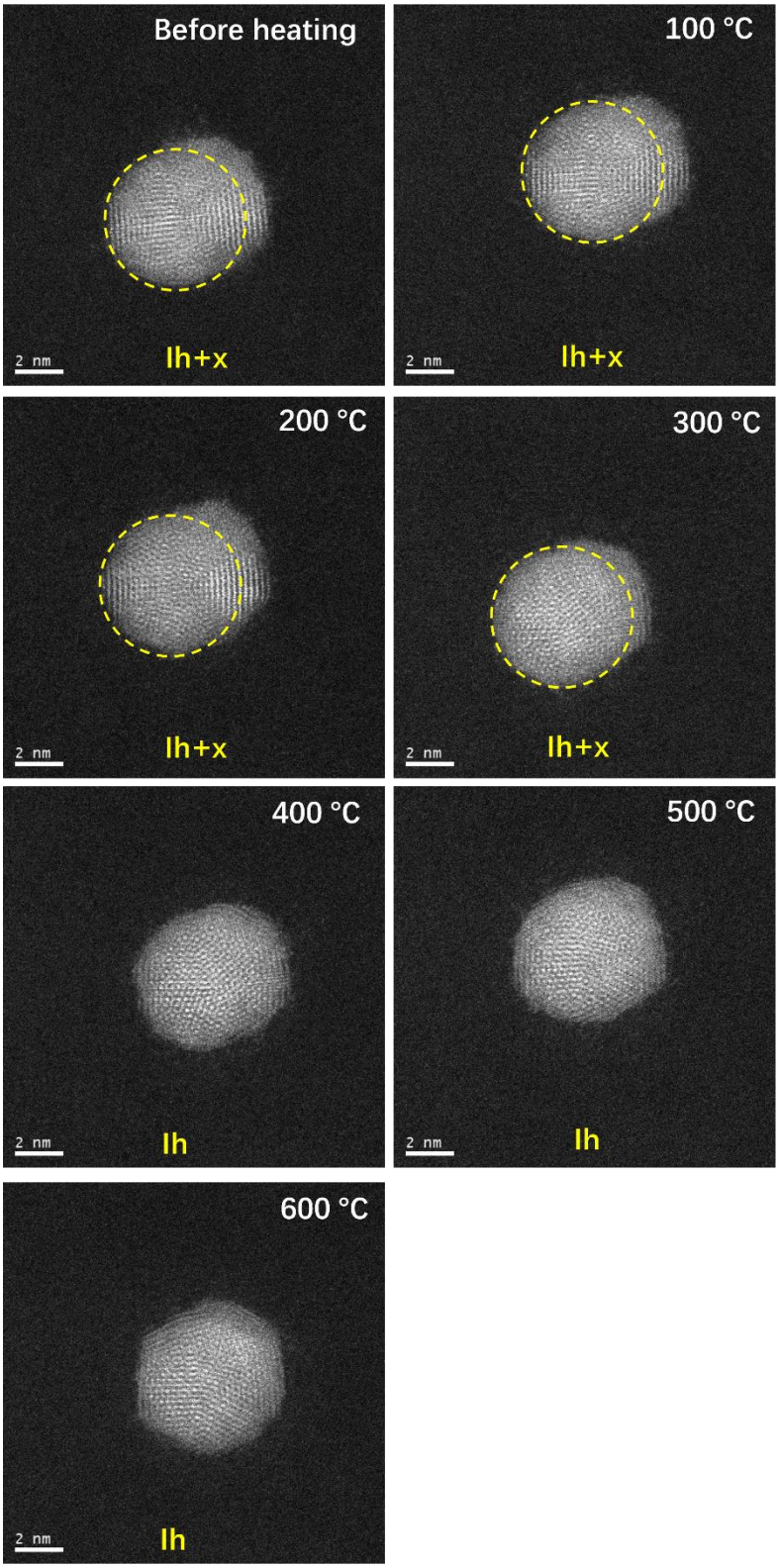


Figure 4.30: The aggregation process of an aggregated Ag8k cluster with Ih+x structure in the temperature range of 20-600 °C. The final structure is Ih. The yellow dotted circles are used to point out the main domains in the elongated clusters.

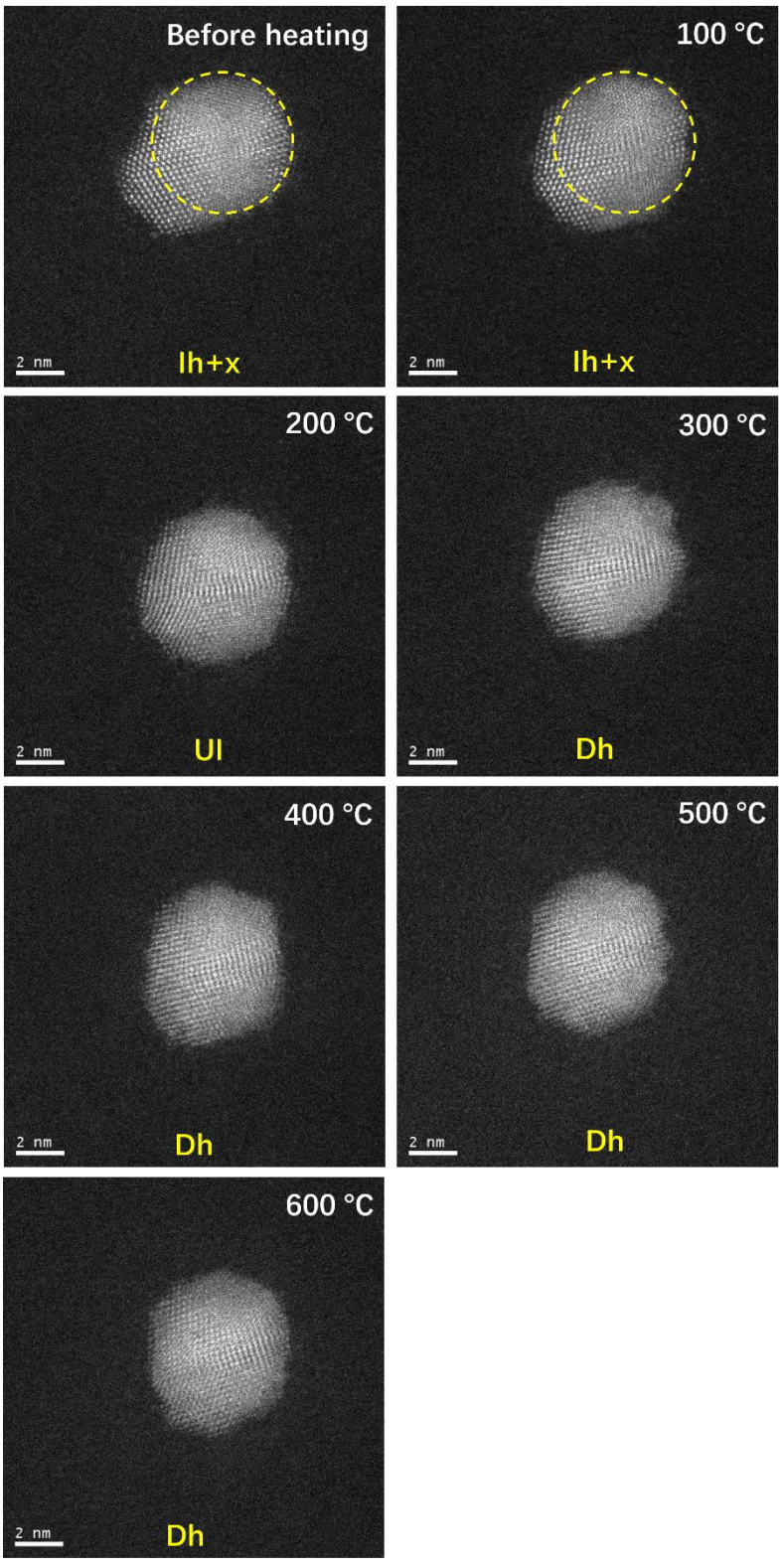


Figure 4.31: The aggregation process of an aggregated Ag8k cluster with Ih+x structure in the temperature range of 20-600 °C. The final structure is Dh. The yellow dotted circles are used to point out the main domains in the elongated clusters.

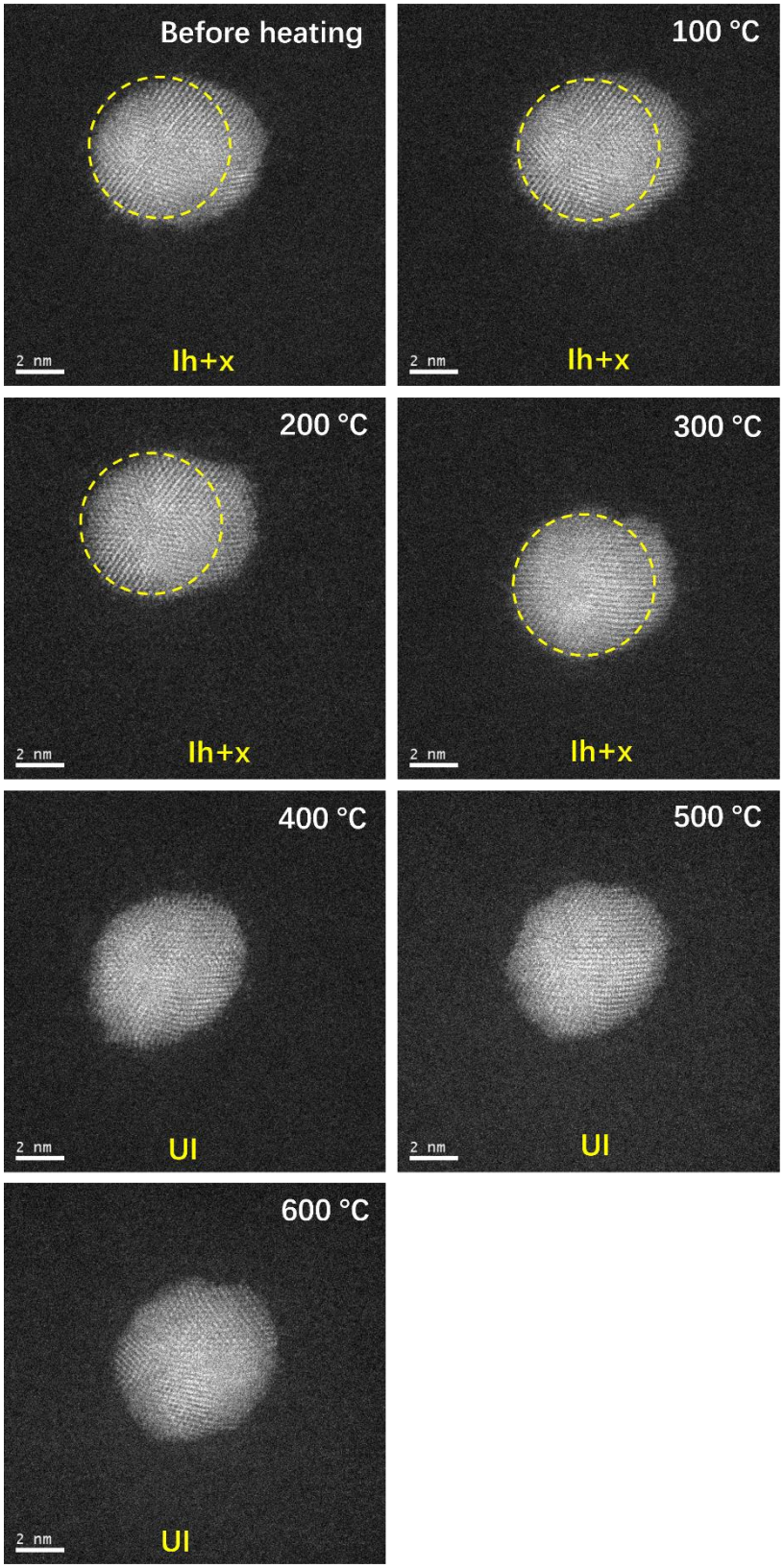


Figure 4.32: The aggregation process of an aggregated Ag8k cluster with Ih+x structure in the temperature range of 20-600 °C. The final structure is UI. The yellow dotted circles are used to point out the main domains in the elongated clusters.

The final structures of the aggregation of Dh+x structures all maintain the characteristic of Dh. A typical example is presented in Figure 4.33.

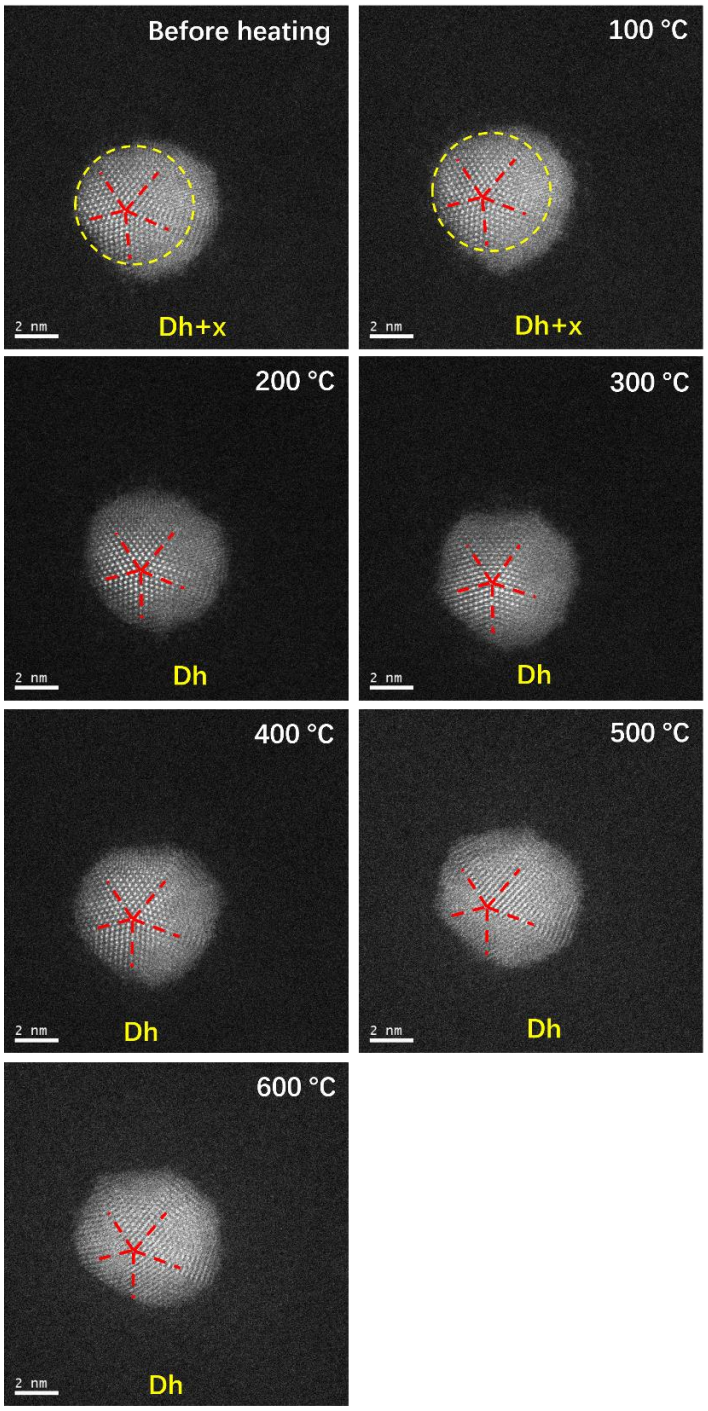


Figure 4.33: The aggregation process of an aggregated Ag8k cluster with Dh+x structure in the temperature range of 20-600 °C. The final structure is Dh. Red dotted lines are used to show typical distinguishing features of five-fold structures. The yellow dotted circles are used to point out the main domains in the elongated clusters.

In summary, the results in Table 4.2 indicate that the aggregation of two Ag clusters with similar size is very likely convert into a Dh structure when heated. In contrast, the evolution is more complicated for aggregations of two Ag clusters with obvious size differences. When the structure of the main domain is Ih, annealing can yield Ih, Dh, and more likely UI structures. On the other hand, the Dh structure will finally be obtained when the structure of the main domain is Dh. Nelli et al. also observed the abundance of Dh structures when one of the collided clusters is Dh in their simulation work[104]. Compared with the results in Table 4.1, it reveals that the energy barrier for the formation of Dh structure is lower for elongated Ag clusters than that of spherical clusters due to the larger fraction of the complete Ih-to-Dh transitions.

4.4 Heating experiment of Ag14k clusters

Considering the largest size is 14k in Figure 3.1, a heating experiment of Ag14k clusters was also conducted to explore the most stable structure of Ag14k clusters. The heating program is very close to the one shown in Figure 4.11, only the heating temperatures were set to 550, 600, 650, and 700 °C. The structure transition mainly happened after the heating at 650 and 700 °C. The Table 4.3 and 4.4 record the structures of Ag14k clusters after heating at these two temperatures, respectively. Only 10 of 72 Ag14k clusters with initial Ih structures transformed to Dh structures after heating at 650 °C, while final Dh structures were formed for about 2/3 of Ih structures after heating at 700 °C.

Table 4.3: The number of Ag14k clusters with different structures after heating at 650 °C.

Cluster number before heating	Structures after heating at 650 °C			
	Ih	Dh	FCC	UI
Ih: 72	58	10	/	4
Dh: 27	/	25	/	2
FCC: 0	/	/	/	/
UI: 5	/	/	/	5

Table 4.4: The number of Ag14k clusters with different structures after heating at 700 °C.

Cluster number before heating	Structures after heating at 700 °C			
	Ih	Dh	FCC	UI
Ih: 72	10	48	/	14
Dh: 27	/	26	/	1
FCC: 0	/	/	/	/
UI: 5	/	/	/	5

The HAADF-STEM images of one Ag14k cluster during heating are shown in Figure 4.34. Only half of the cluster was left due to great mass loss after heating at 700 °C. However, for Ag14k clusters without e-beam irradiation during heating, they can maintain their spherical shape and 76% of the initial mass even after heating at 700 °C. In addition, the results of the e-beam irradiation test before heating experiment show that a single Ag14k cluster can maintain its round shape and mass even for 10-minute

e-beam irradiation at room temperature. So, the change of shape for these observed Ag14k clusters after heating at 550-700 °C is not only caused by e-beam irradiation but caused by two combined effects from e-beam irradiation and the high temperature.

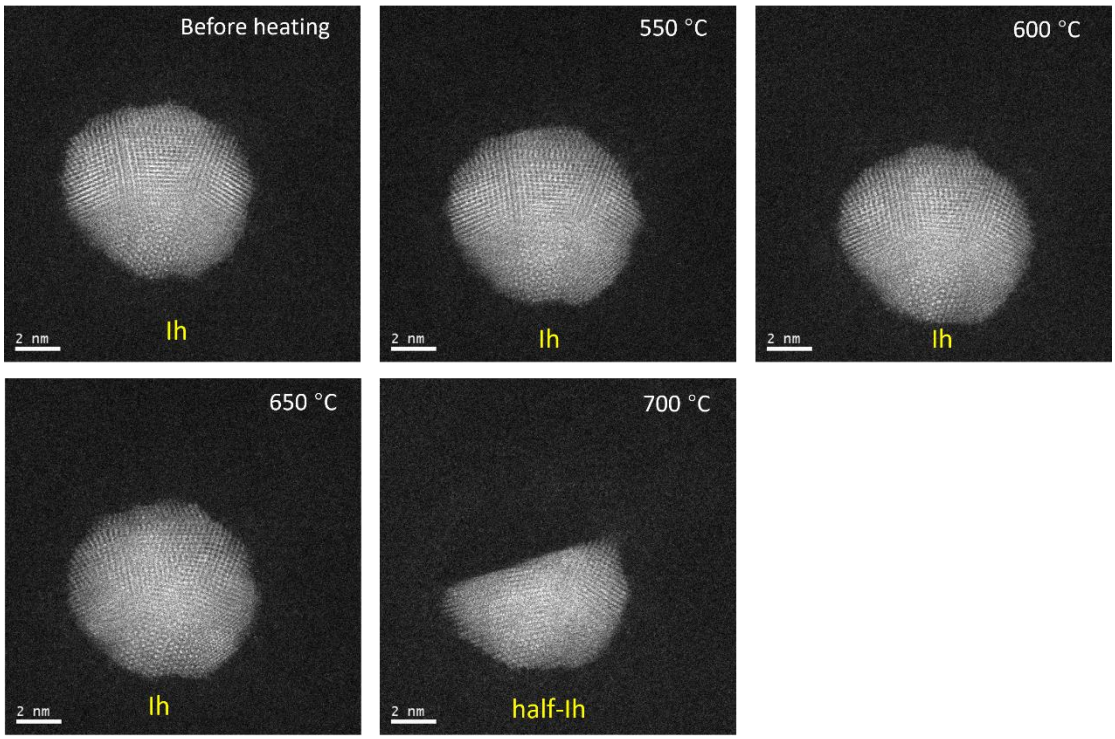


Figure 4.34: One example of a Ag14k cluster with initial Ih structure but no change in the temperature range of 20-650 °C. After heating at 700 °C, only half of the cluster was left due to great mass loss.

To explore the effect of heating without contributions from e-beam irradiation, 110 clusters were imaged after heating at 700 °C in the area without prior e-beam irradiation, and the statistical results are shown in Table 4.5. The strong increase in the Dh fraction of structures after heating at 700 °C indicates that the Dh structure is the equilibrium state of Ag14k clusters.

Table 4.5: The number of Ag14k clusters with different structures after heating at 700 °C.

Structures	Cluster number before heating	Cluster number after heating at 700 °C
Ih	72 (69%)	43 (39%)
Dh	27 (26%)	57 (52%)
FCC	0 (0%)	0 (0%)
UI	5 (5%)	10 (9%)

4.5 Conclusions

E-beam irradiation and chip-heating experiments were performed to investigate the stability of different structures for Ag clusters in the size range of 1k to 14k. The results indicate that the Dh structure is the equilibrium state for Ag clusters within this size range, based on the observations from both e-beam irradiation and chip-heating experiments.

During the e-beam irradiation experiments, the complete Ih-to-Dh structure transition process can be observed for Ag1k, Ag2k, and Ag6525 clusters, but it is not the same case for Ag8k and Ag12k clusters due to the higher energy barrier to achieve the structure transition in the limited e-beam irradiation period. In addition, the Ih-to-Dh transition process of Ag6525 clusters is found to follow the cooperative slip-dislocation mechanism.

During the heating process, Ag clusters experience mass loss due to sublimation as the temperature approaches the melting point. When spherical Ag8k clusters are heated to temperatures ranging from 100 to 600 °C, there is a decrease in the proportion of Ih structure and an increase in the proportion of Dh structure. The proportion of FCC structure does not change significantly, while the proportion of Ag8k clusters with UI structure increases. The heating process of Ag14k clusters also shows the transition from Ih to Dh structure.

The heating experiment of elongated Ag8k clusters yielded valuable results. The aggregation of two Ag clusters with similar sizes is highly likely to form a Dh structure, while the aggregation of two Ag clusters with significant size differences is more complex. When the structure of the main domain is Ih, the resulting aggregation products can be Ih, Dh, or more likely, UI structures. On the other hand, the Dh structure is eventually obtained when the structure of the main domain is Dh. The energy barrier for the formation of the Dh structure is lower for elongated Ag clusters than for spherical clusters.

Chapter 5 Morphology- and Structure-controlled Deposition of Mass-selected Ag8k Clusters by Tuning the Gas Flow Rate of Ar and He

5.1 Introduction

Based on the results of Chapter 3, the morphology and atomic structure can be different for the Ag clusters with a given size but deposited with different parameters, such as the results shown in Figure 3.13 and Figure 3.14. There are four preparation parameters with significant impact on clusters morphologies and structures in our magnetron sputtering setup, namely, the applied power, the condensation length, the gas flow rate of Ar, and the gas flow rate of He. For power and condensation length, Simon R. Plant pointed out that lower power and longer condensation length are conducive to the formation of equilibrium isomers for size-selected Au_{923} clusters[44]. Siqi Lu also investigated the relationship between the atomic structures of Au_{923} clusters and the deposition power [45], which shows the same trend as the results of Simon's work. Compared to structure-controlled deposition by tuning power and condensation length, adjusting the Ar and He gas flow rates is more cost-effective and easier to operate. This approach can help overcome the issue of high target consumption rates associated with high power application and the inconvenience of adjusting the condensation length. However, the effect of the gas flow rate of Ar and He on the atomic structures of clusters is still unclear. In this chapter, the morphologies and atomic structures of Ag8k clusters deposited with different parameters are analyzed by HAADF-STEM images, and the

effects of Ar and He gas flow rates are summarized from the results. In addition, a simulation was proposed to explain the relationship between the shape of mass spectrum and the growth process.

5.2 Effects of Ar and He gas flow rate on growth ways of Ag clusters prepared by magnetron sputtering

In order to investigate the effects of the Ar and He gas flow rate on the morphologies and atomic structures of Ag clusters, a series of mass spectra were obtained with different parameters, as shown in Figure 5.1. Ag8k, a common size for every mass spectrum, was selected as the aim size and deposited with the parameters of the mass spectra shown in Figure 5.1.

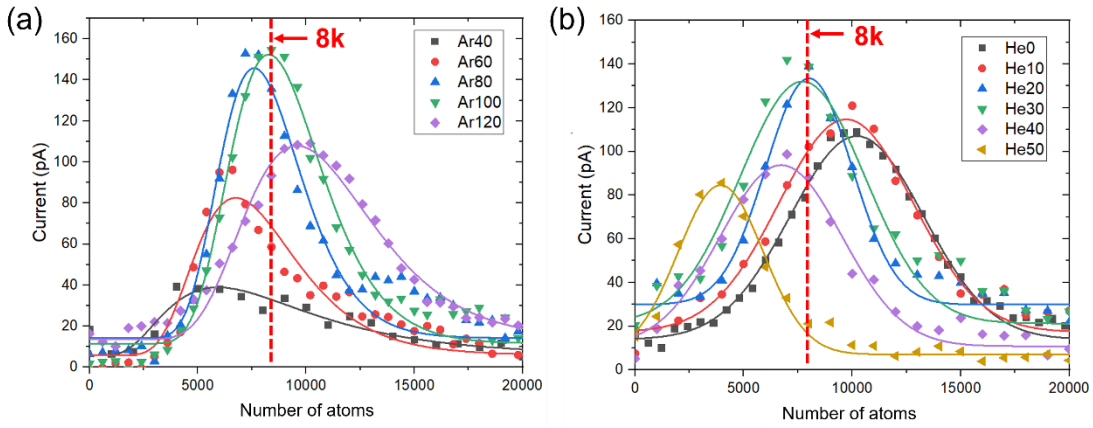


Figure 5.1: (a) Mass spectra of Ag clusters prepared with different Ar gas flow rates. Other parameters are the same, namely, a power of 10 W, a He gas flow rate of 0 sccm, and a condensation length of 250 mm. The mass spectra have been fitted with the Lognormal function. (b) Mass spectra of Ag clusters prepared with different He gas flow rates. Other parameters are the same, namely, a power of 10 W, an Ar gas flow rate of 120 sccm, and a condensation length of 250 mm. The mass spectra have been fitted with the Gaussian function.

The relationship between the peak sizes (maximum positions) of the fitted mass spectra and the applied Ar and He gas flow rates are shown in Figure 5.2. Peak positions of mass spectra show a linear relationship with increasing Ar gas flow rate, indicating that a higher Ar gas flow rate is good for the formation of large clusters because of a higher sputtering rate and more frequent collisions between clusters and Ar atoms to promote cluster nucleation and growth. On the other hand, peak sizes of mass spectra linearly decrease with increasing He gas flow rate. Although the higher He gas flow rate promotes the nucleation of small clusters, the shorter available growth time limits the formation of large clusters.

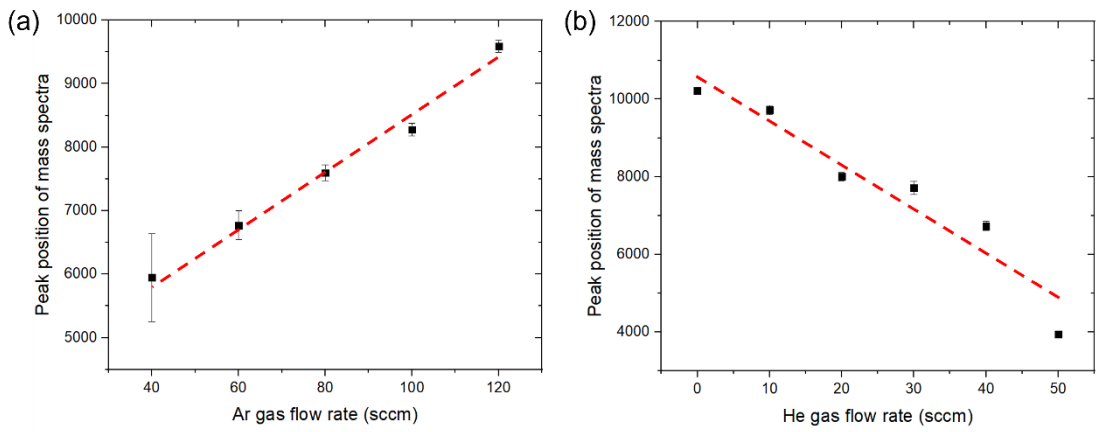


Figure 5.2: Relationship between peak sizes of mass spectra with (a) Ar gas flow rates and (b) He gas flow rates. The values of the peak sizes are from the fitting curves shown in Figure 5.1. The red curves are the linear relationship fitting. The error bars are from the confidence interval of the fitting of the Figure 5.1.

The deposited Ag8k clusters show different morphologies in their HAADF-STEM images. In Figure 5.3 (a), seven Ag8k clusters were selected as examples. Similar integrated intensities in Figure 5.3 (b) mean that these seven clusters have similar mass, but the aspect ratios of these clusters are different. The clusters with high aspect ratios

exhibit domains with different structures, as shown in Figure 5.3 (d) and (e), indicating that these elongated clusters are formed by cluster-cluster coalescence during the growth process and these domains hadn't totally aggregated into one spherical cluster[93]. The Ag8k cluster with a low aspect ratio and round shape in Figure 5.3 (c) cannot be matched with any simulation images, so it was grouped into UI (unidentified).

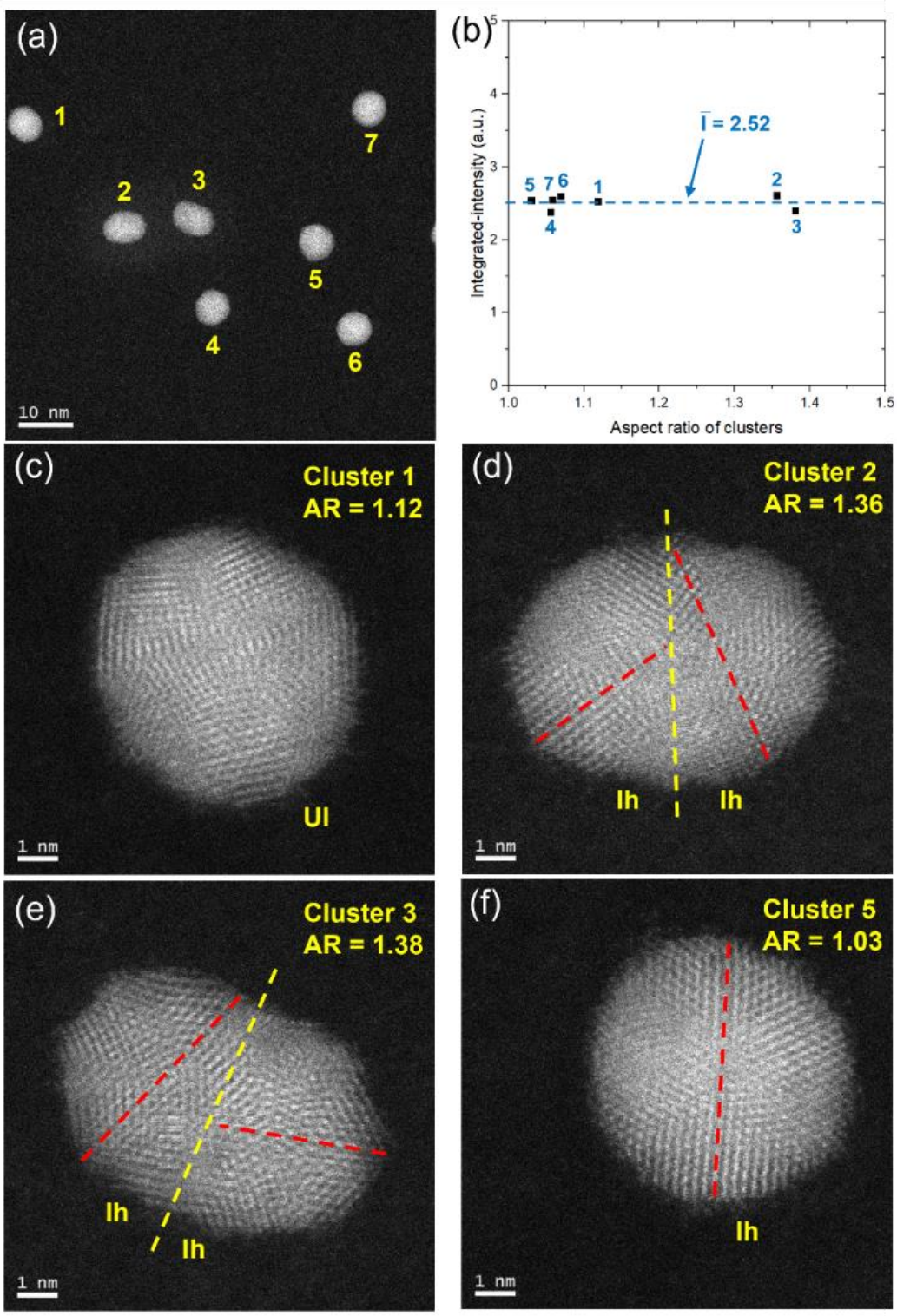


Figure 5.3: (a) One of the HAADF-STEM overview images of Sample Ar40, which includes seven Ag clusters. (b) Relationship between integrated intensities and aspect ratios of these seven Ag clusters. (c)-(f) HAADF-STEM images with the atomic resolution for Cluster 1, 2, 3, and 5 in (a), respectively. AR: aspect ratio; UI: unidentified cluster; Ih: cluster with icosahedron structure. The yellow dashed lines are guidelines separating two individual Ih domains in the elongated clusters. The red dashed lines are guidelines for structure identification.

The aspect ratios of all Ag8k clusters prepared with different Ar and He gas flow rates were analyzed and the results are presented in Figure 5.4 (a) and (b). According to the linear fitting of Figure 5.2, the theoretical peak size of 8k can be obtained with the Ar gas flow rate of 85 sccm and He gas flow rate of 23 sccm. Thus, every figure in Figure 5.4 is divided into two parts according to the Ar and He gas flow rates that can obtain the theoretical peak size of 8k. When Ag8k is larger than the peak size of mass spectra, namely these Ag8k clusters were deposited with low Ar gas flow rate and high He gas flow rate, the aspect ratio and standard deviation of these Ag8k clusters will be higher, indicating there will be more elongated clusters. This conclusion can be further confirmed by checking about 160 clusters for every sample prepared with different Ar and He gas flow rates and the results are shown in Figure 5.4 (c) and (d). Normally, the peak size is considered as the most favored size for every mass spectrum due to the largest fraction in cluster beam, which has been summarized from the experiments in Chapter 3. When the peak size is smaller than 8k, the preparation parameter that obtains this peak size is not favored for Ag8k to form during the growth process, causing the low deposition rate of Ag8k clusters and large fraction of elongated (incomplete aggregated) clusters among them. Specifically, the low Ar gas flow rate cannot support the heating exchange between clusters and cooling gas atoms and limit the formation of large clusters, while the high He gas flow rate will limit the growth time of Ag8k clusters and many of them cannot merge into one cluster with spherical morphology in the magnetron sputtering chamber. Both cases lead to higher proportions of elongated Ag8k clusters.

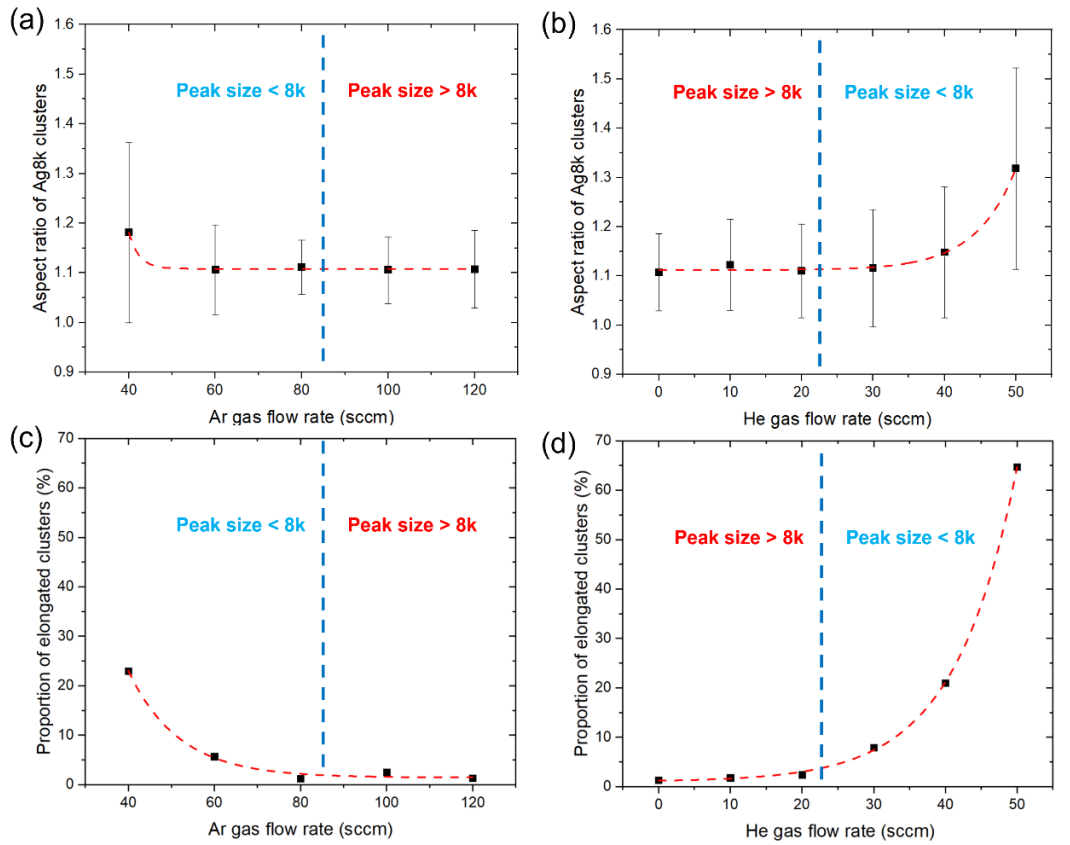


Figure 5.4: (a) and (b) are aspect ratios of all Ag8k clusters in samples prepared with different Ar and He gas flow rates as shown in Figure 5.1. The error bars represent the standard deviation of the statistical results. (c) and (d) are the proportions of elongated clusters in about 160 Ag8k clusters for every sample prepared with different Ar and He gas flow rates. The red dashed lines are exponential fitting. The blue dashed lines show the Ar gas flow rate of 85 sccm and He gas flow rate of 23 sccm, which can obtain 8k atoms as peak size according to the linear fitting in Figure 5.2.

The structure proportions shown in Figure 5.5 are statistical results of spherical Ag8k clusters like Figure 5.3 (f). The elongated clusters have been excluded here. Some research has pointed out that Ih is dominated in the atom by atom growth, while the coalescence prefers to produce Dh and FCC[102–104]. For an Ar gas flow rate ranging from 40 to 120 sccm, an increase in the proportion of Dh and FCC structures suggests a shift in the main growth pathway from atom addition to cluster-cluster coalescence with an increasing Ar gas flow rate. In contrast, the proportion of different structures remains similar for a He gas flow rate ranging from 0 to 30 sccm. However, when the

He gas flow rate exceeds 30 sccm, the formation of Dh structure in spherical Ag8k clusters decreases due to the limit time for overcoming the high energy barrier of structure transition after cluster collisions, on the other hand, resulting in a higher proportion of elongated clusters.

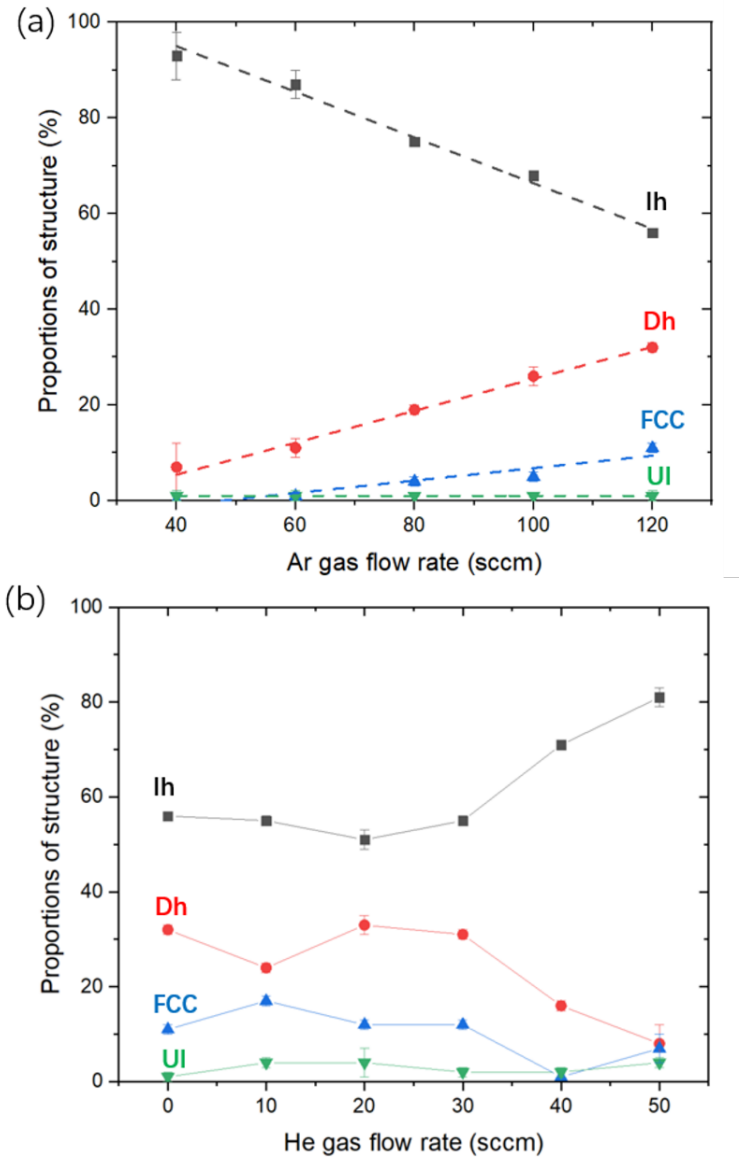


Figure 5.5: (a) Proportion of different structures of spherical Ag8k clusters in samples prepared with different Ar gas flow rates with no He gas. The dashed lines are linear fitting for the trend of every kind of structure. (b) The proportion of different structures of spherical Ag8k clusters in samples prepared with different He gas flow rates with the same Ar gas low rate of 120 sccm. The error bars represent the uncertainties associated with the identification of the structure.

Besides the spherical Ag8k clusters, elongated Ag8k clusters can be classified into two categories based on the presence or absence of a structure change at the interface of the two domains. Figure 5.6 (a) and (b) show two elongated clusters composed of two Ih domains with similar sizes. In addition, there are also elongated clusters composed of two domains with obviously different sizes as shown in Figure 5.6 (c). Elongated clusters composed of Ih and Dh are very rare, an example is shown in Figure 5.6 (d). In summary, the majority of elongated clusters are composed of two Ih domains with different or similar sizes.

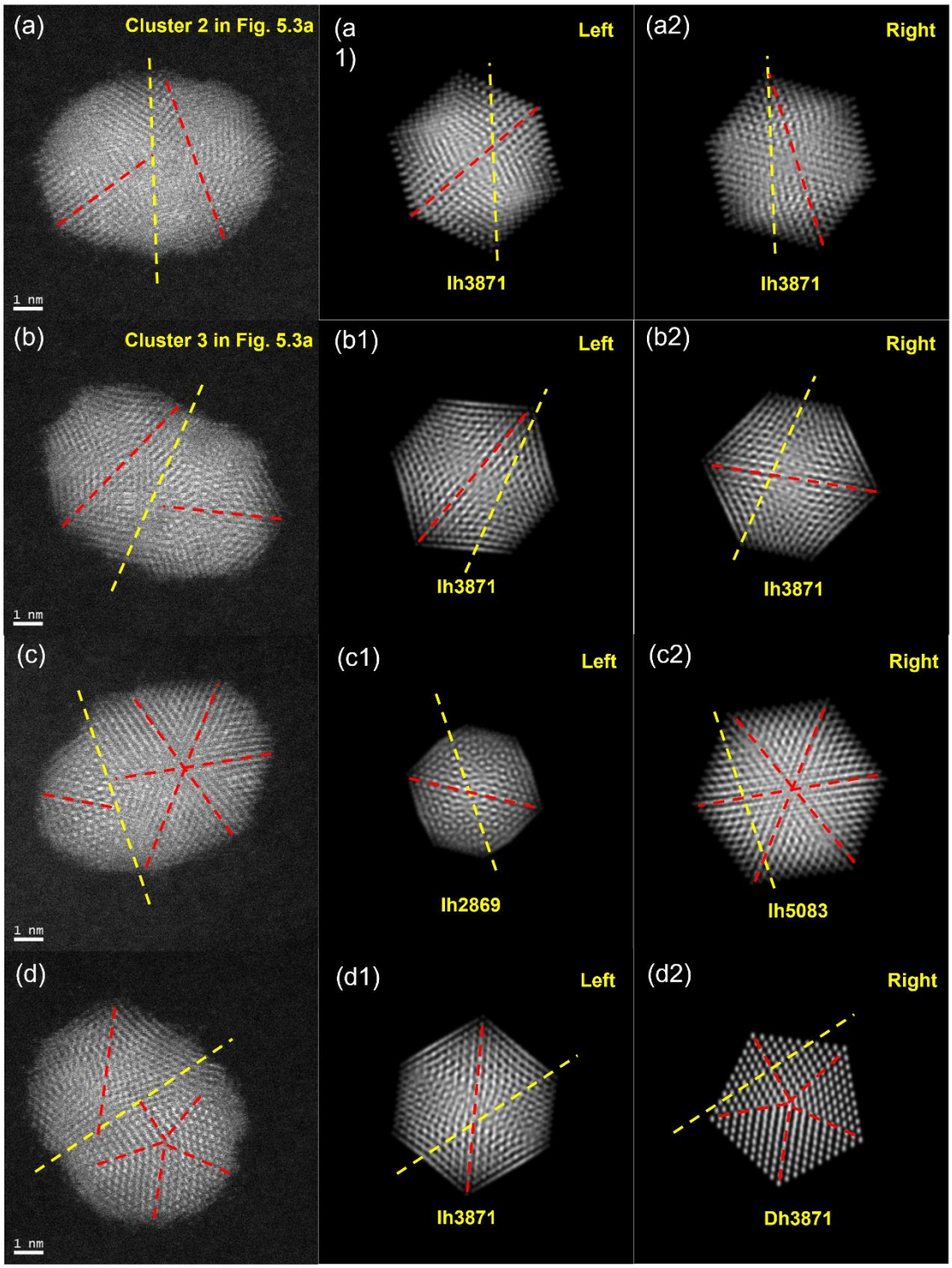


Figure 5.6: (a) and (b) HAADF-STEM images of Cluster 2 and 3 in Figure 5.3 (a). (c) and (d) HAADF-STEM images of two elongated clusters. (a1)-(d1) Simulation images of left domains and (a2)-(d2) simulation images of right domains corresponding to (a)-(d), respectively. Yellow dashed lines are used to guide the domains in HAADF-STEM images and preserved areas in simulation images compared with HAADF-STEM images. The red dashed lines are guidelines for structure identification.

Figure 5.6 shows four elongated clusters but no obvious structural change at the interface of domains can be seen. Here, five elongated clusters composed of two domains with similar sizes are presented in Figure 5.7 to show the structure change. Figure 5.7 (a) and (b) show obviously twisted axes caused by cluster-cluster aggregation, which should be 180° in normal Ih structures as shown in Figure 5.7 (a1) and (b1). This means that cluster-cluster coalescence can greatly induce atom rearrangement inside the clusters, which may lead to structure transition after complete aggregation. Besides, the orange dashed area in Figure 5.7 (a) shows the additional atom layers compared with Figure 5.7 (a1), indicating coalescence process between two clusters with similar sizes needs coordinated displacement of many atoms. The newly formed five-fold structure in Figure 5.7 (c), (d) and (e) can be seen as a symbol of Dh structure, indicating that the Dh structure can be formed by the coalescence of two Ih clusters with similar sizes.

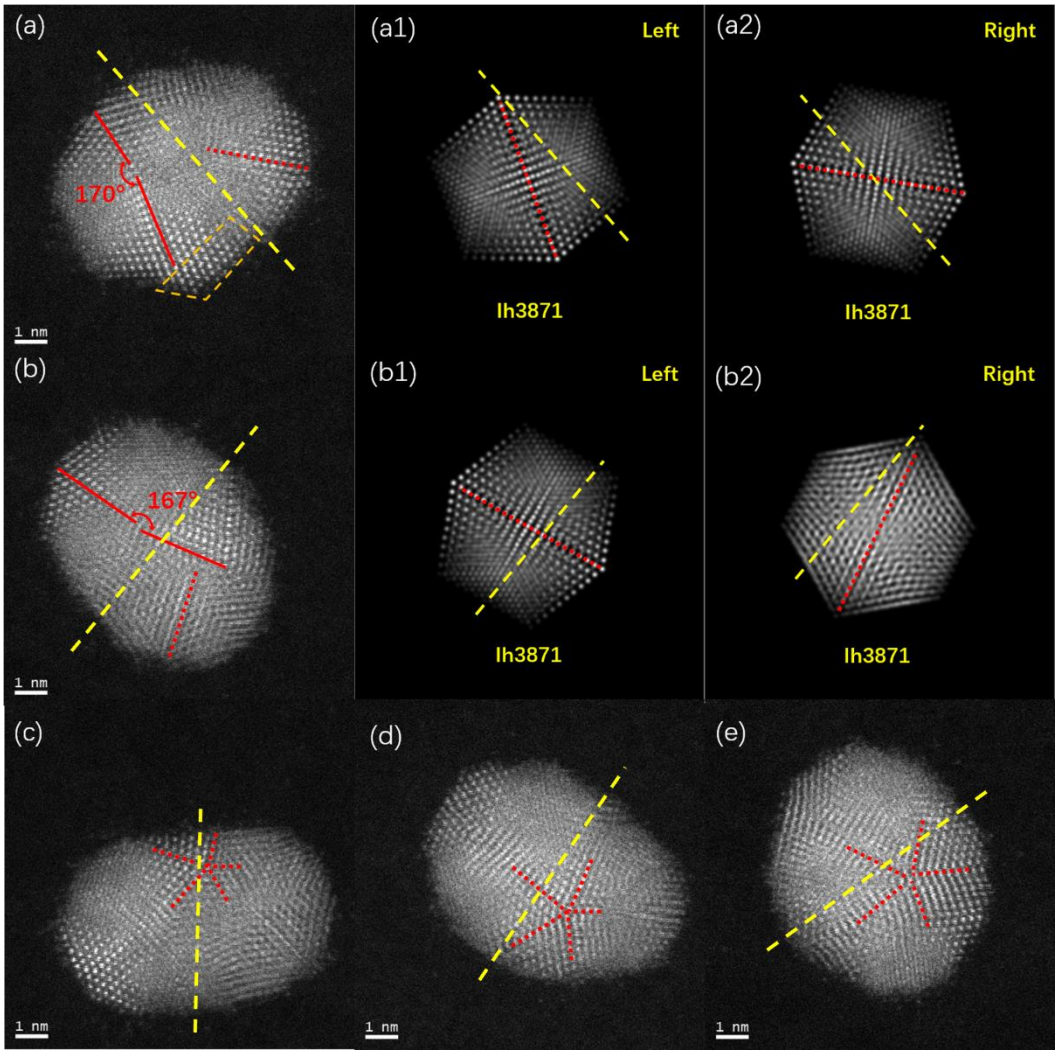


Figure 5.7: (a)-(e) HAADF-STEM images of five elongated Ag8k clusters composed of two domains with similar sizes. (a1) and (a2) Simulation images of left and right domains in (a). (b1) and (b2) Simulation images of left and right domains in (b). Yellow dashed lines are used to guide the preserved area in simulation images compared with HAADF-STEM images. The orange dashed area in (a) shows the additional atom layers compared with (a1). Red solid lines in (a) and (b) show the twisted axis caused by cluster-cluster aggregation, which should be 180° in normal Ih structures. Red dashed lines in (c), (d) and (e) are used to show the five-fold structures formed by cluster-cluster aggregation.

Apart from these elongated Ag8k clusters of which domains can be identified, Figure 5.8 (a1), (b1) and (c1) show elongated clusters composed of two domains with obviously different sizes but no newborn special structure was observed between attached small clusters and the main-body clusters. Figure 5.8 (d1), (e1) and (f1) all show five-fold characteristics between attached clusters and main-body clusters, indicating even small clusters can also induce structure transition. Comparing with Figure 5.8 (b1) and (e1), they own almost the same main-body clusters with Ih structure. The atoms of the attached cluster in Figure 5.8 (b1) follow the same arrangement as the atom of the main-body cluster. However, for the attached small cluster in Figure 5.8 (e1), it did not follow the atom arrangement as atoms of the main-body cluster but formed a five-fold structure. In summary, some coalescence of two clusters with different sizes may induce the structure transition but some do not.

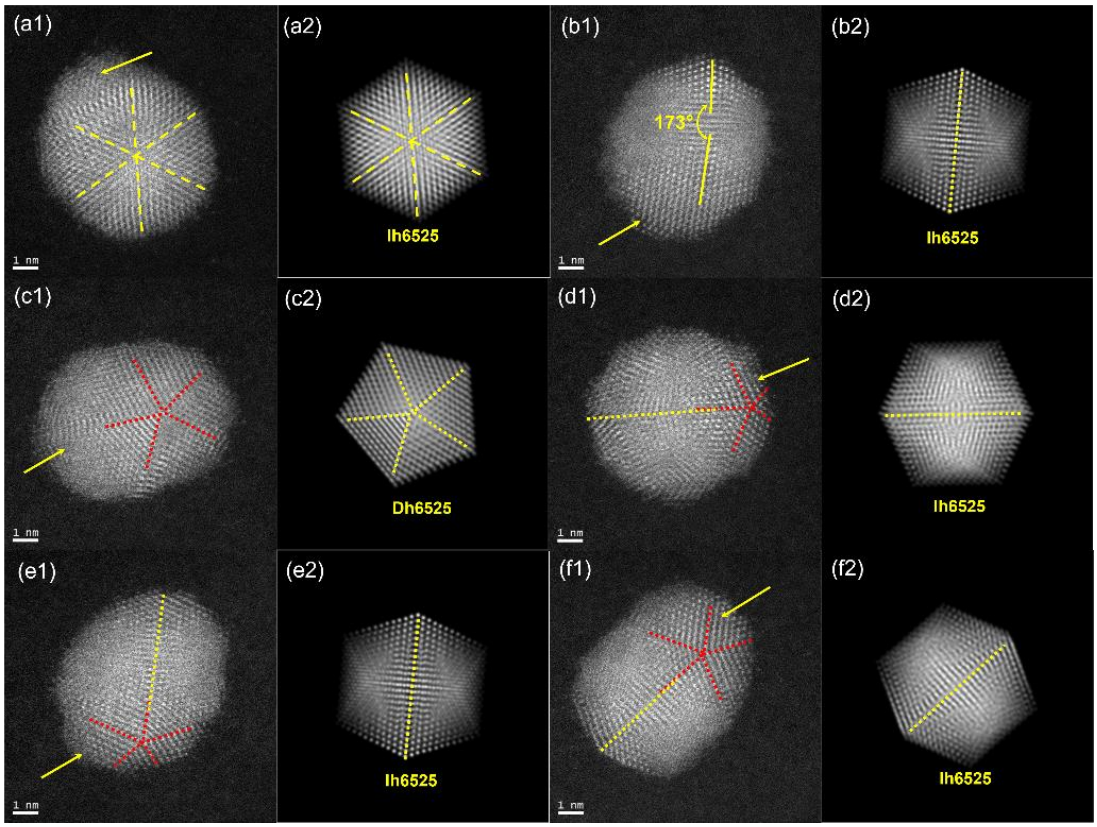


Figure 5.8: (a1)-(f1) HAADF-STEM images of six elongated Ag8k clusters composed by two domains with obviously different sizes. (a2)-(f2) Simulation images of the main-body clusters corresponding to (a1)-(f1), respectively. Yellow arrows show the positions of small domains in every elongated cluster. Red dashed lines are used to show the newly formed five-fold structures between two domains. The yellow dashed lines are guidelines for structure identification.

For all Ag8k clusters prepared with one series of deposition parameters, their growth ways can be atom addition and cluster-cluster coalescence, depending on their growth environment, such as position, temperature, atom density and so on. Here, the percentage of cluster-cluster coalescence events for Ag8k clusters is tried to calculate as the following process.

For one Ag8k sample, the compositions of all prepared clusters are shown in Figure 5.9 (a). These elongated clusters can be directly considered as the product of incomplete coalescence event, and the Dh and FCC in spherical clusters can be seen as the product

of complete coalescence event. Imaging A is the percentage of elongated clusters in all Ag8k clusters of this sample and B is the total percentage of Dh and FCC structures in spherical Ag8k clusters. We have seen that elongated clusters are practically always Ih. Thus, percentage of Dh and FCC structures in all Ag8k clusters is B*(1-A). From Table 4.2, not all elongated clusters can form the Dh structure after heating, so the possibility of the formation of Dh or FCC by cluster-cluster coalescence is not 100%. Assuming the possibility is X, then the percentage of cluster-cluster coalescence events to form Dh or FCC in all Ag8k clusters is B*(1-A)/X. Finally, the percentage of cluster-cluster coalescence events in all Ag8k clusters is A+B*(1-A)/X.

Based on the results of the heating experiment of aggregated Ag8k clusters shown in Table 4.2, there are 33 of 67 aggregated Ag8k clusters finally transformed to Dh structure after heating at 600 °C, namely a possibility of 49%. Considering the observed final UI structure could also be Dh, the Dh structure will be 56 of 67 (84%) observed Ag8k clusters. Thus, the possibility of the formation of Dh or FCC by cluster-cluster coalescence for Ag8k clusters will be in the range of 49% to 84%. Here, we assume that the probability values are the same for Ag8k clusters prepared with different gas flow rates, and we apply values of 60%, 70%, and 80% as the value of X. Then, the result in Figure 5.9 (b) shows that percentage of cluster-cluster coalescence increases from the Ar gas flow rate of 40 sccm to 120 sccm and then keeps a high level with the He gas flow rate from 0 to 50 sccm.

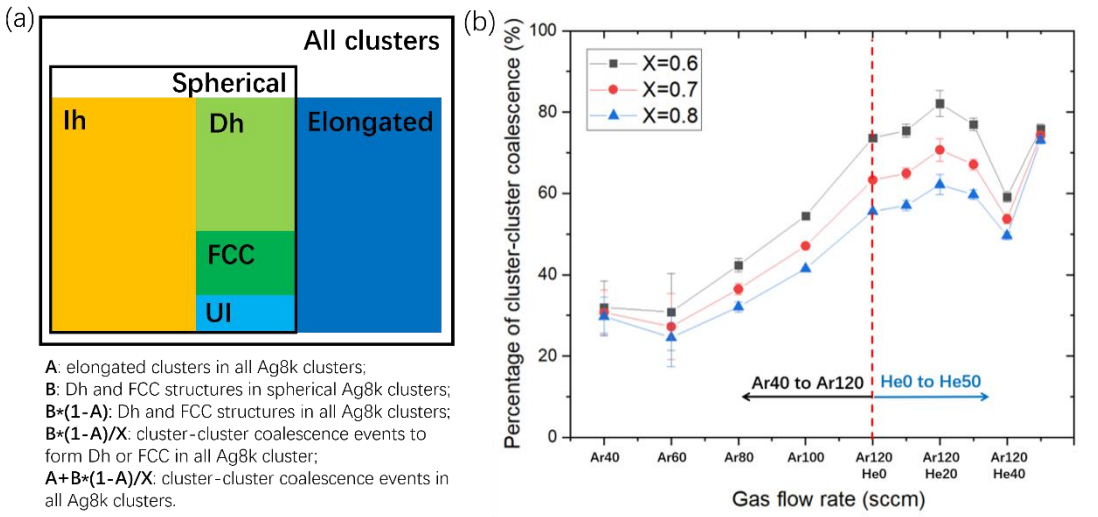


Figure 5.9: (a) A schematic diagram to show the compositions in the prepared Ag clusters. (b) The relationship between the percentage of cluster-cluster coalescence events for Ag8k clusters and gas flow rates. The error bars represent the uncertainties associated with the identification of the structure.

From the literature[69–71], the main roles of Ar and He gas in the magnetron sputtering method are shown as follows.

The increasing Ar gas flow rate:

- reducing the residence time of clusters in the growth zone;
- increasing the local density of sputtered atoms around the x-axis because a higher flow rate limits the radial diffusion and concentrates the metal vapor along the x-axis;
- increasing thermalization by a faster heat exchange process, which can increase the growth rate;
- increasing density of sputtered atoms in the whole chamber through increased sputtering due to a higher Ar ion concentration;

The increasing He gas flow rate:

- increasing the nucleation possibility by increasing three-body collisions;
- reducing the residence time of clusters in the growth zone.

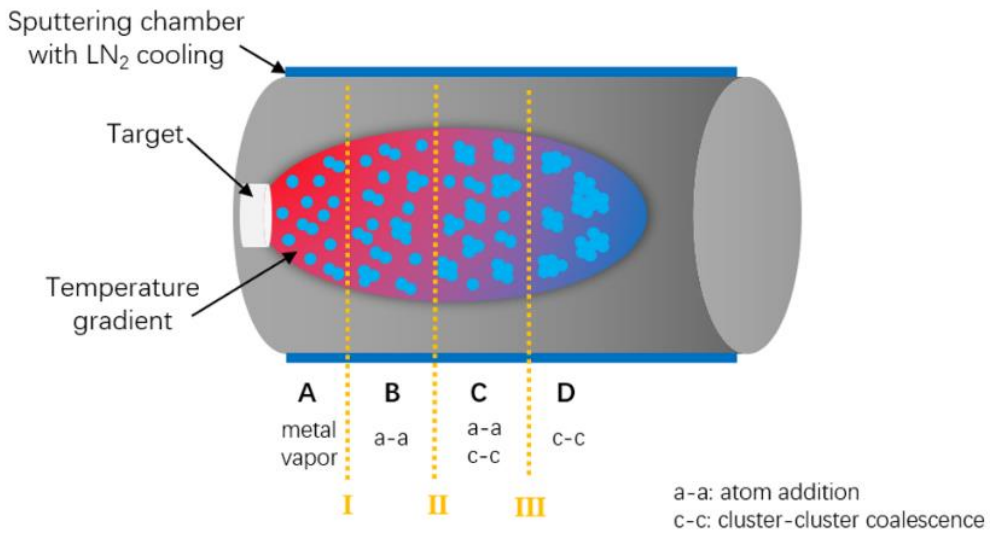


Figure 5.10: A schematic diagram to describe the possible growth process in the sputtering chamber. Copied from Figure 3.17 (a).

To summarize the effects of Ar and He gas flow rates on the growth ways of Ag8k clusters, a schematic diagram in Figure 5.10 is presented. The higher Ar gas flow rate can lead to three main effects: (1) higher atom density in Area A of Figure 5.10 resulting in larger and more clusters in Area B. Then, more cluster-cluster collision events will happen in Area C and D; (2) more powerful thermalization and thus lower kinetic energy of clusters, which can avoid them bouncing off each other during collisions and support the formation of larger clusters; (3) weaker radial diffusion, so that more cluster-cluster collision events in Area C and D. As for higher He gas flow rate, there will be less residence time in Area B, C and D, which finally cause more elongated clusters because of the limitation of coalescence time.

5.3 Relationship between the shapes of mass spectra and cluster growth ways of Ag clusters

In Figure 5.1 presented at the start of the chapter, the mass spectra of Ag clusters prepared with different Ar gas flow rates can be well-fitted with the Lognormal functions, however, a Gaussian function was more suitable for fitting the mass spectra of different He gas flow rates. A detailed comparison between these two fitting relationships for the mass spectra of Ag clusters prepared with different Ar gas flow rates is shown in Figure 5.11. For the Ar gas flow rate from 40 sccm to 100 sccm, the R-square of the Lognormal fitting is closer to 1 than that of the Gaussian fitting, proving that the mass spectra obtained with these Ar gas flow rates are more suitable to be fitted with the Lognormal functions. In addition, σ describes the shape of the Lognormal distribution. Specifically, when σ is small, the shape of the curve will be peaked and narrow; when σ is large, the distribution will be flatter and wider. The larger the value of σ, the flatter the shape of the Lognormal distribution and the more dispersed the data; the smaller the value of σ, the closer the shape of the Lognormal distribution to the Gaussian distribution and the more clustered the data. When the Ar gas flow rate increases from 40 accm to 100 sccm, the decreasing value of σ also indicates the shape of mass spectrum gradually change from the Lognormal function to Gaussian-like distribution.

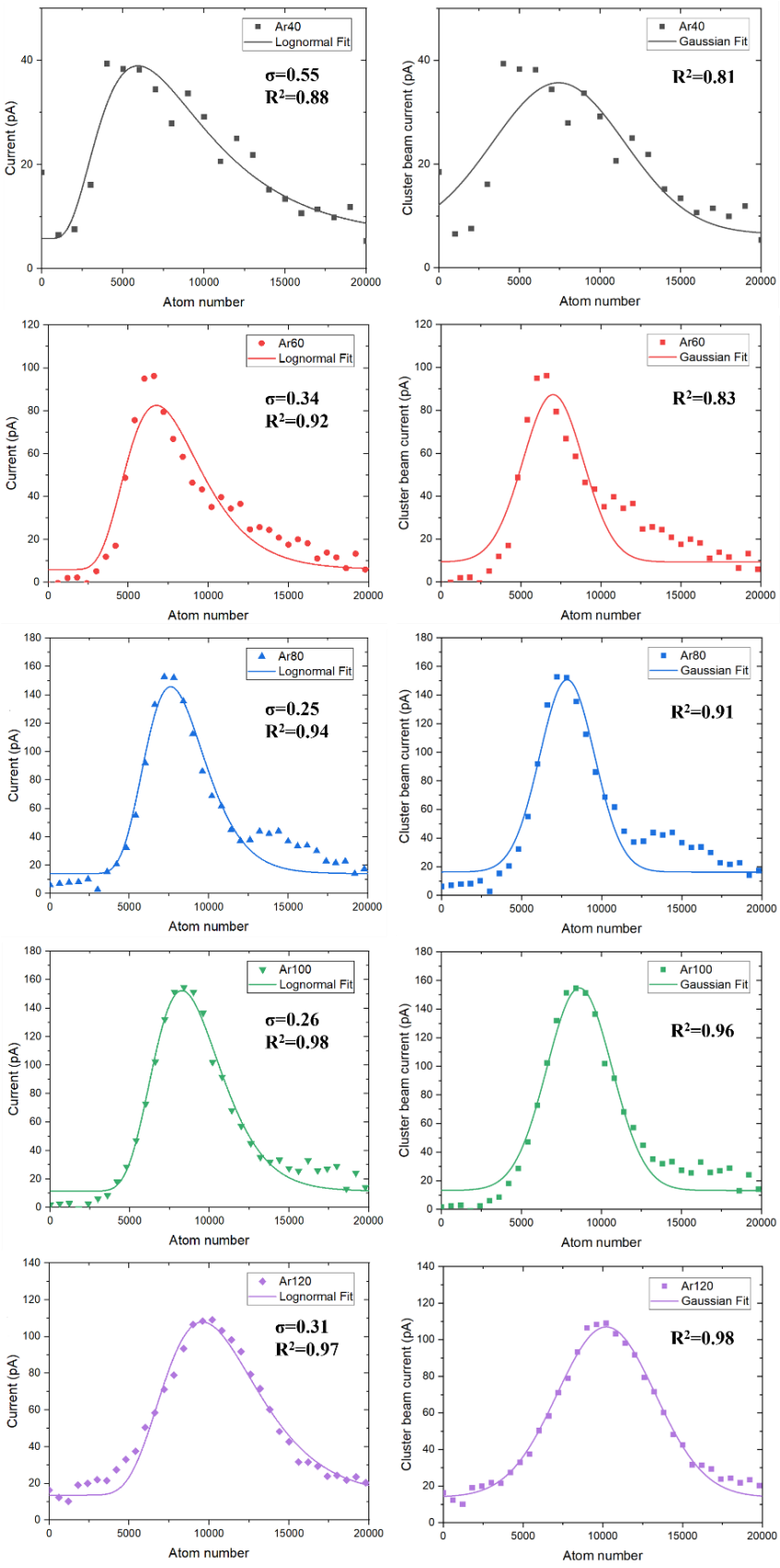


Figure 5.11: A detailed comparison between the Lognormal and Gaussian fitting relationships for the mass spectra of Ag clusters prepared with different Ar gas flow rates.

Furthermore, the comparison of R-squares for the two fitting functions of Figure 5.11 is shown in Figure 5.12. With increasing Ar gas flow rate, the shape of the mass spectrum will gradually change from the Lognormal function to the Gaussian relationship, indicating that there may be relationships between the mass spectrum and the related growth ways of Ag clusters.

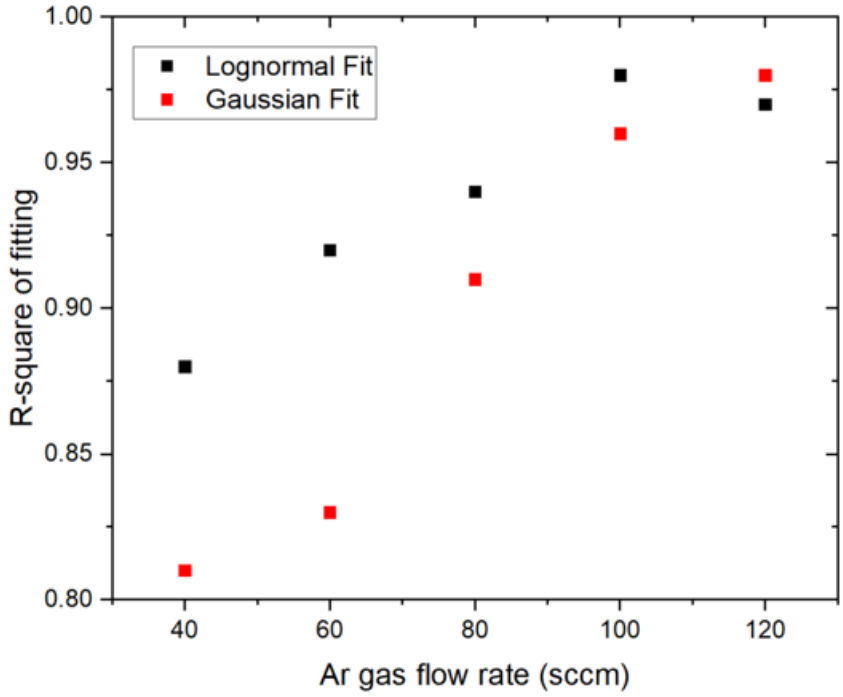


Figure 5.12: The comparison of R-squares for the two fitting functions of Figure 5.11.

To understand why Gaussian and Lognormal distribution can occur in the mass spectra, the size evolution of clusters during growth is simulated. According to K. Sasaki's work[109], about half of sputtering products from metal targets are single atoms and the other half are mainly dimers and trimers. Let's assume the proportions of single atoms, dimers, and trimers are 50%, 30%, and 20%, respectively. Then, assuming these single atoms, dimers, and trimers will collide with each other randomly and aggregate into one cluster. Based on these assumptions, the size distribution after every collision

round was simulated using MATLAB. The schematic drawing of the simulation process is shown in Figure 5.13.

The number of initial particles is assumed as 10,000 and the numbers of single atoms, dimers and trimers are 5000, 3000, and 2000, respectively. Then, every two particles will collide randomly and aggregate into one cluster, so 5000 clusters are left after the collision. Repeating this operation 20 times and obtained a dataset with 100,000 data. This is the 1st random collision round. After that, 10,000 data are randomly selected from this dataset as the initial dataset for the next collision round, whose operation is the same as that of the first one. The effect of every iteration on the result of the next iteration can be greatly eliminated by mixing the data of multiple-time collisions and random selection in every iteration.

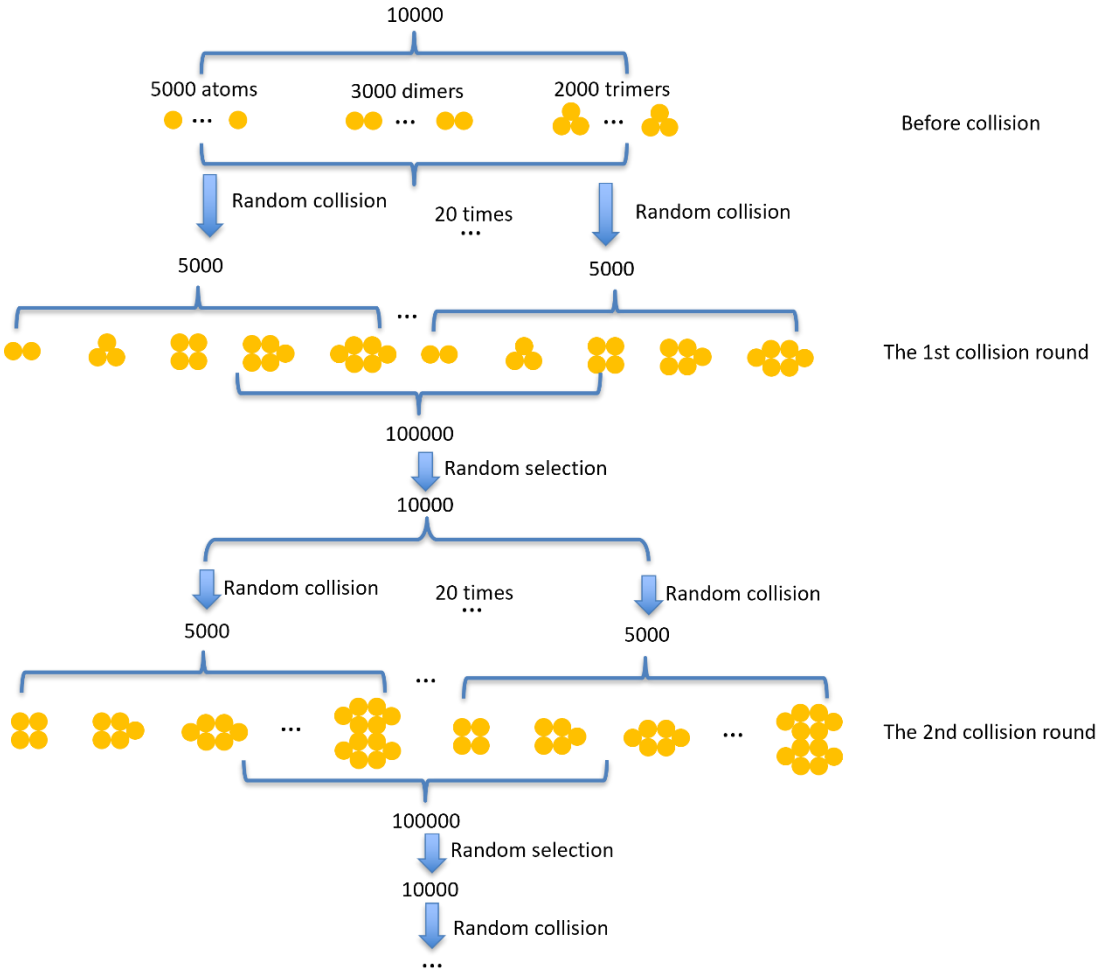


Figure 5.13: A schematic drawing of the simulation process for the size distribution.

The size distributions after every collision round are shown in Figure 5.14. For the 3rd-20th collision round, the size distribution can be well-fitted with Gaussian fitting. The values of R-square all exceed 0.995. This means that the size distribution of random collision follows the Gaussian relationship.

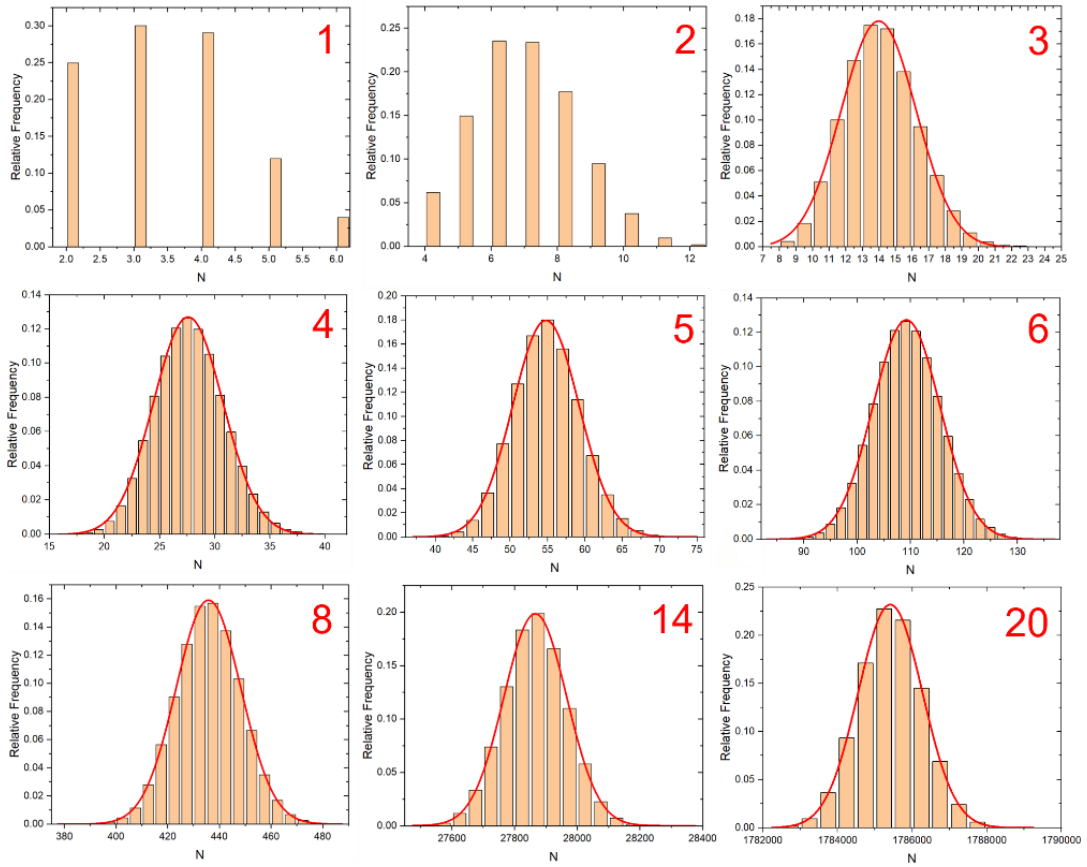


Figure 5.14: The size distributions after every collision round. The red number in the right upper corner is the number of collision round.

In Figure 5.15, there are three results after the 12th collision round based on the described method, in which the shape of size distribution, relative frequency of same size, size range and peak size of these three results are almost the same, indicating that the effect of iteration on the result of next iteration had been limited at a very low level. The best way to eliminate the effect of iteration on the result of the next iteration is by canceling the random selection for every iteration. This means the number of data will multiply by 10 times after every iteration. This method was tested but found to be impractical due to its excessive memory requirements.

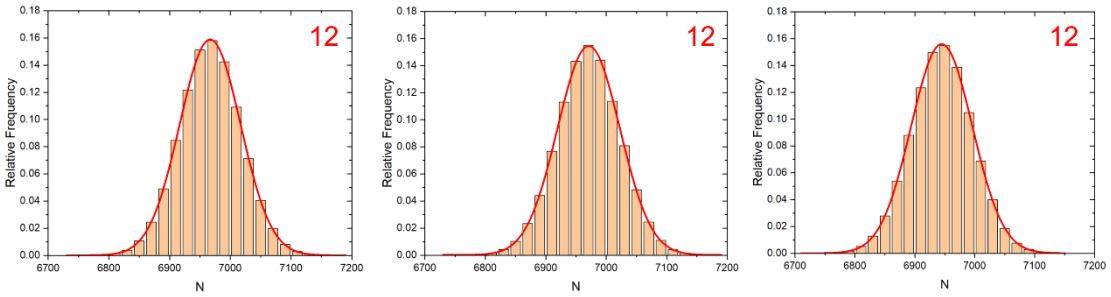


Figure 5.15: The size distributions of the 12th collision round after three-time simulation.

In order to investigate the effect of the proportions of single atoms, dimers, and trimers on the size distribution. Two series of proportions were applied, the first one used 50%, 30%, and 20% as the initial proportions of single atoms, dimers, and trimers, but 80%, 10%, and 10% were applied in the second simulation. Two results after the 12th collision round are shown in Figure 5.16 for these two simulations, whose results can be well fitted with the Gaussian relationship, indicating that the initial proportions of particles will not change the shape of size distribution but will lead to different peak sizes.

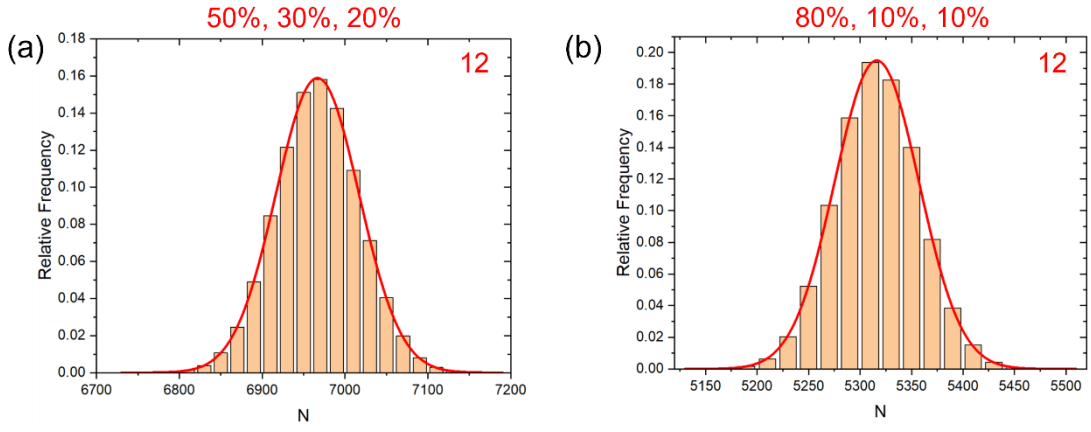


Figure 5.16: The size distributions of different proportions of the initial particles after the 12th collision round. (a) used 50%, 30%, and 20% as the initial proportions of single atoms, dimers, and trimers, but 80%, 10%, and 10% were applied in (b).

Furthermore, the former simulations assume all clusters will collide with another cluster, but 60% of clusters are assumed to conduct collisions in the following part, namely, after the random collision of 60% of particles, 7000 clusters will be obtained, including 3000 aggregated clusters and 4000 initial clusters. The schematic drawing of this simulation method is shown in Figure 5.17. After the collision for 20 times, a dataset with 140000 data can be obtained. Then randomly select 10000 data as the initial dataset for the next collision round.

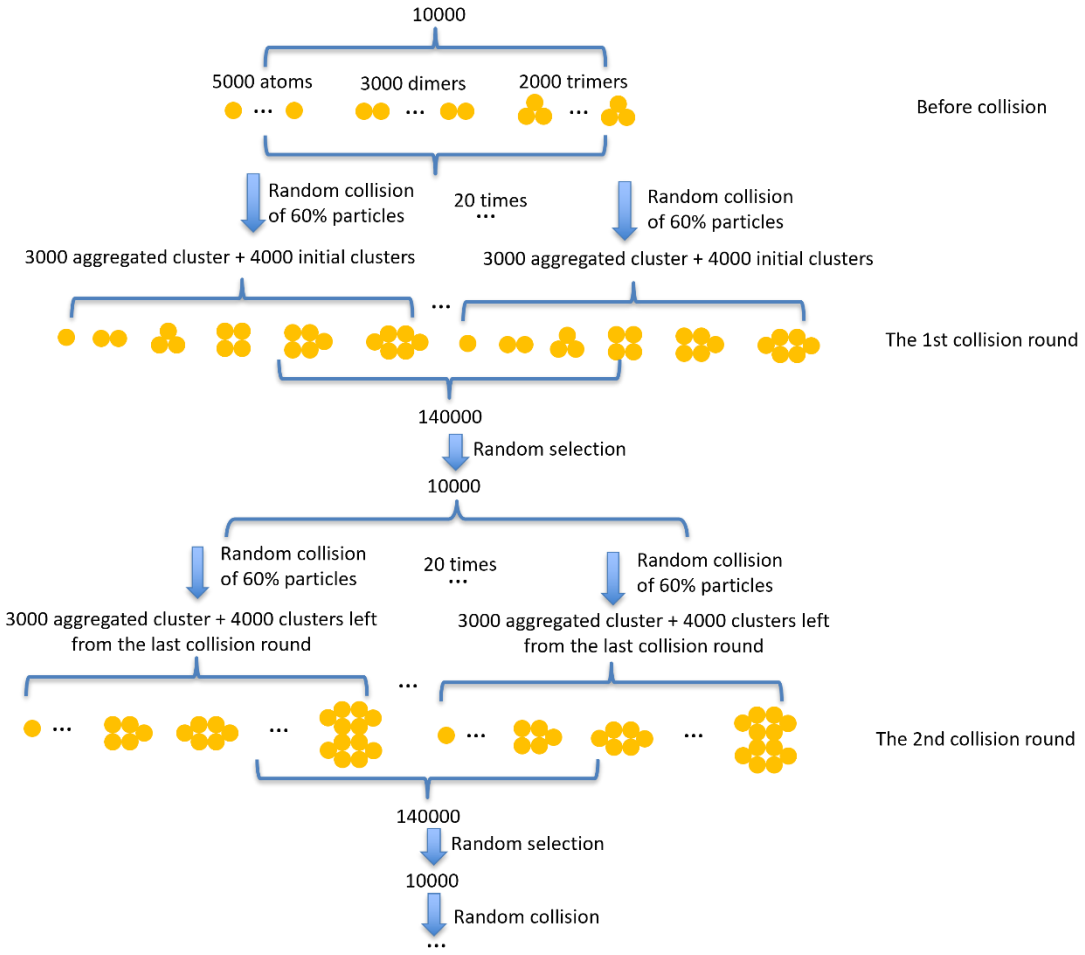


Figure 5.17: A schematic drawing of simulation about the size distribution of clusters after collisions of 60% particles in every collision round.

The results of this insufficient collision simulation are shown in Figure 5.18. For the 3rd-26th collision round, the size distribution can be well fitted with Lognormal fitting. The values of R-square all exceed 0.95. This means that the size distribution of 60% random collision follows the Lognormal relationship.

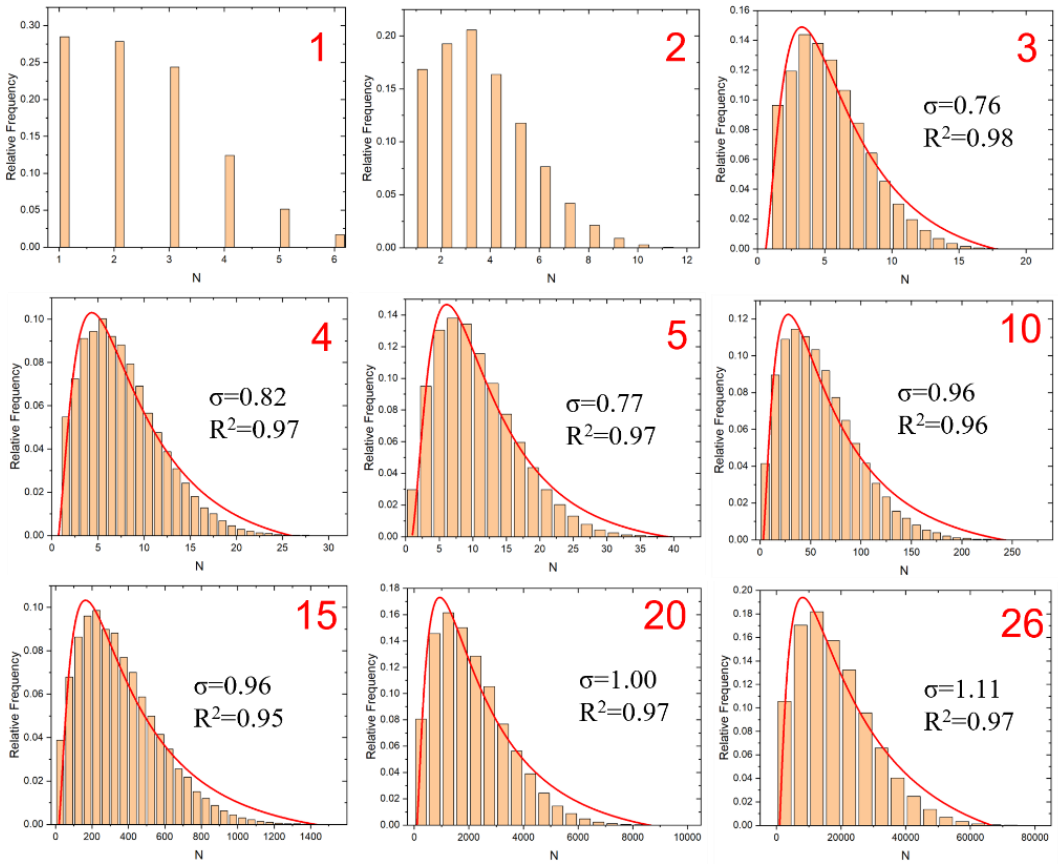


Figure 5.18: The size distributions after collisions of 60% particles in every collision round. The red number in the right upper corner is the collision round.

There are two results after the 23rd collision round of 60% collided particles every round as shown in Figure 5.19, the first one used 50%, 30% and 20% as the initial proportions of single atoms, dimers, and trimers, but 80%, 10% and 10% were applied in the second simulation. These two results can be well-fitted with the Lognormal relationship and their σ, R square and peak sizes are almost the same, indicating that the initial proportions of particles won't change the size distribution too much.

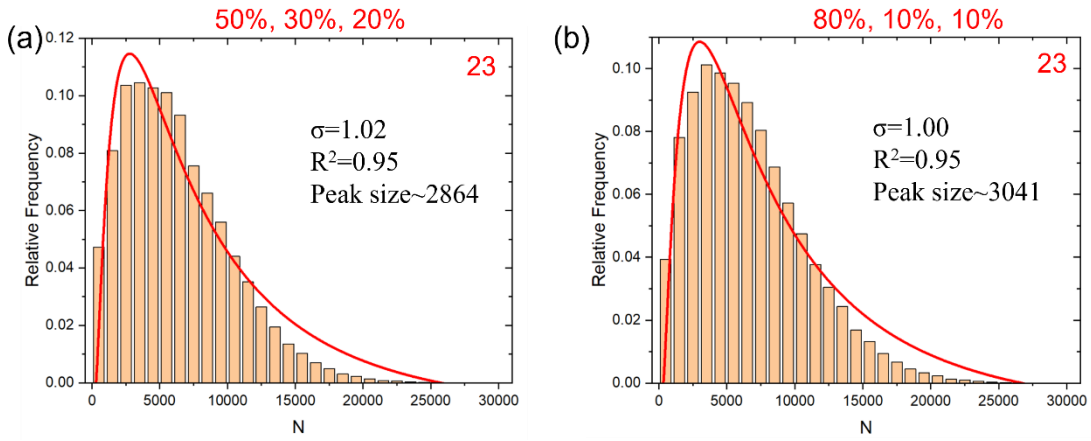


Figure 5.19: The size distributions of different proportions of the initial particles after the 23rd collision round. The fraction of collided particles in every collision round is 60%. (a) used 50%, 30%, and 20% as the initial proportions of single atoms, dimers, and trimers, but 80%, 10%, and 10% were applied in (b).

In Figure 5.20, there are two results after the 20th collision round, the first one used 60% collided particles for every iteration, but 80% were applied in the second simulation. The first simulation can be well fitted with Lognormal fitting with a large value of σ, while the second one is more suitable to be fitted with Gaussian fitting because the R-square of Lognormal fitting is much smaller than that of Gaussian fitting. The results indicate that the percentage of collided particles for every iteration will change the size distribution and a higher percentage of collided particles will lead to size distribution

with the Gaussian relationship.

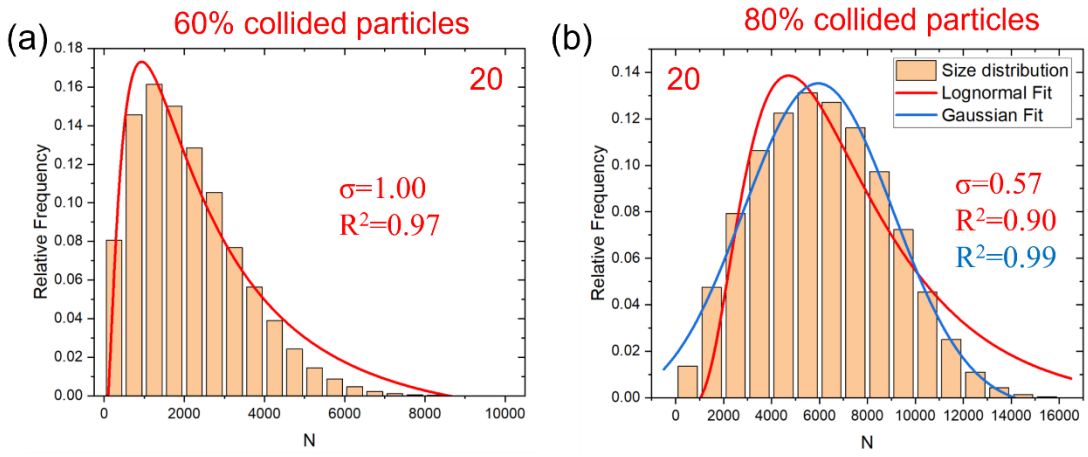


Figure 5.20: The size distributions of different proportions of the initial particles after the 20th collision round. (a) used 50%, 30%, and 20% as the initial proportions of single atoms, dimers, and trimers, but 50%, 30%, and 20% were applied in (b).

In a real situation of cluster growth in the magnetron chamber, a lower Ar gas flow rate will lead to a longer mean free path[115], namely a higher rate of collisions among clusters. The mass spectrum with low Ar gas flow rate is very similar as the size distribution in the simulation with 60% collided particles. In contrast, a higher Ar gas flow rate increases the cluster density and limits the radial diffusion, which will result in more sufficient collisions among clusters. The results of simulations with different percentages of collided particles can explain the size distribution obtained from different Ar gas flow rates.

Several factors during the cluster growth process have not been considered here, such as cluster charging status, the difference in cluster density in different parts of the magnetron chamber, the loss of small clusters by attachment to the walls. Although these factors have not been considered in the simulations, the results of simulations

clearly show that the size distribution will present a Lognormal shape when the collisions between clusters are sufficient, which is corresponding to the trend of size distribution observed in the experiments. When a higher Ar gas flow rate is applied, an increased number of cluster-cluster coalescence events occur, leading to the formation of a size distribution that follows the Lognormal relationship.

5.4 Conclusions

To understand the role of Ar and He gas in the cluster growth process, Ag8k clusters were prepared with different Ar and He gas flow rates. The findings suggest that low Ar flow rates and high He flow rates lead to a significant proportion of elongated clusters. This is believed to be due to the ineffective aggregation process when the Ag8k size is much larger than the peak size.

At low Ar gas flow rates, atom addition is the dominant growth mechanism for Ag8K clusters. However, as the Ar gas flow rate increases, the growth mechanism shifts from atom addition to cluster-cluster coalescence. On the other hand, variations in He gas flow rate do not significantly affect the growth pathway, as the cluster-cluster coalescence pathway remains the dominant mechanism even at a He gas flow rate of 50 sccm.

A simulation has been proposed to explain the relationship between the shape of mass spectrum and the growth process. With sufficient collisions, a size distribution with a Gaussian distribution will be obtained, while the size distribution will show a

Lognormal shape for lower collision rates. The simulation results are consistent with the experimental results observed in Ag8k deposited with different Ar gas flow rates. As for He gas flow rate, it has almost no effect on the cluster growth pathways, so the mass spectrum obtained with different He gas flow rates can always be fitted with Gaussian functions in this work.

Chapter 6 Fabrication of Ag@Cu and Cu@Ag Core-shell Clusters by Magnetron Sputtering Cluster Source

6.1 Introduction

The unique design of the dual-target system of the cluster source, as shown in Figure 2.5 (b), provides the possibility to deposit bimetallic clusters with various structures, including the morphological structures (alloy, core-shell, or Janus) and the atomic structures (such as Ih, Dh, FCC, BCC, or HCP). Investigations about the growth process of Ag clusters have been presented in the previous chapters. Based on the results of Ag clusters, this chapter explores the preparation of AgCu bimetallic clusters. There are large atomic size differences between Ag and Cu atoms (atomic radii: 0.128 nm of Cu atom and 0.1445 nm of Ag atom), and Ag and Cu are bulk immiscible materials. In addition, the large difference between atom numbers of Ag and Cu provides the potential to recognize them separately in HAADF-STEM mode due to the unique Z-contrast imaging. Several investigations have proved that the Cu@Ag (Cu core and Ag shell) and Cu@Au core-shell structures are more stable than Ag@Cu and Au@Cu core-shell structures[48,59]. Moreover, the fast and non-equilibrium growth process of magnetron sputtering method leads to the formation of dominant unstable Ih structure for pure Ag clusters and the abundant FCC structure for Cu clusters. When considering AgCu core-shell clusters, a notable aspect to explore is whether the atoms in the shell adhere to the arrangement of core atoms, resulting in an unconventional structure

compared to their monometallic clusters.

To answer the questions proposed above, the preparation parameters of Ag@Cu and Cu@Ag core-shell clusters were explored with magnetron sputtering in this chapter. The morphological and atomic structures of AgCu bimetallic clusters were confirmed by analyzing the HAADF-STEM images. The results indicate that adjusting the condensation lengths of the two targets can lead to the formation of core-shell structures, and varying the sputtering power of the Cu target can influence the thickness of the Cu shell.

6.2 Fabrication of Ag@Cu core-shell clusters

To prepare Ag@Cu core-shell clusters, different condensation lengths of Ag and Cu targets were applied, namely, 250 mm for the Ag target and 150 mm for the Cu target. With this setting, the Cu atoms and tiny clusters can hopefully attach to the surface of the pre-nucleated Ag clusters in the magnetron sputtering and further lead to the preparation of Ag@Cu core-shell clusters.

Different parameters were applied to explore the preparation of Ag@Cu core-shell clusters, whose mass spectra are shown in Figure 6.1. The power of the Ag target was fixed at 10 W, leading to a similar peak size of mass spectra of Ag target, about Ag12k and about 21k when taking the mass of Cu atom as standard (64 unit per atom). Then, the power of the Cu target was increased from 10 W to 30 W, causing the increasing peak size of Cu. The peak size of the AgCu dual-target system is close to the summary

of the peak size of single Ag and Cu targets when the power of 15 W, 20 W, and 25 W of Cu target were applied.

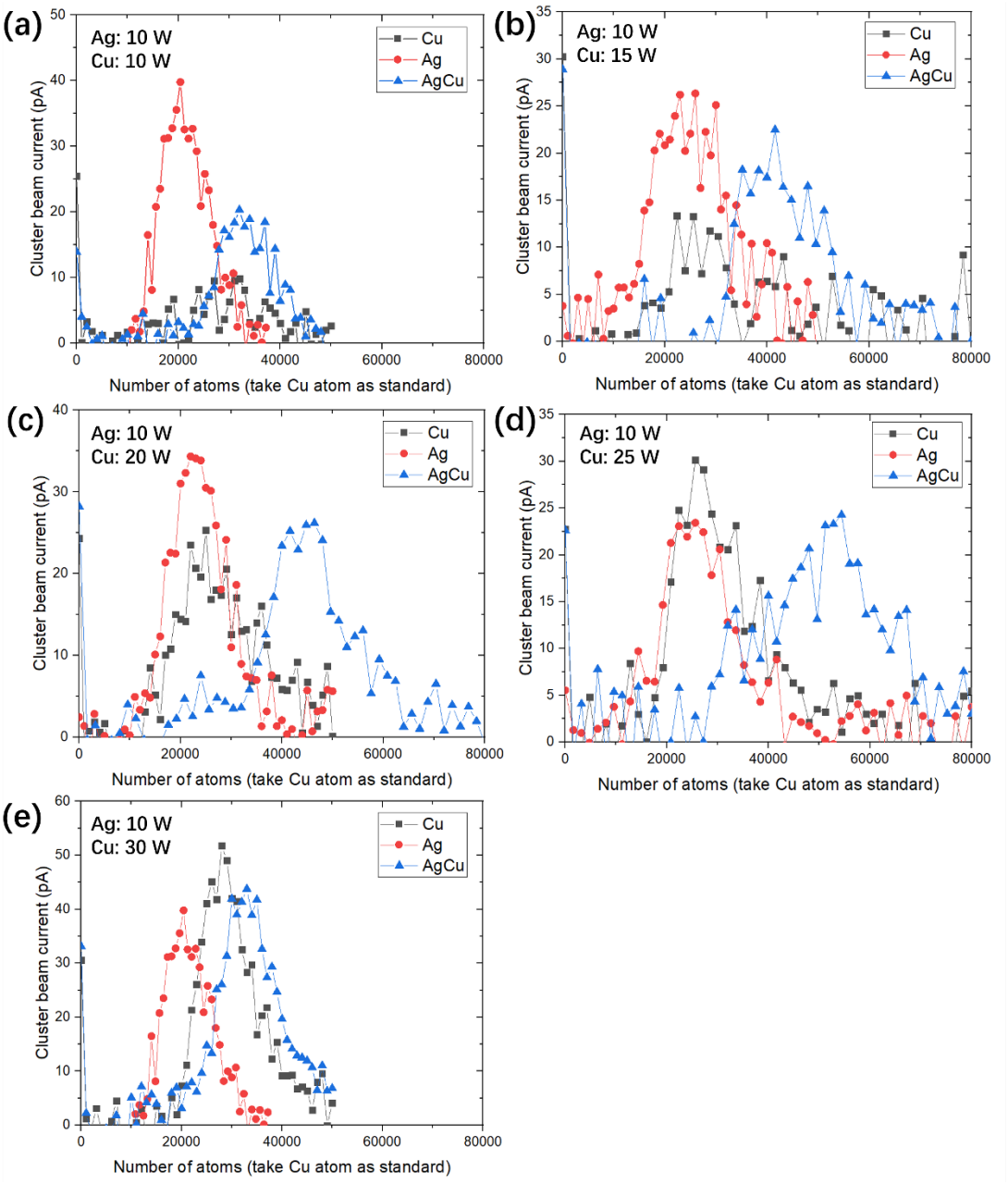


Figure 6.1: Mass spectra of single Ag or Cu target and AgCu dual-target when different parameters were applied to the dual-target system. The X-axis represents the number of atoms in the cluster when the units of Cu mass are used, calculated by dividing the mass of the cluster by the mass of Cu. (a)-(e) 10 W power of Ag target, 80 sccm Ar gas flow rate, no He gas, 250 mm condensation lengths of Ag target, 150 mm condensation lengths of Cu target, and different powers of Cu target. (a) 10 W; (b) 15 W; (c) 20 W; (d) 25 W; and (e) 30 W.

6.2.1 The effect of the Cu target power on the preparation of Ag@Cu core-shell clusters

In order to investigate the impact of the Cu target power on the synthesized bimetallic AgCu clusters, AgCu45k clusters were produced while varying the Cu target power within the range of 10 W to 25 W. When a power of 10 W was applied to each of the Ag and Cu targets, AgCu45k clusters were selected with the mass filter. The overview HAADF-STEM images of AgCu45k clusters are shown in Figure 6.2 (d). In the statistical analysis of the integrated intensity and projected-area-equivalent circle diameter, the AgCu45k clusters exhibit clear clustering behavior, as shown in Figure 6.2 (b). There are three kinds of groups, namely Ag clusters, Cu clusters, and Ag clusters with double mass. No Ag@Cu clusters were found. Ag clusters with double mass can be divided into two parts, as shown in the green ellipse of Figure 6.2 (b). Cluster 2, in the left part of the green ellipse and thus exhibiting a small diameter, is a spherical cluster with double mass according to the HAADF-STEM image of Figure 6.2 (d). However, clusters like Cluster 3, in the right part of the green ellipse and showing a larger diameter, are dumbbell-like clusters, as shown in Figure 6.2 (d). The enlarged image of the blue box in Figure 6.2 (b) is presented in Figure 6.2 (c), in which the clusters marked with ellipses can be identified as pure Ag clusters by their HAADF-STEM images. However, these Ag clusters can be divided into two groups, icosahedral structure (Ag-Ih) marked with a dark green ellipse and decahedral structure (Ag-Dh) marked with a light green ellipse. Figure 6.2 (e) and (f) are two typical examples of Ag-

Dh and Ag-Ih clusters, respectively, in which the projected-area-equivalent circle diameter of Ag-Dh is larger than that of Ag-Ih. The reason for this will be discussed in detail in the third part of this chapter.

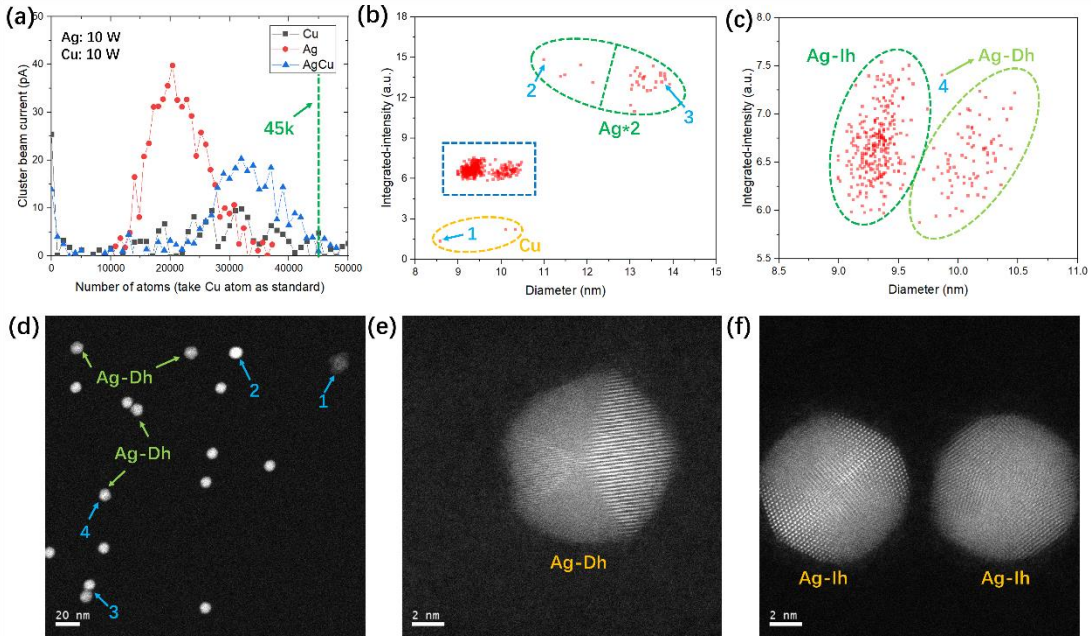


Figure 6.2: (a) Mass spectra of single Ag or Cu target and AgCu dual-target when the power of 10 W was applied on the two targets. (b) The relationship between integrated intensity and projected-area-equivalent circle diameter of 436 analyzed AgCu45k clusters. (c) The enlarged image of the blue box of (b). (d) HAADF-STEM images of prepared clusters. (e) and (f) Examples of prepared Ag-Ih and Ag-Dh clusters.

When the power of the Cu target increased to 15 W, AgCu45k clusters were deposited and the relationship between the integrated intensity and diameter is presented in Figure 6.3 (b). All clusters in the dark green ellipse are Ag@Cu core-shell clusters, whose intensity and diameter depend on the ratio of Ag and Cu atoms. Three examples of Ag@Cu clusters are shown in Figure 6.3 (d), (e), and (f). The false-color images, shown in Figure 6.3 (g), (h), and (i), reveal that the Cu shell is incomplete on the surface of the Ag core.

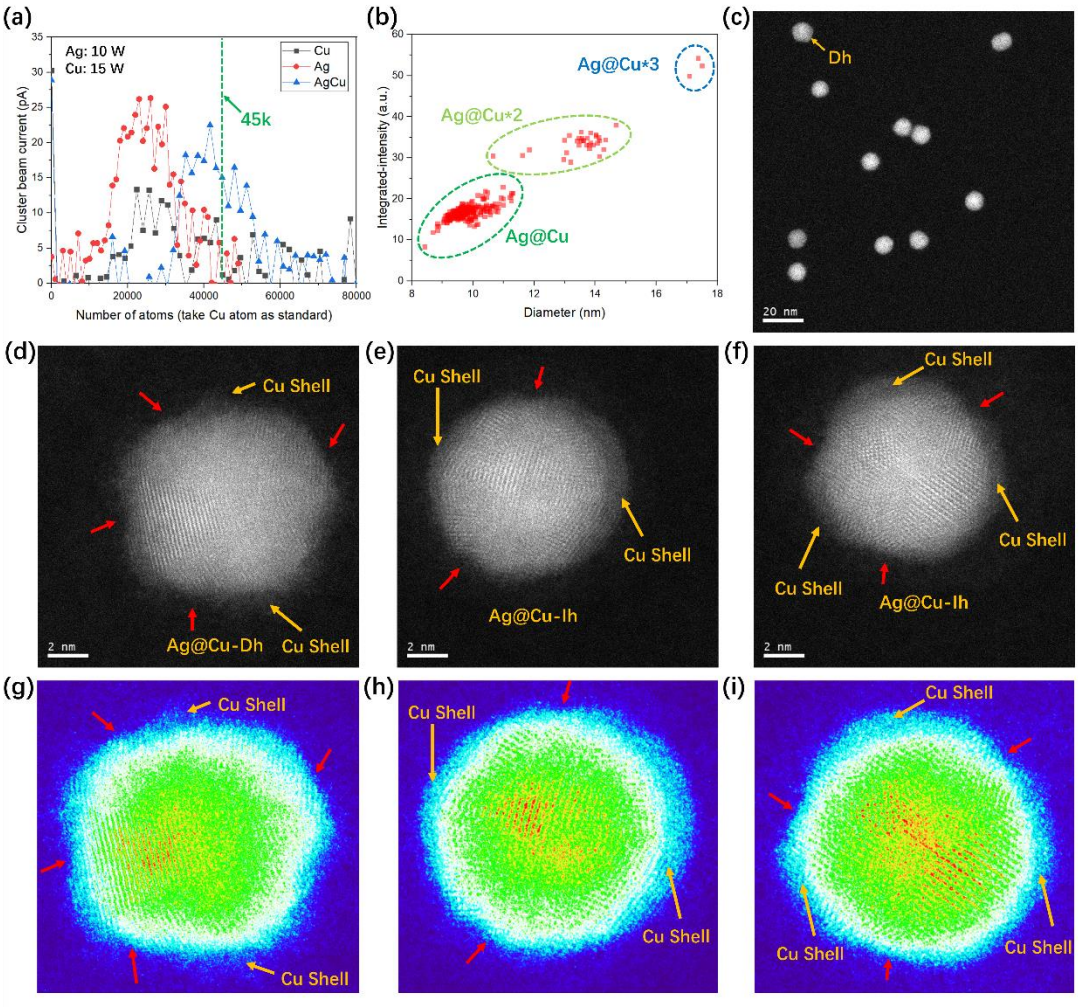


Figure 6.3: (a) Mass spectra of single Ag or Cu target and AgCu dual-target when the power of 10 W and 15 W was applied on the Ag and Cu target, respectively. (b) The relationship between integrated intensity and projected-area-equivalent circle diameter of 353 analyzed AgCu45k clusters. (c) A HAADF-STEM image of prepared clusters. (d)-(f) Examples of prepared Ag@Cu clusters. (g)-(i) The corresponding false-color images of (d)-(f), in which different colors represent the intensities of pixels. The discontinuous Cu shells are marked with yellow arrows and the positions with no shell are pointed out with red arrows.

For AgCu45k clusters deposited with a Cu target power of 20 W, a large percentage of Ag@Cu clusters could also be found as shown in Figure 6.4 (c). Five Ag@Cu clusters with obvious complete Cu shells and their enlarged HAADF-STEM images are shown in Figure 6.4 (d)-(i).

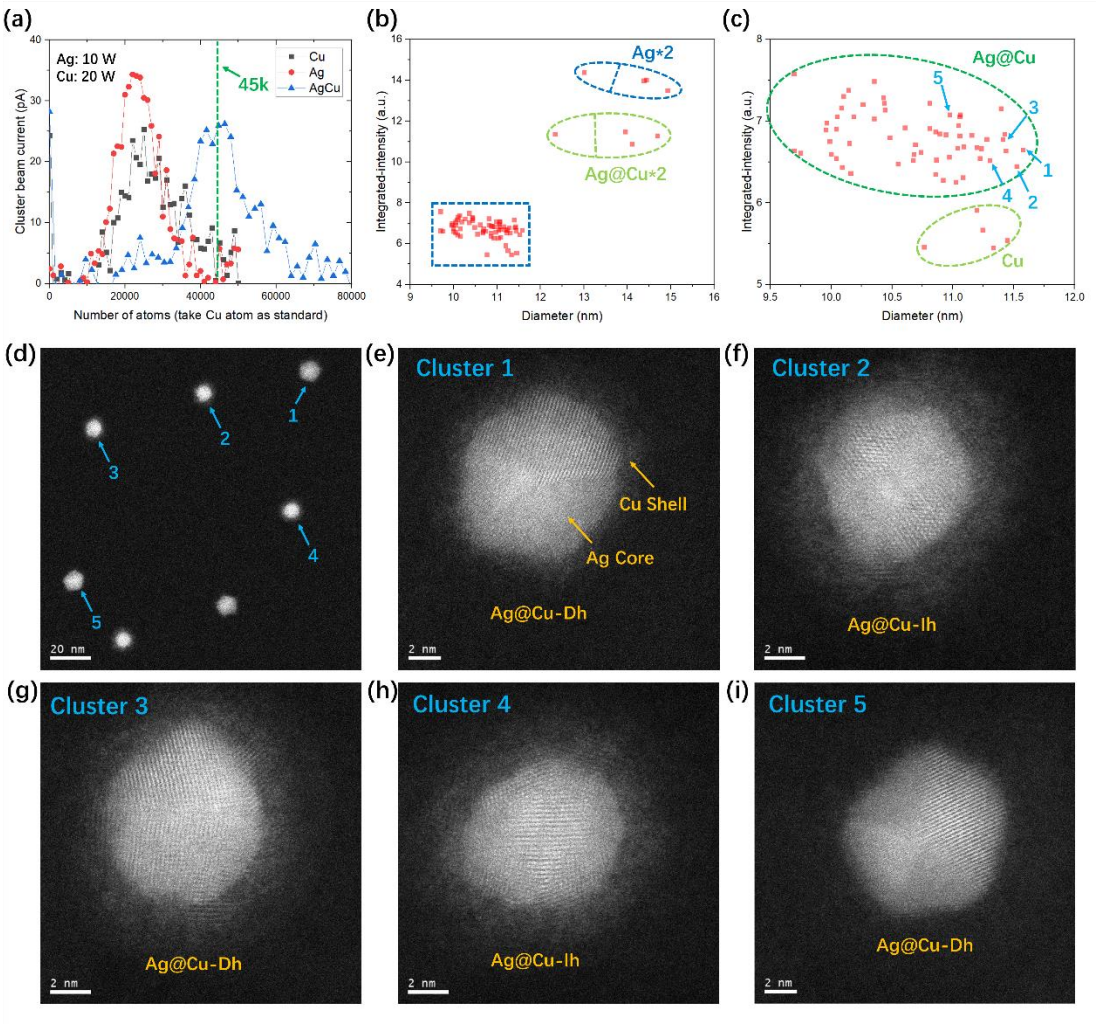


Figure 6.4: (a) Mass spectra of single Ag or Cu target and AgCu dual-target when the power of 10 W and 20 W was applied on the Ag and Cu target, respectively. (b) The relationship between integrated intensity and projected-area-equivalent circle diameter of 73 analyzed AgCu45k clusters. (c) The enlarged image of the blue box of (b). (d)-(i) HAADF-STEM images of prepared clusters.

When the power of the Cu target came to 25 W, the prepared clusters are all Ag@Cu core-shell clusters as shown in Figure 6.5 (b). The enlarged HAADF-STEM images and false-color images presented in Figure 6.5 (d)-(i) clearly show the complete Cu shell on the surface of AgCu45k clusters.

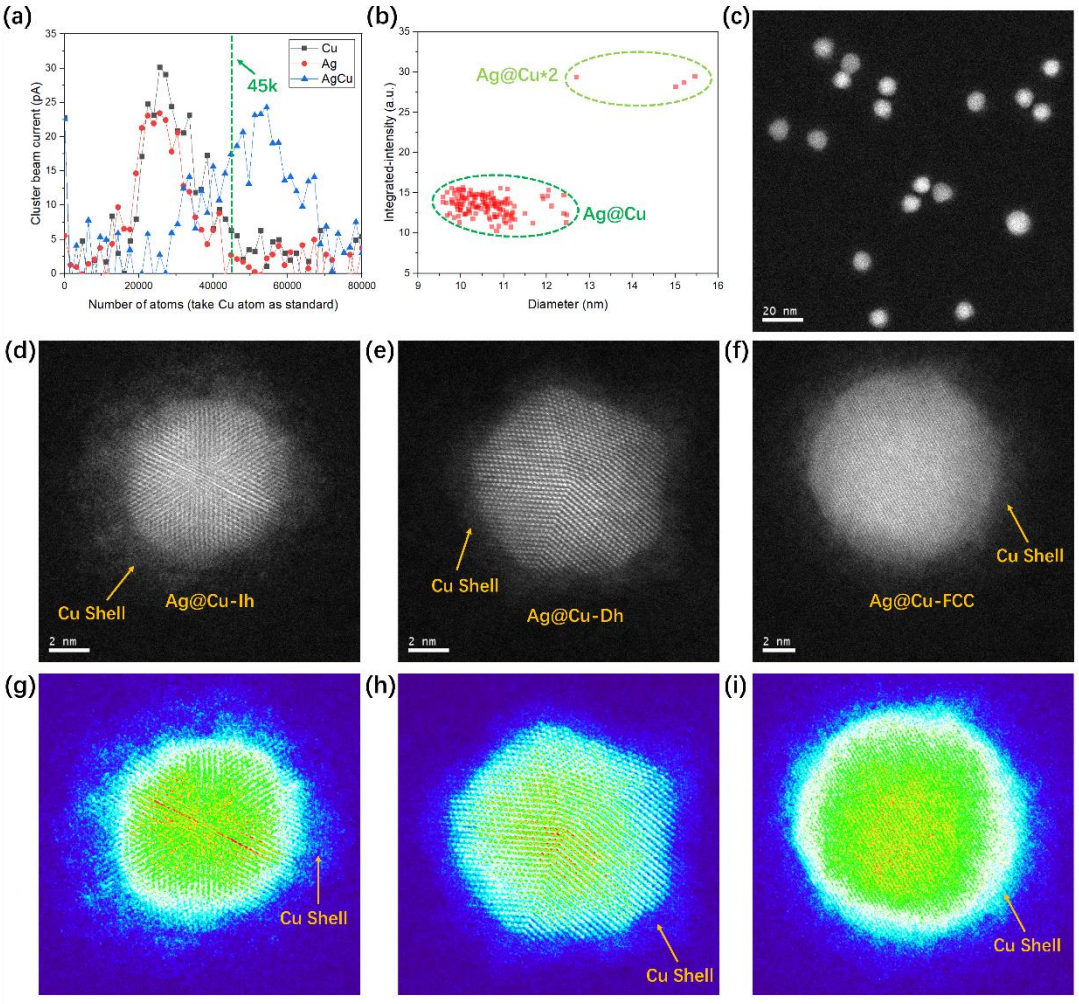


Figure 6.5: (a) Mass spectra of single Ag or Cu target and AgCu dual-target when the power of 10 W and 25 W was applied on the Ag and Cu target, respectively. (b) The relationship between integrated intensity and projected-area-equivalent circle diameter of 142 analyzed AgCu45k clusters. (c) A HAADF-STEM image of prepared clusters. (d)-(f) Examples of prepared Ag@Cu clusters. (g)-(i) The corresponding false-color images of (d)-(f), in which different colors represent the intensities of pixels. The complete Cu shells are marked.

Figure 6.6 presents typical examples of Ag@Cu clusters that were prepared using Cu target powers ranging from 10 W to 25 W. The results indicate that the thickness of the Cu shell in Ag@Cu core-shell clusters increases as the Cu target power increases. It's reasonable that more Cu atoms will be sputtered with the higher power, providing more possibility for the attachment of Cu atoms on the pre-nuclear Ag core and further lead to thicker Cu shell in Ag@Cu core-shell structure. Singh et al. have reported that the Janus and core–satellite structures of Si and Ag dual-target system can be obtained by applying different Si–Ag sputtering power ratios[116]. The two Si and Ag targets were placed in the same plate, leading to the same condensation lengths, which is quite different from our work. The Cu target with shorter condensation length in our work can be seen as providing a coating role for the pre-nucleated Ag clusters.

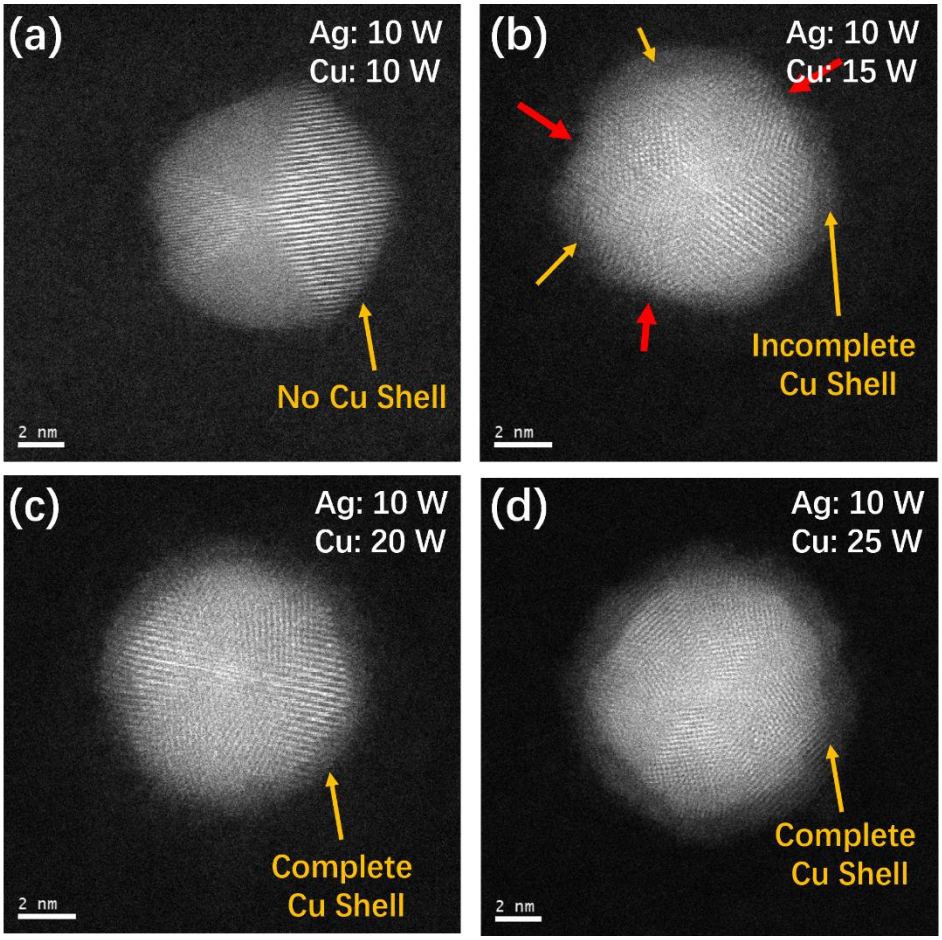


Figure 6.6: HAADF-STEM images of clusters prepared with different powers of Cu target. (a) 10 W; (b) 15 W; (c) 20 W; and (d) 25 W. The discontinuous Cu shells are marked with yellow arrows and the positions with no shell are pointed out with red arrows in (b).

6.2.2 The effect of the selected size on the preparation of Ag@Cu core-shell clusters

To investigate the effect of the selected size on the deposition of Ag@Cu core-shell clusters, AgCu32k, AgCu45k, and AgCu60k clusters were deposited with the Cu target power of 20 W, and the details are shown in Figure 6.7, 6.4, and 6.8, respectively. For AgCu32k clusters, most of them are Cu clusters and the rest are Ag@Cu clusters, according to the statistical results shown in Figure 6.7 (c). Cluster 1, 4 and 5, three examples of Cu clusters shown in Figure 6.7 (e), (k), and (l), present core-shell structures.

The shells may be Cu oxide formed by the oxygen atoms adsorbed on the surface of the carbon film, although the sample was stored in a high vacuum environment of about $10E^{-7}$ mbar for about one or two days after preparation. The Ag@Cu clusters, shown in Figure 6.7 (f) and (h), present obvious Ag core and Cu shell structures, which can be clearly revealed from the false-color image of Figure 6.7 (g) and (i), respectively.

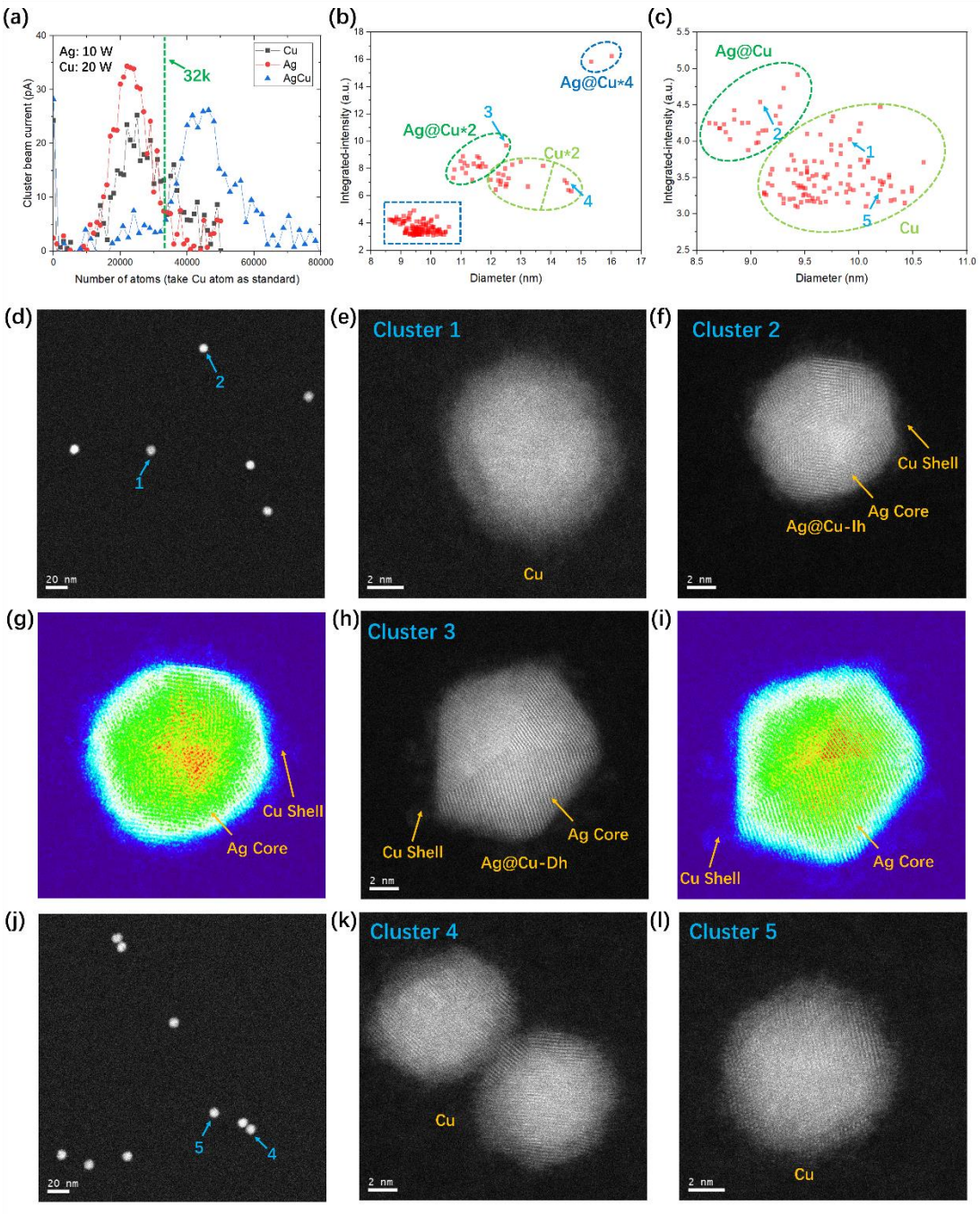


Figure 6.7: (a) Mass spectra of single Ag or Cu target and AgCu dual-target when the power of 10 W and 20 W was applied on the Ag and Cu target, respectively. (b) The relationship between integrated intensity and projected-area-equivalent circle diameter of 162 analyzed AgCu32k clusters. (c) The enlarged image of the blue box of (b). (d) and (j) Low-magnification HAADF-STEM images of prepared clusters. (e), (k), and (l) Examples of prepared Cu clusters. (f) and (h) Examples of prepared Ag@Cu clusters. (g) and (i) The corresponding false-color images of (f) and (h), in which different colors represent the intensities of pixels.

As for deposited AgCu60k clusters, the statistical results shown in Figure 6.8 (c) indicate that the fraction of Ag@Cu clusters is still in a high level. The high-magnification HAADF-STEM and the respective false-color image shown in Figure 6.8 (g) and (h) demonstrate the existence of Ag@Cu clusters. In addition, the Ag@Cu core-shell structure can be further confirmed by the elemental mapping images of EDS results in Figure 6.9. The yellow arrows in different images clearly indicate the Ag and Cu signals comes from the core and the shell of the observed cluster, respectively. Other core-shell clusters with larger sizes than those Ag@Cu clusters, shown in Figure 6.8 (e) and (f), are considered as Cu core-shell clusters. With the evidence provided in Figure 6.9, the large core-shell clusters are further confirmed as pure Cu clusters during deposition and then transformed to core-shell.

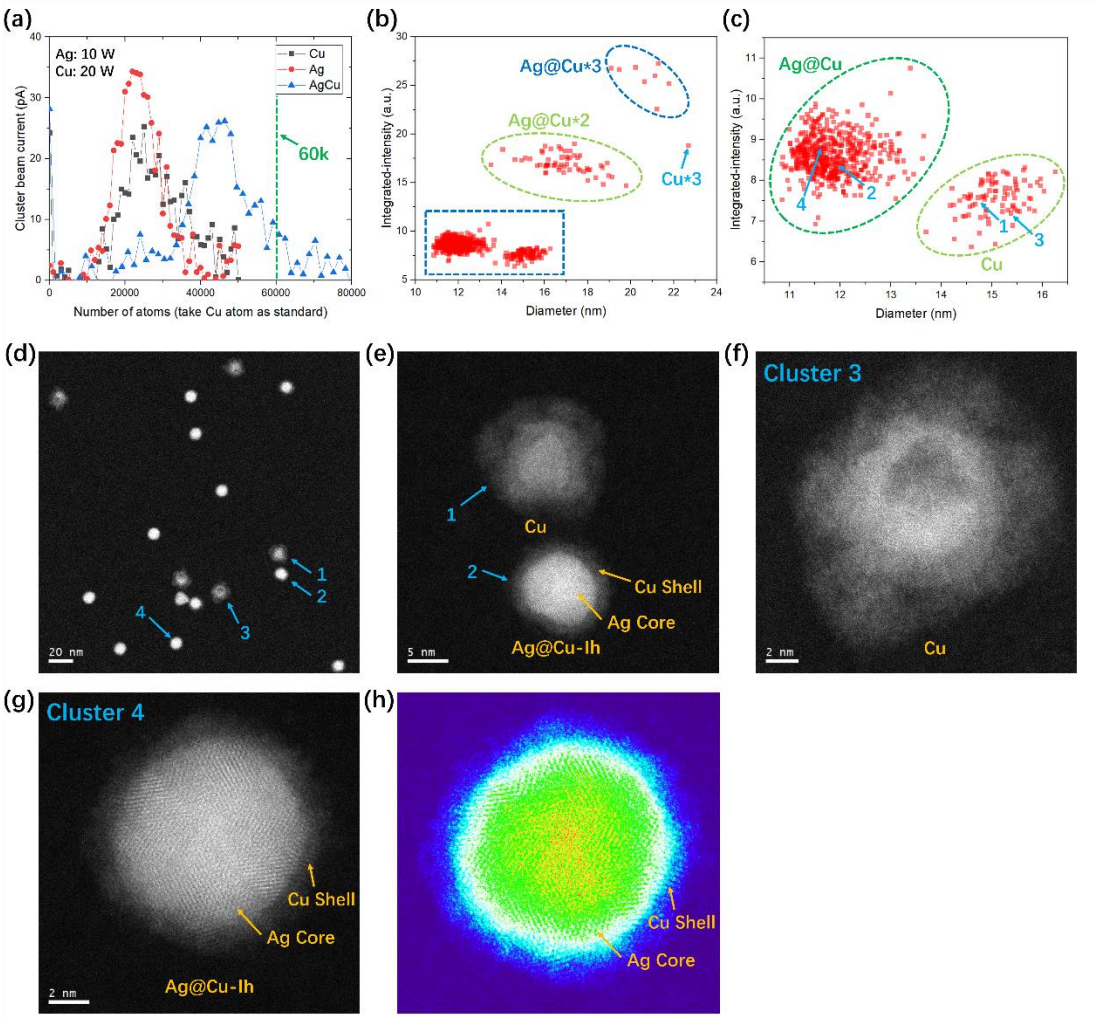


Figure 6.8: (a) Mass spectra of single Ag or Cu target and AgCu dual-target when the power of 10 W and 20 W was applied on the Ag and Cu target, respectively. (b) The relationship between integrated intensity and projected-area-equivalent circle diameter of 736 analyzed AgCu60k clusters. (c) The enlarged image of the blue box of (b). (d)-(g) HAADF-STEM images of prepared clusters. (h) The corresponding false-color image of (g), in which different colors represent the intensities of pixels.

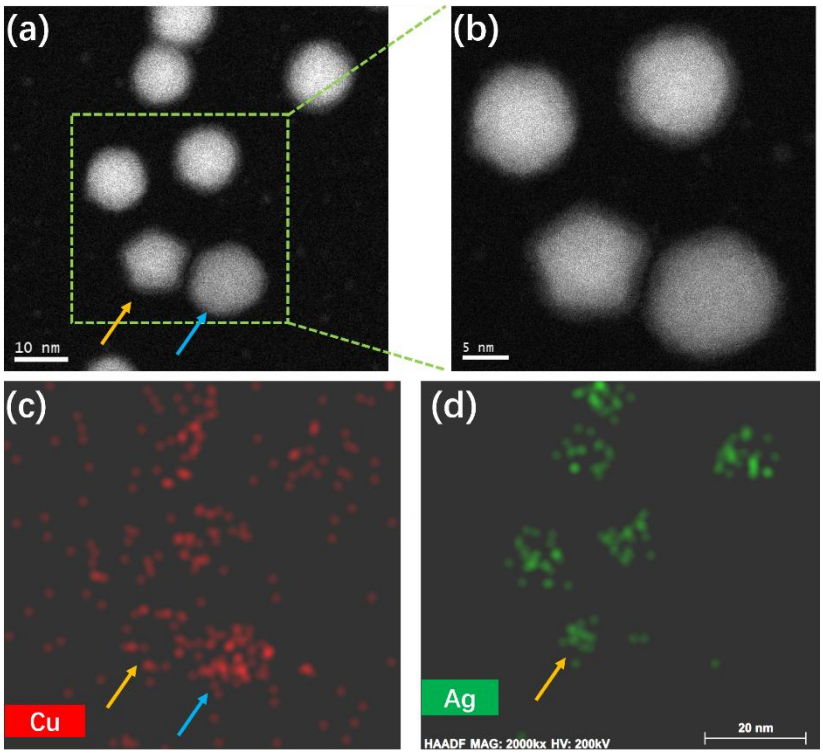


Figure 6.9: (a) A HAADF-STEM image of prepared AgCu60k clusters. (b) The enlarged image of the green box of (a). (c) and (d) The elemental map of Cu and Ag, respectively. The yellow arrows in different images indicate the existence of a Ag@Cu core-shell cluster, while the blue arrows provide the evidence to confirm a pure Cu cluster in (a).

Based on the statistical results in Figure 6.7, 6.4, and 6.8, it is found that 16% of AgCu32k, 95% of AgCu45k, and 85% of AgCu60k clusters are Ag@Cu core-shell clusters, indicating that a high fraction of Ag@Cu clusters can be obtained with a larger cluster size. This can be explained by the fact that the prepared large clusters are typically the products of AgCu bimetallic clusters, which tend to form Ag@Cu core-shell structures when the different condensation lengths of Ag and Cu targets are purposefully applied. In contrast, these small clusters are more likely to be monometallic clusters, such as the pure Cu clusters found in these three samples.

6.2.3 The effect of the Cu target plasma on the preparation of Ag@Cu core-shell clusters

When applying a power of 10 W to both Ag and Cu targets simultaneously, a mass spectrum with a peak size of approximately 32k can be obtained, as shown in Figure 6.2 (a). The increased peak size in the dual-target system compared to the peak size of about 21k when only the Ag target was on can be due to the effect of Cu target plasma. When the dual-target system is on, the prepared Ag clusters pass through the Cu target plasma because of the longer condensation length of the Ag target. The high temperature environment of the Cu target plasma can promote the growth of Ag clusters, resulting in larger Ag cluster sizes and spherical morphologies. To further verify this effect, AgCu32k clusters were deposited under the same parameters as Figure 6.2, and the details are presented below.

The overview HAADF-STEM images of AgCu32k clusters are shown in Figure 6.10 (e) and (h). In the statistical analysis of the integrated intensity and projected-area-equivalent circle diameter, the AgCu32k clusters exhibit clear clustering behavior, as shown in Figure 6.10 (b). The enlarged image of the blue box in Figure 6.10 (b) is presented in Figure 6.10 (c), in which the clusters marked with ellipses can be identified as Ag-Ih and Ag-Dh clusters by their HAADF-STEM images. One example, each of these two structures is shown in Figure 6.10 (d). Except for pure Ag clusters marked with ellipses in Figure 6.10 (c), there are a further three data points marked with 1, 2, and 3. The respective HAADF-STEM images and false-color image are shown in

Figure 6.10 (e), (f), and (g), identifying these clusters as exhibiting a Ag@Cu core-shell structure. The Cu shell of Cluster 3 is thicker than that of another two clusters, leading to a larger projected-area-equivalent circle diameter. Clusters in the orange ellipse of Figure 6.10 (b), which exhibit large diameters but low intensities, are identified as pure Cu clusters. The HAADF-STEM image with low and high magnification of Cluster 4 in Figure 6.10 (b) is shown in Figure 6.10 (h) and (i), respectively. The amorphous structure and uncomplete spherical morphology of pure Cu clusters may be caused by Cu atom diffusion on the surface of the carbon film or oxidation with the oxygen atoms adsorbed on the surface of carbon film. The formation of clusters 5 and 6 in Figure 6.10 (h) can be caused by the coincidental attachment of two clusters during deposition. Another possibility is that these clusters are coalescence clusters with double mass and double charge, so that they can pass the mass filer successfully. These dumbbell-like clusters are clustered in one group marked with a green ellipse in Figure 6.10 (b).

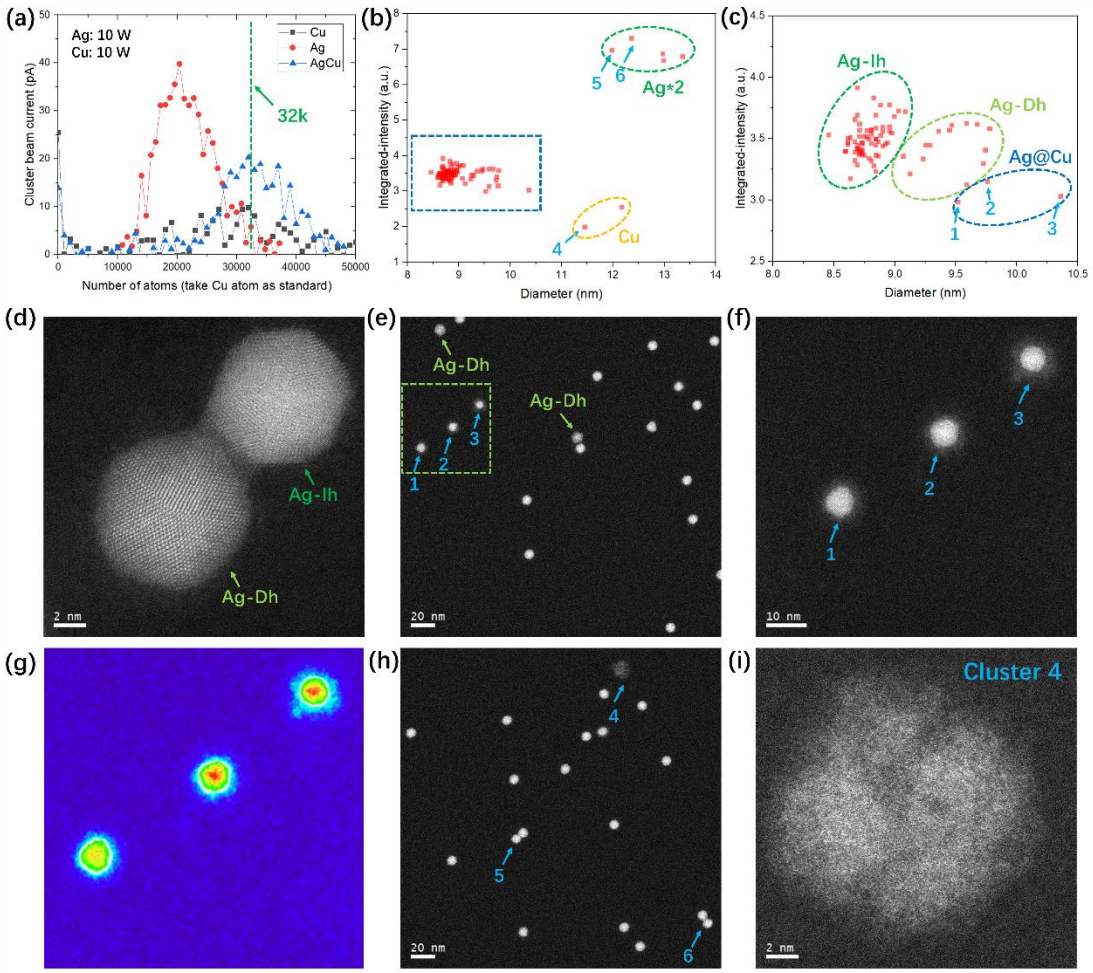


Figure 6.10: (a) Mass spectra of single Ag or Cu target and AgCu dual-target when 10 W was applied on the two targets. (b) The relationship between integrated intensity and projected-area-equivalent circle diameter of 90 analyzed AgCu32k clusters. (c) The enlarged image of the blue box of (b). (d) An example of prepared Ag-Ih and Ag-Dh clusters. (e) and (h) HAADF-STEM images of prepared clusters. (f) The enlarged image of the green box in (e). (g) The corresponding false-color image of (f), in which different colors represent the intensities of pixels. (i) The high-magnification HAADF-STEM image of cluster 4 marked in (b) and (h).

The dominant spherical Ag clusters in Figure 6.10 confirm the promotion effect of the Cu target plasma on the growth of Ag clusters. In addition, the results shown in Figure 6.6 indicate that the thicker Cu shell can be obtained with higher power applied on the Cu target. Thus, AgCu32k and AgCu45k clusters were deposited to check this rule when the power of the Cu target was increased to 30 W. All AgCu32k clusters are Cu clusters, which can be revealed from the relationship between the integrated intensity and diameter in Figure 6.11 (b), as well as the FFT pattern in Figure 6.11 (e) and the lattice distance in Figure 6.11 (f). To further confirm the composition of clusters under these parameters, AgCu45k clusters were analyzed and details are shown in Figure 6.12. The vast majority of the prepared clusters are Cu clusters.

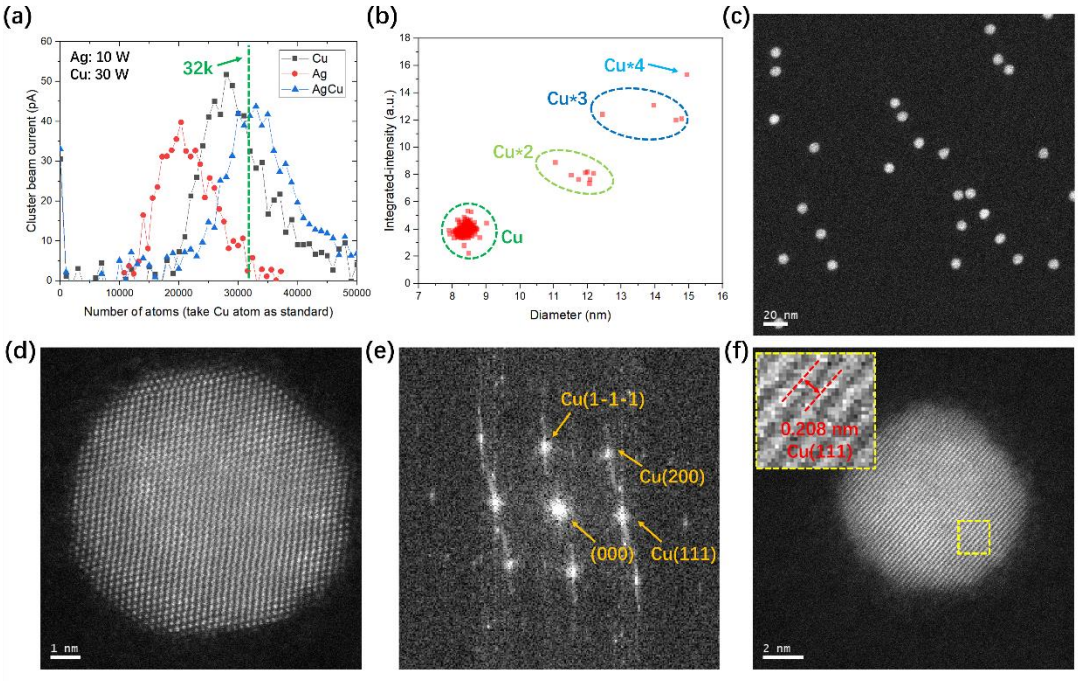


Figure 6.11: (a) Mass spectra of single Ag or Cu target and AgCu dual-target when the power of 10 W and 30 W was applied on the Ag and Cu target, respectively. (b) The relationship between integrated intensity and projected-area-equivalent circle diameter of 298 analyzed AgCu32k clusters. (c), (d), and (f) HAADF-STEM images of prepared clusters. (e) The FFT pattern of the cluster shown in (d). The inserted image of (f) is the enlarged image of the yellow box to show the Cu [111] lattice.

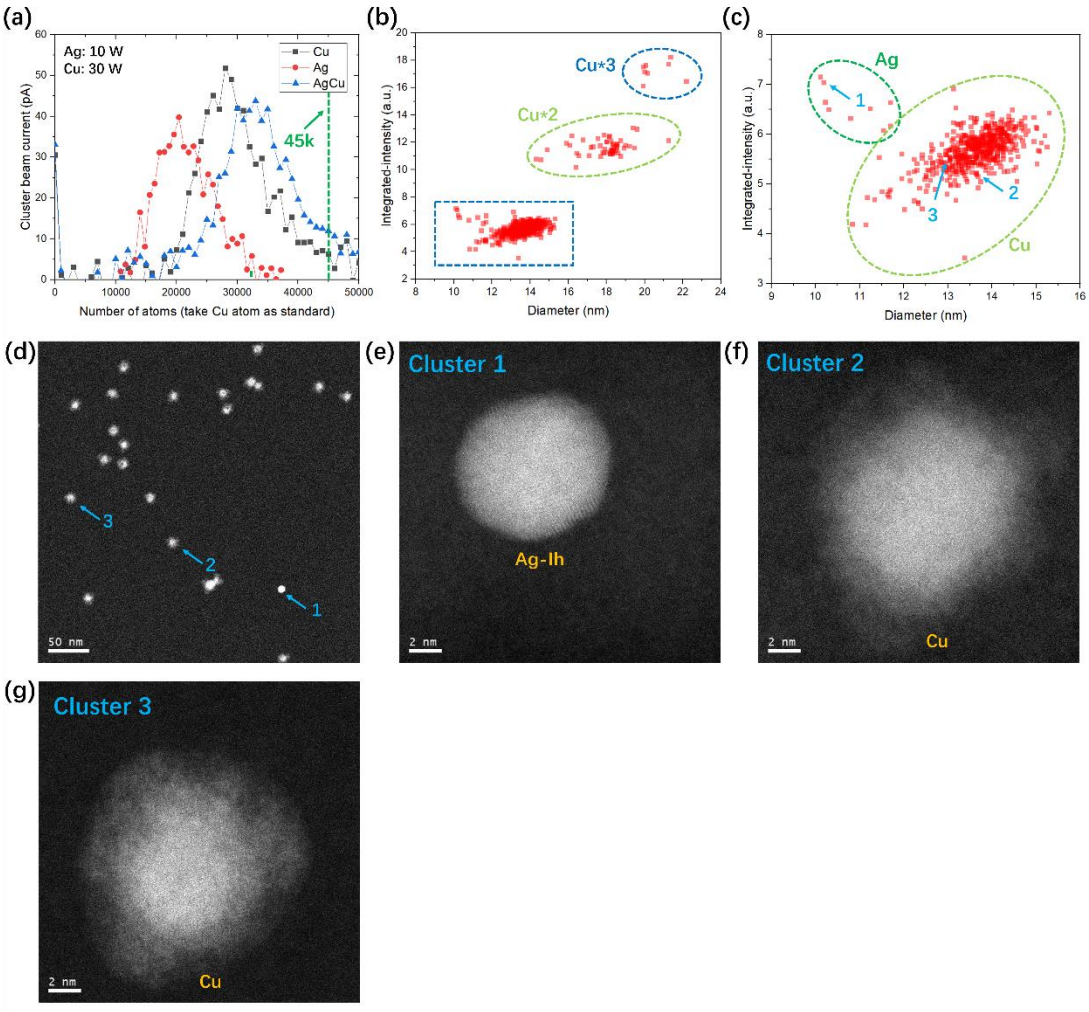


Figure 6.12: (a) Mass spectra of single Ag or Cu target and AgCu dual-target when the power of 10 W and 30 W was applied on the Ag and Cu target, respectively. (b) The relationship between integrated intensity and projected-area-equivalent circle diameter of 593 analyzed AgCu45k clusters. (c) The enlarged image of the blue box of (b). (d)-(g) HAADF-STEM images of prepared clusters.

The disappearance of Ag@Cu clusters is unexpected when the power of 30 W was applied to the Cu target. To explore the reason for the disappearance of Ag@Cu clusters, a sample was directly deposited after the magnetron sputtering chamber. As shown in Figure 6.13, Ag@Cu and Cu clusters can be clearly recognized by comparing the HAADF-STEM images and their respective bright-field (BF) images. In this sample, the statistical percentage of Ag@Cu clusters is about 45% in 375 prepared clusters with various sizes. As for clusters deposited after the mass filter, a sample with cluster size

in the range of 10k to 50k was deposited to eliminate the composition differences between clusters of different sizes. The results are presented in Figure 6.14. Almost all of the prepared clusters are Cu, although these Cu clusters were dissociated when stored in a high vacuum environment of about $10E^{-7}$ mbar for five days after preparation. The absence of Ag@Cu clusters after the mass filter could be due to a predominantly negative or neutral charge status of Ag@Cu clusters caused by the high power of the Cu target, so that no Ag@Cu clusters passed the mass filter.

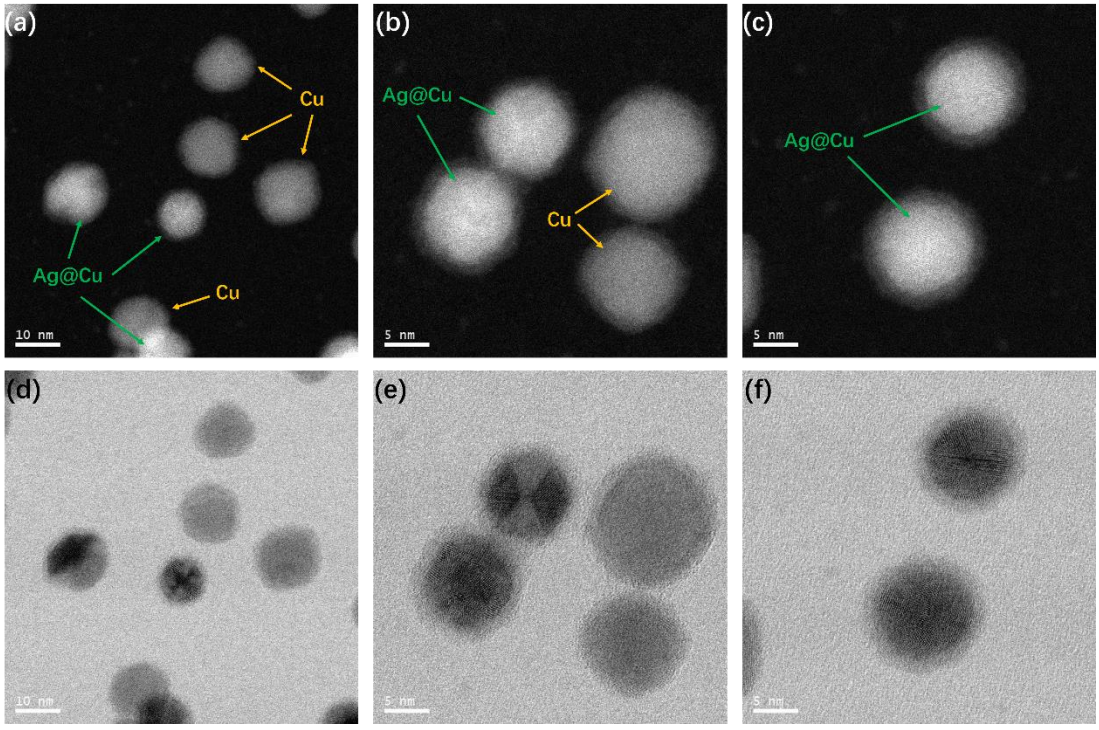


Figure 6.13: (a), (b), and (c) HAADF-STEM images of clusters prepared after the magnetron sputtering chamber. (d), (e), and (f) BF images of (a), (b), and (c), respectively.

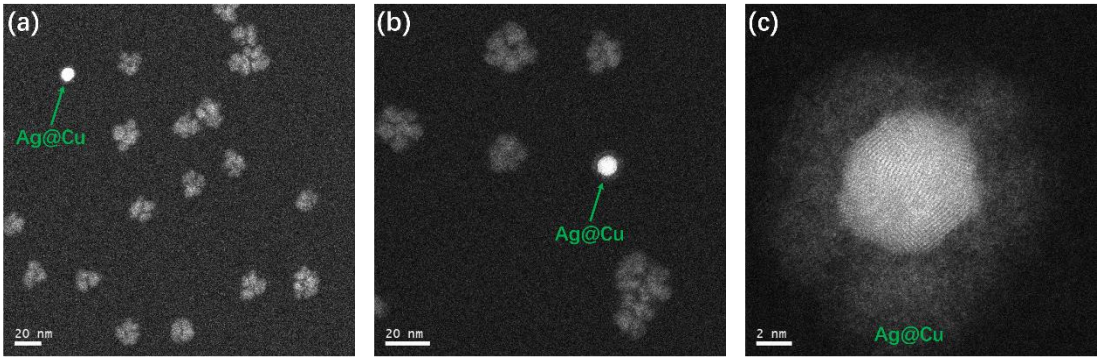


Figure 6.14: HAADF-STEM images of clusters prepared after the mass filer in the size range of 10k to 50k.

6.2.4 The atomic structures of Ag@Cu core-shell clusters

The atomic structures of Ag@Cu clusters are shown in detail in Figure 6.15. The Cu atoms arrange according to the surface arrangement of the Ag core, as shown in Figure 6.15 (b) and (d). The intensity profile in Figure 6.15 (f) shows the expected decrease in the intensity of Cu layers. The layer spacing of Ag and Cu atoms is about 0.231 nm and 0.200 nm, respectively, which is close to the Ag (111) and Cu (111) atom plane distances, respectively.

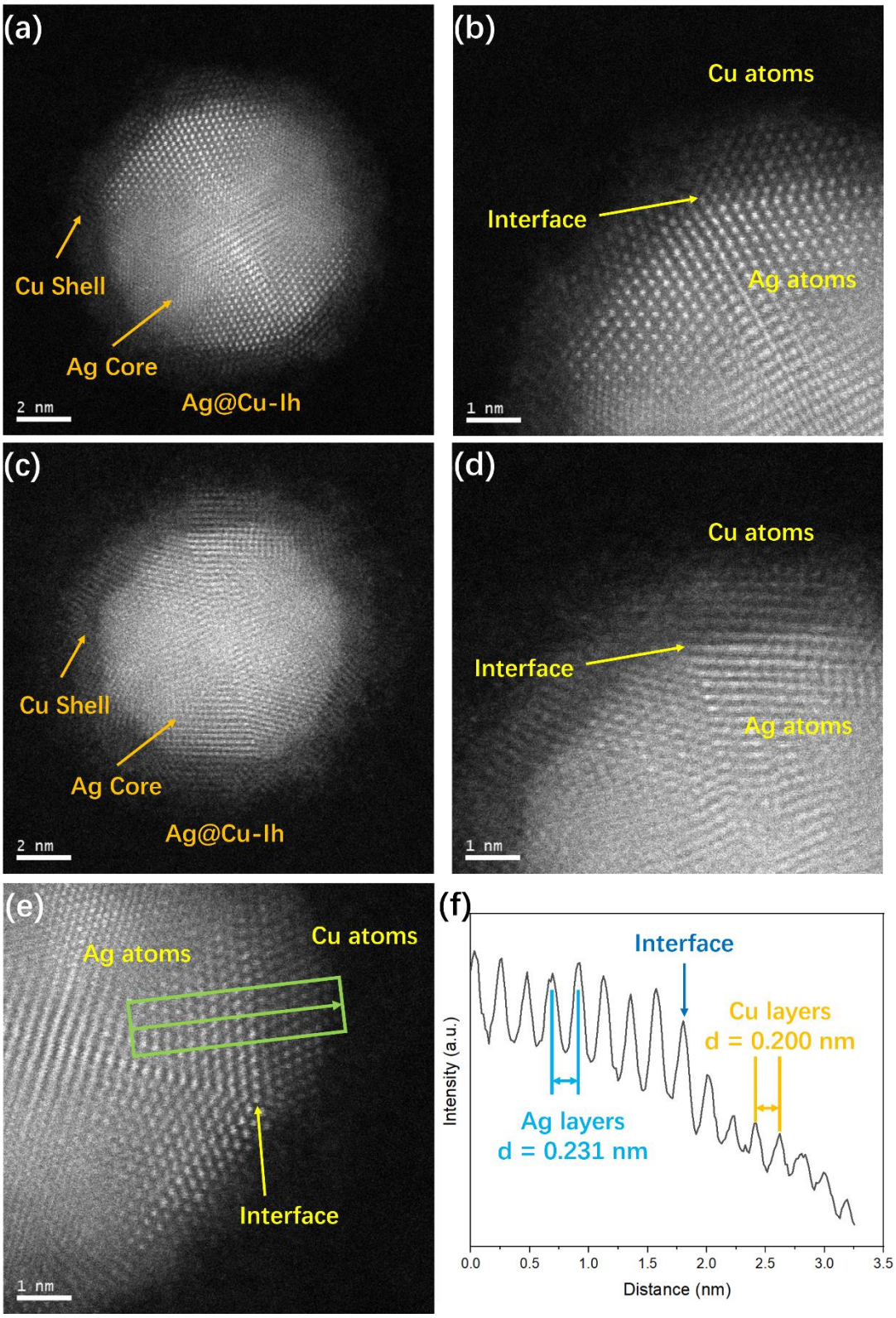


Figure 6.15: (a)-(e) HAADF-STEM images of prepared Ag@Cu 45k clusters. (f) The intensity profile of the green box in (e). The green box is oriented perpendicular to the atomic plane and indicates the scanning direction of the intensity profile. A wider box width is chosen to maximize the signal strength, thereby obtaining a more precise measurement of the atomic plane distance.

6.2.5 Summary

A table that summarizes the main compositions of prepared clusters with different parameters is shown in Table 6.1. When the power of the Cu target is 10 W, the deposited clusters are almost all Ag clusters. With increasing power of the Cu target, Ag@Cu clusters start to be observed and the thickness of Cu shell will increase. However, at high power of 30 W the charge of Ag@Cu clusters changes to negative or neutral, causing the disappearance of Ag@Cu clusters after the mass filter. The results indicate that a power range of 15 W to 25 W for the Cu target is optimal for synthesizing size-selected Ag@Cu clusters. For the AgCu clusters prepared with the same parameters, a high fraction of Ag@Cu core-shell clusters will be obtained with larger sizes. Regarding the atomic structures of the prepared Ag@Cu clusters, the Cu atoms always arrange according to the surface arrangement of the Ag core. In addition, the Cu target plasma will promote the growth of the passing Ag clusters, leading to a larger size and the spherical morphology. On the other hand, the Cu target plasma can alter the charge status of passing clusters. The absence of Ag@Cu core-shell clusters in Figure 6.11 and Figure 6.12 can be the consequence of negatively or neutrally charged Ag@Cu clusters.

Table 6.1: The main compositions of prepared clusters with different applied power on the Cu target.

Power of Cu target (W)	Size of clusters	Number of analyzed clusters	Composition
10	32k	85	95% Ag + 2% Cu + 3% Ag@Cu
	45k	423	99% Ag + 1% Cu
15	45k	335	100% Ag@Cu
20	32k	148	16% Ag@Cu + 84% Cu
	45k	196	95% Ag@Cu + 5% Cu
	60k	608	85% Ag@Cu + 15% Cu
25	45k	138	100% Ag@Cu
30	32k	290	100% Cu
	45k	572	2% Ag + 98% Cu

6.3 Fabrication of Cu@Ag core-shell clusters

With different condensation lengths of Ag and Cu targets, Ag@Cu core-shell clusters have been successfully prepared, as described in the last part. In this subsection, the outcome when using the same condensation length of 250 mm for both the Ag and Cu target is explored. An overview of the resulting clusters at 10 W per target is shown in Figure 6.16. About 73% and 27% of the prepared AgCu20k clusters are Ag and Cu@Ag clusters, respectively. The false-color image in Figure 6.16 (f) and the intensity profile in Figure 6.16 (h) both indicate a higher intensity at the edge of the prepared clusters. As the intensity in HAADF-STEM is Z-dependent, this reveals that the shell of the

core-shell cluster is Ag.

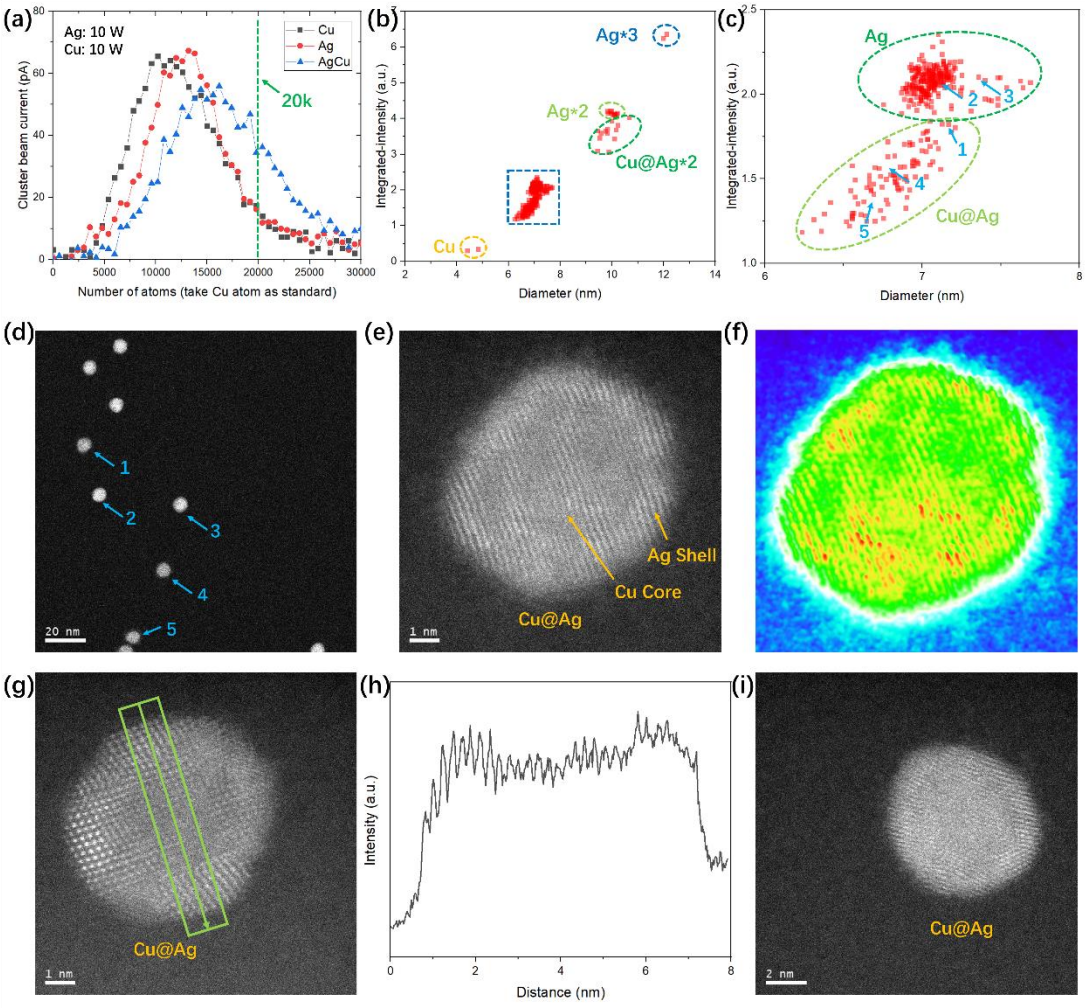


Figure 6.16: (a) Mass spectra of single Ag or Cu target and AgCu dual-target when the power of 10 W was applied on the Ag and Cu target, respectively. The other parameters are 120 sccm Ar gas flow rate, no He gas, and the same condensation length of 250 mm for both the Ag and Cu target. (b) The relationship between integrated intensity and projected-area-equivalent circle diameter of 372 analyzed AgCu20k clusters. (c) The enlarged image of the blue box of (b). (d), (e), (g), and (i) HAADF-STEM images of prepared clusters. (f) The corresponding false-color image of (e), in which different colors represent the intensities of pixels. (h) The intensity profile of the green box in (g). The green box is oriented perpendicular to the atomic plane and indicates the scanning direction of the intensity profile. A wider box width is chosen to maximize the signal strength, thereby obtaining a more precise measurement of the atomic plane distance.

The atomic details of Cu@Ag clusters are shown in Figure 6.17. The intensity profile of Figure 6.17 (b) indicates the lattice spacing of the inner and outer atom layers are 0.207 nm and 0.234 nm, which are close to Cu (111) and Ag (111), respectively, proving the cluster shown in Figure 6.17 (a) is a Cu@Ag core-shell cluster. Meanwhile, the fast Fourier transform (FFT) images shown in Figure 6.17 (d) and (f) further point out the Ag atoms in Figure 6.17 (c) and (e) arrange as FCC structures in the shells of the prepared core-shell clusters. The absence of distinctive features of Cu cores in Figure 6.17 (c) and (e) makes it difficult to identify the structures of cores. However, the shape of the Cu core in Figure 6.17 (e) is close to a regular hexagon, and the three FCC domains pointed out by the yellow trapezoids seems to arrange on the three edges of the hexagon. Based on this, two possible core-shell structures are proposed, shown in Figure 6.17 (g) and (h). Both the Dh and Ih inside as the core can meet the projected hexagon-shape. This special configuration has been observed by Alvaro Mayoral et al. in Co@Au core-shell clusters, as shown in Figure 6.17 (i), in which the Co-Ih core is surrounded by 10 Au FCC domains[117].

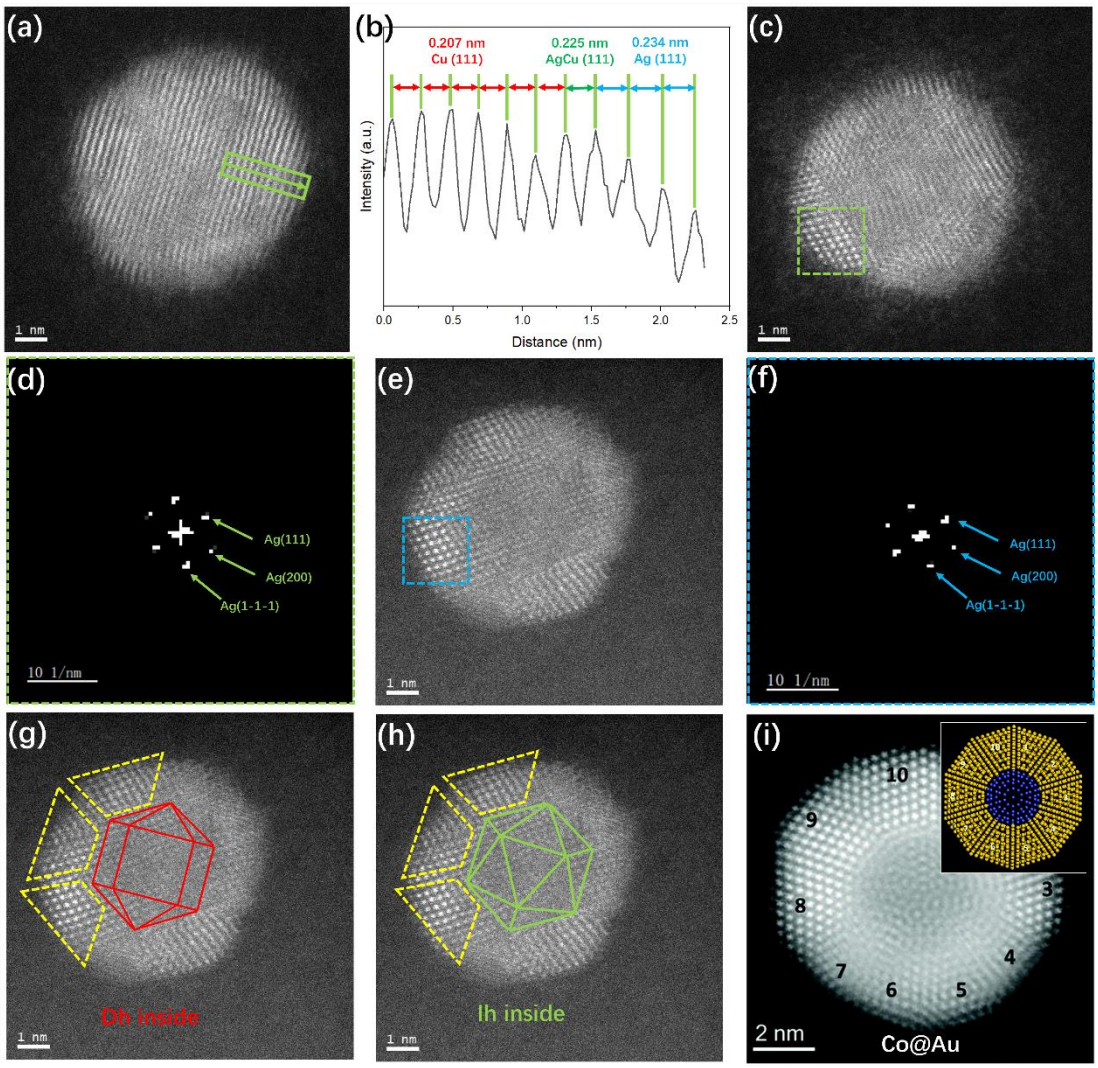


Figure 6.17: (a), (c), and (e) HAADF-STEM images of prepared Cu@Ag 20k clusters. (b) The intensity profile of the green box in (a). The green box is oriented perpendicular to the atomic plane and indicates the scanning direction of the intensity profile. A wider box width is chosen to maximize the signal strength, thereby obtaining a more precise measurement of the atomic plane distance. (d) and (f) The FFT images of the green and blue box in (c) and (e), respectively. (g) and (h) Two possible structures for (e). The yellow trapezoids indicate three domains of Ag shell, and the possible inside Dh and Ih are shown with red and green structures in (g) and (h), respectively. (i) HAADF-STEM image of a Co-Ih core and a shell formed by 10 Au FCC domains. The inset is the schematic model of this Co@Au cluster[117].

A AgCu@Ag core-shell cluster with a clear crystalline arrangement of inner atoms was selected to observe the phase separation process under e-beam irradiation. The FFT image of Figure 6.18 (b) indicates that the inner part is AgCu alloy. Then, the intensity of the inner part gradually decreases in 3 minutes. The FFT images of the final HAADF-STEM image in Figure 6.18 (h) and (i) reveal that the initial AgCu@Ag core-shell cluster had separated into a Cu core and Ag shell. By analyzing the Figure 6.18 (e), the core-shell structure can be considered as a Cu-Ih or Cu-Dh core and a shell formed by six Ag FCC domains. The surface segregation of Ag atoms has been confirmed by other simulation works[59,118,119].

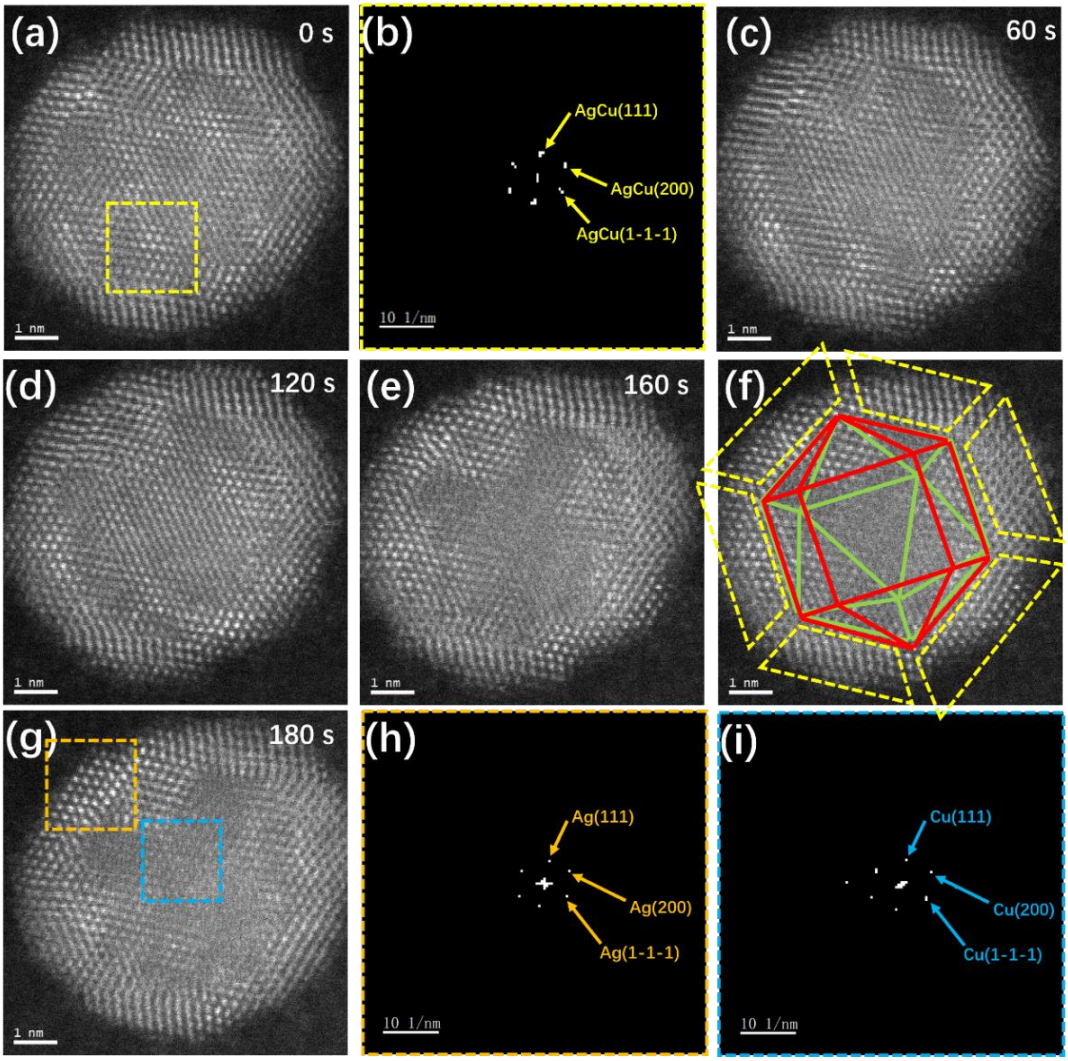


Figure 6.18: The phase separation process of prepared AgCu@Ag core-shell cluster under the e-beam irradiation for three minutes with a dose of 1.52×10^5 e^-/angstrom^2/frame. (a) and (c)-(g) HAADF-STEM images of the same cluster at different time. (b), (h), and (i) The FFT images of the yellow, orange, and blue boxes in (a) and (g), respectively. (f) The schematic image to show the core-shell structure in (e) can be considered as a Cu-Ih or Cu-Dh core and a shell formed by six Ag FCC domains.

6.4 Conclusions

Ag@Cu and Cu@Ag core-shell clusters were prepared by using different condensation lengths of separate targets. To prepare mass-selected Ag@Cu clusters, a power range of 15 W to 25 W was used. By adjusting the sputtering powers of the Cu target, the thickness of the Cu shell could be modified. For the AgCu clusters prepared with the

same parameters, a high fraction of Ag@Cu core-shell clusters will be obtained with larger sizes. Regarding the atomic structures of the prepared Ag@Cu clusters, the Cu atoms always arrange according to the surface arrangement of the Ag core. However, a Cu-Ih or Cu-Dh core with a shell formed by Ag FCC domains is common to observe in Cu@Ag core-shell clusters. Compared to the common Ih structure of single Ag clusters and FCC structure of Cu clusters, the atomic arrangement of the shell exhibited different atomic structures, potentially providing a novel method for surface structure-controlled preparation.

Furthermore, when longer condensation length of Ag target is used, the Cu target plasma can promote the growth of the passing Ag clusters, resulting in larger sizes and a spherical morphology. Additionally, the charge status of the passing clusters can be altered by the Cu target plasma, leading to the absence of Ag@Cu clusters when the power of the Cu target is set at 30 W.

Chapter 7 Conclusions and Outlook

7.1 Conclusions

This thesis investigates the growth of size-selected Ag and AgCu clusters using a magnetron sputtering inert gas condensation mass-selected cluster source. The morphologies and atomic structures of clusters were analyzed using aberration corrected high-angle annular dark field scanning transmission electron microscopy (HAADF-STEM), enabling a detailed exploration and understanding of the growth process of Ag and AgCu clusters in the magnetron chamber.

First, size-selected Ag clusters ranging from 1k to 14k were prepared using the magnetron sputtering method, and their morphologies and atomic structures were analyzed through HAADF-STEM images. Several series of experiments were conducted to demonstrate that Ag clusters exhibit spherical shapes when their size is smaller than the peak size of the mass spectrum. Conversely, as the size surpasses the peak size, there is an increase in elongated clusters. Hence, the peak size serves as the largest size that allows Ag clusters to maintain a spherical shape. The structures of spherical Ag clusters exhibit a linear dependence with mass-selected size, wherein the proportion of the Ih structure decreases while that of the Dh and FCC structure increases. On the other hand, the Ih structure dominates the structures of domains in aggregated clusters for the full range of studied sizes.

A possible model of the growth process is proposed for Ag clusters in the magnetron sputtering chamber. Most spherical clusters are formed in the area close to the target, so there will be a high fraction of Ih structures for small clusters because the Ih structure is the most stable structure for clusters with small sizes and the atom-addition growth can help small clusters keep their initial Ih structure during growth. In contrast, most elongated clusters are formed in areas away from the target by cluster-cluster coalescence growth. Some of these aggregated clusters can aggregate completely and achieve a structure transition, while others cannot completely aggregate into clusters with spherical shapes and keep the elongated shape even after they escape from the magnetron chamber.

E-beam irradiation and chip-heating experiments were conducted to investigate the most stable structure for Ag clusters in the size range of 1k to 14k. The results revealed that the Dh structure is the equilibrium state of Ag clusters in this size range. E-beam irradiation experiments showed a complete Ih-to-Dh structure transition process for Ag1k, Ag2k, and Ag6525 clusters, but Ag8k and Ag12k clusters required higher energy barriers to achieve the structure transition. Heating spherical Ag8k clusters at 100 to 600 °C resulted in a decrease in the proportion of Ih structure and an increase in the proportion of Dh structure, while the proportion of FCC structure remained relatively stable. Moreover, some Ag8k clusters with UI structure were observed due to the rearrangement of atoms. The Ih-to-Dh structure transition was also observed during the heating process of Ag14k clusters.

The heating experiment conducted on elongated Ag8k clusters revealed insightful findings. When two Ag clusters with similar sizes aggregate, it is highly probable that a Dh structure is formed, whereas the aggregation of two clusters with significant size differences is complicated. In cases where the main domain has an Ih structure, the products of aggregation could be Ih, Dh, and UI structures. Conversely, when the main domain has a Dh structure, the Dh structure will be obtained. The energy barrier for the formation of a Dh structure is lower for elongated Ag clusters than for spherical ones.

To understand the role of Ar and He gases in the cluster growth process, Ag8k clusters were prepared with varying flow rates of these gases. The results indicate that a low Ar gas flow rate and a high He gas flow rate will both result in the formation of many elongated clusters due to the inefficient aggregation process when Ag8k is much larger than the peak size. Atom addition is the dominant growth path for Ag8k clusters when the Ar gas flow rate is low. With an increase in the Ar gas flow rate, the growth path shifts from atom addition to cluster-cluster coalescence. In contrast, the He gas flow rate has little effect on the cluster-cluster coalescence growth path. Even with a He gas flow rate of 50 sccm, cluster-cluster coalescence remains the dominant path.

A simulation was proposed to explain the relationship between the mass spectrum and the growth process. With sufficient collision, a Gaussian size distribution is obtained, while the size distribution shows a Lognormal shape with insufficient collision. The simulation results are consistent with the experimental results observed in Ag8k deposited with different Ar gas flow rates.

Finally, Ag@Cu and Cu@Ag core-shell clusters were prepared using a magnetron sputtering gas condensation source. The material of the core or shell can be chosen by using different condensation lengths of separate targets. In addition, the thickness of the shell can be adjusted with different sputtering powers. The core-shell structure was confirmed by STEM and EDX analysis of the particles. Regarding the atomic structures of the prepared Ag@Cu clusters, the Cu atoms always arrange according to the surface arrangement of the Ag core. However, a Cu-Ih or Cu-Dh core with a shell formed by Ag FCC domains is common to observe in Cu@Ag core-shell clusters. Furthermore, when longer condensation length of Ag target is used, the Cu target plasma can promote the growth of the passing Ag clusters, resulting in larger sizes and a spherical morphology. Additionally, the charge status of the passing clusters can be altered by the Cu target plasma, leading to the absence of Ag@Cu clusters when the power of the Cu target is set at 30 W.

7.2 Outlook

Chapter 2.3 highlights the ageing process of Ag clusters, revealing that the shell composition of Ag clusters exposed to air is mainly S. Based on these results, further investigation using Environmental Transmission Electron Microscopy (ETEM) is helpful to understand the detailed transition process of the core-shell morphology. Additionally, the characterization of the atomic structures of the sulfide shell can help to reveal the impact of the shell on the initial atomic structures of Ag cores.

In chapter 3, the study shows that the peak size of the mass spectrum is the largest size that can maintain a spherical shape for Ag clusters deposited under the same parameters. A further simulation work can help to gain deeper insights into the growth process of Ag clusters in a magnetron sputtering chamber.

Chapter 4 reports the Ih-to-Dh transition process under e-beam irradiation. Well-designed ETEM or liquid-cell TEM experiments can potentially provide real-time observations of the structure formation process in organic or inorganic solutions. The nuclear and formation environments of metal clusters in these methods are different, and hence, the mechanisms of the structure formation will differ. Such experiments could help to explain the abundance of these non-crystalline structures in nature.

Chapter 6 has provided new insights into the morphological and atomic controlled preparation of bimetallic clusters. Further investigations on the phase or structure transition process of bimetallic clusters under elevated temperatures or gas phases are

exciting fields to explore, which are significant in revealing the real reaction sites in catalysis.

References

[1] K. An, G.A. Somorjai, Size and Shape Control of Metal Nanoparticles for Reaction Selectivity in Catalysis, ChemCatChem. 4 (2012) 1512–1524.

[2] I. Lee, F. Delbecq, R. Morales, M.A. Albiter, F. Zaera, Tuning selectivity in catalysis by controlling particle shape, Nat Mater. 8 (2009) 132–138.

[3] G.Y. Tonga, K. Saha, V.M. Rotello, 25th anniversary article: Interfacing nanoparticles and biology: New strategies for biomedicine, Adv Mater. 26 (2014) 359–370.

[4] H.A. Atwater, A. Polman, Plasmonics for improved photovoltaic devices, Nat Mater. 9 (2010) 205–213.

[5] S. Linic, U. Aslam, C. Boerigter, M. Morabito, Photochemical transformations on plasmonic metal nanoparticles, Nat Mater. 14 (2015) 567–576.

[6] A. Gurlo, Nanosensors: Towards morphological control of gas sensing activity. SnO_2, In_2O_3, ZnO and WO_3 case studies, Nanoscale. 3 (2011) 154–165.

[7] S. Syrenova, C. Wadell, F.A.A. Nugroho, T.A. Gschneidtner, Y.A. Diaz Fernandez, G. Nalin, D. Witlik, F. Westerlund, T.J. Antosiewicz, V.P. Zhdanov, K. Moth-Poulsen, C. Langhammer, Hydride formation thermodynamics and hysteresis in individual Pd nanocrystals with different size and shape, Nat Mater. 14 (2015) 1236–1244.

[8] F. Baletto, Structural properties of sub-nanometer metallic clusters, J Phys Condens Matter. 31 (2019) 113001-113041.

[9] I. Ban, J. Stergar, M. Drofenik, G. Ferk, D. Makovec, Synthesis of copper-nickel nanoparticles prepared by mechanical milling for use in magnetic hyperthermia, J Magn Magn Mater. 323 (2011) 2254–2258.

[10] P.P. Chin, J. Ding, J.B. Yi, B.H. Liu, Synthesis of FeS_2 and FeS nanoparticles by high-energy mechanical milling and mechanochemical processing, J Alloys Compd. 390 (2005) 255–260.

[11] M. Hu, S. Furukawa, R. Ohtani, H. Sukegawa, Y. Nemoto, J. Reboul, S. Kitagawa, Y. Yamauchi, Synthesis of Prussian blue nanoparticles with a hollow interior by controlled chemical etching, Angew Chem Int Ed Engl. 51 (2012) 984–988.

[12] K. An, S.G. Kwon, M. Park, H. bin Na, S.I. Baik, J.H. Yu, D. Kim, J.S. Son, Y.W. Kim, I.C. Song, W.K. Moon, H.M. Park, T. Hyeon, Synthesis of uniform hollow oxide nanoparticles through nanoscale acid etching, Nano Lett. 8 (2008) 4252–4258.

[13] S. Mohammadi, A. Harvey, K.V.K. Boodhoo, Synthesis of TiO_2 nanoparticles in a spinning disc reactor, Chem Eng J. 258 (2014) 171–184.

[14] C.Y. Tai, C. te Tai, M.H. Chang, H.S. Liu, Synthesis of magnesium hydroxide and oxide nanoparticles using a spinning disk reactor, Ind Eng Chem Res. 46 (2007) 5536–5541.

[15] S. Mann, S.L. Burkett, S.A. Davis, C.E. Fowler, N.H. Mendelson, S.D. Sims, D. Walsh, N.T. Whilton, Sol-Gel Synthesis of Organized Matter, Chem Mater. 9 (1997) 2300-2310.

[16] S. Bhaviripudi, E. Mile, S.A. Steiner, A.T. Zare, M.S. Dresselhaus, A.M. Belcher, J. Kong, CVD synthesis of single-walled carbon nanotubes from gold nanoparticle catalysts, J Am Chem Soc. 129 (2007) 1516–1517.
[17] M. Adachi, S. Tsukui, K. Okuyama, Nanoparticle synthesis by ionizing source gas in chemical vapor deposition, Jpn J Appl Phys. 42 (2003) 77-79.
[18] S. Bao, M. Vara, X. Yang, S. Zhou, L. Figueroa-Cosme, J. Park, M. Luo, Z. Xie, Y. Xia, Facile Synthesis of Pd@Pt3–4L Core–Shell Octahedra with a Clean Surface and Thus Enhanced Activity toward Oxygen Reduction, ChemCatChem. 9 (2017) 414–419.
[19] B. Qiao, A. Wang, X. Yang, L.F. Allard, Z. Jiang, Y. Cui, J. Liu, J. Li, T. Zhang, Single-atom catalysis of CO oxidation using Pt_1/FeO_x, Nat Chem. 3 (2011) 634–641.
[20] Z.W. Chen, L.X. Chen, C.C. Yang, Q. Jiang, Atomic (single, double, and triple atoms) catalysis: Frontiers, opportunities, and challenges, J Mater Chem A Mater. 7 (2019) 3492–3515.
[21] M. Li, K. Duanmu, C. Wan, T. Cheng, L. Zhang, S. Dai, W. Chen, Z. Zhao, P. Li, H. Fei, Y. Zhu, R. Yu, J. Luo, K. Zang, Z. Lin, M. Ding, J. Huang, H. Sun, J. Guo, X. Pan, W.A. Goddard, P. Sautet, Y. Huang, X. Duan, Single-atom tailoring of platinum nanocatalysts for high-performance multifunctional electrocatalysis, Nat Catal. 2 (2019) 495–503.
[22] Y. Zhu, T. Wang, T. Xu, Y. Li, C. Wang, Size effect of Pt co-catalyst on photocatalytic efficiency of g-C3N4 for hydrogen evolution, Appl Surf Sci. 464 (2019) 36–42.
[23] M. Xiao, J. Zhu, G. Li, N. Li, S. Li, Z.P. Cano, L. Ma, P. Cui, P. Xu, G. Jiang, H. Jin, S. Wang, T. Wu, J. Lu, A. Yu, D. Su, Z. Chen, A Single-Atom Iridium Heterogeneous Catalyst in Oxygen Reduction Reaction, Angew Chem Int Ed Engl. 131 (2019) 9742–9747.
[24] Z. Zhang, C. Ma, Y. Tu, R. Si, J. Wei, S. Zhang, Z. Wang, J.F. Li, Y. Wang, D. Deng, Multiscale carbon foam confining single iron atoms for efficient electrocatalytic CO_2 reduction to CO, Nano Res. 12 (2019) 2313–2317.
[25] X. Cao, Y. Ji, Y. Luo, Dehydrogenation of propane to propylene by a Pd/Cu single-atom catalyst: Insight from first-principles calculations, J Phys Chem C. 119 (2015) 1016–1023.
[26] B. Long, Y. Tang, J. Li, New mechanistic pathways for CO oxidation catalyzed by single-atom catalysts: Supported and doped Au_1/ThO_2, Nano Res. 9 (2016) 3868–3880.
[27] P. Song, M. Luo, X. Liu, W. Xing, W. Xu, Z. Jiang, L. Gu, Zn Single Atom Catalyst for Highly Efficient Oxygen Reduction Reaction, Adv Funct Mater. 27 (2017) 1700802.
[28] X. Zhou, Q. Shen, K. Yuan, W. Yang, Q. Chen, Z. Geng, J. Zhang, X. Shao, W. Chen, G. Xu, X. Yang, K. Wu, Unraveling Charge State of Supported Au Single-Atoms during CO Oxidation, J Am Chem Soc. 140 (2018) 554–557.
[29] Z.Y. Wu, X.X. Xu, B.C. Hu, H.W. Liang, Y. Lin, L.F. Chen, S.H. Yu, Iron Carbide Nanoparticles Encapsulated in Mesoporous Fe-N-Doped Carbon Nanofibers for

Efficient Electrocatalysis, Angew Chem Int Ed Engl. 54 (2015) 8179-8183A.
[30] X. Hong, K. Chan, C. Tsai, J.K. Nørskov, How Doped MoS_2 Breaks Transition-Metal Scaling Relations for CO_2 Electrochemical Reduction, ACS Catal. 6 (2016) 4428–4437.
[31] X.L. Ma, J.C. Liu, H. Xiao, J. Li, Surface Single-Cluster Catalyst for N_2-to-NH_3 Thermal Conversion, J Am Chem Soc. 140 (2018) 46–49.
[32] J.C. Liu, X.L. Ma, Y. Li, Y.G. Wang, H. Xiao, J. Li, Heterogeneous Fe_3 single-cluster catalyst for ammonia synthesis via an associative mechanism, Nat Commun. 9 (2018) 1610.
[33] J.-C. Liu, H. Xiao, X.-K. Zhao, N.-N. Zhang, Y. Liu, D.-H. Xing, X. Yu, H.-S. Hu, J. Li, Computational Prediction of Graphdiyne-Supported Three-Atom Single-Cluster Catalysts, CCS Chemistry. (2022) 1–12.
[34] S. Ji, Y. Chen, S. Zhao, W. Chen, L. Shi, Y. Wang, J. Dong, Z. Li, F. Li, C. Chen, Q. Peng, J. Li, D. Wang, Y. Li, Atomically Dispersed Ruthenium Species Inside Metal–Organic Frameworks: Combining the High Activity of Atomic Sites and the Molecular Sieving Effect of MOFs, Angew Chem Int Ed Engl. 58 (2019) 4271–4275.
[35] L. Liu, A. Corma, Metal Catalysts for Heterogeneous Catalysis: From Single Atoms to Nanoclusters and Nanoparticles, Chem Rev. 118 (2018) 4981–5079.
[36] W. Pei, S. Zhou, J. Zhao, X. Xu, Y. Du, S.X. Dou, Immobilized trimeric metal clusters: A family of the smallest catalysts for selective CO_2 reduction toward multi-carbon products, Nano Energy. 76 (2020) 105049.
[37] H. Li, L. Wang, Y. Dai, Z. Pu, Z. Lao, Y. Chen, M. Wang, X. Zheng, J. Zhu, W. Zhang, R. Si, C. Ma, J. Zeng, Synergetic interaction between neighbouring platinum monomers in CO_2 hydrogenation, Nat Nanotechnol. 13 (2018) 411–417.
[38] J. Wang, R. You, C. Zhao, W. Zhang, W. Liu, X.P. Fu, Y. Li, F. Zhou, X. Zheng, Q. Xu, T. Yao, C.J. Jia, Y.G. Wang, W. Huang, Y. Wu, N-Coordinated Dual-Metal Single-Site Catalyst for Low-Temperature CO Oxidation, ACS Catal. 10 (2020) 2754–2761.
[39] G. Casillas, J.J. Velázquez-Salazar, M. Jose-Yacaman, A new mechanism of stabilization of large decahedral nanoparticles, J Phys Chem C. 116 (2012) 8844–8848.
[40] C.L. Johnson, E. Snoeck, M. Ezcurdia, B. Rodríguez-González, I. Pastoriza-Santos, L.M. Liz-Marzán, M.J. Htch, Effects of elastic anisotropy on strain distributions in decahedral gold nanoparticles, Nat Mater. 7 (2008) 120–124.
[41] L.D. Marks, Modified Wulff constructions for twinned particles, J Cryst Growth. 61 (1983) 556-566.
[42] R. Vajtai, Springer handbook of nanomaterials, Springer, 2013.
[43] I. V Chepkasov, Y.U. Ya Gafner, S.L. Gafner, S.P. Bardakhanov, The general mechanisms of Cu cluster formation in the processes of condensation from the gas phase, Bull Mater Sci. 38 (2015) 701-706.
[44] S.R. Plant, L. Cao, R.E. Palmer, Atomic structure control of size-selected gold nanoclusters during formation, J Am Chem Soc. 136 (2014) 7559–7562.

[45] S. Lu, K. Hu, Z. Zuo, S. Hu, G. Wang, F. Song, L. Cao, Beam generation and structural optimization of size-selected Au923clusters, Nanoscale Adv. 2 (2020) 2720–2725.
[46] R. Ferrando, J. Jellinek, R.L. Johnston, Nanoalloys: From theory to applications of alloy clusters and nanoparticles, Chem Rev. 108 (2008) 845–910.
[47] F. Yin, Z.W. Wang, R.E. Palmer, Controlled formation of mass-selected Cu-Au core-shell cluster beams, J Am Chem Soc. 133 (2011) 10325–10327.
[48] F. Yin, Z.W. Wang, R.E. Palmer, Ageing of mass-selected cu/au and au/cu core/shell clusters probed with atomic resolution, J Exp Nanosci. 7 (2012) 703–710.
[49] A.I. Ayesh, N. Qamhieh, S.T. Mahmoud, H. Alawadhi, Fabrication of size-selected bimetallic nanoclusters using magnetron sputtering, J Mater Res. 27 (2012) 2441–2446.
[50] P. Grammatikopoulos, J. Kioseoglou, A. Galea, J. Vernieres, M. Benelmekki, R.E. Diaz, M. Sowwan, Kinetic trapping through coalescence and the formation of patterned Ag-Cu nanoparticles, Nanoscale. 8 (2016) 9780–9790.
[51] R. Cai, P.R. Ellis, J. Yin, J. Liu, C.M. Brown, R. Griffin, G. Chang, D. Yang, J. Ren, K. Cooke, P.T. Bishop, W. Theis, R.E. Palmer, Performance of Preformed Au/Cu Nanoclusters Deposited on MgO Powders in the Catalytic Reduction of 4-Nitrophenol in Solution, Small. 14 (2018) 5375-5383.
[52] G. Krishnan, M.A. Verheijen, G.H. Ten Brink, G. Palasantzas, B.J. Kooi, Tuning structural motifs and alloying of bulk immiscible Mo-Cu bimetallic nanoparticles by gas-phase synthesis, Nanoscale. 5 (2013) 5375–5383.
[53] F. Ruffino, E.F. Pecora, M.G. Grimaldi, Generation and self-organization of bimetallic Pd/Au nanoparticles on SiO2 by sequential sputtering depositions and annealing processes, J Nanosci Nanotechnol. 12 (2012) 8537–8545.
[54] L. Martínez, M. Díaz, E. Román, M. Ruano, D. Llamosa P., Y. Huttel, Generation of nanoparticles with adjustable size and controlled stoichiometry: Recent advances, Langmuir. 28 (2012) 11241–11249.
[55] E. Pérez-Tijerina, S. Mejía-Rosales, H. Inada, M. José-Yacamán, Effect of temperature on AuPd nanoparticles produced by inert gas condensation, J Phys Chem C. 114 (2010) 6999–7003.
[56] J.L. Rodríguez-López, J.M. Montejano-Carrizales, U. Pal, J.F. Sánchez-Ramírez, H.E. Troiani, D. García, M. Miki-Yoshida, M. José-Yacamán, Surface reconstruction and decahedral structure of bimetallic nanoparticles, Phys Rev Lett. 92 (2004) 196102.
[57] A. Mayoral, D. Llamosa, Y. Huttel, A novel Co@Au structure formed in bimetallic core@shell nanoparticles, ChemComm. 51 (2015) 8442–8445.
[58] T. Kretková, J. Hanuš, O. Kylián, P. Solař, M. Dopita, M. Cieslar, I. Khalakhan, A. Choukourov, H. Biederman, In-flight modification of Ni nanoparticles by tubular magnetron sputtering, J Phys D Appl Phys. 51 (2019) 205302.
[59] V. Moreno, J. Creuze, F. Berthier, C. Mottet, G. Tréglia, B. Legrand, Site segregation in size-mismatched nanoalloys: Application to Cu-Ag, Surf Sci. 600

(2006) 5011–5020.
[60] A. Mayoral, L. Martínez, J.M. García-Martín, I. Fernández-Martínez, M. García-Hernández, B. Galiana, C. Ballesteros, Y. Huttel, Tuning the size, composition and structure of Au and $Co_{50}Au_{50}$ nanoparticles by high-power impulse magnetron sputtering in gas-phase synthesis, Nanotechnology. 30 (2019) 065606.
[61] S. Swann, Magnetron sputtering, Physics in technology. 19 (1988) 67-75.
[62] O. Polonskyi, A.M. Ahadi, T. Peter, K. Fujioka, J.W. Abraham, E. Vasiliauskaite, A. Hinz, T. Strunskus, S. Wolf, M. Bonitz, H. Kersten, F. Faupel, Plasma based formation and deposition of metal and metal oxide nanoparticles using a gas aggregation source, Eur Phys J D. 72 (2018) 1-13.
[63] S. Pratontep, S.J. Carroll, C. Xirouchaki, M. Streun, R.E. Palmer, Size-selected cluster beam source based on radio frequency magnetron plasma sputtering and gas condensation, Rev Sci Instrum. 76 (2005) 045103.
[64] B. Von Issendorff, R.E. Palmer, A new high transmission infinite range mass selector for cluster and nanoparticle beams, Rev Sci Instrum. 70 (1999) 4497–4501.
[65] H. Hsieh, R.S. Averback, H. Sellers, C.P. Flynn, Molecular-dynamics simulations of collisions between energetic clusters of atoms and metal substrates, Phys Rev B. 45 (1992) 4417-4430.
[66] V.N. Popok, I. Barke, E. E.B. Campbell, K. Meiwes-Broer, Cluster-surface interaction: From soft landing to implantation, Surf Sci Rep. 66 (2011) 347-377.
[67] H. Haberland, M. Karrais, M. Mall, Y. Thurner, Thin films from energetic cluster impact: A feasibility study, J Vac Sci Technol A. 10 (1992) 3266–3271.
[68] G.E. Johnson, R. Colby, J. Laskin, Soft landing of bare nanoparticles with controlled size, composition, and morphology, Nanoscale. 7 (2015) 3491–3503.
[69] K.R. Bray, C.Q. Jiao, J.N. Decerbo, Nucleation and growth of Nb nanoclusters during plasma gas condensation, J Appl Phys. 113 (2013) 234307.
[70] E. Quesnel, E. Pauliac-Vaujour, V. Muffato, Modeling metallic nanoparticle synthesis in a magnetron-based nanocluster source by gas condensation of a sputtered vapor, J Appl Phys. 107 (2010) 054309.
[71] K.R. Bray, C.Q. Jiao, J.N. DeCerbo, Influence of carrier gas on the nucleation and growth of Nb nanoclusters formed through plasma gas condensation, J Vac Sci Technol B. 32 (2014) 031805.
[72] M. Khojasteh, V. V. Kresin, Influence of source parameters on the growth of metal nanoparticles by sputter-gas-aggregation, Appl Nanosci. 7 (2017) 875–883.
[73] M. Gracia-Pinilla, E. Martínez, G.S. Vidaurri, E. Pérez-Tijerina, Deposition of Size-Selected Cu Nanoparticles by Inert Gas Condensation, Nanoscale Res Lett. 5 (2010) 180–188.
[74] E. Rutherford, LXXIX. The scattering of α and β particles by matter and the structure of the atom, Lond Edinb Dublin philos mag j sci. 21 (1911) 669–688.
[75] Z.W. Wang, Z.Y. Li, S.J. Park, A. Abdela, D. Tang, R.E. Palmer, Quantitative Z-contrast imaging in the scanning transmission electron microscope with size-selected clusters, Phys Rev B Condens Matter Mater Phys. 84 (2011) 073408.
[76] D.B. Williams, C.B. Carter, Transmission electron microscopy: a textbook for

materials science, Springer, 2009.
[77] L. Rayleigh, Investigations in optics, with special reference to the spectroscope, Lond Edinb Dublin philos mag j sci. 8 (1879) 261-274.
[78] N. Tanaka, Scanning Transmission Electron Microscopy of Nanomaterials: Basics of Imaging and Analysis, World Scientific, 2014.
[79] P.W. Hawkes, Aberration correction past and present, Philos Trans Royal Soc A. 367 (2009) 3637–3664.
[80] N. Otsu, A Threshold Selection Method from Gray-Level Histograms, IEEE Trans Syst Man Cybern Syst. 9 (1979) 62-66.
[81] J. Thibaud, Behaviour of a Particle of Very Small Mass in a Magnetic Field, Nature. 162 (1948) 329-329.
[82] M. Seidl, M. Brack, Liquid Drop Model for Charged Spherical Metal Clusters, Ann Phys. 245 (1996) 275-310.
[83] W.D. Knight, K. Clemenger, W.A. De Heer, W.A. Saunders, M.Y. Chou, M.L. Cohen, Electronic shell structure and abundances of sodium clusters, Phys Rev Lett. 52 (1984) 2141.
[84] D.S. He, Z.Y. Li, J. Yuan, Kinematic HAADF-STEM image simulation of small nanoparticles, Micron. 74 (2015) 47-53.
[85] H.E. Bennett, R.L. Peck, D.K. Burge, J.M. Bennett, Formation and growth of tarnish on evaporated silver films, J Appl Phys. 40 (1969) 3351–3360.
[86] T.E. Graedel, J.P. Franey, G.J. Gualtieri, G.W. Kammlott, D.L. Malm, On the mechanism of silver and copper sulfidation by atmospheric H_2S and OCS, Corros Sci. 25 (1985) 1163-1180.
[87] F. Zacharatos, I. Theodorakos, P. Karvounis, S. Tuohy, N. Braz, S. Melamed, A. Kabla, F.D. Vega, K. Andritsos, A. Hatziapostolou, D. Karnakis, I. Zergioti, Selective laser sintering of laser printed Ag nanoparticle micropatterns at high repetition rates, Materials. 11 (2018) 2142.
[88] M. Gracia-Pinilla, E. Martínez, G.S. Vidaurri, E. Pérez-Tijerina, Deposition of Size-Selected Cu Nanoparticles by Inert Gas Condensation, Nanoscale Res Lett. 5 (2010) 180–188.
[89] I. Shyjumon, M. Gopinadhan, O. Ivanova, M. Quaas, H. Wulff, C.A. Helm, R. Hippler, Structural deformation, melting point and lattice parameter studies of size selected silver clusters, Eur Phys J D. 37 (2006) 409–415.
[90] R.M. Nielsen, S. Murphy, C. Strebel, M. Johansson, I. Chorkendorff, J.H. Nielsen, The morphology of mass selected ruthenium nanoparticles from a magnetron-sputter gas-aggregation source, J Nanopart Res. 12 (2010) 1249–1262.
[91] K.J. Hu, S.R. Plant, P.R. Ellis, C.M. Brown, P.T. Bishop, R.E. Palmer, Atomic Resolution Observation of a Size-Dependent Change in the Ripening Modes of Mass-Selected Au Nanoclusters Involved in CO Oxidation, J Am Chem Soc. 137 (2015) 15161–15168.
[92] A. Beniya, S. Higashi, N. Ohba, R. Jinnouchi, H. Hirata, Y. Watanabe, CO oxidation activity of non-reducible oxide-supported mass-selected few-atom Pt single-clusters, Nat Commun. 11 (2020) 1888.

[93] D. Pearmain, S.J. Park, A. Abdela, R.E. Palmer, Z.Y. Li, The size-dependent morphology of Pd nanoclusters formed by gas condensation, Nanoscale. 7 (2015) 19647–19652.
[94] J.P.K. Doye, F. Calvo, Entropic effects on the size dependence of cluster structure, Phys Rev Lett. 86 (2001) 3570–3573.
[95] F. Baletto, R. Ferrando, A. Fortunelli, F. Montalenti, C. Mottet, Crossover among structural motifs in transition and noble-metal clusters, J Chem Phys. 116 (2002) 3856–3863.
[96] K. Koga, K. Sugawara, Population statistics of gold nanoparticle morphologies direct determination by HREM observations, Surf Sci. 529 (2003) 23-35.
[97] Z.Y. Li, N.P. Young, M. Di Vece, S. Palomba, R.E. Palmer, A.L. Bleloch, B.C. Curley, R.L. Johnston, J. Jiang, J. Yuan, Three-dimensional atomic-scale structure of size-selected gold nanoclusters, Nature. 451 (2008) 46–48.
[98] Z.W. Wang, Z.Y. Li, S.J. Park, A. Abdela, D. Tang, R.E. Palmer, Quantitative Z-contrast imaging in the scanning transmission electron microscope with size-selected clusters, Phys Rev B Condens Matter Mater Phys. 84 (2011) 073408.
[99] M. Ganeva, A.V. Pipa, R. Hippler, The influence of target erosion on the mass spectra of clusters formed in the planar DC magnetron sputtering source, Surf Coat Technol. 213 (2012) 41-47.
[100] M. Khojasteh, V. V. Kresin, Influence of source parameters on the growth of metal nanoparticles by sputter-gas-aggregation, Appl Nanosci. 7 (2017) 875–883.
[101] D.M. Wells, G. Rossi, R. Ferrando, R.E. Palmer, Metastability of the atomic structures of size-selected gold nanoparticles, Nanoscale. 7 (2015) 6498–6503.
[102] G. Grochola, S.P. Russo, I.K. Snook, On morphologies of gold nanoparticles grown from molecular dynamics simulation, J Chem Phys. 126 (2007) 164707.
[103] J. Penuelas, P. Andreazza, C. Andreazza-Vignolle, H.C.N. Tolentino, M. De Santis, C. Mottet, Controlling structure and morphology of CoPt nanoparticles through dynamical or static coalescence effects, Phys Rev Lett. 100 (2008) 115502.
[104] D. Nelli, G. Rossi, Z. Wang, R.E. Palmer, R. Ferrando, Structure and orientation effects in the coalescence of Au clusters, Nanoscale. 12 (2020) 7688–7699.
[105] I. V Chepkasov, Y.U. Ya Gafner, S.L. Gafner, S.P. Bardakhanov, The general mechanisms of Cu cluster formation in the processes of condensation from the gas phase, B Mater Sci. 38 (2015) 701-706.
[106] K. Koga, T. Ikeshoji, K.I. Sugawara, Size- and Temperature-Dependent Structural Transitions in Gold Nanoparticles, Phys Rev Lett. 92 (2004) 115507.
[107] F. Baletto, R. Ferrando, Structural properties of nanoclusters: Energetic, thermodynamic, and kinetic effects, Rev Mod Phys. 77 (2005) 371.
[108] F. Baletto, C. Mottet, R. Ferrando, Microscopic mechanisms of the growth of metastable silver icosahedra, Phys Rev B Condens Matter Mater Phys. 63 (2001) 155408.
[109] K. Sasaki, N. Nafarizal, J.S. Gao, K. Shibagaki, Are dominant sputtering products from metal targets really monatomic? Vacuum. 83 (2008) 463–466.
[110] B. Wang, M. Liu, Y. Wang, X. Chen, Structures and energetics of silver and gold

nanoparticles, J Phys Chem C. 115 (2011) 11374–11381.
[111] K.D. Gilroy, J. Puibasset, M. Vara, Y. Xia, On the Thermodynamics and Experimental Control of Twinning in Metal Nanocrystals, Angew Chem Int Ed Engl. 129 (2017) 8773–8777.
[112] Q. Zhang, J. Xie, Y. Yu, J. Yang, J.Y. Lee, Tuning the crystallinity of Au nanoparticles, Small. 6 (2010) 523–527.
[113] A.A. Tal, E.P. Münger, I.A. Abrikosov, Morphology transition mechanism from icosahedral to decahedral phase during growth of Cu nanoclusters, Phys Rev B Condens Matter Mater Phys. 92 (2015) 020102.
[114] A.S. Barnard, N.P. Young, A.I. Kirkland, M.A. Van Huis, H. Xu, Nanogold: A quantitative phase map, ACS Nano. 3 (2009) 1431–1436.
[115] N.K. Manninen, N.M. Figueiredo, S. Carvalho, A. Cavaleiro, Production and characterization of Ag nanoclusters produced by plasma gas condensation, Plasma Process Polym. 11 (2014) 629–638.
[116] V. Singh, C. Cassidy, P. Grammatikopoulos, F. Djurabekova, K. Nordlund, M. Sowwan, Heterogeneous gas-phase synthesis and molecular dynamics modeling of janus and core-satellite Si-Ag nanoparticles, J Phys Chem C. 118 (2014) 13869–13875.
[117] A. Mayoral, D. Llamosa, Y. Huttel, A novel Co@Au structure formed in bimetallic core@shell nanoparticles, ChemComm. 51 (2015) 8442–8445.
[118] Z.Y. Jiang, K.H. Lee, S.T. Li, S.Y. Chu, Structures and charge distributions of cationic and neutral $Cu_{n-1}Ag$ clusters (n=2-8), Phys Rev B Condens Matter Mater Phys. 73 (2006) 235423.
[119] F. Lequien, J. Creuze, F. Berthier, B. Legrand, Superficial segregation in nanoparticles: From facets to infinite surfaces, J Chem Phys. 125 (2006) 094707.

Appendix

This appendix includes enlarged images of simulation atlases for Ag6525 COh, Ih, and square Ino-Dh structures, which can be found in Figure 2.18-2.20.

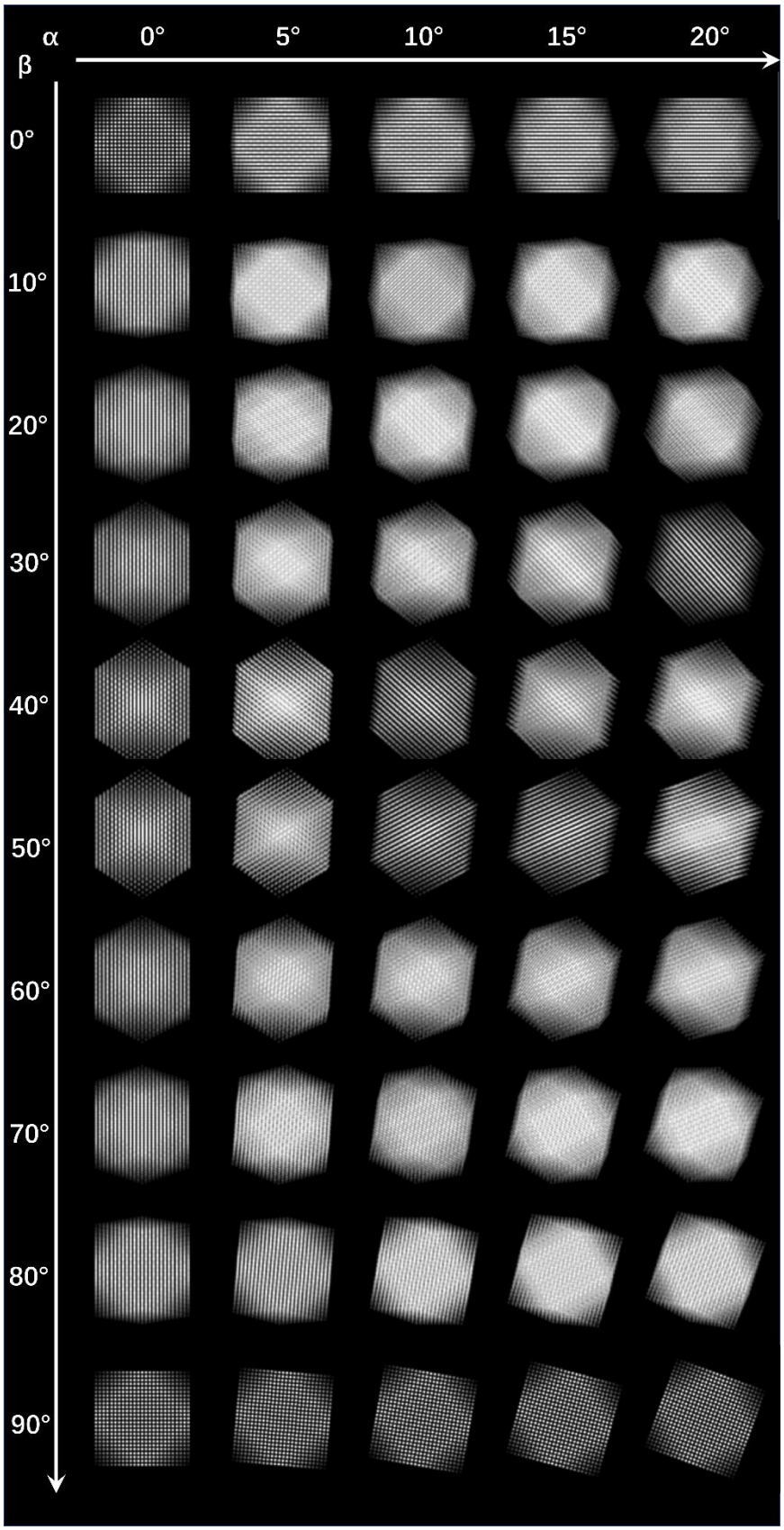


Figure 9.1: The enlarged simulation atlas of Ag6525 COh with α in 0-20° and β in 0-90°.

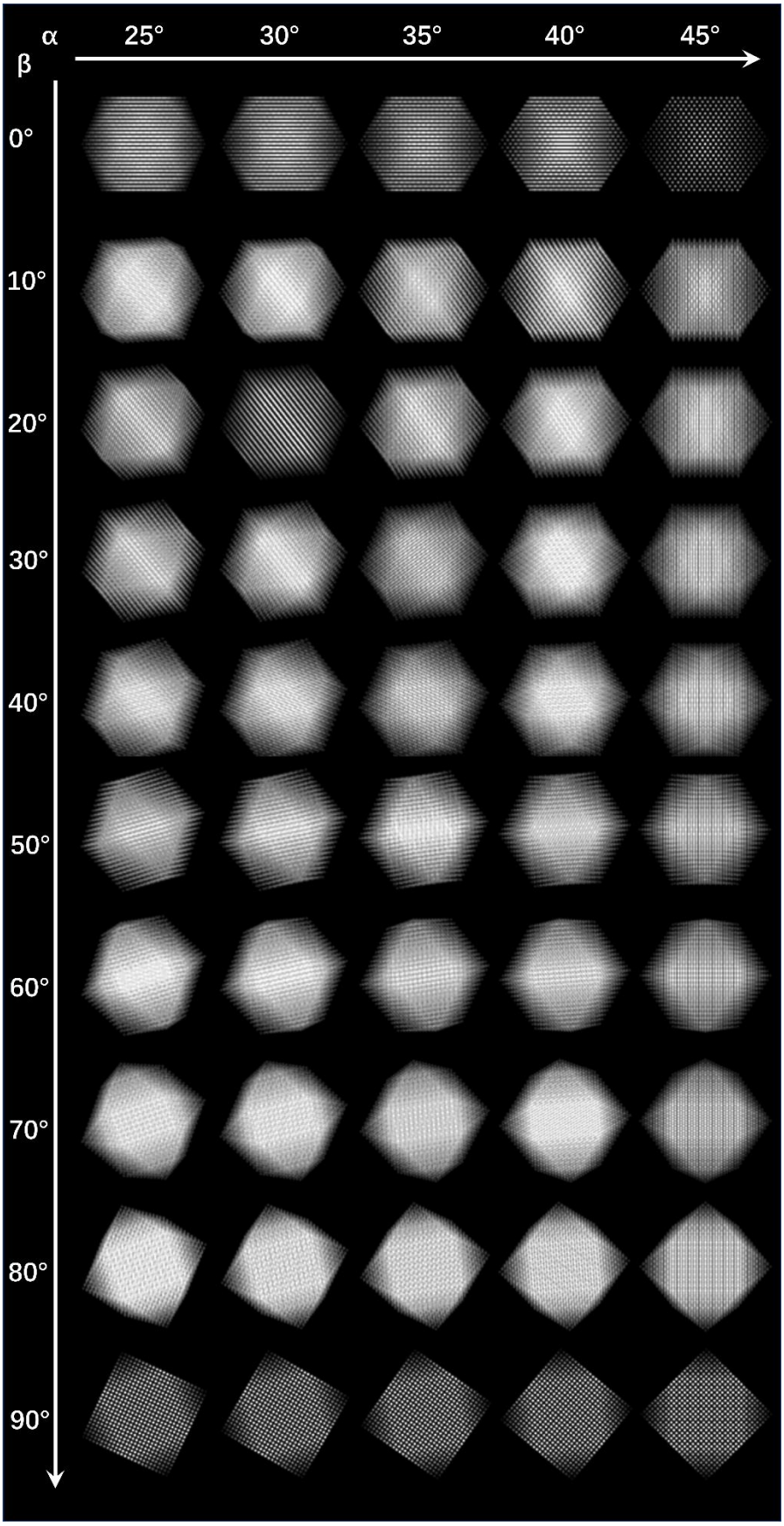


Figure 9.2: The enlarged simulation atlas of Ag6525 COh with α in 25-45° and β in 0-90°.

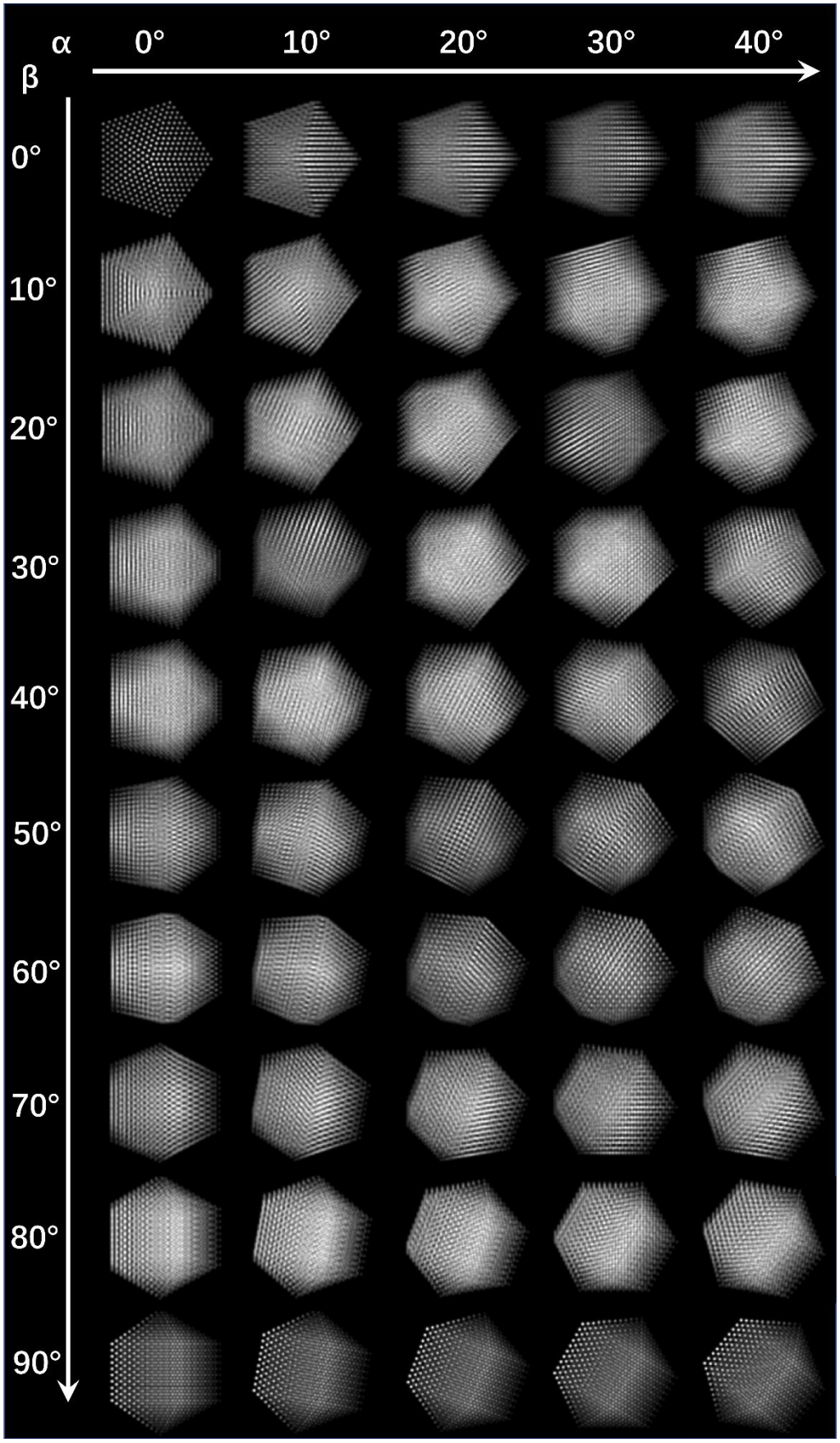


Figure 9.3: The enlarged simulation atlas of Ag6525 Dh with α in 0-40° and β in 0-90°.

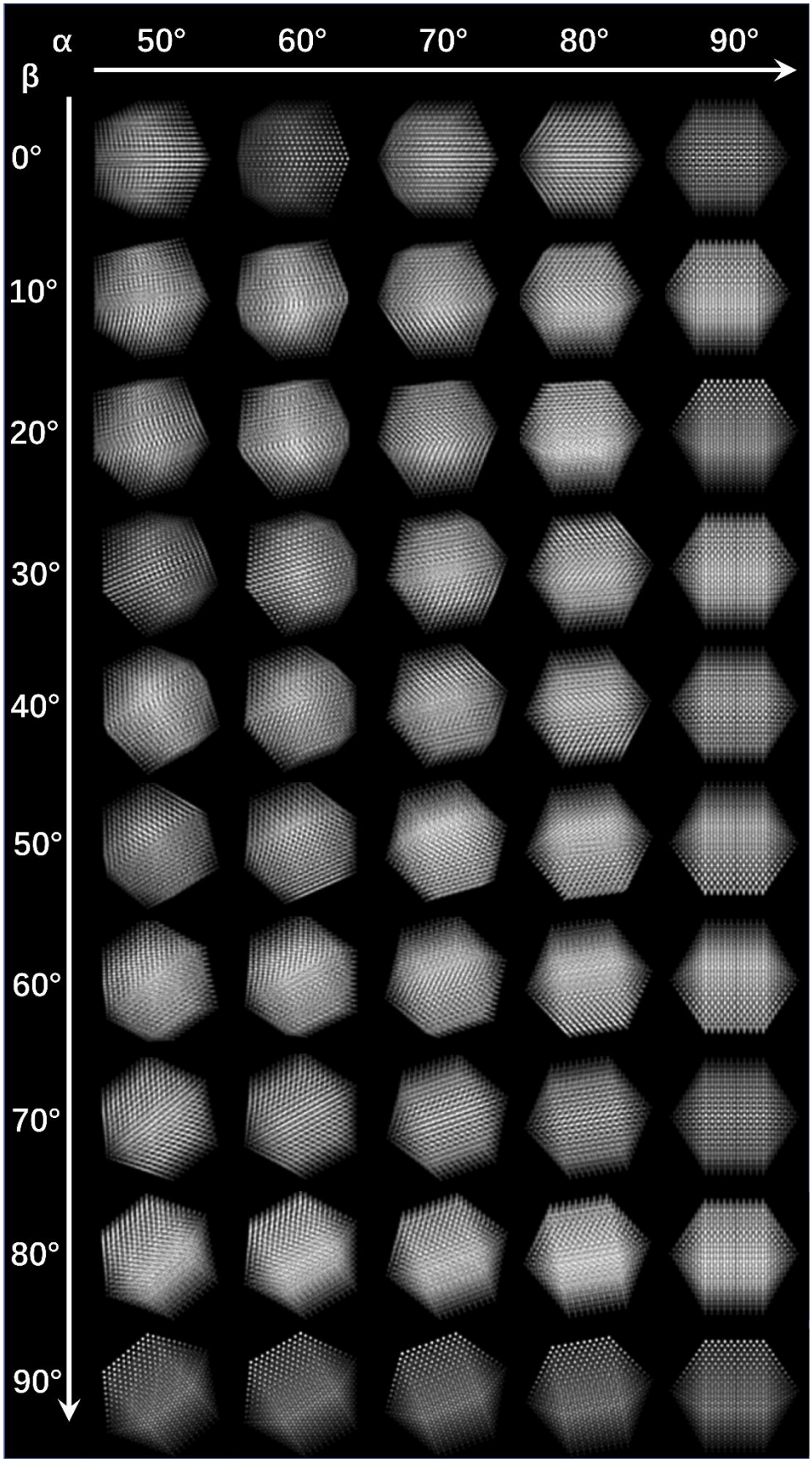


Figure 9.4: The enlarged simulation atlas of Ag6525 Dh with α in 50-90° and β in 0-90°.

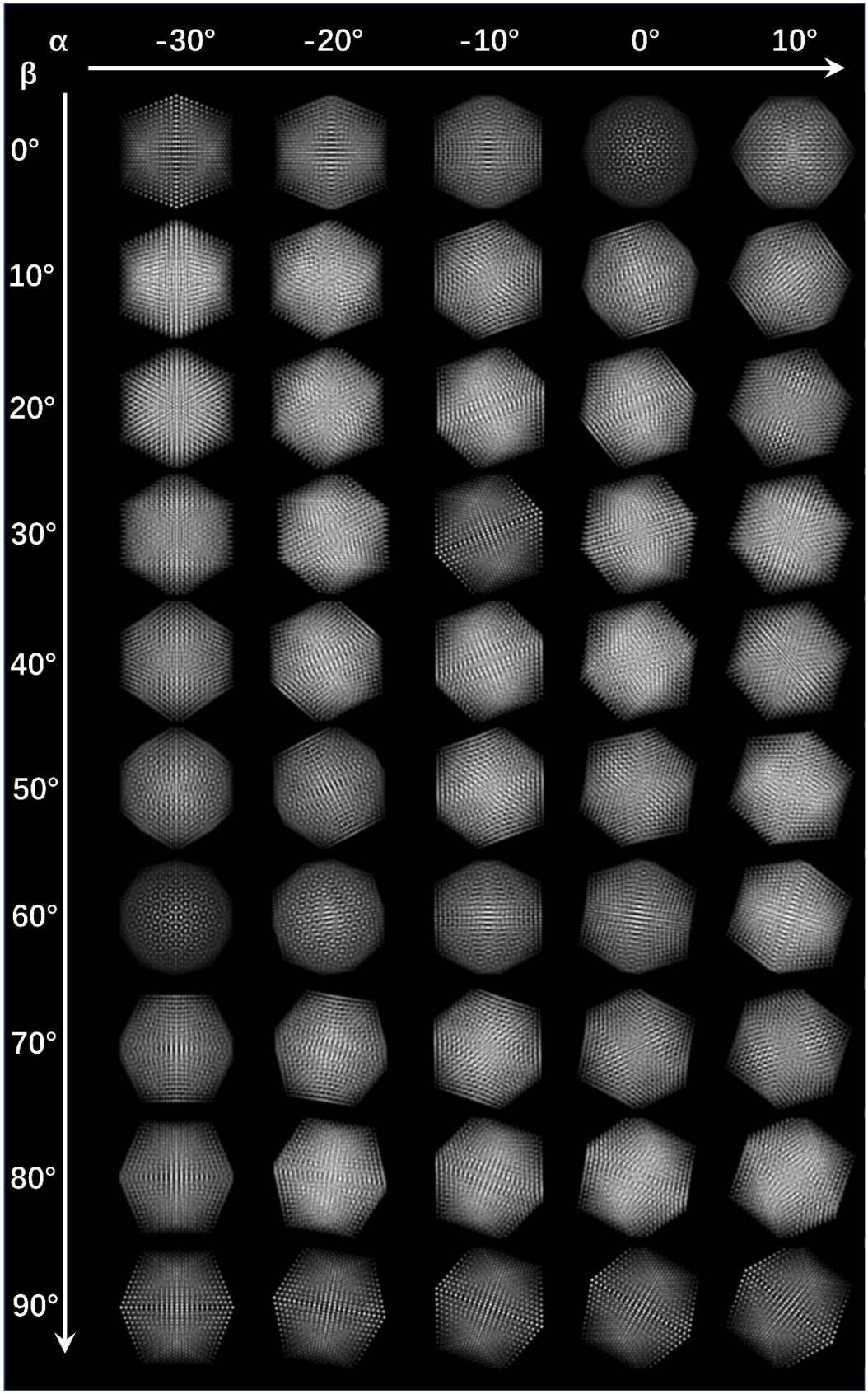


Figure 9.5: The enlarged simulation atlas of Ag6525 Ih with α in -30-10° and β in 0-90°.

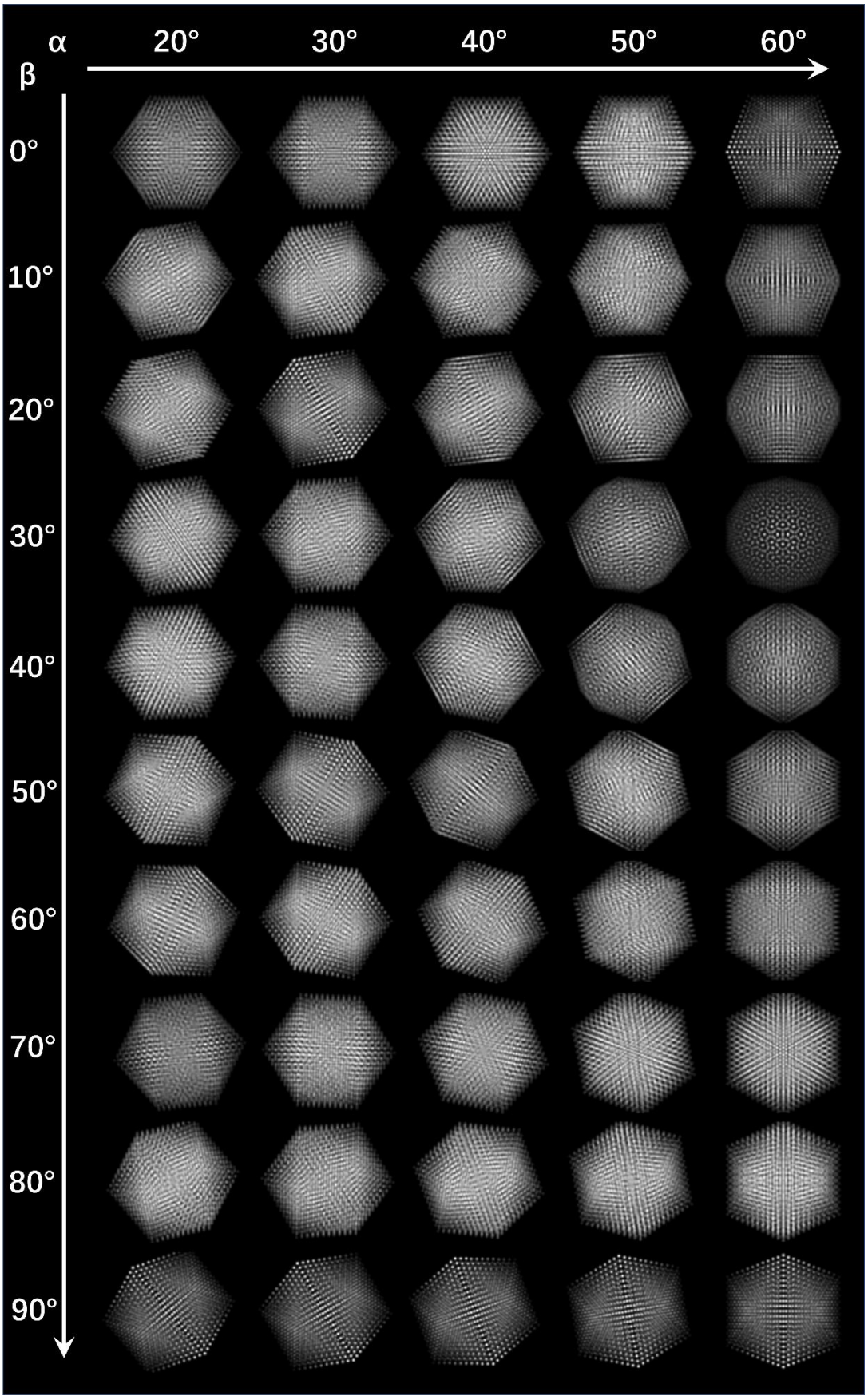


Figure 9.6: The enlarged simulation atlas of Ag6525 Ih with α in 20-60° and β in 0-90°.